IMAGING EARTHQUAKE RUPTURE BY WAVEFORM INVERSION

A DISSERTATION
SUBMITTED TO THE DEPARTMENT OF GEOPHYSICS
AND THE COMMITTEE ON GRADUATE STUDIES
OF STANFORD UNIVERSITY
IN PARTIAL FULFILLMENT OF THE REQUIREMENTS
FOR THE DEGREE OF
DOCTOR OF PHILOSOPHY

Brian P. Cohee

November 1995

© Copyright by Brian P. Cohee 1995
All Rights Reserved

I certify that I have read this dissertation and that in my opinion it is fully adequate, in scope and quality, as a dissertation for the degree of Doctor of Philosophy.

Gregory C. Beroza (Principal Advisor)

I certify that I have read this dissertation and that in my opinion it is fully adequate, in scope and quality, as a dissertation for the degree of Doctor of Philosophy.

Paul Segall

I certify that I have read this dissertation and that in my opinion it is fully adequate, in scope and quality, as a dissertation for the degree of Doctor of Philosophy.

Mark D. Zoback

Approved for the University Committee on Graduate Studies:

Abstract

Three inversion methods are presented that use near-source seismic waveforms to image rupture properties of large earthquakes. In each case, the objective is to solve for a detailed time and space description of rupture by minimizing the misfit between observed and predicted ground motion. The first two inversion methods are both linear and solved by non-negative least squares but the slip function is treated differently. The third method is nonlinear, assumes the slip amplitude distribution in advance, and solves for rupture propagation characteristics by reducing seismogram residuals iteratively; the assumed slip distribution is obtained from seismograms or geodetic measurements of co-seismic surface deformation.

Models of the 1992 M_W 7.3 Landers, California earthquake obtained with each method are compared. A fundamental trade-off between slip amplitude and rupture time exists in near-source seismograms and degrades model resolution; however, this trade-off is reduced when slip is resolved independently by geodetic measurements or surface fault offset. The models of the Landers earthquake reveal a highly variable distribution of slip amplitude, which is likely related to pre-existing strength or stress heterogeneity in the fault zone, and there is evidence that the rupture front slows down before and accelerates through high-slip regions. Slip terminated in the middle of a relatively straight fault segment, indicating that something other than segmentation was responsible for stopping rupture. The models are similar away from the hypocenter; near the hypocenter, either the slip duration is relatively long, or rupture growth is facilitated by dynamic stresses resulting from an immediate foreshock.

The greatest source of error in near-source waveform inversions results from an idealized theoretical description of the forward problem. An alternative approach is to define the forward problem empirically. Empirical Green's functions are derived from aftershock seismograms of the 1989 M_W 6.9 Loma Prieta, California earthquake; the accuracy of the models are assessed with cross-validation.

Broadband seismograms recorded next to earthquakes are analyzed to discern dynamic properties of stress release during earthquake nucleation. Evidence is presented that most earthquakes begin slowly, characterized by a weak initial *P*-wave, and the duration of this weak beginning increases with earthquake size.

To Shelby

Acknowledgments

Many people have contributed to my education and the research presented in this dissertation. Greg Beroza provided a hardware-rich working environment, generous funding, and continual guidance and editing throughout this work. He also taught numerous courses in seismology, showed me how to snorkel, and shared the secret of *coco loco*. Paul Spudich dealt patiently with my incompetence and made many suggestions that improved the manuscript. Mark Zoback expected professionalism and competence from everyone, and led by example. Paul Segall co-taught an enlightening course in geophysical inverse theory and offered fresh insight on my research. Norm Sleep demonstrated how to transcend the mundane in the pursuit of curiosity.

I am particularly thankful to Thorne Lay for his encouragement at The University of Michigan. Thorne established a high standard and displayed a refreshing lack of pretense. His genuine enthusiasm for seismology and intrepid approach to research were inspiring.

I shared many great and memorable experiences with classmates at Stanford who made these years extremely enjoyable; in particular, tee-times at dawn with Martijn, skiing with Mark in Aspen, conversations with Dawn, and playing 'bee on warm evenings with Fran, Jaime, Ramón, Jeff, Brad, Ben and others of the ultimate persuasion. I enjoyed the company of fellow students Tony, Sue, Thora, Carl, Marian, Thomas, Hal, Brian, and Doug. Doug was a walking CD-ROM on subjects ranging from signal processing to torque wrenches. Ramón shared his enthusiasm and a template of his thesis.

Chapter 2 and 3 were derived from papers co-authored with Greg Beroza. I thank Jeff Freymueller for the geodetic slip model presented in Chapter 4. Paul Spudich provided guidance on Chapter 5. Chapter 6 benefited greatly from the wisdom of Bill Ellsworth. I thank my examination committee (Greg Beroza, Lynn Orr, Paul Segall, Paul Spudich, and Mark Zoback) for reading the manuscript and suggesting improvements.

Finally, I am indebted to others who have freely shared their ideas and data, in particular, N. Abrahamson, J. Boatwright, L. Burdick, R. Bürgmann, D. Dreger, E. Garnero, S. Hartzell, D. Helmberger, S. Hough, H. Kanamori, T. Lay, J. McLaren, D. Ponti, C. Saikia, M. Sen, P. Somerville, K. Righter, L. Ruff, B. Woods, and C. Young. I want to thank my parents and siblings for their love and advice, the Hunsinger family for their encouragement, and my brother Bruce for his friendship.

Most importantly, Shelby provided moral support, apples and carrots, and never questioned the purpose (thanks for the runs at Black Mtn., basketball, and tennis). She rode her bicycle through Michigan snow, woke up at 4 am to commute from Pasadena to UCLA, and gave me Alison. Alison introduced me to the Count, Elmo, and others, and unknowingly gave me a new sense of purpose.

Table of Contents

List of Tables

List of Illustrations

Chapter 1 — Introduction

This thesis addresses the fundamental question of how to determine properties of an earthquake from measurements of ground motion at the Earth's surface. More accurate images of earthquake rupture will lead to an improved understanding of earthquake source mechanics and the many factors that control rupture nucleation, growth, and termination. A more accurate theory will address such questions as: What controls where an earthquake begins? What factors influence the propagation and termination of rupture? What are the temporal characteristics of the slip function, how are they related to the slip amplitude, and how do they influence strong ground motion? Do areas of large slip remain fixed over subsequent earthquake repetitions or are they transient dynamic features? Why do aftershocks occur and are their locations predictable? Are there measurable properties at the beginning of an earthquake that may influence its eventual size? These questions have obvious societal significance; with increased urbanization occurring near fault zones and seismogenic areas, their relevance will certainly increase.

Ground motion observations customarily take the form of seismograms (time series) but also include permanent distortions of the Earth's surface measured with geodetic methods. The foremost goal of this thesis is to use these observations to obtain a complete space and time description of the faulting process. This is accomplished by minimizing the misfit between the observed data and data predicted by a model using inverse theory. Solutions to the inverse problem depend strongly on the forward physical theory that relates (maps) the model space to the data space. Every inverse problem is different: in some cases, for example, the paramount issue is reconciling inconsistent data, in others it is matching measurements that contain large variance. In the present problem, the foremost concern is the error in the forward theory (the Green's functions) because this error most significantly degrades the solution accuracy. More accurate fault models can be obtained either by reduction of this error or a better characterization of it; reduction of the error makes the forward problem more deterministic, characterization of the error provides a basis for more appropriate covariance weighting that is used in the inversions.

A complementary objective is to improve the method used to derive earthquake models from near-source seismograms. Near-source recordings provide better model resolution than regional or teleseismic seismograms because they are less attenuated and contain shorter wavelengths, and because the forward problem is more accurate at comparable frequencies. Additionally, near-source Green's functions vary more strongly with position on the fault than do their regional and teleseismic analogs. The strategy consists of identifying and reducing error in the forward problem, and recognizing solution attributes caused by the inversion method (artifacts). The forward problem is examined to identify sources of error and determine the frequency band over which modeling assumptions are most valid, and when necessary, sensitivity tests with synthetic data are employed to identify artifacts of the model parameterization and inversion method. The inversions are carried out in the time domain because that currently provides the most direct link between the model and data (more complete knowledge of the covariance may require frequency domain inversions in the future). Although time-domain least-squares methods have been used to examine many earthquakes in the last decade, not much attention has been directed toward quantifying errors or estimating model variance.

A second goal of the thesis is to use the methods to detect properties of specific earthquakes. The M_W 7.3 1992 Landers, California event is scrutinized in the greatest detail because of the extraordinary collection of ground motion observations for it. The Landers earthquake was noteworthy for many reasons: it was the largest earthquake in Southern California in forty years (a period that saw critical improvements in instrumentation); the combined seismic and geodetic data set is more complete and of higher quality than for any other earthquake of its size (and four sites that recorded the mainshock also recorded the aftershock sequence); the rupture broke through the ground surface for over 70 km; and it triggered numerous smaller earthquakes at distances in excess of 1000 km – an occurrence without known precedent. Because the event occurred in the sparsely populated Mojave Desert, there was only one death and the societal impact was small for an earthquake of its size.

Studying earthquakes is fundamentally an observational science. The observations are most often based on seismograms that describe time-dependent ground motion. In many cases, inferences about an earthquake can be made by examination of a raw seismogram, but this is difficult if there are multiple observations, or if the wave propagation is complex. In this case it is necessary to model the seismograms by means of

an appropriate theory. When inverse theory is applied, the data is fit well but the model is nonunique. It is therefore useful to evaluate the solution stability with the aid of sensitivity tests; models are difficult to interpret without an estimate of their variance.

This thesis refers to approximately thirty-one publications that use strong-motion seismograms to infer rupture characteristics of eighteen separate earthquakes (Table 1.1). Almost all of them occurred in California where strong motion networks operated by the U.S. Geological Survey (USGS) and the California Strong Motion Instrumentation Program (CSMIP) combine to provide coverage for most seismogenic areas in the state. The methods used to study these earthquakes have many features in common. They all use strong-motion seismograms recorded close to the earthquake to derive models of slip intensity on the fault surface. The propagation of rupture and the slip-velocity time function (rise time) are treated in various ways; however, all methods use time-domain waveforms as data and solve the inverse problem by minimizing a 2-norm of the residuals (least squares). Each study uses some regularization, most commonly in the form of spatial smoothing that minimizes either slip gradient or slip curvature on the fault.

It is not surprising that the techniques used in these studies are similar. Following the pioneering work of *Olson and Apsel* [1982] and *Hartzell and Heaton* [1983], the same generic algorithm has been applied by others, essentially unchanged, to examine subsequent earthquakes. The method uses non-negative least squares to solve a linear system for the slip amplitude on planar faults. Rupture time is prescribed *a priori* and a range of rupture velocities are evaluated. In some cases, the slip-velocity time function is constant over the entire fault, in others this assumption is relaxed and each element of the fault is allowed to rupture repeatedly (for example, three to six times) in adjacent time windows.

Although researchers have applied this approach to many earthquakes, it has been slow to evolve. There are three notable exceptions. First, *Mendez et al.* [1990] introduced a frequency domain inversion technique that was used to infer the spatial and temporal evolution of the 1985 M_W 8.0 Michoacán rupture [*Mendez and Anderson*, 1991]. A similar formulism was adopted by *Cotton and Campillo* [1995] in their analysis of the Landers earthquake. Second, *Beroza and Spudich* [1988] solved for slip and rupture time *simultaneously* using a linearized (iterative) inversion. They were forced to grapple with a strong trade-off between slip amplitude and rupture time much more directly than the previous linear method. The third development was to combine seismic and geodetic

Table 1.1. Earthquakes with Near-Source Observations

Location†	Date	M_W	Area (km^2)	Dur (s)	V_r (km/s)	Seis (#)	Geo	Reference
Michoacán, Mexico	19 Sep 1985	8.1	18000	42	2.6	4	P	*Mendoza and Hartzell* [1989]
Valparaíso, Chile	3 Mar 1985	8.0	16000	54	NA	3	P	*Somerville et al.* [1991]
Akita-Oki, Japan	26 May 1983	7.7	2700	45	2.2	7	NA	*Fukuyama and Irikura* [1986]
Landers	28 Jun 1992	7.3	920	24	2.5	20	G	*Cohee and Beroza* [1994a]
Borah Peak, Idaho	28 Oct 1983	7.3	800	NA	2.9	0	G	*Mendoza and Hartzell* [1988]; *Du et al.* [1992]
Kobe, Japan	17 Jan 1995	6.9	960	12	2.8	17	G	*Wald* [1995]
Loma Prieta	18 Oct 1989	6.9	440	6	2.8	16	G	*Beroza* [1991]
Irpinia, Italy	23 Nov 1980	6.9	460	13	2.0	7	N	*Cocco and Pacor* [1993]
Naganoken-Seibu, Japan	14 Sep 1984	6.8	220	3	2.7	4	NA	*Takeo* [1987]
Northridge	17 Jan 1994	6.7	280	7	2.8	26	G	*Wald and Heaton* [1994b]
Superstition Hills	24 Nov 1987	6.6	200	10	2.4	10	N	*Frankel and Wennerberg* [1989]
San Fernando	9 Feb 1971	6.5	170	6	2.8	5	P	*Heaton* [1982]
Imperial Valley	15 Oct 1979	6.5	340	16	2.6	15	N	*Hartzell and Heaton* [1983]
Morgan Hill	24 Apr 1984	6.2	260	7	2.8	5	P	*Beroza and Spudich* [1988]
N. Palm Springs	8 Jul 1986	6.0	220	4	3.0	9	N	*Hartzell* [1989]
Coyote Lake	6 Aug 1979	5.9	40	2	2.8	6	N	*Liu and Helmberger* [1983]
Whittier Narrows	1 Oct 1987	5.9	100	2	2.5	17	N	*Hartzell and Iida* [1990]
Sierra Madre	28 Jun 1991	5.6	10	2	2.7	14	N	*Wald* [1992]
Parkfield	28 Jun 1966	5.5	400	12	2.7	5	G	*Beroza* [1989]; *Segall and Du* [1993]

† California unless noted otherwise
Dur earthquake duration
V_r rupture velocity
Seis number of near-source seismic stations
Geo co-seismic geodetic data: G–good, P-poor, N-none, NA-unknown

observations to constrain the rupture models. This approach, first advanced by *Heaton* [1982], has the advantage of decreasing the aforementioned trade-off because the geodetic data are sensitive only to slip amplitude and have no temporal dependence.

Until the 1992 Landers earthquake, implementation of this latter approach was prevented by the poor quality of existing geodetic data and the paucity of pre-event surveys. *Wald and Heaton* [1994a] used geodetic displacements together with strong-motion and teleseismic waveforms in the first comprehensive treatment of a large earthquake (Landers) and obtained a rupture model that simultaneously fit the three data types. They were forced to contend with novel difficulties, most notably how to weight each data type in a simultaneous inversion. Ideally, the relative weight of each data type would be inversely proportional to its variance, but since earthquakes are not repeatable phenomena, it is notoriously difficult to quantify error in strong-motion and teleseismic seismograms. The full data covariance was available for the geodetic measurements but was not used by *Wald and Heaton* [1994a].

Without information about error in the seismograms, the most conservative strategy is to separate completely common influences in the geodetic and seismic data: geodetic data are used to find the slip model and seismograms are used to determine the rupture propagation. Notwithstanding the effort required, it is possible in theory to estimate error in the seismograms if aftershock recordings are available at the same stations at which the mainshock was recorded. *Spudich and Archuleta* [1987] described the procedure as follows:

> To our knowledge, no one has yet attempted to estimate these errors and carry them along as uncertainty estimates in subsequent calculations. Estimation of these errors would be relatively easy if microearthquake recordings were available in the study region. One could simply examine the spectrum of the difference between the observed microearthquake seismograms and synthetic seismograms calculated in the identical source-observer geometry for point dislocations. For frequencies below the microearthquake's corner frequency, the synthetic point-dislocation seismograms should match the observed seismograms. Probably it would be observed that the difference between the observed and synthetic seismogram spectra would increase as a function of frequency, corresponding to our progressively less accurate knowledge of earth structure on decreasing length scales. If quantitative measurements of these discrepancies were available, they could be used to estimate uncertainties in both forward modeling and inverse modeling of earthquake seismograms.

This approach is only possible when aftershock recordings are made at the same seismometer sites that recorded the mainshock. In the Landers earthquake, four TERRAscope stations recorded the mainshock and the entire aftershock sequence on the same broadband seismometer. In this thesis, these aftershock recordings are used to find the best one-dimensional (1D) seismic velocity structure and to estimate the misfit associated with theoretical point-source Green's functions. If aftershock seismograms had been available for all stations used in the inversion, it would have been possible to determine the associated covariance more formally.

There are many reasons why better models of earthquake rupture are sought-after. Strong ground motion at the surface is strongly connected to the details of rupture – an improved understanding of this relationship would permit building design codes to represent expected ground motions more faithfully.

There is a spatial correlation between areas of high slip amplitude and low aftershock activity. The tendency for areas of high slip during mainshocks to be deficient in aftershocks has been noted by a number of investigators [e.g., *Beroza and Spudich*, 1988; *Mendoza and Hartzell*, 1988] and is of obvious importance in understanding the cause of slip heterogeneity and the relationship between mainshocks and aftershocks. One interpretation is that aftershocks are driven by the stress change induced by the mainshock; however, in the Loma Prieta earthquake *Beroza and Zoback* [1993] showed that the sense of aftershock slip did not act in the direction of the mainshock traction change for the majority of the aftershocks. A better understanding of earthquake interaction – both between mainshocks and aftershocks, and mainshocks and subsequent large earthquakes – could help mitigate seismic hazard.

Seismic observations require that kinematic dislocation models contain heterogeneous slip amplitude and complex rupture propagation. These models do not take into account the stresses generated during rupture and their implications for the faulting process, which are fundamental to an understanding of earthquake physics. Theoretical and numerical approaches based on spontaneous, dynamic shear-crack models suggest that these complex rupture processes arise from non-uniform stress and fault strength [e.g., *Mikumo*, 1992]. It is possible to use kinematic solutions to constrain dynamic theories, but only if the models are accurate; small features in the kinematic models can have a significant effect on the dynamic solutions. To date, there has been little effort to reconcile these two complementary views of the rupture process (partly because the resolution of the

kinematic models is generally too poor to warrant the considerable computational effort), although there are some noteworthy exceptions [e.g., *Quin*, 1990; *Mikumo and Miyatake*, 1993; *Mikumo and Miyatake*, 1995].

Another motivation for obtaining better rupture models is to understand the causes of rupture heterogeneity and the implications for the variability and time-dependence of far-field earthquake triggering [*Hill et al.*, 1993]. More accurate rupture models will not explain far-field triggering, but they will improve modeling of the dynamic stresses radiated from earthquakes. The seismicity triggered at great distances following the Landers earthquake, for which the static stress change was far smaller than the tidal stresses, provides further evidence for a more complex mechanism of earthquake interaction than that explained by current theory. One explanation for the observations is that the large transient stress changes in the dynamic field weaken faults as they propagate through them. If such stress changes (fractions of a MPa) can trigger seismicity at a great distance following the Landers earthquake, it is reasonable to assume that they can also trigger aftershocks since the stresses experienced in the near-source region where aftershocks occur are on the order of the stress drop (at least several MPa).

In the Landers earthquake, the slip propagates across discontinuous fault segments with a negligible effect on either the slip amplitude or rupture velocity. This suggests that fault segmentation, at least in its geologic expression at the Earth's surface, is not a reliable indicator of the characteristic size of future earthquakes. Additionally, slip on the Camp Rock-Emerson segment terminated in the middle of a relatively straight fault segment, indicating that something other than segmentation was responsible for stopping the rupture. Better fault models will improve our understanding of the importance of fault segmentation on the progression and termination of rupture.

Although there remains considerable room for improvement in the methods used to extract rupture models from recorded ground motion, it is possible that in the short-term, higher quality and more plentiful data will overshadow theoretical improvements. Seismic instrumentation is evolving rapidly and seismometers that record ground motion over many decades of frequency (e.g., the STS-2) are routinely used in modern deployments. New techniques are being developed to utilize more efficiently this explosion in the quantity of waveforms, and these advances in data collection are paralleled with progress in methods that use the data. In any problem, additional data is most useful when the errors in it are understood and the covariance can be determined. In the earthquake

problem, this requires either that recording systems have sufficient dynamic range to capture both mainshock and aftershocks, or that co-located seismometers are deployed following large events. Table 1.1 summarizes all earthquakes to date for which realistic space-time descriptions of faulting have been obtained from near-source data. Methods used in these studies are still in their infancy, yet a few lessons have been learned:

- Site instrumentation with sufficient dynamic range to record the mainshock and aftershocks are necessary to facilitate the use of empirical Green's functions and quantify the theory covariance.
- Geodetic measurements of surface deformation are useful for constraining co-seismic slip in mainshocks and reducing the trade-off between slip amplitude and rupture time in the seismic wavefield.
- The sources of error in finite-fault earthquake models need to be better understood.

In Chapter 2, I present two time-domain inversion methods and perform sensitivity tests with synthetic waveforms computed for a simulated Landers earthquake. The strengths and weaknesses of each method are evaluated and discussed. In Chapter 3, I apply the two methods to recordings of the Landers earthquake to image the spatial variation of slip amplitude, the propagation of the rupture front, and the duration of slip at each point on the fault, while making assumptions about the fault geometry, the surface displacement, and the slip direction.

Chapter 4 presents results obtained from an approach that, in the absence of the full covariance, exploits the complementary nature of seismic and geodetic observations: the slip model is determined from geodetic measurements with known covariance and the rupture propagation and slip history are derived from seismograms. I apply this approach using seismic and geodetic measurements of the Landers earthquake. This partitioned inversion method yields more reliable rupture propagation models than those based only on seismic data.

The results in Chapter 4 are encouraging, but it is important to recognize that the validity of the rupture model is strongly dependent on the accuracy of the slip model. Errors in the geodetic forward problem and other unaccounted-for sources of error will map into slip model errors; however, it is reassuring that most features of the slip models derived independently from seismic and geodetic data are very similar.

Chapter 5 explores a method for obtaining more accurate seismic Green's functions for the M_W 6.9 1989 Loma Prieta, California earthquake through the interpolation of aftershock recordings (termed empirical Green's functions). The purpose of the chapter is to test a method at Loma Prieta that could have utility in the analysis of future earthquakes. The quality of the solutions are evaluated using cross-validation statistics. A singular value decomposition (SVD) is applied to filter the data in a manner that enhances the site-effect and yields an improved cross-validation result. Although the overall success of this implementation at Loma Prieta is disappointing, it does provide insight into how aftershock deployments can be improved to enhance the usefulness of empirical Green's functions.

Finally, Chapter 6 presents a study of the dynamic stress release during earthquake initiation using high-dynamic-range, broadband seismograms recorded at close distance for earthquakes over a wide range of magnitude. The inversion method is similar to that used in earlier chapters, but the context is different – the earthquake is assumed to be a point source, each station is treated separately, and the broadband seismogram is unfiltered. This strategy is permitted by the use of recordings made at very close distance (within one source-depth) where theoretical Green's functions are extremely simple.

Chapter 2 — Finite Fault Inversion Using Near-Source Seismograms

Abstract

In this chapter I compare two time-domain inversion methods that have been widely applied to the problem of modeling earthquake rupture using strong-motion seismograms. In the *multi-window method* each point on the fault is allowed to rupture multiple times; this allows flexibility in the rupture time and hence the rupture velocity. Variations in the slip function are accommodated by variations in the slip amplitude in each time-window. The *single-window method* assumes that each point on the fault ruptures only once when the rupture front passes. Variations in slip amplitude are allowed and variations in rupture velocity are accommodated by allowing the rupture time to vary. Because the multi-window method allows greater flexibility it has the potential to describe a wider range of faulting behavior; however, with this increased flexibility comes an increase in non-uniqueness and the solutions are comparatively less stable. I demonstrate this trait using synthetic data for a test model of the M_W 7.3 1992 Landers, California, earthquake. The two approaches yield similar fits to the synthetic data with different seismic moments indicating that the moment is constrained poorly by strong-motion data alone. Recovery of the input slip amplitude distribution is similar using either approach but important differences exist in the rupture propagation models. The single-window method does a better job of recovering the true moment and the average rupture velocity. The multi-window method is preferable when rise time is strongly variable but tends to overestimate the moment. Both methods work well when the rise time is constant or short compared to the periods modeled. Neither approach can recover the temporal details of rupture propagation unless the distribution of slip amplitude is constrained by independent data.

2.1 Introduction

Inverse methods have been applied to estimate the rupture time and slip amplitude using near-source (< 200 km) strong motion seismograms for many well-recorded earthquakes [*Olson and Apsel*, 1982; *Hartzell and Heaton* 1983; *Fukuyama and Irikura*, 1986; *Takeo*, 1987; *Beroza and Spudich*, 1988; *Hartzell*, 1989; *Mendez and Luco*, 1990; *Mendez and Anderson*, 1991; *Cocco and Pacor*, 1993]. The common goal of this research is to determine the complete space and time history of coseismic slip on an assumed planar fault surface or surfaces by matching recorded seismograms with theoretical seismograms. The kinematic rupture models derived in this way provide important constraints on the dynamics of earthquake rupture [*Heaton*, 1990; *Scholz*, 1990]. Moreover, an accurate description of faulting aids in understanding the strong ground motion, leading to an enhanced ability to design structures that withstand shaking in future earthquakes.

Despite much research in this area there remain important discrepancies between rupture models of the same earthquake published by different authors. It is typically difficult to assess the relative accuracy of the models. For the most part, past studies have concentrated on deriving a model that fits the strong motion data without much emphasis on assessing the solution stability or spatial resolution. The use of standard inverse methods makes it easy to obtain a solution that matches the data acceptably well; the greater challenge lies in estimating the reliability. Some solution discrepancies result from differences in the portion or bandwidth of the wavefield used in the inversion. An under-appreciated source of discrepancies result from the different model parameterizations and inversion methods. It is important to understand the origin of the model differences because they often have more to do with assumptions made about the model than about the earthquake.

Examples of recent earthquakes about which authors using similar strong-motion data have found dissimilar solutions include the 1979 Imperial Valley earthquake [*Olson and Apsel*, 1982; *Hartzell and Heaton*, 1983], the 1984 Morgan Hill earthquake [*Hartzell and Heaton*, 1986; *Beroza and Spudich*, 1988], the 1987 Superstition Hills earthquake [*Frankel and Wennerberg*, 1989; *Wald et al.*, 1990], the 1989 Loma Prieta earthquake [*Beroza*, 1991; *Steidl et al.*, 1991; and *Wald et al.*, 1991], and the 1993 Landers earthquake [*Cohee and Beroza*, 1994a; *Wald and Heaton*, 1994a]. Authors often cite these

discrepancies as indicative of the amount of uncertainty in rupture models obtained from strong-motion data.

For example, *Frankel* [1992] suggested in the case of the 1987 Superstition Hills earthquake that differences in the data and data weighting were the cause of solution discrepancies, noting, in particular, that without applying some weighting, close stations with larger seismogram amplitudes dominated the least-squares inversion. In this example, the model parameterizations and inverse methods were very different (*Frankel and Wennerberg* [1989] solved for a line-source using impulsive Green's functions) and it was not easy for identical data and weighting to be used with each inversion method. *Wald et al.* [1991] discussed dissimilarities in the rupture solutions of the 1989 Loma Prieta earthquake. They speculated that differences in the particular stations used and the data weighting, and to a lesser extent the Green's functions, might have been responsible for solution differences; however, they did not assess the relative importance of each or identify features attributable to different inversion methods.

In this chapter we compare two established time-domain inversion methods using identical data, weighting, and Green's functions in order to isolate the influence of the model parameterization and inversion method on the solutions. We conduct sensitivity tests using synthetic data computed for a hypothetical 1992 Landers, California, earthquake with known source properties; the synthetic test model includes variations in slip amplitude, rupture velocity, and slip duration (displacement rise time). We finally determine how well the two methods recover the known rupture model in the presence of realistic noise.

Although the *multi-window method* contains greater flexibility and has the potential to describe fully the wide range of faulting behavior included in the synthetic test case, the results are less stable and much of the noise is incorrectly mapped into source properties. The multi-window method works best when the rise time is strongly variable, but it also systematically overestimates the seismic moment. The *single-window method* does a better job of recovering the input moment and the average rupture velocity. Neither method can reliably recover detailed rupture time variations unless the slip model is known independently (e.g., from geodetic data).

2.2 Rupture Model Parameterization

The two inverse methods compared in this chapter have been described in previous studies [*Hartzell*, 1989; *Cohee and Beroza*, 1994a]. In each case, the forward problem consists of representing a continuous planar fault by numerous point sources (Figure 2.1). The contribution from each point source to each seismometer is described by a theoretical Green's function computed for a layered Earth model. The objective of the inverse modeling is to find the strength and timing of each point source. The most important difference between the two methods is how the rupture propagation is represented. In the multi-window approach, each element of the fault is allowed to rupture some fixed number of times. This approach was introduced by *Olson and Apsel* [1982] and has been used in many later studies. By allowing each element to rupture more than once, the multi-window model has the flexibility to accommodate variations in both the rupture velocity and the duration of the slip function (Figure 2.2); however, the number of unknowns increases with the addition of each time window.

In the single-window parameterization, each fault element ruptures once, but rupture time variations are allowed by perturbing a constant-rupture-velocity starting model [*Fukuyama and Irikura*, 1986, *Takeo*, 1987; *Beroza and Spudich*, 1988; *Hartzell and Iida*, 1990]. The perturbations are determined in a separate, linearized inversion. In this latter approach, the rise time is assumed to be constant over the entire fault and is optimized by finding the value which produces the best overall fit to the data.

Both methods improve the data fit by allowing the rupture time to vary. This improved fit is not achieved without expense: the model dimension is larger and the solution has greater variance. An advantage of the single-window method is that it can accommodate larger variations in rupture time with fewer model parameters because there are only two model parameters per grid point (slip amplitude and rupture time). An advantage of the multi-window method is that it allows the source time-function (and the rise time) to vary across the fault surface.

2.3 Inversion Methods

In the multi-window approach, slip can occur at each point on the fault in a finite number of subsequent time-windows. The complexity of the slip function (and the size of the model dimension) increases with the number of prescribed windows. With this approach it is possible to obtain a variable rupture velocity; the slip can move to earlier or

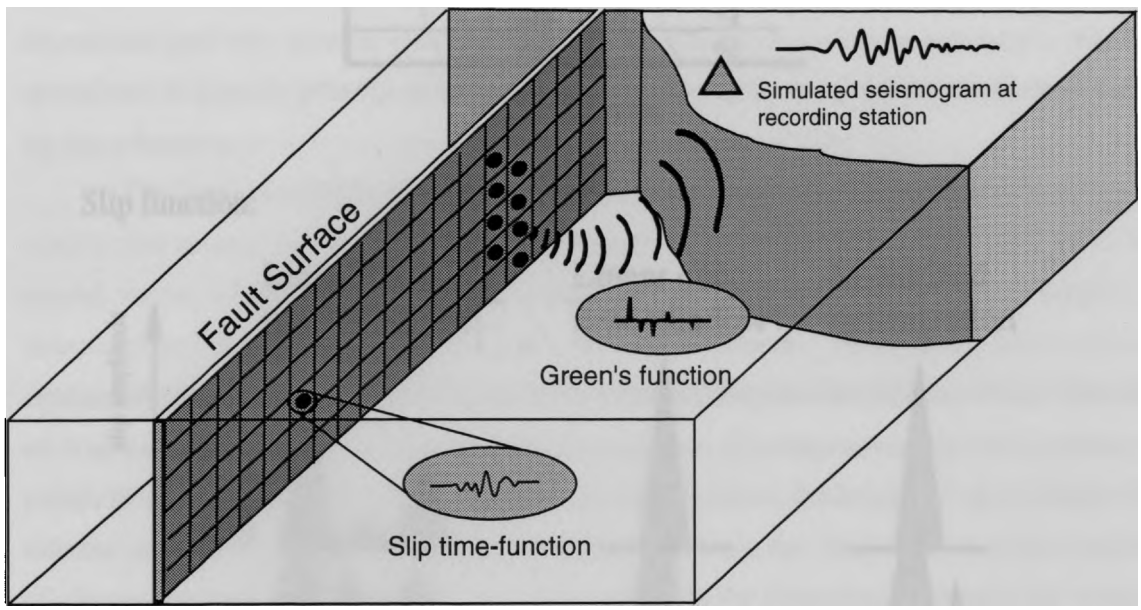

Figure 2.1. Schematic description of the forward problem. Contributions from fault elements are summed to produce a simulated seismogram at a receiver at the ground surface.

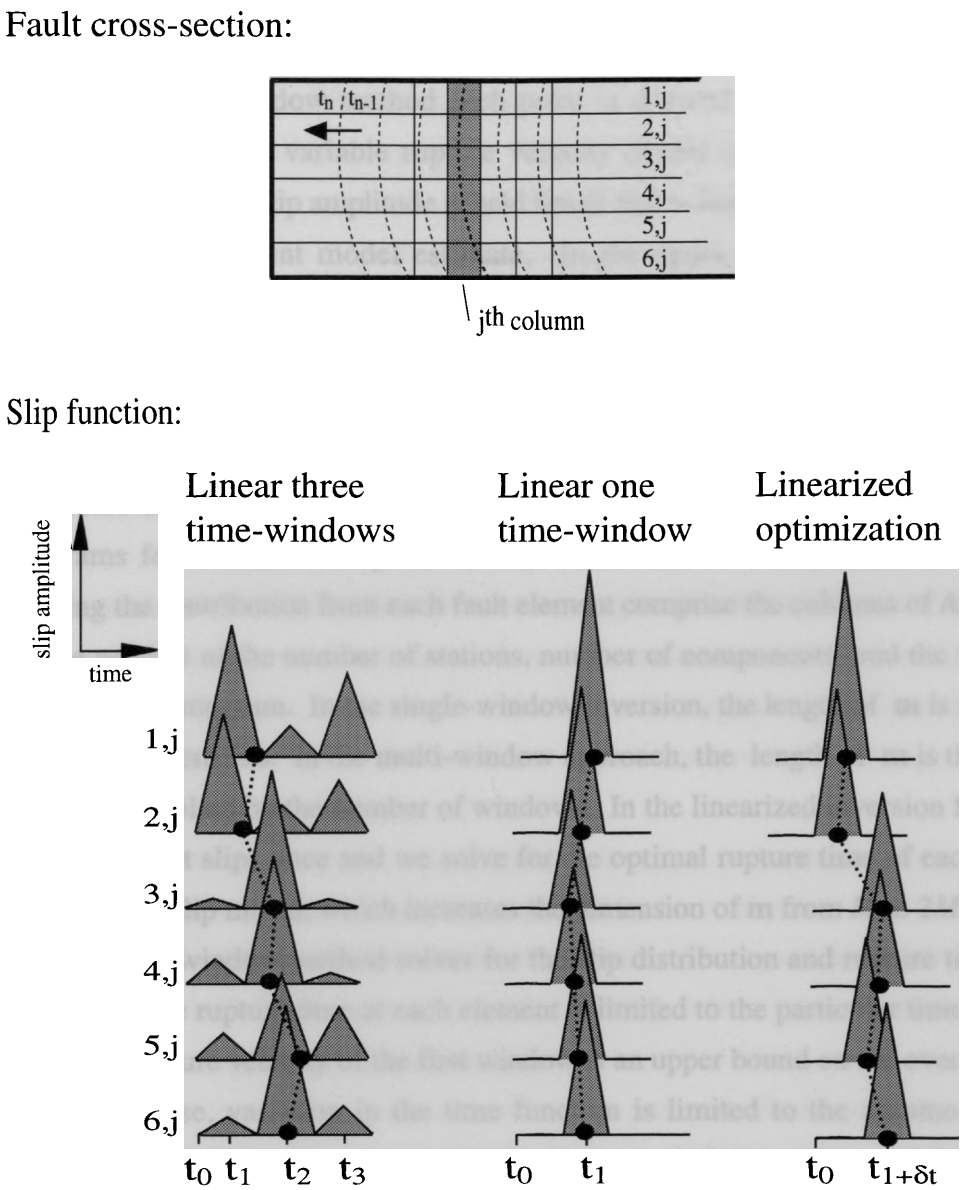

Figure 2.2. Schematic cartoon showing the single and three time-window rupture parameterizations. A cross section of a rectangular fault plane is shown at the figure top and is divided into square fault elements. The rupture propagates from right to left. Below the cross section, example slip-velocity functions are shown for the *j*th column of fault elements. The slip-velocity functions used in this study are triangular and symmetric. The width of the triangle is the displacement rise time. The linear three time-window method has the flexibility to distribute unevenly the slip across the three windows. With this method, the rupture time is defined as the slip-weighted temporal centroid for each element. The centroid is shown schematically. In the single time-window method each element slips once, and the timing of the slip is optimized with a nonlinear inversion. In this cartoon both the multi-window and the nonlinear model show a delay of the 2,*j* element, but differ in the rupture time of the 5,*j* element.

later windows for different areas of the fault plane. The slip amplitude for all windows is found simultaneously in one large inversion.

In the single-window method each point is allowed to slip just once when the rupture front passes. A variable rupture velocity model is then found in a separate, nonlinear inversion (the slip amplitude is held fixed) that is linearized using a Taylor series expansion and the current model estimate. In the multi-window approach, modest deviations in rupture velocity are allowed and the rise-time varies within the time spanned by the windows.

The linear inversions have the familiar form $\mathbf{Am} = \mathbf{d}$. The kernel $\mathbf{A}$ is a N x M matrix that relates slip at each point on the fault to the recorded seismograms, $\mathbf{m}$ is the model vector of slip amplitude with length M, and $\mathbf{d}$ is the data vector of length N. Seismograms for the three components of motion form $\mathbf{d}$. Theoretical seismograms representing the contribution from each fault element comprise the columns of $\mathbf{A}$. The size of N is the product of the number of stations, number of components, and the number of points in each seismogram. In the single-window inversion, the length of $\mathbf{m}$ is simply the number of fault elements. In the multi-window approach, the length of $\mathbf{m}$ is the number of elements multiplied by the number of windows. In the linearized inversion for rupture time, each element slips once and we solve for the optimal rupture time of each element assuming a fixed slip model, which increases the dimension of $\mathbf{m}$ from M to $2M$.

The three-window method solves for the slip distribution and rupture time in one step. The possible rupture time at each element is limited to the particular time-windows used, thus the rupture velocity of the first window is an upper bound on the overall rupture velocity. Likewise, variation in the time function is limited to the assumed window spacing (see Figure 2.2). In contrast, the single time-window result is obtained using a constant rupture velocity and a separate, linearized inversion is used to optimize the rupture time of each element. This latter approach is similar to the *linearized inversion* of *Beroza and Spudich* [1988] and the *nonlinear inversion* of *Hartzell* [1989], except they both solved for slip amplitude and rupture time simultaneously. The difficulty with a simultaneous inversion is that it is unclear how to weight two groups of unknowns that have different physical dimensions (i.e., time and distance). There is a strong trade-off between slip amplitude and rupture time and it is difficult to solve this problem without other information to constrain the solution. One technique that shows promise is to use

geodetic measurements to determine the static slip distribution and seismic data to determine the rupture propagation – this approach is the subject of Chapter 4.

Unfortunately, it is difficult to quantify the sources of error in the forward problem and determine the appropriate covariance. Error in the Green's functions is different for each station and each component of motion. If they are available, aftershocks recorded at the same sites can be used to quantify the error for specific propagation paths – if sufficient recordings exist, it is theoretically possible to construct a full covariance matrix (Section 4.4). In the absence of such data, the weighting is somewhat arbitrary.

One approach is to use no covariance, but then the largest amplitude seismograms dominate the solution. An alternative approach is to normalize each seismogram by its power and solve the system $\mathbf{RAm} = \mathbf{Rd}$, with the N x N matrix $\mathbf{R} \equiv diag[1/\text{power}^i]$, where power^i is the power of the ith seismogram. The problem with this choice of $\mathbf{R}$ is that small amplitude vertical motions have equal weight as horizontal motions that contain the transverse shear waves for which the Green's functions are relatively more accurate; the *P-SV* wavefield is more sensitive to local velocity heterogeneity and, in particular, the relative partitioning of energy on the radial and vertical components is strongly dependent on the velocity of the surface layer.

For the present purpose of comparing the two inverse methods, the three components of motion at each station are normalized by the total power at that station; each station has equal weight and the contribution of the vertical component is minimized. This weighting matrix is defined as $\mathbf{R} \equiv diag[1/\text{power}^{sta}]$, where power^{sta} is the summed power of the three components at each station.

The size of the model space in each of the parameterizations is large and it is necessary to stabilize the solution by regularization. An example of this stability problem is found in *Hartzell* [1989]. He used a multi-window approach and found that the earthquake moment increased with the addition of each time window. One technique for overcoming this particular problem is to append a moment minimization constraint [*Hartzell and Heaton*, 1983]. A more widely-used regularization method is to require the solution to be spatially smooth. In earthquake source inversions, this is accomplished by simultaneously minimizing either the first or second spatial derivative of the model.

We apply three types of regularization to the problem. We append a smoothing constraint that minimizes the slip amplitude gradient (first derivative) of $\mathbf{m}$. This augmented linear system is written

$$\begin{pmatrix} \mathbf{RA} \\ \varepsilon_0\mathbf{D} \end{pmatrix} \mathbf{m} = \begin{pmatrix} \mathbf{Rd} \\ 0 \end{pmatrix}, \tag{2.1}$$

where **D** is the smoothing matrix and ε_0 is a scalar that weights **D**. There is a predictable trade-off between model roughness, defined as $\|\mathbf{Dm}\|^2$, and data fit – a rougher model fits the data better but is less stable. In some circumstances, independent observations of surface displacement, **s**, can be used to estimate the best smoothing weight [*Cohee and Beroza,* 1994a]; **s** can also be used as a constraint in the inversion. Finally, a homogeneous boundary condition is prescribed at the bottom of the fault plane, which is meant to enforce a zero slip constraint at the base of the seismogenic zone. This system is written

$$\begin{pmatrix} \mathbf{RA} \\ \varepsilon_0\mathbf{D} \\ \tau\mathbf{T} \\ \gamma\mathbf{B} \end{pmatrix} \mathbf{m} = \begin{pmatrix} \mathbf{Rd} \\ 0 \\ \tau\mathbf{s} \\ 0 \end{pmatrix}. \tag{2.2}$$

When the boundary conditions are enforced $\gamma = \varepsilon_0/2$, and τ is determined by trial and error such that the model slip amplitudes at the ground surface match the observations within a prescribed tolerance, T:

$$\left(\sum_{i=1}^{N} \left[obs_i - (pred_i, m) \right]^2 \right)^{1/2} \leq T \tag{2.3}$$

where obs_i is the average observed slip for element i and $pred_i$ the prediction for model m (the error is assumed to be the same for each element). For both the multi- and single-window inversion, the system is solved with the non-negative least squares algorithm of *Lawson and Hanson* [1974].

Recall that the single-window approach assumes a constant rupture velocity. To optimize the rupture time we use a Newton-Raphson linearization [*Press et al.*, 1989] and iteratively solve for perturbations, **dm**, to the starting rupture time model, **m**. The strength of this approach is that the fit to data is improved by relatively small changes (< 2 s) in the rupture time of each fault element; however, this approach only finds the minimum norm that is closest to the starting model, which may not be the global

minimum. The linearized system is written $\mathbf{g(m+dm) = g(m) + Jdm}$, where $\mathbf{J}$ is the Jacobian matrix of partial derivatives relating change in the rupture time model to each of the residual seismograms,

$$\mathrm{J}_{ij} = \frac{\partial g_i}{\partial \mathrm{m}_j}, \tag{2.4}$$

and $\mathbf{g(m)}$ is the functional that yields synthetic seismograms for a particular rupture and slip model. The Jacobian matrix is computed using a fourth-order central difference operator with error proportional to $(\Delta t)^4$, where Δt is the sampling interval of the data. This linearized system is written

$$\begin{pmatrix} \mathbf{RJ} \\ \hline \varepsilon_1 \mathbf{D} \end{pmatrix} \delta\mathbf{m} = \begin{pmatrix} \mathbf{Rr} \\ \hline 0 \end{pmatrix}, \tag{2.5}$$

where the residual $\mathbf{r = d - g(m)}$ and the first-derivative smoothing operator $\mathbf{D}$ (weighted by ε_1) smoothes the perturbation vector $\delta\mathbf{m}$. We iterate on the system $\mathbf{m}_n = \mathbf{m}_{n-1} + \mathbf{dm}_n$ until a convergence criterion is met: the data is fit to the prescribed tolerance. At each iteration the system is solved using either singular value decomposition (SVD) [*Press et al.*, 1989] or a simultaneous iterative reconstruction technique (SIRT) algorithm [*Olson*, 1987]. SVD finds the true least-squares inverse but is computationally expensive. SIRT is approximate but computationally efficient since it does not require a matrix inverse. We use the SIRT algorithm to evaluate the large range of starting models and smoothing weights and verify the important results using the SVD.

2.4 Theoretical Green's Functions

The inversion methods described in the preceding section require that the model is connected to the data by a physical theory, or forward model. In the present problem, the data are time-varying ground motions measured at the surface (seismograms), and the discrete approximation to the continuous model is represented by point sources that, when summed together, approximate the complete time and space history of faulting. There are various approaches to computing ground motion from a point-source dislocation in an

idealized Earth structure, and each has unique attributes. There is no one method that is clearly superior in all circumstances.

Three important considerations in choosing a method for calculating theoretical seismograms are the source-receiver distance, the frequency band of interest, and the dimension of the Earth model. These considerations are not independent. For example, larger source-receiver distances imply lower frequencies because of attenuation. Moreover, small-scale structural heterogeneity has a negligible influence on long-period waves, and large-scale heterogeneity is only relevant at large distances.

Strong-motion accelerometers are designed to record large-amplitude high-frequency motions. Typically, the recorded acceleration is integrated to velocity or displacement to produce a less oscillatory waveform with more deterministic phase. Each integration divides the original spectra by the complex angular frequency $-i\omega$; in simple terms, the frequency content of the power spectra is lowered with each integration. Since energy travels fewer wavelengths at shorter distances, the impact of attenuation is minimal at near-source distances, and high-frequencies (up to 5 Hz) remain even after integration. Therefore, we need a theory accurate to high frequencies; however, this in turn, requires that the velocity structure be known at small scale-lengths. Methods of determining Earth properties at small scale-lengths are complicated and usually require active-source experiments, which is beyond the scope of this research. In most near-source earthquake studies there are a few one-dimensional (1D) models available; in rare circumstances 2D models exist for specific paths. Because of the tremendous effort required in acquiring them, high-resolution 3D velocity models are presently only developed for isolated areas of commercial (oil and gas) interest.

A well-known development in theoretical seismology is the analytical expression for the displacement **u** from a point dislocation source in a whole-space. For an isotropic homogeneous medium, the equation of motion is expressed by the Stokes-Navier equation

$$\ddot{\mathbf{u}} = \frac{\mathbf{f}}{\rho} + \alpha^2 \nabla(\nabla \cdot \mathbf{u}) - \beta^2 \nabla \times (\nabla \times \mathbf{u}), \tag{2.6}$$

where α and β are P- and S-wave velocities, and $\underline{f}$ is a body force. Taking the divergence of equation 2.6, we get the curl-free component (the P wave)

$$\frac{\partial^2}{\partial t^2}(\nabla \cdot \mathbf{u}) = \nabla \cdot \frac{\mathbf{f}}{\rho} + \alpha^2 \nabla^2 (\nabla \cdot \mathbf{u}), \tag{2.7}$$

and if we take the curl of equation 2.6, we get the divergence-free component (the S wave)

$$\frac{\partial^2}{\partial t^2}(\nabla \times \mathbf{u}) = \nabla \times \frac{\mathbf{f}}{\rho} + \beta^2 \nabla^2 (\nabla \times \mathbf{u}). \tag{2.8}$$

Both equation 2.7 and equation 2.8 have the general form of the wave equation

$$\frac{\partial^2 \mathbf{u}}{\partial t^2} = c^2 \nabla^2 \mathbf{u}. \tag{2.9}$$

Lame's theorem exploits the similarity of equation 2.9 to the scalar Helmholtz equation

$$\nabla^2 u + k^2 u = 0 \tag{2.10}$$

(in the frequency domain) to show, after some lengthy manipulation, that the displacement in the ith direction from a delta function force in the jth direction can be written (in the time-domain) as

$$\begin{aligned} u_i = {} & \frac{1}{4\pi\rho\alpha^2 r}\gamma_i\gamma_j\,\delta\left(t - r/\alpha\right) + \frac{1}{4\pi\rho\beta^2 r}\left(\delta_{ij} - \gamma_i\gamma_j\right)\delta\left(t - r/\beta\right) \\ & + \frac{1}{4\pi\rho\alpha r^2}\left(3\gamma_i\gamma_j - \delta_{ij}\right)\mathrm{H}\left(t - r/\alpha\right) + \frac{1}{4\pi\rho\beta r^2}\left(\delta_{ij} - 3\gamma_i\gamma_j\right)\mathrm{H}\left(t - r/\beta\right) \\ & + \frac{1}{4\pi\rho r^3}\left(3\gamma_i\gamma_j - \delta_{ij}\right)\mathrm{R}\left(t - r/\alpha\right) - \frac{1}{4\pi\rho r^3}\left(3\gamma_i\gamma_j - \delta_{ij}\right)\mathrm{R}\left(t - r/\beta\right) \end{aligned} \tag{2.11}$$

where γ_i are direction cosines

$$\gamma_i = \frac{x_i}{r} = \frac{\partial r}{\partial x_i} \tag{2.12}$$

[*Aki and Richards*, chapter 4, 1980]. In equation 2.11, $\delta\left(t - r/\alpha\right)$ is the delta function acting at retarded time r/α, $\mathrm{H}\left(t - r/\alpha\right)$ is the step function with value of unity at times greater than r/α, and $\mathrm{R}\left(t - r/\alpha\right)$ is the ramp function whose first non-zero value is at time r/α.

Since the first two terms of equation 2.11 decay the most slowly with distance, r, they dominate at large r and are termed the far-field P- and S-wave contributions. Likewise, the third and fourth terms with r^{-2} decay are intermediate-field terms and the fifth and six terms with r^{-3} dependence are the near-field contributions. According to common nomenclature, the intermediate- and near-field terms are combined into a single "near-field" term; then equation 2.11 can be reduced to

$$\begin{aligned} u_i = & \frac{1}{4\pi\rho\alpha^2 r}\gamma_i\gamma_j\,\delta\left(t - r/\alpha\right) + \frac{1}{4\pi\rho\beta^2 r}\left(\delta_{ij} - \gamma_i\gamma_j\right)\delta\left(t - r/\beta\right) \\ & + \frac{1}{4\pi\rho r^3}\left(3\gamma_i\gamma_j - \delta_{ij}\right)\int_{r/\alpha}^{r/\beta}\tau\,\mathrm{R}(t-\tau)\,d\tau \end{aligned} \tag{2.13}$$

[*Aki and Richards*, chapter 4, 1980]. There are important features to recognize in equation 2.13. The near-field term decays rapidly with increasing r and is negligible for almost all recorded seismic data. Consequently, most methods for calculating seismograms do not include the near-field contribution. Since strong-motion seismograms are recorded close to the source, the near-field contribution cannot be ignored. An examination of equation 2.13 reveals that all static displacement is contained in the near-field term. The importance of including the near-field in the theoretical Green's functions for the Landers earthquake is demonstrated by the significant displacements identified in geodetic measurements made at comparable near-source distances (Section 4.2).

One approach for calculating Green's functions is the propagator-matrix formulism introduced by *Haskell* [1964]. This method yields the complete response for a stack of horizontally-stratified isotropic layers, but is increasingly expensive for higher frequencies that are required for modeling strong-motion seismograms. *Wang and Herrmann* [1980] made various improvements to *Haskell's* [1964] method in their frequency-wavenumber/reflectivity algorithm. In both methods, the ground motion spectrum at distance r, $f(\omega, r)$, is expressed as an integral of the product of a frequency-wavenumber kernel $f(k, \omega)$ and the nth order Bessel function:

$$f(\omega,r)=\int_0^\infty f(k,\omega)J_n(kr)dk. \tag{2.14}$$

The evaluation of this integral proves to be problematic because $f(k,\omega)$ has numerous poles and branch cuts along the real wavenumber axis. This impediment generated further research into improving the quadrature method, most of it focused on decreasing the computational requirements; in the present study, we use the algorithm developed by *Saikia* [1994]. As a result of these numerical improvements and the contemporaneous advancements in modern computing, it is now feasible to compute high-frequency theoretical seismograms that include the near-field term. In contrast to seismograms computed with ray-theory methods, these so-called *complete* seismograms include the entire response from the layered velocity model, in particular, the reverberated energy that leads to the regional surface waves *Lg* and *Rg*, which are especially important for shallow sources, and the whispering gallery phase *Pnl*, which is most relevant at regional distances and high frequencies.

Even a precise method can produce inaccurate results – although the theoretical method is precise, the theoretical seismograms are only as good as the velocity model used to compute them. The propagator-matrix approach assumes an 1D input model, which is a gross simplification of the true earth; however, in practice, it is rare to have models of greater complexity available in most regions. Enough important differences typically exist among available 1D models that it is necessary to determine the accuracy of each to find the best model. One way this can be done is by modeling aftershock seismograms, which is discussed in Section 3.3. An alternative approach is to interpolate Green's functions from empirical recordings in the identical source-receiver geometry – this is the subject of Chapter 5.

2.5 Synthetic Test Case for the Landers Earthquake

2.5.1 Landers Earthquake Geometry

This comparison of the single- and multi-window inversion methods uses the strong-motion station locations, frequency band, and fault geometry of the M_W 7.3 1992 Landers, California, earthquake. The Landers mainshock was the largest earthquake to occur in Southern California since the M_W 7.7 1952 Kern County earthquake. The slip

propagated unilaterally from south to north, producing right-lateral offsets (≤ 6 m) at the ground surface for over 70 km on a sequence of vertical strike-slip faults. The assumed location of the fault in this study is based on surface displacements and aftershock locations. The fault is represented by three segments extending from the surface to 18 km depth. The location of each segment is shown in Figure 2.3: the southern segment is 27 km long, the middle segment is 30 km long, and the northern segment is 45 km long. The segments are further subdivided into a total of 204 (3x3 km^2) elements. The rupture initiates at a depth of 4.5 km.

The fault geometry and the seismometer sites are described in Section 3.2. Eighteen three-component stations are used; they provide good azimuthal coverage of the fault zone (Figure 2.3). It is important to recognize that in the following tests there is no modeling error because the artificial data are calculated with the same geometry and Green's functions that are used in the inversion.

2.5.2 *Model Parameterization*

The use of the multi-window rupture model makes it simple to add additional time windows; **d** remains unchanged. Columns in **A** are repeated (with a time shift) for each additional window and the size of the **m** is increased accordingly. The window is delayed by a fixed amount (in this study 2 s) from a reference rupture time. The only deterrent to using many windows is the practical limitation of increased memory storage and the added solution instability that results from the larger model dimension.

The addition of multiple windows permits variable rupture velocity by allowing slip to occur in adjacent time windows. There are no smoothing constraints relating slip in adjacent windows. If required by the data, the fault element may repeatedly rupture and stop, or have an extended duration. The degree of rise-time complexity depends on the duration and number of windows used; in the following tests there are three. Up to six windows have been used with this method [*Wald and Heaton*, 1994a], resulting in a model with many free parameters.

Alternatively, in the single window approach, the rupture time of each element is prescribed and the best-fitting variable-slip model is found. We use a rise-time duration of 2 s; however, because of the low frequencies used, any rise time of 3 s or less yields similar results. With both inversion methods, the model is not sensitive to differences in rise time less than 3 s because the data were filtered to remove short-period (<4 s) energy.

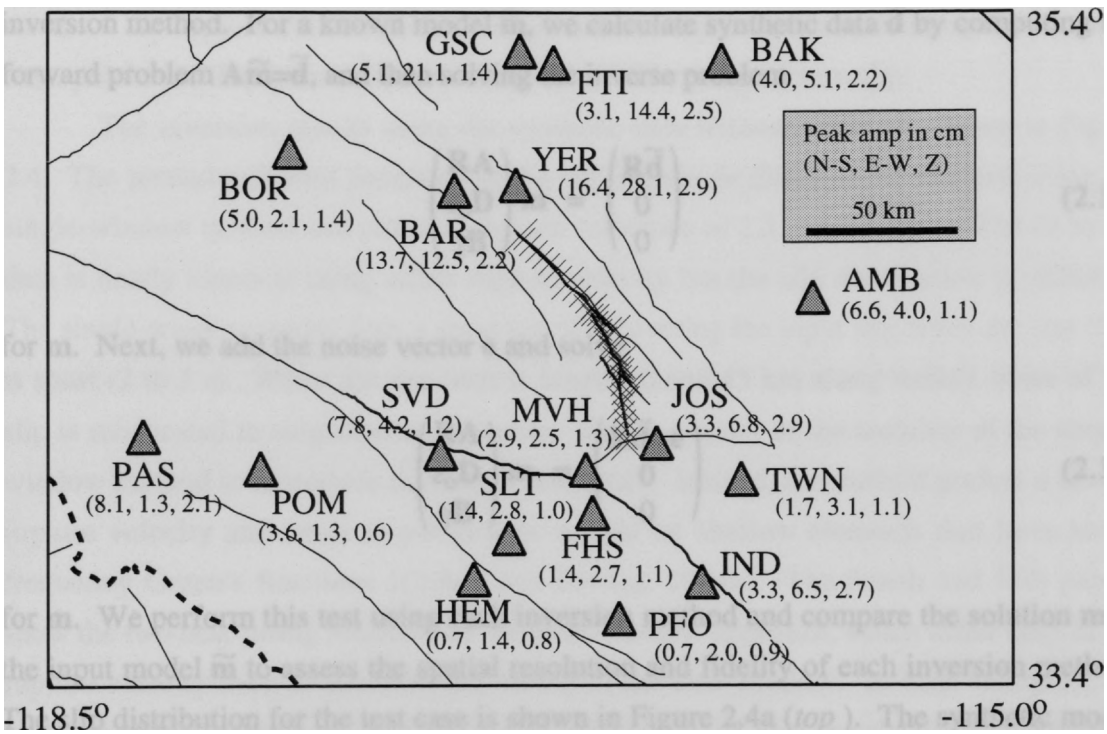

Figure 2.3. Map of the 18 low-gain, accelerometer stations used in this study. The stations are identified by three-letter code. The mainshock rupture zone is indicated by symbols that show the surface projection of each fault element. The fault elements form three linear fault segments, representing (from south to north) the Johnson Valley, Homestead Valley, and Camp Rock-Emerson faults. The four TERRAscope stations are PAS, SVD, PFO, and GSC.

2.5.3 *Inversion Results Using Synthetic Data*

We compute synthetic data for a hypothetical rupture using the Landers fault geometry, add uncorrelated white noise of comparable amplitude to that found when modeling aftershocks, and image the slip distribution and rupture time using each inversion method. For a known model $\tilde{\mathbf{m}}$, we calculate synthetic data $\tilde{\mathbf{d}}$ by computing the forward problem $\mathbf{A}\tilde{\mathbf{m}}=\tilde{\mathbf{d}}$, and then solving the inverse problem

$$\begin{pmatrix} \mathbf{RA} \\ \varepsilon_0\mathbf{D} \\ \gamma\mathbf{B} \end{pmatrix} \mathbf{m} = \begin{pmatrix} \mathbf{R}\tilde{\mathbf{d}} \\ 0 \\ 0 \end{pmatrix} \tag{2.15}$$

for $\mathbf{m}$. Next, we add the noise vector $\mathbf{e}$ and solve

$$\begin{pmatrix} \mathbf{RA} \\ \varepsilon_0\mathbf{D} \\ \gamma\mathbf{B} \end{pmatrix} \mathbf{m} = \begin{pmatrix} \mathbf{R}\tilde{\mathbf{d}}+\mathbf{e} \\ 0 \\ 0 \end{pmatrix} \tag{2.16}$$

for $\mathbf{m}$. We perform this test using each inversion method and compare the solution $\mathbf{m}$ to the input model $\tilde{\mathbf{m}}$ to assess the spatial resolution and fidelity of each inversion method. The slip distribution for the test case is shown in Figure 2.4a (*top*). The synthetic model has right-lateral displacement of either 0, 2, or 4 m, as shown by the 1 m contours. Note that the three rectangular fault segments are projected onto a single fault plane. The rupture velocity varies along the length of the fault: it is 2.2 km/s on the southern (Johnson Valley) segment, increases to 2.8 km/s on the middle (Homestead Valley) segment, and decreases to 2.5 km/s on the northern (Camp Rock-Emerson) segment. Additionally, each slip patch has a rise time duration of either 2, 3, or 4 s, which is labeled in Figure 2.4a (*top*). This rupture time model does not contain small-scale perturbations that may occur in earthquake rupture – in this test we only seek to reproduce the average rupture of each segment and the rise time variability. The rupture time for the input model is contoured in Figure 2.4b (*top*).

This strategy of using sensitivity tests for resolution analysis is discussed in *Beroza and Spudich* [1988] and *Cocco and Pacor* [1993] for the earthquake rupture problem, and in *Spakman and Nolet* [1988] for the delay-time tomography problem. The ability of each inversion method to recover the known slip and rupture model is indicative

of the resolution expected with the observed data and realistic noise levels. Artifacts of each method evident with synthetic data are also likely to exist with the recorded data. The range of rupture velocity, rise time, and slip amplitude in the synthetic model is intended to be representative of the variation found in the actual Landers earthquake. The rupture velocity varies from 2.2 to 2.8 km/s; rise times are 2 to 4 s, which is reasonable given the width of the rupture surface [*Day*, 1982]; and the slip is spatially heterogeneous, with large patches of displacement (asperities) separated by areas of zero slip.

The inversion results using the synthetic data without noise are shown in Figure 2.4. The second and third panels show the slip amplitude distribution obtained using the single-window method and constant rupture velocities of 2.3 and 2.4 km/s. The fit to the data is nearly identical using either rupture velocity but the slip distribution is different. The single-window model does a good job of recovering the input slip when the rise time is short (2 to 3 s). When the rise time is longer (0 and 45 km along strike), more of the slip is mislocated in neighboring elements. This is a result of the inability of the single-window method to reproduce the longer rise times. Instead, the method prefers a slower rupture velocity and tends to put greater weight on shallow elements that have lower frequency Green's functions [*Cohee and Beroza*, 1994a]. The fourth and fifth panels show the two best-fitting solutions of the three-window approach, which differ only in the rupture velocity used to establish the timing of the first window. In both solutions, the multi-window approach recovers the variable rise time and rupture velocity by distributing slip across the three windows. The slip amplitude solution locates the slip correctly for the long rise-time (4 s) asperities but tends to mislocate the slip in the shorter rise-time patches. In general, the corresponding rupture time model is a more accurate representation of the input model than a constant propagation velocity, but some artifacts are introduced to reconcile the mislocated slip (for example, between 5 and 15 km along strike).

One practical problem encountered with the three time-window approach is that the fit to seismograms is nearly constant over a wide range of rupture velocity (using the time of the first window). This is expected because slip is simply shifted to later windows when a higher rupture velocity is used. Even though the slip distributions are quite similar for the two cases shown, the rupture propagation models demonstrate important differences. These differences using noise-free data demonstrate a best-case scenario with this method for this data. Thus, without additional information, it appears

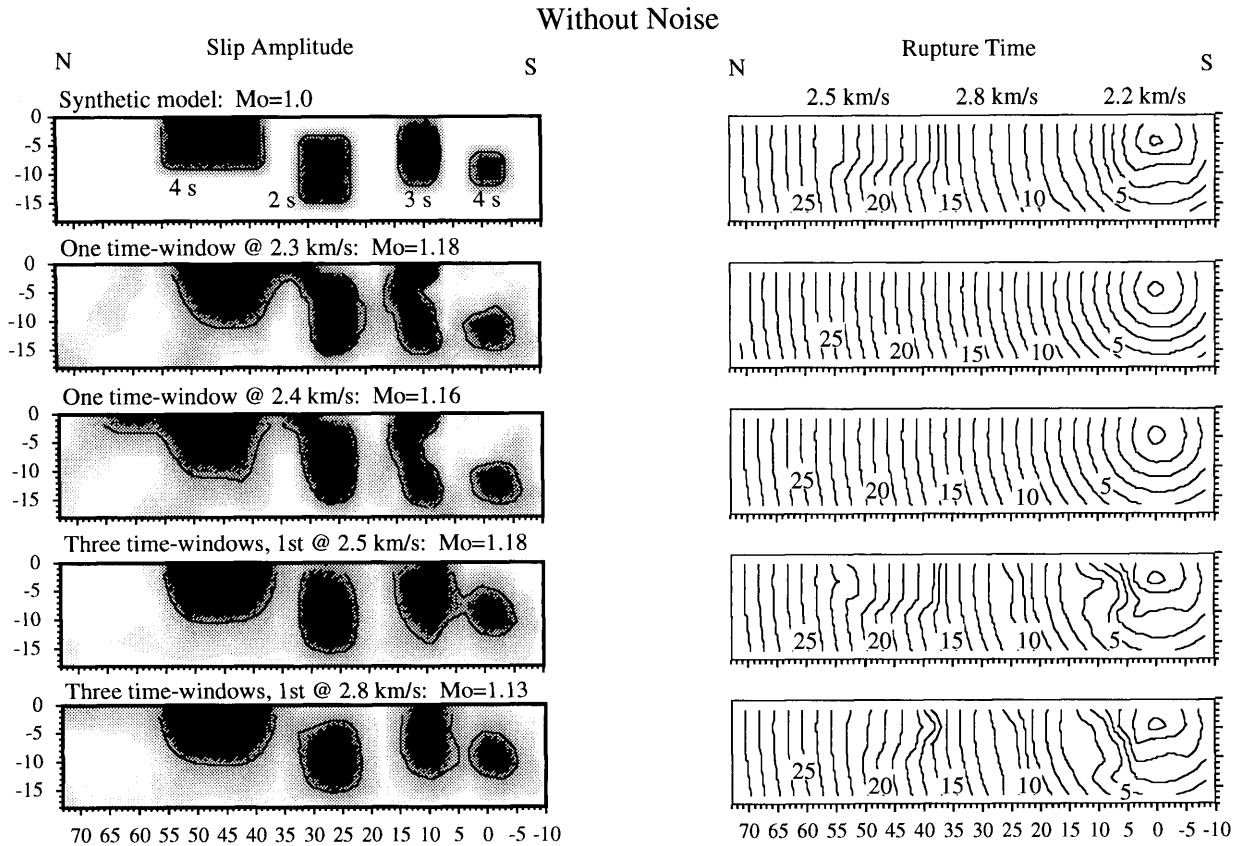

Figure 2.4. Input synthetic test model (slip amplitude and rupture time), and the inversion results using the two linear inversion methods. In these cross section projections of the fault, the overlapping regions are superimposed. The hypocenter is at 4.5 km depth and defines the horizontal origin. The two slip patches in the South fall on the Johnson Valley fault, the center slip patch is on the Homestead Valley fault, and the northernmost patch falls on the Camp Rock-Emerson fault. In each patch, the displacement is right-lateral. The rise time of each patch is either 2, 3 or 4 s; the slip amplitude is either 0, 2, or 4 m (shown by 1 m contours). The second and third panels are the solutions using the one time-window inversion method and a rupture velocity of 2.3 and 2.4 km/s. The fourth and fifth panels are three time-window solutions where the rupture velocity of the first window is 2.5 and 2.8 km/s, respectively. For these multi-window solutions, the slip-weighted temporal centroid is contoured for those elements with slip above 1 m. For elements with less slip, the rupture time is poorly determined and the 2.5 km/s rupture velocity is contoured. The normalized seismic moment is labeled for each solution.

unlikely that fine details of the propagation can be accurately recovered using the strong-motion data alone.

We quantify the fit to the data using a weighted measure of the variance reduction ($\Delta\sigma^2$) between the model and data defined as

$$\Delta\sigma^2 = \left(1 - \frac{(\mathbf{d} - \mathbf{g}(\mathbf{m}))^T \mathbf{C}_d^{-1} (\mathbf{d} - \mathbf{g}(\mathbf{m}))}{\mathbf{d}^T \mathbf{C}_d^{-1} \mathbf{d}}\right) \times 100\ \% \tag{2.17}$$

where $\mathbf{C}_d^{-1}$ represents the weighting (inverse data covariance) matrix and $\mathbf{g}(\mathbf{m})$ is the model prediction. In the noise-free test case the fit to seismograms is better using the three time-window inversion ($\Delta\sigma^2$= 92% at 2.8 km/s), compared to that obtained using the single-window inversion ($\Delta\sigma^2$= 73% at 2.4 km/s). In all preferred solutions the seismic moment is overestimated by 10% to 20%.

To make the test more realistic, Gaussian white noise is added to the synthetic data. The power spectra of the noise is flat and is filtered identically as the data. The amplitude of noise is adjusted to mimic the level of variance reduction (approximately 30%) found in modeling the Landers mainshock and aftershock seismograms [*Cohee and Beroza*, 1994a]. Note that the absolute level of variance reduction depends strongly on the passband and is much higher at lower frequencies. Synthetic displacement seismograms computed using the input model shown in Figure 2.4 (*top*) are plotted in Figure 2.5 for three representative strong-motion stations. The solid seismograms are the noise-free synthetic data and the dashed seismograms are with noise added.

The inversion results using the noisy data are shown in Figure 2.6. Again, the one time-window approach recovers the average rupture velocity (2.3 to 2.4 km/s). Recovery of the input slip distribution is degraded slightly relative to the noise-free solution for those asperities with a long (4 s) rise time. The moment is again overestimated by 20%. Nevertheless, even in the presence of noise, the patches with 2 and 3 s rise times are accurately located. With noise added, the seismogram variance reduction is reduced from 73% to 28%. In contrast, the results using the three-window method have changed considerably from the noise-free case. The slip is less accurately located for all slip patches. In particular, the long rise-time patches now have considerable slip in neighboring elements and the asperity edges are poorly defined. Compared with the one-window solutions, there is substantially more slip (and seismic moment) in these models,

suggesting that the increased number of free parameters allows the inversion to fit the uncorrelated noise with erroneous slip. As a result, the total moment is overestimated by about 50%. This overestimation of moment was also found by *Hartzell* [1989] using the same multi-window approach – he found the seismic moment increased with the addition of each successive time window. More importantly, the rupture time solution shows important differences from the input model; in particular, the propagation of the rupture front near the hypocenter is dissimilar. The measure of fit to the seismograms is marginally improved over the one-window model (32% versus 28%).

The estimated seismic moment and fit to seismograms for the synthetic tests are summarized in Figure 2.7. The top panel shows the moment obtained for a range of rupture velocities (1.8 to 3.5 km/s) using the one time-window method. The middle panel shows the moment in each time window using the three-window approach. Note that as the rupture velocity is increased (in the range from 2.4 to 3.0 km/s), the method places a greater percentage of moment in the second and third windows. The bottom panel quantifies the fit to the synthetic data using both inversion methods (*solid* - one window, *dashed* - three windows). The broad peak in the variance reduction using the three-window method makes it difficult to choose a best average rupture velocity and is indicative of the degraded stability inherent in the multi-window approach. In contrast, the single-window method has a peak in variance reduction at 2.3 to 2.4 km/s and a corresponding seismic moment that is 20% larger than the true moment. The fit to the synthetic data is plotted in Figure 2.8 for the one-window (2.4 km/s) and three-window (first window at 2.5 km/s) solutions presented in Figure 2.6. Differences in the visual fit to the data are subtle; however, close examination suggests the three-window model fits more of the noise in the seismograms.

Finally, we evaluate the ability of the linearized inversion to recover the rupture time model using three different assumed slip distributions. The top panel in Figure 2.9 is again the synthetic (input) rupture time model. The next panel is the solution of the linearized inversion assuming the true slip distribution and noise-free data. Most features of the input model are recovered, including the delayed rupture in the fourth slip patch at 45 km along strike, and the different rupture velocity on each fault segment. When the noise is added to the data, the solution is worse but still contains the principal features of the input model (third panel). In practice, we do not know the true slip distribution and instead use the estimate from the linear one-window inversion at a rupture velocity of 2.4

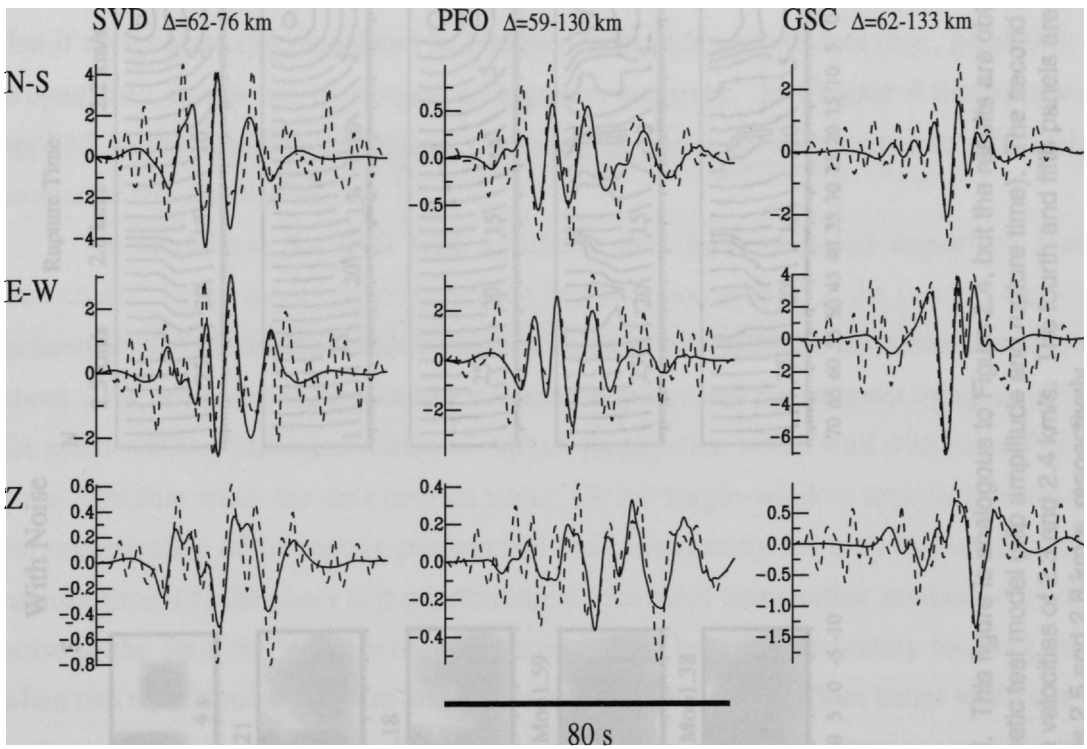

Figure 2.5. Synthetic displacement seismograms from hypothetical Landers earthquake shown in Figure 2.4 (*top*) for three seismic stations at representative azimuths (see Figure 2.3). The synthetic data is shown with and without noise added. In each case, the seismograms are filtered the same as the recorded data (see text). The level of noise was chosen to be representative of the uncorrelated noise present in the Landers mainshock seismograms.

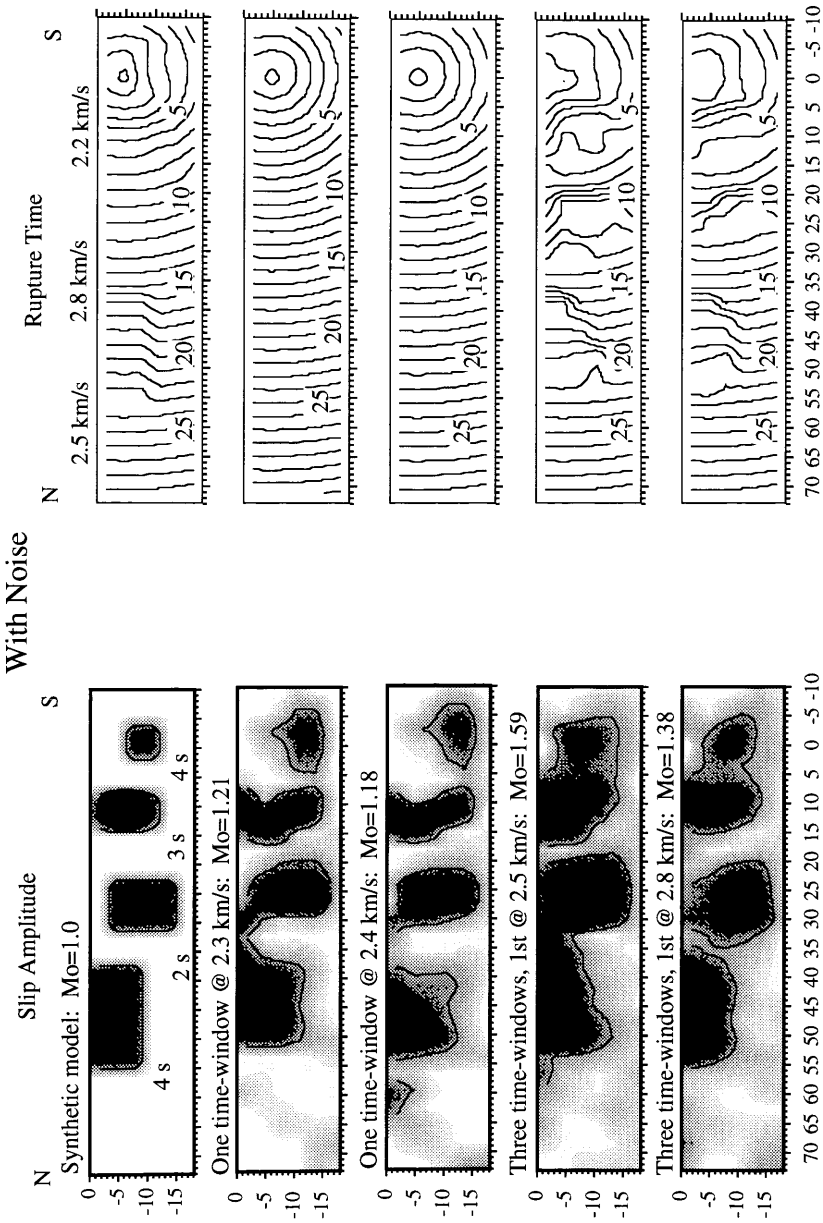

Figure 2.6. Input synthetic test model with noise added. This figure is analogous to Figure 2.4, but the results are obtained using synthetic data with noise added. The top panel is the input synthetic test model (slip amplitude and rupture time). The second and third panels are the results using the single-window method and rupture velocities of 2.3 and 2.4 km/s. The fourth and fifth panels are three time-window solutions where the rupture velocity of the first window is 2.5 and 2.8 km/s, respectively.

km/s. This result is shown using both noise-free and noisy synthetic data assuming the two slip models shown in Figures 2.4 and 2.6. Both of these inversions recover the true rupture variation to some extent; however, the fit to the seismograms is only slightly improved. This suggests that some of the variations in rupture time were mapped as mislocated slip in the previous linear inversion. Most importantly, if the correct slip distribution is used, it is possible to recover the input rupture time variation. This suggests that if an accurate slip model can be obtained from independent data (e.g., geodetic), than propagation details can be imaged with greater accuracy. In Chapter 4 this approach is applied to the Landers earthquake by using geodetic measurements to establish the coseismic slip distribution.

In summary, the tests with synthetic data have revealed important features attributable to each model parameterization and inversion method in the Landers earthquake geometry: (1) the single-window method tends to overestimate the seismic moment by about 20%, while the multi-window method overestimates the moment by up to 60%; (2) the multi-window parameterization of rupture propagation works well with noise-free data, but is unstable when the data contain noise; (3) the single-window approach is a simpler parameterization of the rupture propagation and consequently can only recover the average rupture time; (4) the gross slip distribution is recovered using either method; (5) without noise in the data, the single-window approach does better at accurately locating the slip when rise time is more uniform and the multi-window approach does better when rise time is strongly variable; (6) with noise in the data, the single window approach more precisely locates the distribution of slip amplitude; and (7) the nonlinear inversion for rupture time works well only if the assumed slip distribution is a good approximation of the true slip distribution. Having performed these sensitivity tests using the Landers fault geometry, station distribution, and data passband, we are now in a much better position to carry out the same inversions on the real Landers earthquake data and to interpret the results.

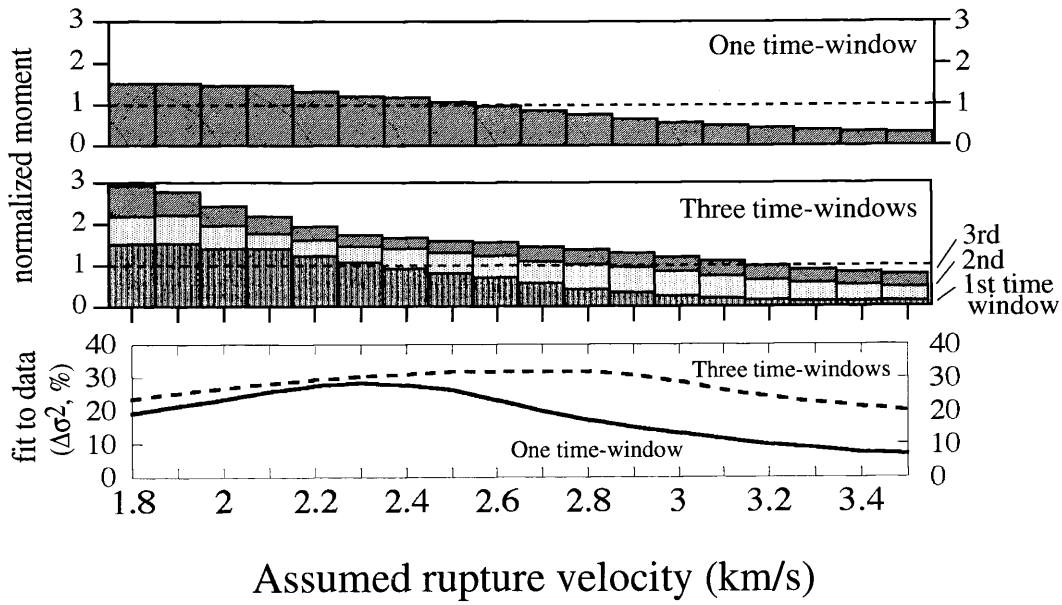

Figure 2.7. The seismic moment obtained for each average rupture velocity is shown in the *top* bar chart for the one time-window model (the input moment is normalized to unity). The moment in each time-window is shown for the three-window model in the *middle* bar chart (rupture velocity is determined by the time of the first window). The *bottom* panel shows the seismogram variance reduction ($\Delta\sigma^2$) as a function of rupture velocity using each method.

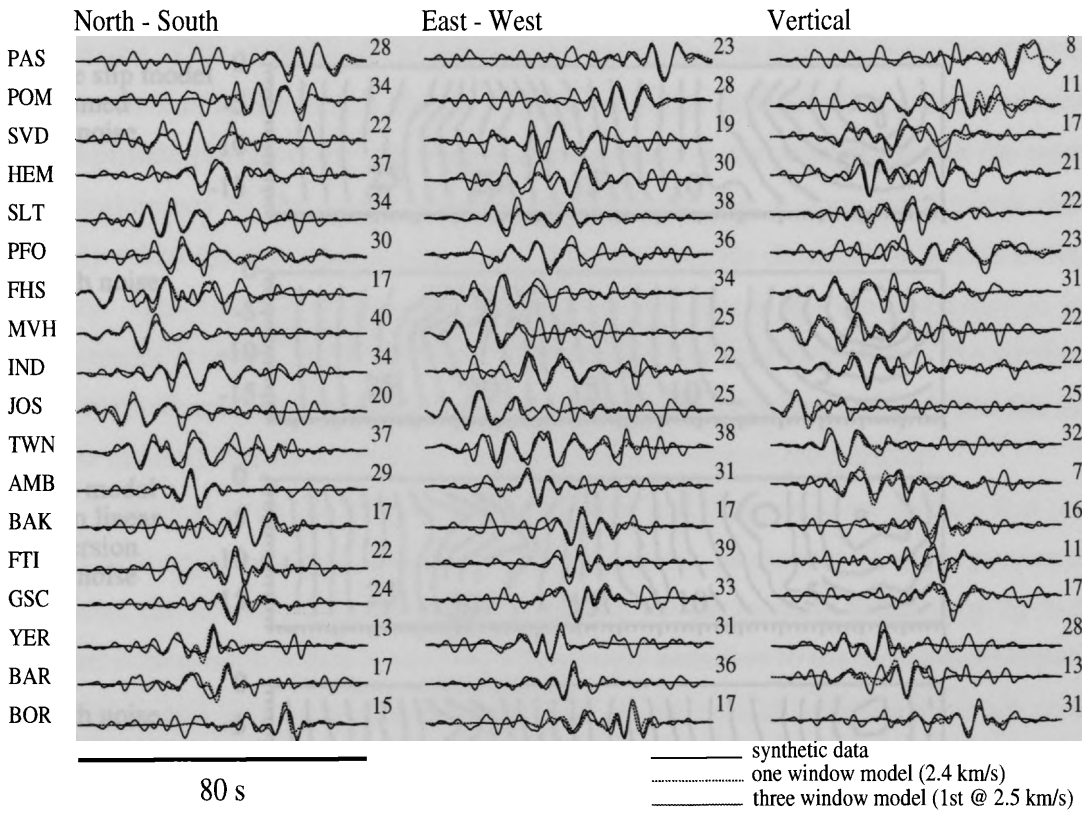

Figure 2.8. Fit to synthetic data seismograms with noise added for two inversion solutions shown in Figure 2.6. The solid seismograms are the synthetic data, the dashed seismograms are from the one time-window model (v = 2.4 km/s), and the gray seismograms are from the three time-window model (first window at 2.5 km/s). The variance reduction for each station component is listed to the right of the corresponding seismograms for the one-window solution. The average weighted variance reduction is 27.6% using one window, and 31.8% using three windows.

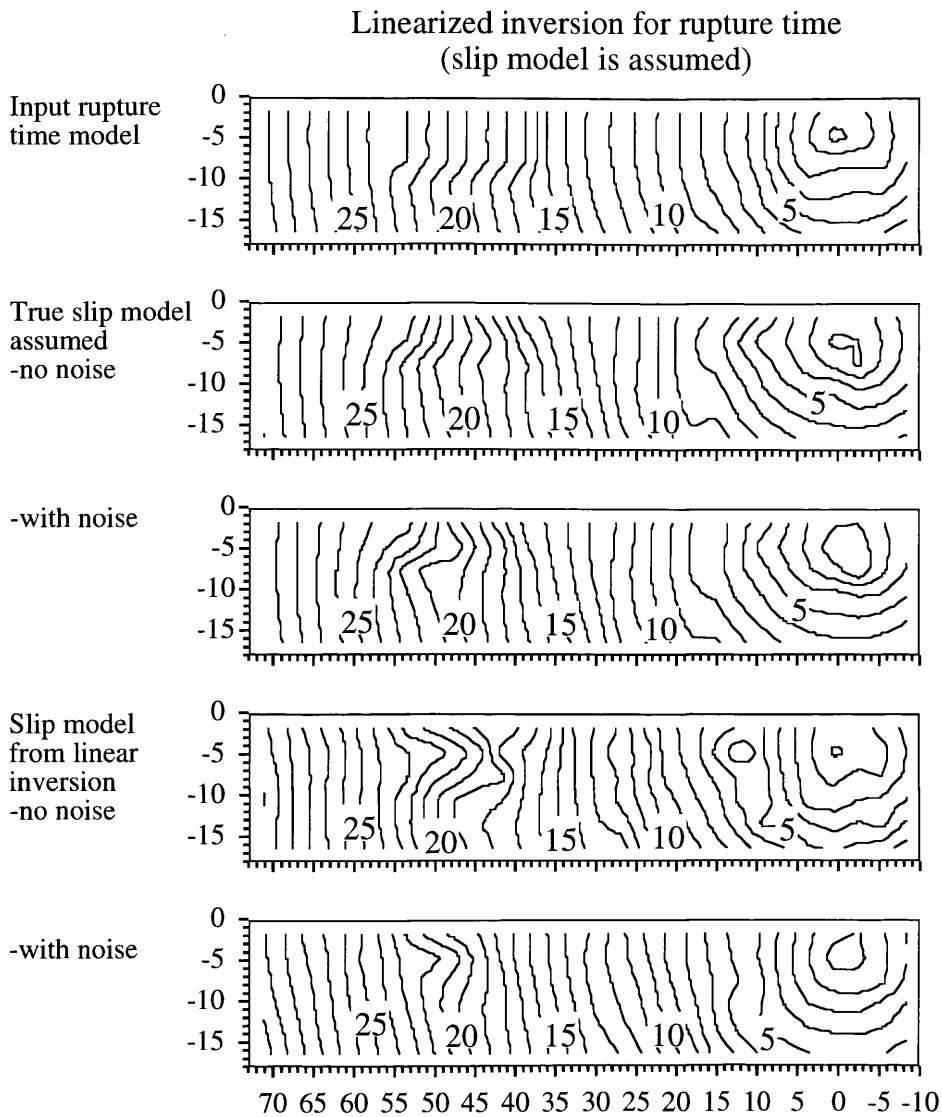

Figure 2.9. Four results of the linearized inversion for rupture time. The results differ only in the slip distribution assumed in each case, and whether or not noise was added to the synthetic data. The top panel shows the input rupture time model, which is the same as that shown in Figs. 3 and 5 (*top right*). The second and third panels assume the true slip model, and use a starting rupture model with a constant rupture velocity. The fourth and fifth panels also use a starting rupture model with a constant rupture velocity, but assume the slip distribution model that was determined in the corresponding linear one-window inversion.

Conclusions

In this chapter we compared two different approaches for recovering the rupture behavior of a fault using strong-motion seismograms. We first examined the properties of the solutions and their ability to recover a general rupture model in the presence of realistic noise. The results of the synthetic tests indicate both methods have strengths and weaknesses. One strength of the single-window method is that it appears to recover the seismic moment fairly well; it also recovers the average rupture velocity and variations in slip amplitude provided the rise time is short relative to the periods used in the analysis. The weaknesses of the single-window approach are that it does not recover the slip properly when the rise time is long and it does not recover detailed variations in rupture velocity. One strength of the multi-window case is that it has the flexibility to locate displacement correctly in the presence of substantial rise time variability. The weaknesses of this method are that it tends to overestimate the seismic moment and that, like the single-window method, it does not reliably recover details of rupture propagation.

It is clear from the comparison of the one- and three-window models that strong-motion seismograms alone cannot estimate the seismic moment with great precision. In both cases the fit to the data was nearly identical, yet the moment differed by up to 50%. In short, strong-motion data is not overwhelmingly sensitive to the moment (compared to other data), and that moments obtained from strong-motion seismograms are strongly influenced by the choice of model parameterization and inversion method.

Including other data types to constrain the slip model will reduce the trade-off between slip amplitude and rupture time that affect solutions based on seismic data alone. Clearly, including other types of data will improve the accuracy and decrease the model variance in studies of future earthquakes.

Chapter 3 — Rupture of the 1992 Landers Earthquake

Abstract

I use near-source (10 to 164 km) displacement seismograms to image the slip distribution and rupture history of the 1992 M_W 7.3 Landers, California, earthquake. Aftershock seismograms from similar distances are modeled to find the velocity model and frequency range (0.05 to 0.25 Hz) over which theoretical Green's functions are most accurate, and the measure of fit is used as an upper bound on theoretical error in the mainshock inversion. I represent the rupture surface with three planar segments divided into 3x3 km^2 elements extending from the surface to 18 km depth and solve for the slip distribution and rupture time model that minimizes misfit to both recorded seismograms and mapped surface displacement in a least-squares sense. I investigate two faulting models, one with a uniformly short (< 3 s) rise time everywhere on the fault surface and the other with a variable rise time (2 to 6 s). Sensitivity tests indicate both fault models recover similar slip and rupture features but neither is capable of imaging details of the rise time. For the Landers earthquake, I find an average rupture velocity of 2.5 km/s and use this average for a starting model in a linearized inversion for rupture time. In our solutions of slip amplitude distribution, the southernmost, Johnson Valley fault segment has 20% of the total seismic moment (6 to 7×10^{19} N-m) with small displacements near the hypocenter; the Homestead Valley segment contributes half of the moment with the largest slip amplitudes 25 to 35 km northwest of the hypocenter at 4 to 12 km depth; and the Camp Rock-Emerson segment contributes 30% of the total moment with the largest slip amplitude 35 to 50 km northwest of the hypocenter in the shallow crust (< 9 km). There is some evidence that the rupture front is delayed as it encounters high-slip regions suggesting that prior to the mainshock these areas were further from failure due to greater strength excess.

3.1 Introduction

Discrete inverse methods are routinely applied to estimate earthquake parameters in the point-source approximation [*Dziewonski et al.*, 1981; *Nabelek*, 1984; *Ekstrom*, 1987]. However, for large earthquakes or earthquakes recorded in the near-source region, the effects of fault finiteness are important and provide an opportunity to learn more about the details of rupture. Near-source seismograms are particularly valuable for imaging the rupture time and slip amplitude distributions of large earthquakes. These data are also less sensitive to velocity and attenuation heterogeneity in the source-receiver path than teleseismic recordings at comparable frequencies and thus the Green's functions used to relate model to data are more accurate.

Methods for estimating rupture time and slip amplitude distributions using near-source seismograms have been developed and applied to many earthquakes in California [*Olson and Apsel*, 1982; *Hartzell and Heaton* 1983, 1986; *Beroza and Spudich*, 1988; *Frankel and Wennerberg*, 1989; *Beroza*, 1991; *Steidl et al.*, 1991; *Wald et al.*, 1991]. Similar techniques have also been used to image rupture characteristics of earthquakes in Japan and elsewhere [*Fukuyama and Irikura*, 1986; *Takeo*, 1987; *Das and Kostrov*, 1990; *Hartzell and Mendoza*, 1991; *Fukuyama and Mikumo*, 1993]. In these studies the spatial and temporal distribution of slip on a planar rupture surface is estimated by modeling seismic waveforms. Propagation of the rupture front is modeled in several different ways. In some studies each element of the fault is allowed to rupture a number of times repeatedly [*Olson and Apsel*, 1982; *Hartzell and Heaton* , 1983, 1986; *Wald et al.*, 1991, *Wald and Heaton*, 1994a]. In others, each element ruptures only once, but rupture time variations are allowed by perturbation of a constant-rupture-velocity starting model [*Beroza and Spudich*, 1988; *Hartzell and Iida*, 1990]. Both approaches improve the fit to data by allowing some rupture time-variation, but they also increase the model space dimension (number of variables) and decrease the solution uniqueness.

The June 28, 1992, Landers earthquake provided an exceptional opportunity to apply inverse methods to a major strike-slip earthquake. Early studies of the Landers earthquake indicated a unilateral rupture of roughly 3.0 km/s with two sub-events separated by about 30 km [*Kanamori et al.*, 1992; *Ammon et al.*, 1993; *Campillo and Archuleta*, 1993; *Dreger*, 1994a]. These subevents were interpreted as being associated with slip on the Johnson Valley fault near the hypocenter and the Camp Rock-Emerson

fault to the north, with little slip on the intervening Homestead Valley fault [*Hauksson et al.*, 1993; *Lees and Nicholson*, 1993]. This interpretation was corroborated in part by a gap in the mapped surface slip on the southern portion of the Homestead Valley fault [*Ponti*, 1992; *Sieh et al.*, 1993].

Our slip models suggest the Landers earthquake was more complicated than a two-source event and that there was substantial slip on the Homestead Valley segment. In other words, we find significant slip on all three major fault segments. Other features of our source model are *i)* relatively low slip on the Johnson Valley fault, including the region near the hypocenter, *ii)* half of the total seismic moment on the Homestead Valley fault in a broad region centered near 8 km depth, and *iii)* peak slip displacements at shallow depth (<9 km) where the Camp Rock and Emerson faults overlap. In our model of the Landers earthquake, slip and rupture continue unimpeded through several fault segment boundaries. This suggests that fault segmentation alone can not be used to anticipate the size of future earthquakes.

In this paper we use complete point-source seismograms calculated in a one-dimensional (1D) velocity model to study the Landers earthquake rupture. The theoretical error in the Green's functions is determined by modeling aftershock seismograms for events with known source parameters. We parameterize the fault with three segments comprised of fault elements that slip either once when the rupture front passes, or several times in adjacent time windows, and explore *i)* linear inversions for slip given assumed rupture times, and *ii)* linearized inversions for rupture time given estimates of the slip distribution. The separation of the effects of slip amplitude and rupture time variation facilitates the investigation of their relative importance in fitting the seismograms.

3.2 The 1992 Landers, California, Earthquake

3.2.1 Model Parameterization

The Landers mainshock was the largest earthquake to occur in southern California since the 1952 M_W 7.7 Kern County event. The Landers earthquake started 6 km southwest of the town of Landers and ruptured northward for 22 s. It produced right-lateral displacements at the surface for over 70 km on a sequence of right-stepping vertical faults that form the northward extension of faulting that began approximately two months earlier in the M_W 6.1 Joshua Tree earthquake [*Hauksson et al.*, 1993]. Together with

previous earthquakes across the Central Mojave, these events ruptured a series of fault segments that cut across the predominant northwest trending faults in the region [*Hauksson et al.*, 1993; *Nur et al.*, 1993].

The locations of the fault segments used in our model parameterization are based on the surface trace of mapped rupture [*Sieh et al.*, 1993; *Johnson et al.*, 1994] and aftershock locations [*Hauksson et al.*, 1993]. We represent the rupture surface with three planar segments that extend vertically from the surface to 18 km depth (Figure 3.1). The high-frequency epicenter, found from arrival times on the short-period Southern California array, is shown by a star at 34.20°N and 116.43°W [*Kanamori et al.*, 1992; *Hauksson et al.*, 1993]. In our model, the southern segment of the fault is 27 km long and strikes 354°, the middle segment is 30 km long and strikes 331°, and the northern segment is 45 km long and strikes 322°. These three segments represent the Johnson Valley, Homestead Valley, and Camp Rock-Emerson faults, respectively [*Sieh et al.*, 1993; *Johnson et al.*, 1994]. Our representation of the Landers rupture surface as three planar segments is an idealization for at least two reasons. First, rupture at the surface occurs across shear zones that are 50 to 200 m wide [*Johnson et al.*, 1994], and second, the Camp Rock and Emerson are two distinct faults at the surface that are near-parallel and offset by 1 to 2 km; however, because we use longer period energy (> 4 s) in the analysis, error introduced by the simplified fault parameterization is small.

The Landers earthquake occurred in the middle of the TERRAscope array of high-quality broadband seismometers and triggered numerous low-gain accelerometers in the near-source region. Initial source parameters were estimated within hours of the origin time [*Kanamori et al.*, 1992]. The focal mechanism determined from regional *P*-wave first motion data indicates almost pure right-lateral strike-slip motion with a dip of 90° [*Hauksson et al.*, 1993], consistent with rupture of the Johnson Valley segment. The best point-source double-couple obtained from teleseismic surface waves suggests right-lateral, strike-slip motion on an almost vertical plane (strike 343°, dip 81°, rake 180°: USGS CMT) indicating substantial slip on faults that strike more westerly than the Johnson Valley fault. The mapped surface slip indicates little vertical displacement (< 2 m) at the surface; vertical displacements vary with position and appear to be mostly influenced by pre-existing topography and near-surface geology [*Sieh et al.*, 1993; *Johnson et al.*, 1994].

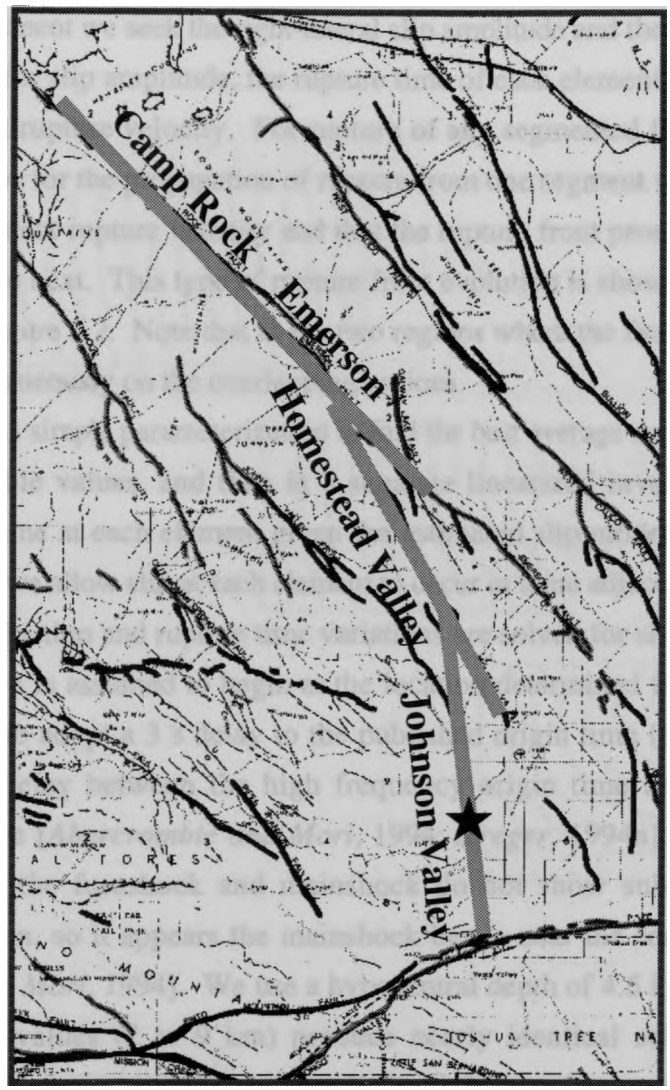

Figure 3.1. Map view of Landers region showing mapped faults and the surface projection of the three planar segments assumed in the mainshock modeling. These three segments represent the Camp Rock-Emerson, Homestead Valley, and Johnson Valley faults. The location and geometry of the segments is based on measured displacements at the ground surface and aftershock locations [see *Ponti*, 1992; *Sieh et al.*, 1993]. Fault map from *Bortugno* [1986].

The cross section of the three fault segments is shown in Figure 3.2. The hypocenter defines the horizontal origin. In our modeling of the Landers earthquake, we divide up the three fault segments into 204 total elements each with a dimension of 3x3 km^2. For each element we seek the right-lateral slip amplitude and the rupture time. In the linear inversions for slip amplitude, the rupture time of each element is determined by an assumed constant rupture velocity. For rupture of any segmented fault, there are many plausible scenarios for the propagation of rupture from one segment to the next. Initially, we assume a constant rupture velocity and that the rupture front proceeds smoothly from one segment to the next. This type of rupture front evolution is shown by the contours of rupture time in Figure 3.2. Note that in the two regions where the fault segments overlap, slip occurs simultaneously on the overlapping regions.

We use this simple parameterization to find the best average rupture velocity from a range of reasonable values, and then in a separate linearized inversion, solve for the optimal rupture time at each element given the estimated slip model. As an alternative parameterization, we allow slip at each element to occur in three adjacent time windows, so both the slip distribution and rupture time variations are solved for simultaneously. In all models the rupture is assumed to begin at the location determined from high-frequency recordings, and we adopt a 3 s delay to the published origin time (11:57:34.1 UTC) to account for the delay between the high frequency origin time and the initiation of mainshock rupture [*Abercrombie and Mori*, 1994; *Dreger*, 1994a]. The separation of arrival times for the foreshock and mainshock do not show substantial systematic azimuthal variation, so it appears the mainshock began near the foreshock hypocenter [*Abercrombie and Mori*, 1994]. We use a hypocentral depth of 4.5 km [*Hauksson et al.*, 1993], but other values (2 to 9 km) produce nearly identical solutions. Since the mainshock displacement recordings have little high frequency energy, they are not particularly sensitive to the hypocentral depth.

3.2.2 Mainshock Displacement Seismograms

The eighteen near-source, low-gain stations used in this study come from three sources: TERRAscope [*Kanamori et al.*, 1992], the California Strong Motion Instrumentation Program [*CSMIP*, 1992], and the U.S. Geological Survey [*Hough et al.*, 1993]. The station name, location, and other characteristics are listed in Table 3.1, and

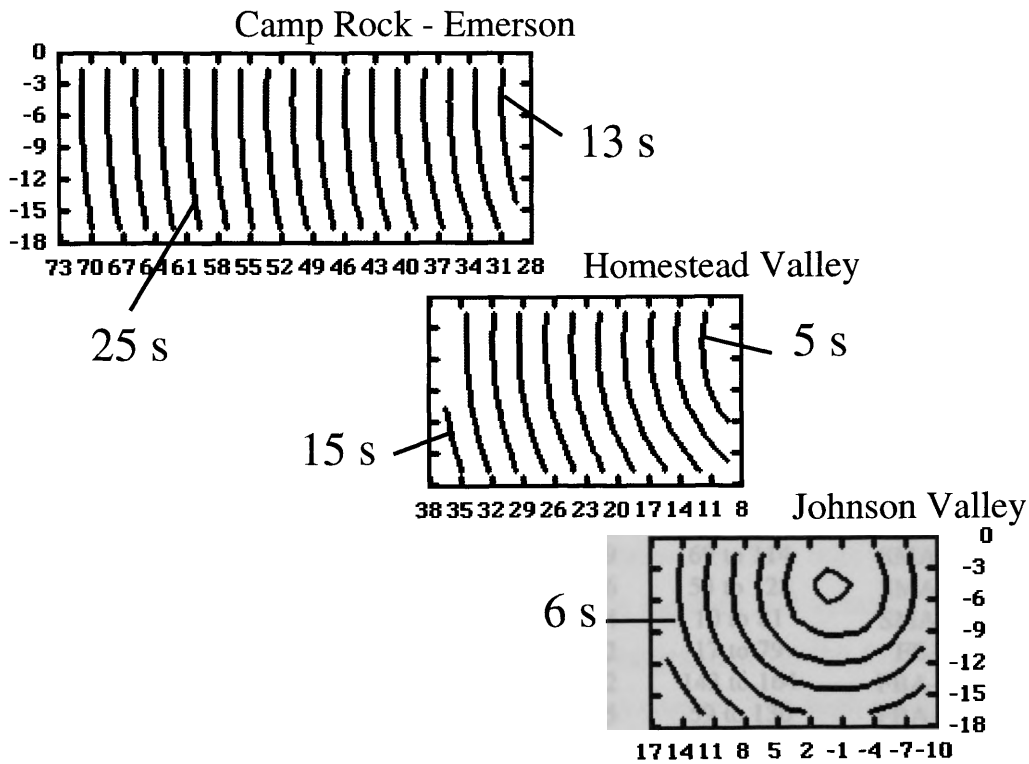

Figure 3.2. Cross section of the fault segments with 1 s rupture time contours shown using an average rupture velocity of 2.5 km/s. The dimensions of the segments are given in km.

their areal distribution is shown in Figure 2.3. The different recording characteristics of these seismic stations influence several aspects of the modeling effort.

The four TERRAscope sites (GSC, SVD, PFO, PAS) are equipped with FBA-23 accelerometers. These seismograms are the most useful for three reasons: first and most importantly, recordings from numerous aftershocks are available at the same sites, allowing the accuracy of Green's functions used in the inversion to be evaluated; second, the broadband response of these systems is superior to analog systems, allowing longer periods to be recovered; and third, the data is recorded in absolute time.

Table 3.1. Seismometer Stations

Code	Station	Lat°N	Long°W	Range (km)	Instrument
AMB	Amboy ◊	34.560	115.743	67 to 98	SMA-1 Ω
BAK	Baker ◊	35.272	116.066	88 to 129	SMA-1 Ω
BAR	Barstow ◊	34.887	117.047	28 to 100	SMA-1 Ω
BOR	Boron ◊	35.002	117.650	83 to 147	SMA-1
FHS	Fire House §	33.925	116.549	27 to 94	FBA Ω
FTI	Fort Irwin ◊	35.268	116.684	59 to 127	SMA-1 Ω
GSC	Goldstone †	35.303	116.808	62 to 133	FBA-23 Ω
HEM	Hemet ◊	33.729	116.979	69 to 114	SMA-1 Ω
IND	Indio ◊	33.717	116.156	53 to 128	SMA-1 Ω
JOS	Joshua Tree ◊	34.131	116.314	10 to 81	SMA-1 Ω
MVH	Morengo Valley §	34.053	116.572	17 to 79	FBA Ω
PAS	Pasadena †	34.148	118.172	143 to 164	FBA-23 Ω
PFO	Pinon Flats †	33.609	116.455	59 to 130	FBA-23 Ω
POM	Pomona ◊	34.056	117.748	116 to 127	SMA-1 Ω
SLT	Silent Valley ◊	33.851	116.852	51 to 99	SMA-1 Ω
SVD	Seven Oaks Dam †	34.104	117.098	62 to 76	FBA-23 Ω
TWN	Twentynine Palms ◊	34.021	116.009	41 to 108	SMA-1 Ω
YER	Yermo ◊	34.903	116.823	18 to 92	SMA-1

◊ CSMIP
† TERRAscope
§ USGS
Ω stations with absolute time

The strong-motion seismograms collected by CSMIP were recorded on SMA-1 instruments. This group comprises the majority of data used in this study (twelve stations) and, with two exceptions (BOR, YER), was also recorded with absolute time. The timing for BOR and YER was determined using predicted waveforms obtained from inversion with these stations having zero weight. We include them because they are located in a poorly-sampled area of the near-source region. These displacement seismograms are

derived from the recorded accelerograms by CSMIP and have a long-period response that is stated to be reliable to about 15 s [*CSMIP*, 1992].

We also use two stations (FHS, MVH) deployed by the USGS to record aftershocks of the Joshua Tree earthquake [*Hough et al.*, 1993]. This system consists of a Kinemetrics FBA sensor and a digital GEOS recorder. MVH is an important record since it is the closest station west of the hypocenter.

It is preferred to use all available data in the study; however, some characteristics of particular data preclude their use. For example, seismograms recorded on two SMA-2 instruments operated by Southern California Edison are among the closest to the surface rupture but are not used because the instruments have unknown response at periods longer than a few seconds and our Green's functions are not accurate at periods shorter than a few seconds. Also, these two stations do not have absolute time. Moreover, because there is greater station density in the urban area to the southwest of the epicenter, some similar CSMIP and USGS seismograms from this region are not included in the final data set.

The recorded accelerograms are twice integrated to displacement and high-pass filtered using a zero-phase (two-pass), four-pole butterworth filter with a 0.08 Hz (12.5 s) corner. The sharp filter is necessary to assure that the data and synthetic have similar power at frequencies beyond the corner. The seismograms from the four TERRAscope stations are high-pass filtered using a 0.05 Hz (20 s) corner. The high-pass filter corners are required by the increased signal-to-noise ratio at lower frequencies. For all stations, we use a low-pass filter corner at 0.25 Hz (4 s). The corresponding Green's functions are filtered in an identical manner. A low-pass filter is used to provide more accurate Green's functions – this particular corner was determined by modeling aftershock seismograms recorded at TERRAscope. The final set of eighteen three-component seismograms is shown in Figure 3.3 (using a four-pole low-pass filter at 0.25 Hz). The data are aligned with the delayed mainshock origin time as the start time. The peak amplitude (in cm) of each seismogram component is labeled next to the station symbol in Figure 2.3. In Figure 3.3, we indicate (as a percentage) the ratio of the power of each component to the summed power of the three components at each station; this relative power measure is used in the inversions to weight the seismograms.

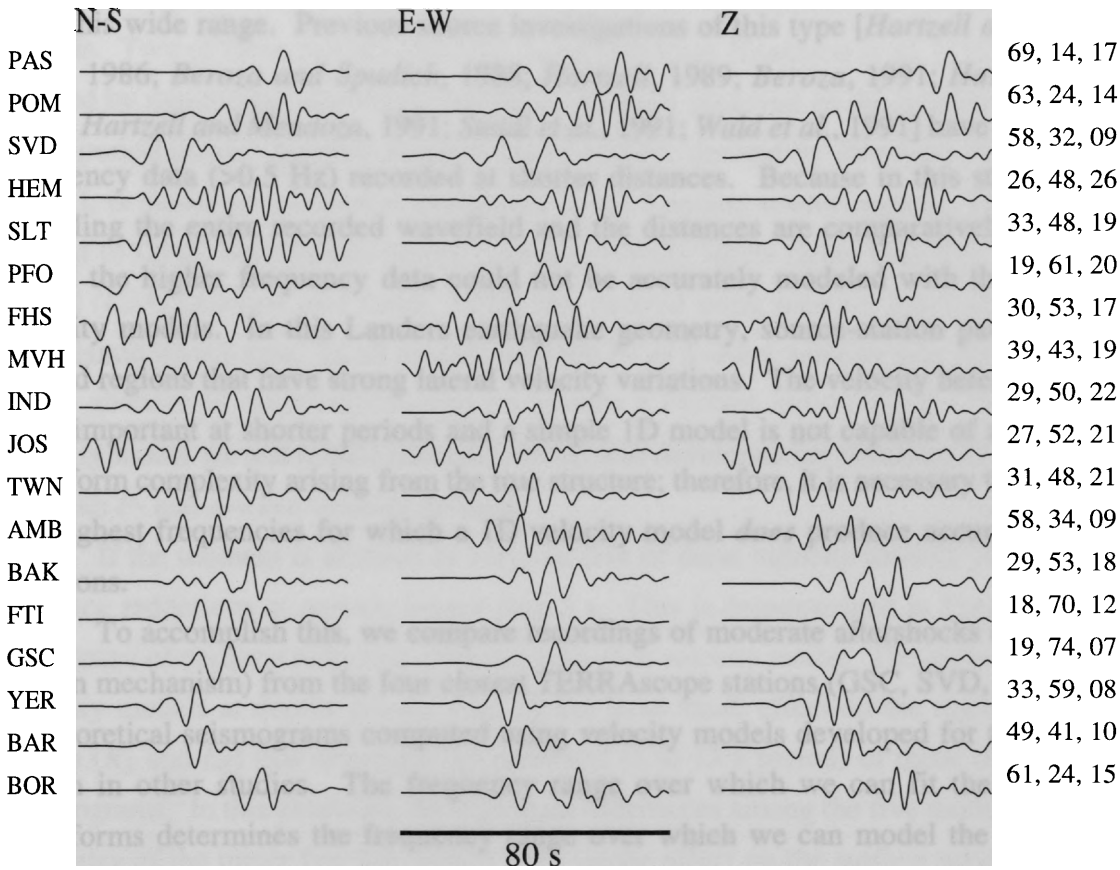

Figure 3.3. Plot of the filtered displacement data for the three components of motion (N-S, E-W, Z). Most data are bandpass filtered between 4 and 12.5 s period. The TERRAscope stations (GSC, PFO, SVD, and PAS) have better long-period response and are filtered using a highpass corner of 20 s. The power of each component as a percentage of the total power of the three components at each station is listed to the right.

3.3 Green's Function Accuracy

The distances from the over 70 km long mainshock fault to the low-gain stations range from 10 to 164 km (Figure 2.3). The inversions require accurate Green's functions over this wide range. Previous source investigations of this type [*Hartzell and Heaton*, 1983, 1986; *Beroza and Spudich*, 1988; *Hartzell*, 1989; *Beroza*, 1991; *Hartzell et al.*, 1991; *Hartzell and Mendoza*, 1991; *Steidl et al.*, 1991; *Wald et al.*, 1991] have used higher frequency data (>0.5 Hz) recorded at shorter distances. Because in this study we are modeling the entire recorded wavefield and the distances are comparatively large, we found the higher frequency data could not be accurately modeled with the proposed velocity models. In this Landers earthquake geometry, source-station paths traverse faulted regions that have strong lateral velocity variations. The velocity heterogeneity is most important at shorter periods and a simple 1D model is not capable of reproducing waveform complexity arising from the true structure; therefore, it is necessary to determine the highest frequencies for which a 1D velocity model *does* produce accurate Green's functions.

To accomplish this, we compare recordings of moderate aftershocks (that have a known mechanism) from the four closest TERRAscope stations (GSC, SVD, PFO, PAS) to theoretical seismograms computed using velocity models developed for the Landers region in other studies. The frequency range over which we can fit the aftershock waveforms determines the frequency range over which we can model the mainshock waveforms and the measure of fit is an upper bound on the theoretical error in the mainshock inversion. The distances (Δ = 56 to 175 km) and azimuths spanned by the aftershocks are similar to those of the mainshock.

The TERRAscope stations recorded thousands of aftershocks in the Landers earthquake sequence [*Kanamori et al.*, 1992; *Hauksson et al.*, 1993]. We use 1D velocity models to compute theoretical seismograms using a frequency-wavenumber integration method [*Wang and Herrmann*, 1980; *Saikia*, 1994] for twelve aftershocks located close to the rupture surface with hypocenter locations and mechanisms determined in an independent study [*Thio and Kanamori*, 1995]. We use this comparison both to evaluate the different velocity structures and to assess Green's function accuracy. In this analysis, we seek a single velocity model that best predicts the entire aftershock waveforms at the four TERRAscope stations and to determine the passband over which the velocity model is adequate. Although there is some error in the assumed aftershock depth and focal

mechanism, which will degrade the fit somewhat, the source parameters were estimated in a detailed study and should be more precise than those obtained from arrival times and first-motions [*Thio and Kanamori*, 1995].

In Figure 3.4 the *P*-wave velocity is plotted versus depth for five different velocity models. Two of these models (*SoCalR, LanR*) are from *Hauksson et al.* [1993] and were derived by minimizing aftershock traveltime residuals observed on the Southern California short-period array. Another *P*-wave model (*DEP*), derived by *Eberhart-Phillips et al.* [1992], is based on calibration explosions in the Landers source region. This model is similar to *LanR*, but contains eleven constant-velocity layers rather than five. The fourth model (*CJA*) [*Ammon and Zandt*, 1993] was derived using receiver function analysis of teleseismic waveforms. In all models only the *P*- or *S*-wave velocity was determined, so in the absence of other information we assume a Poisson solid ($\alpha = \beta\sqrt{3}$). The fifth velocity model we test (*DSD*) [Dreger, 1994a] was developed for Southern California and has both *P*- and *S*-wave velocity defined.

If the moment is allowed to vary, all five of these velocity models yield positive variance reductions at periods longer than 5 s. This is demonstrated in Figure 3.4 with histograms of variance reduction obtained with each velocity model. The differences in the velocity models at depths greater than 10 km have small effect on the regional surface waves (R_g and L_g) that dominate the passband (5 to 15 s period) of these displacement seismograms. In this passband, the important differences among the five models are in the velocities of the upper few km, which have strong effect on the surface wave amplitude and dispersion. For each velocity model, we compute the variance reduction between data and theoretical seismograms for twelve representative aftershocks recorded at the three-component TERRAscope stations. The *LanR* velocity model works best and produces the smallest overall misfit to the aftershock waveforms.

We compute theoretical aftershock seismograms using the *LanR* velocity model and a triangular source time function of 0.3 s duration. Using a constant time function is valid because we are interested in frequencies lower than the aftershock corner frequencies. We evaluate the fit to the aftershock data as a function of the passband using different low-pass filter corners. The variance reduction obtained with the aftershock seismograms indicates the level of fit we expect when modeling mainshock seismograms.

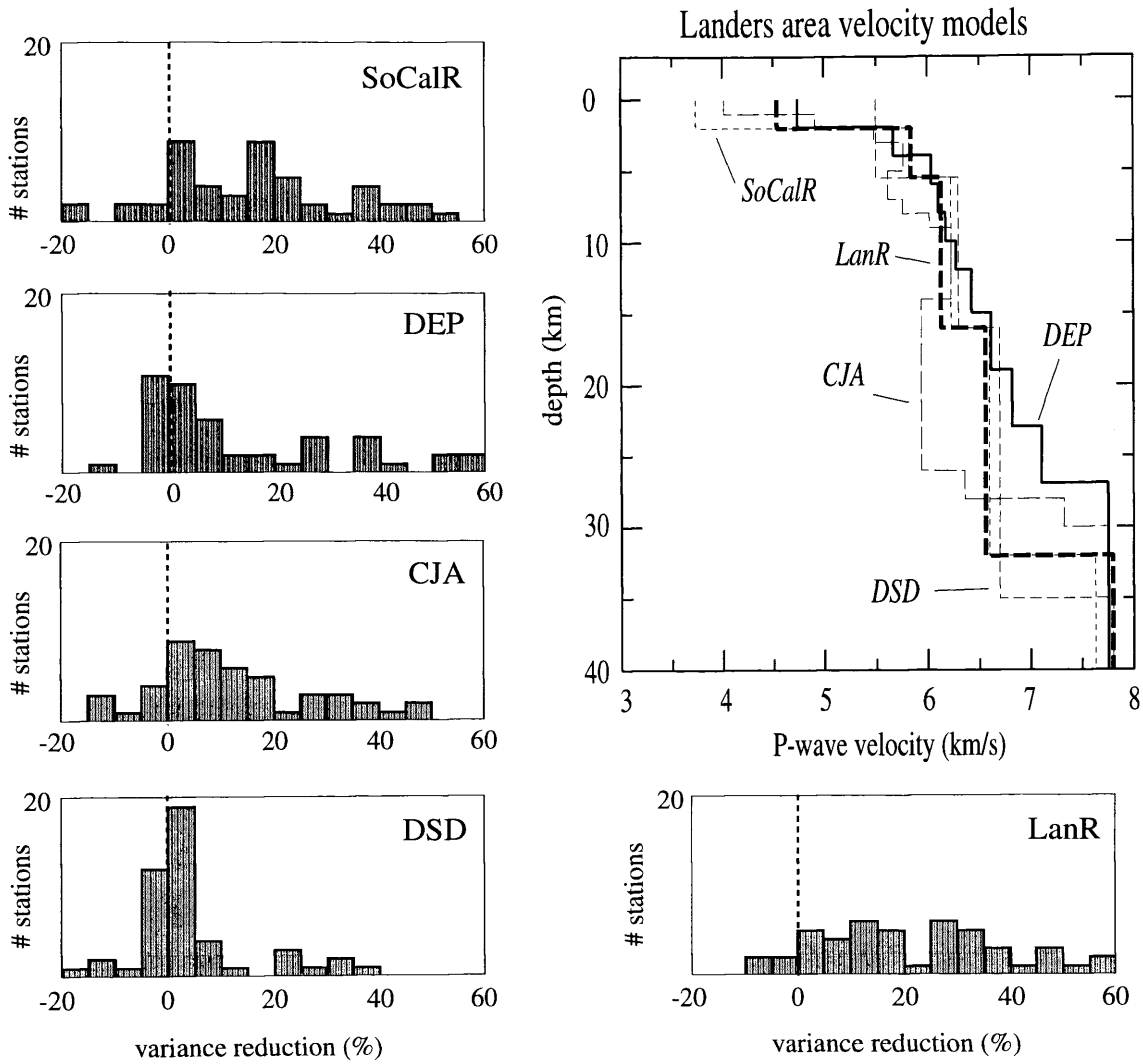

Figure 3.4. Variance reduction obtained using five 1D velocity models determined for the Landers region by *Hauksson et al.* [1993] (*LanR*, *SoCalR*), *Eberhart-Phillips et al.* [1992] (*DEP*), *Dreger* [1994a] (*DSD*), and *Ammon and Zandt* [1993] (*CJA*). Each histogram shows the variance reduction for each station for 12 aftershocks near the Landers fault zone recorded at four TERRAscope stations (GSC, SVD, PFO, PAS). With each *P*-wave model (except *DSD*) we assume a Poisson solid, and standard density and attenuation relations. At the periods used in this study, the important differences among these models are in the upper 10 km. The *LanR* model provides the best fit to the aftershock waveforms and we use it to compute Green's functions for the models shown in this paper.

Figure 3.5 shows some of the effect of the different low-pass filter corners on the fit to aftershock seismograms. These displacement seismograms are bandpass filtered using a zero-phase, four-pole butterworth filter with a high-pass corner at 0.067 Hz (15 s period) and three different low-pass corners at 2.0, 0.5, and 0.25 Hz (0.5, 2, and 4 s period). The observed and theoretical seismogram pairs are plotted together for the east-west component of motion for eight of the aftershocks. Figure 3.6 shows the aftershock locations and mechanisms. For the velocity models tested, the theoretical-data seismogram fit is better at lower frequencies. When we allow higher frequencies (>0.25 Hz), the modeling assumptions are less accurate and the fit to the data is poor.

At large propagation distances (e.g., PAS) the homogeneous layering in the velocity model produces short-period dispersed surface waves that are not seen in the recorded seismograms. This ringing phenomena is an undesirable artifact of the perfect layering in the 1D velocity model. These unnatural arrivals are not a problem when the seismograms are filtered to remove periods shorter than 4 s. For some aftershocks, error in the assumed mechanism appears to have an important contribution to the misfit. For example, the uniformly poor fit for event #14 suggests that either the mechanism or depth is not well determined. In general, the smaller magnitude aftershocks (e.g., events #4 and 18) have smaller amplitude displacements with low signal-to-noise ratios. An additional contribution to the misfit at the shortest periods is attributable to the unknown rise time (duration of slip function) of each aftershock.

Histograms are shown in Figure 3.7 of the variance reduction obtained with the *LanR* model and the three different low-pass filter corners at 2.0, 0.5, and 0.25 Hz. The histograms in Figure 3.7 show the variance reduction for each passband. As shown in Figure 3.5, we cannot reliably model the entire seismogram at frequencies much higher than 0.25 Hz. Based on this analysis we only seek to fit data at frequencies below 0.25 Hz when modeling the mainshock and expect a variance reduction of approximately 25%.

Just as the rise time is an unknown when modeling aftershocks, we also do not know how and to what extent the rise time varies across the rupture surface of the mainshock. The relationship of rise time to slip amplitude and propagation has important implications for earthquake physics. In the fault model, when we constrain each point on the fault to slip just once, we find that rise times greater than 3 s generate pulses broader than those observed in the mainshock seismograms. This result is consistent with that of *Dreger* [1994a], who found that mainshock seismograms recorded on TERRAscope

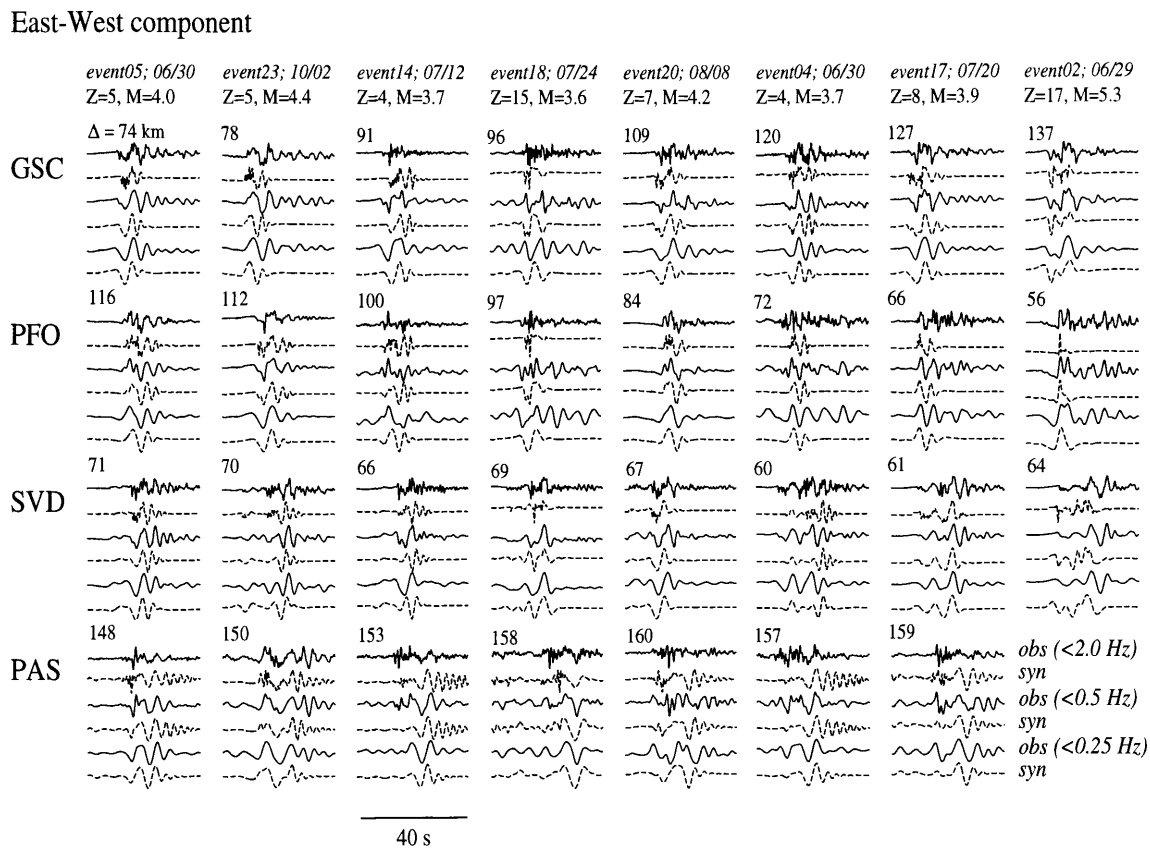

Figure 3.5. Example of modeling of aftershock displacement seismograms and the effect of using different low-pass filter corners (east-west component). The legend is shown in the lower right. For each station and aftershock, three pairs of seismograms are shown using low-pass filter corners at 2.0 Hz (0.5 s period), 0.5 Hz (2 s), and 0.25 Hz (4 s), and a high-pass corner at 0.067 Hz (15 s). The rows show same-station variability due to changing distance, depth and mechanism. The columns show the same earthquake at the TERRAscope stations (GSC, SVD, PFO, PAS). In each case, the horizontal distance in km is indicated in the upper left, and the depth and magnitude are shown at the top of each column. Paths to these four stations from these aftershocks are representative of those encountered in the mainshock geometry. The regional surface waves *Lg* and *Rg* are the largest amplitude arrivals at long periods.

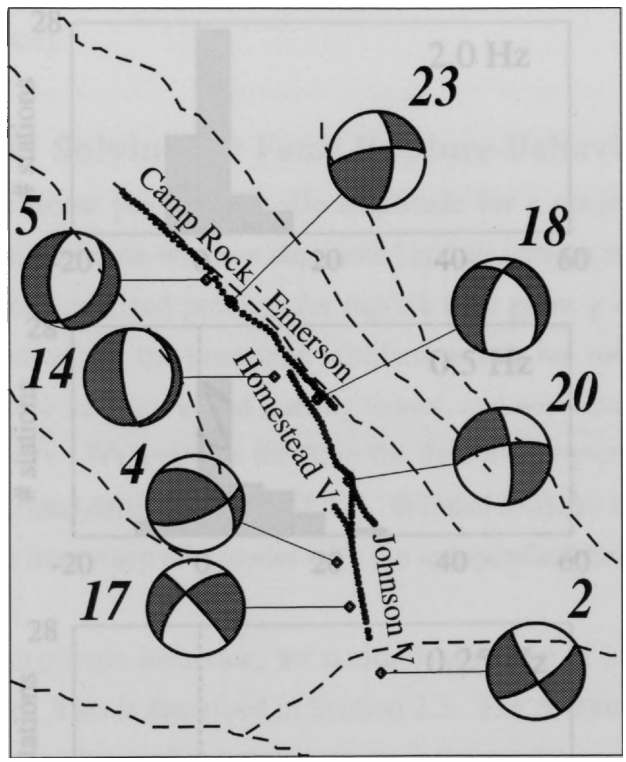

Figure 3.6. Map view of the aftershock epicenters and focal mechanisms used in Figure 3.5. The label for each mechanism is the event number.

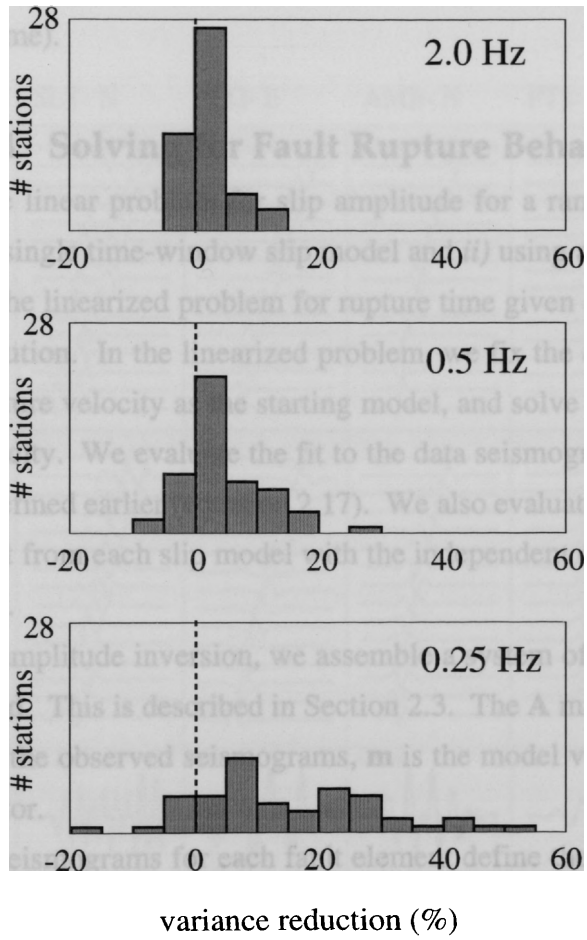

Figure 3.7. Histograms of variance reduction obtained by modeling aftershocks using the *LanR* velocity model and three different low-pass filter corners at 2.0 Hz (0.5 s period), 0.5 Hz (2 s), and 0.25 Hz (4 s), and a high-pass corner at 0.067 Hz (15 s). When the higher frequencies are removed, the fit to the data is improved. We use this analysis to determine the passband over which the theoretical Green's functions are adequate for modeling the mainshock. The level of variance reduction obtained in this manner is an upper bound on theoretical error in the mainshock inversion.

require short (1 to 3 s) rise times. The longer period data (> 4 s) used in this study is insensitive to the high frequency characteristics of the rise time. In other words, because the seismograms are low-pass filtered removing energy shorter than 4 s period, any rise time of 2 s or less produces essentially the same results as does a step function response (instantaneous rise time).

3.4 Solving for Fault Rupture Behavior

We solve the linear problem for slip amplitude for a range of assumed rupture velocities *i)* using a single time-window slip model and *ii)* using a multiple time-window slip model, and *iii)* the linearized problem for rupture time given a starting model and an assumed slip distribution. In the linearized problem, we fix the distribution of slip, use the best average rupture velocity as the starting model, and solve for perturbations to the average rupture velocity. We evaluate the fit to the data seismograms using the variance reduction measure defined earlier (equation 2.17). We also evaluate the fit of the predicted surface displacement from each slip model with the independent observations of mapped surface displacement.

For the slip amplitude inversion, we assemble a system of linear equations in the familiar form $\mathbf{Am} = \mathbf{d}$. This is described in Section 2.3. The $\mathbf{A}$ matrix relates slip at each point on the fault to the observed seismograms, $\mathbf{m}$ is the model vector (slip amplitudes), and $\mathbf{d}$ is the data vector.

Theoretical seismograms for each fault element define the columns of $\mathbf{A}$. Figure 3.8 shows some of these Green's functions from the top and bottom row of elements for six stations at representative azimuths (see Figure 2.3). The variation of the Green's functions for the azimuths shown and the difference between the top and bottom element rows is characteristic of the entire station set and a qualitative indicator of the depth resolution possible using this model parameterization, station geometry, and passband.

For each of the 54 seismograms we use 80 s of data sampled at 0.25 s, so the data dimension is 17,280. When we restrict each element to only slip once, the size of the model space N is 204, which is simply defined by the chosen discretization of the fault surface. When slip is permitted to occur on the same element in adjacent time windows, the size of the model space is multiplied by the number of windows. In the linearized inversion for rupture time, each element slips once and we solve for the best rupture time for each of the 204 elements. For comparison, the number of unknowns in other source

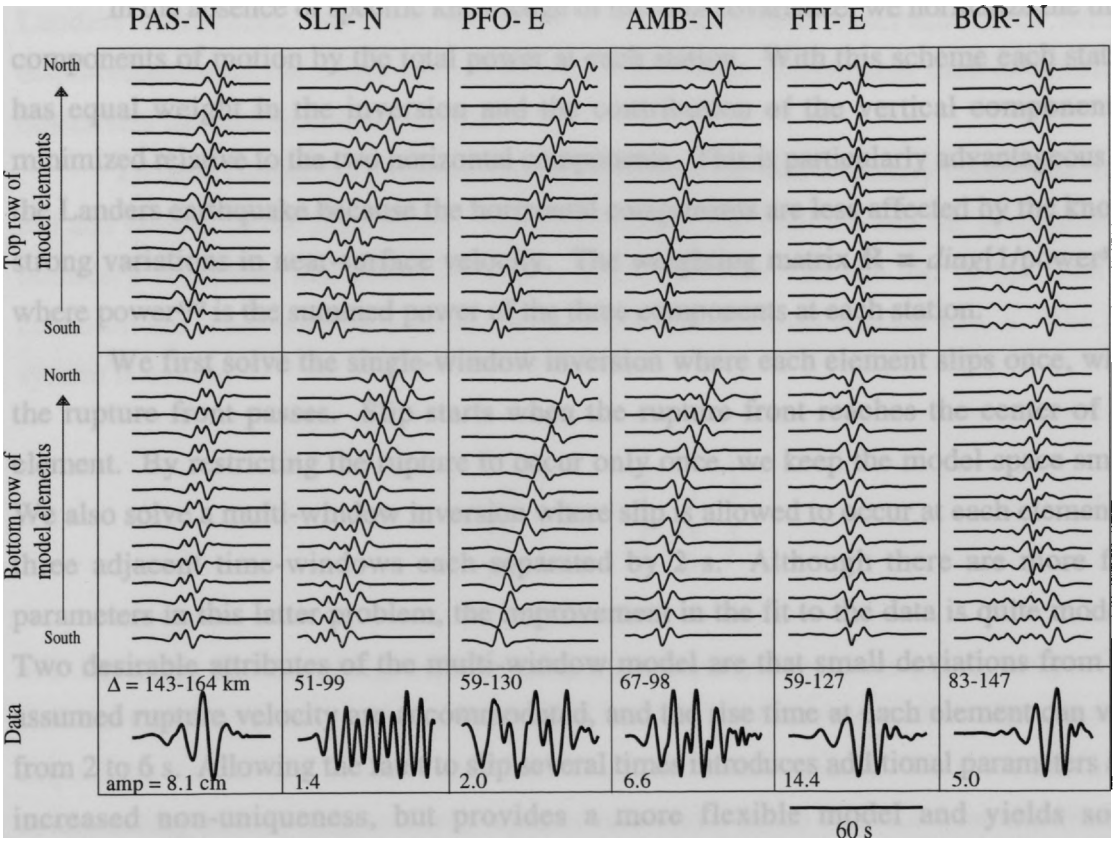

Figure 3.8. Theoretical seismograms for the top and bottom row of selected model elements for six stations at representative azimuths (see Figure 2.3): PAS (Δ=143 to 164 km), SLT (Δ=51 to 99 km), PFO (Δ=59 to 130 km), AMB (Δ=67 to 98 km), FTI (Δ=59 to 127 km), and BOR (Δ=84 to 147 km). For each station one horizontal component is shown with the peak amplitude (cm) labeled below. Theoretical seismograms are arranged from north (top) to south (bottom). Each row displays displacement seismograms for the appropriate component and station. These seismograms are representative of those used in the inversions.

inversions that use seismic data range from 400 to 600 [*Hartzell and Heaton*, 1986; *Beroza and Spudich*, 1988; *Hartzell*, 1989; *Hartzell and Iida*, 1990; *Wald et al.*, 1991; *Steidl et al.*, 1991] to 1700 [*Beroza*, 1991] to as many as 10,000 in the clearly under-determined case [*Frankel and Wennerberg*, 1989]. In this study we seek to keep the model space dimension as small as possible while still fitting the seismic waveforms acceptably well.

In the absence of specific knowledge of the data covariance, we normalize the three components of motion by the total power at each station. With this scheme each station has equal weight in the inversion and the contribution of the vertical component is minimized relative to the two horizontal components. This is particularly advantageous for the Landers earthquake because the horizontal components are less affected by the known strong variations in near-surface velocity. The weighting matrix $\mathbf{R} \equiv diag[1/\text{power}^{sta}]$, where power^{sta} is the summed power of the three components at each station.

We first solve the single-window inversion where each element slips once, when the rupture front passes. Slip starts when the rupture front reaches the center of the element. By restricting the rupture to occur only once, we keep the model space small. We also solve a multi-window inversion where slip is allowed to occur at each element in three adjacent time-windows each separated by 2 s. Although there are more free parameters in this latter problem, the improvement in the fit to the data is quite modest. Two desirable attributes of the multi-window model are that small deviations from the assumed rupture velocity are accommodated, and the rise time at each element can vary from 2 to 6 s. Allowing the fault to slip several times introduces additional parameters and increased non-uniqueness, but provides a more flexible model and yields some improvement in the fit to the data.

We regularize the system to yield a slip model that varies smoothly across the fault plane by finding the distribution of right-lateral slip that simultaneously minimizes the 2-norm between observed and predicted seismograms, and minimizes the first-derivative smoothing norm. By minimizing the gradient of slip amplitude we lower the condition number (ratio of largest to smallest eigenvalue) and recover a more stable slip distribution. This augmented linear system is written

$$\begin{pmatrix} \mathbf{RA} \\ \varepsilon_0 \mathbf{D} \end{pmatrix} \mathbf{m} = \begin{pmatrix} \mathbf{Rd} \\ 0 \end{pmatrix}, \tag{3.1}$$

where $\mathbf{D}$ represents the smoothing matrix and ε_0 is the scalar that weights $\mathbf{D}$. The value of ε_0 controls the smoothness of the model and is usually based on the *desired* solution

smoothness. Although it is better to compute ε_0 using an objective approach like generalized cross-validation [*Wahba*, 1990; *Matthews and Segall*, 1993], it is difficult to implement without improved knowledge of data and model covariance. There is a predictable trade-off between model roughness, defined as $\|\mathbf{Dm}\|^2$, and data fit – a rougher model fits the seismic data better but is a less stable result. In the case of the Landers earthquake, we have the benefit of independent observations of surface displacement over the entire fault length. We use these independent data to determine objectively the best smoothing weight.

To limit further the possible range of solutions, we add boundary conditions to the top and bottom of the fault model. At the bottom of the fault we add the homogeneous boundary condition and constrain slip to approach zero. At the top of the fault we constrain the shallowest fault elements to match the observed surface slip, **s**. The new system is written

$$\begin{pmatrix} \mathbf{RA} \\ \varepsilon_0\mathbf{D} \\ \tau\mathbf{T} \\ \gamma\mathbf{B} \end{pmatrix} \mathbf{m} = \begin{pmatrix} \mathbf{Rd} \\ 0 \\ \tau\mathbf{s} \\ 0 \end{pmatrix}. \tag{3.2}$$

We first vary the smoothing without using the boundary conditions ($\varepsilon_0 \neq 0$, $\tau = \gamma = 0$) to find the value of ε_0 that yields a solution that best fits the observed surface slip. Next we impose the surface and bottom constraints to obtain refined models. We solve this linear system using the non-negative least squares subroutine (nnls) from *Lawson and Hanson* [1974].

The Newton-Raphson iterative procedure described in Section 2.4 estimates the optimal rupture time of each element assuming the distributed slip model found in the previous single time-window inversion step, and solves for perturbations $\delta\mathbf{m}$ to a starting rupture time model **m**. We iterate on $\mathbf{m}_n = \mathbf{m}_{n-1} + \delta\mathbf{m}_n$ until the solution converges.

3.4.1 Model Resolution

We have presented two linear inversion methods for finding the distribution of slip amplitude. The first model assumes each fault element ruptures once. This is equivalent to restricting the rise time to be 3 s or less everywhere on the fault surface; both data and theoretical seismograms only contain periods longer than 4 s, so the model is not sensitive

to variations in rise time duration when less than about 3 s. Using this single time-window method, it is only possible to find a best-fitting constant rupture velocity. The second method permits variable rupture velocity by allowing slip to occur in three adjacent time windows each separated by 2 s. The two methods each have shortcomings. The single time-window model can not recover potentially important changes in the rupture velocity or rise time. The multiple-window model has more free parameters and allows some variability in both rupture velocity and rise time; however it does not significantly improve the fit to the data.

The shortcomings of each method can be demonstrated with synthetic test cases. We compute synthetic data for known, hypothetical rupture models using the Landers mainshock fault geometry, add uncorrelated white noise, and image the slip distribution and rupture time using each method. The details of these synthetic tests are presented in Section 2.5.3; the results are summarized below.

The single time-window method finds the best *average* rupture velocity; variations in the rupture velocity and the rise time are not recovered. This single time-window method does a good job of recovering the known seismic moment. In contrast, the three time-window model can image the variable rise time and rupture velocity by putting slip in later time windows; however, in the Landers geometry this method does a poor job of recovering details of the input rupture velocity in the presence of noise. The image of rise time at each slip patch is similar to the test model, but the seismic moment is overestimated by more than 70% (because much of the noise is modeled as slip). Finally, the fit to the seismograms is only marginally improved over the single-window model (29 vs. 26% variance reduction).

We might note that if we start with the correct slip distribution and use the linearized inversion to solve for rupture time only, we recover the input rupture velocity variation, suggesting that if we can determine the slip distribution using independent methods (e.g., geodetic), we can reliably image the rupture velocity variation. In Chapter 4, we use this approach in modeling the Landers mainshock by using geodetic measurements and fault offset at the surface to establish the slip model.

3.5 Inversion Results

3.5.1 Slip Amplitude Distribution

Five solutions to equation 3.2 that use different smoothing weights and boundary conditions are shown in Figure 3.9. The vertical cross sections extend from the surface to 18 km depth. The length of the fault with overlapping regions superimposed is 83 km, and the dimensions of the individual segments are labeled in the figure. The contour lines (interval of 1 m) denote right-lateral slip amplitude.

The result for the unsmoothed case without prescribed boundary conditions ($\varepsilon_0 = \tau = \gamma = 0$) is shown in Figure 3.9a. This solution is rough with slip concentrated in small patches and peak displacements in excess of 14 m near the surface. In contrast, the mapped fault offset is more smoothly varying with a maximum amplitude of approximately 6 m [*Ponti*, 1992; *Sieh et al.*, 1993; *Johnson et al.*, 1994]; comparison of the observed and predicted surface slip using this model gives a variance reduction of -30.0%. The condition number for this **A** matrix (2.2×10^6) is close to the reciprocal of our computer's accuracy (single precision), indicating that numerical round-off error is appreciable. The large condition number also suggests that components of the solution are poorly constrained. The seismogram variance reduction is 28.3%. Although the roughness and instability of this solution is unappealing, it fits the seismograms the best and is in some respects similar to smoother models; for example, the percentage of moment on each fault segment remains approximately constant independent of the smoothing value. The total seismic moment is in fair agreement with other studies as discussed below.

Because the unsmoothed model is inconsistent with the continuity and amplitude of the mapped surface slip, a smoothing constraint is used to stabilize the solution. Solutions using three different smoothing weights are shown in Figure 3.9b-d. With the addition of light smoothing (Figure 3.9b), the variance reduction is decreased only slightly (28.0 vs. 28.3%), and the system is better conditioned. The model in Figure 3.9c uses the preferred value of smoothing ($\varepsilon_0 = 30$). The value of ε_0 depends on how the rows of **A** and **d** are normalized and has meaning only for this particular application. Figure 3.9d shows an heavily smoothed model ($\varepsilon_0 = 200$) that fits the seismograms poorly (16.3%), although the surface slip variance reduction is comparable to that found in Figure 3.9c (37.0 vs. 37.1%).

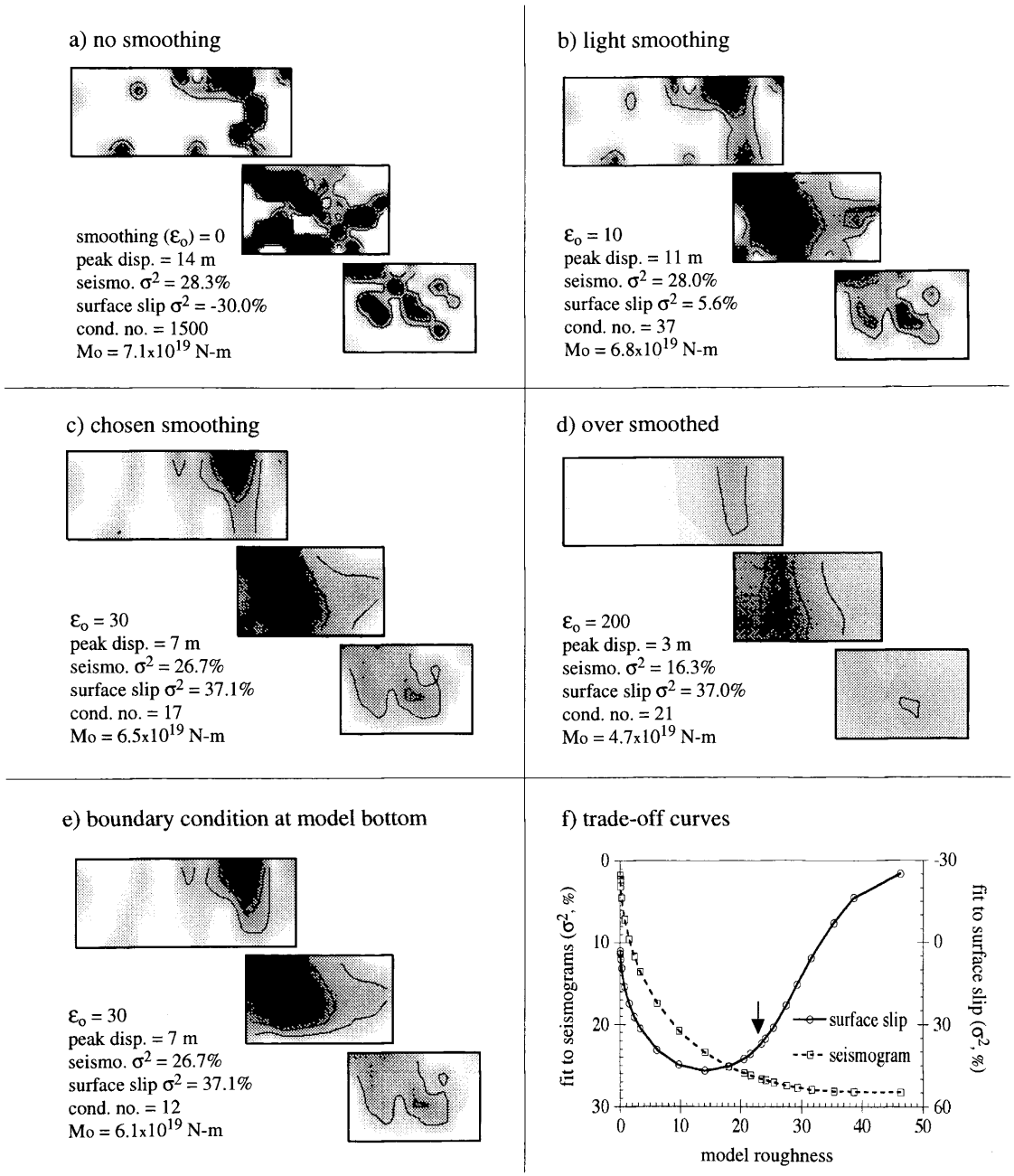

Figure 3.9. Summary of slip on the three fault segments obtained using different smoothing values, and the effect of a homogeneous boundary condition for the deepest element. The cross sections are the same as those shown in Figure 3.2, and, in each case, the rupture velocity is 2.5 km/s. The optimal smoothing is found by minimizing the misfit between the predicted slip on the shallowest element and the geologically mapped surface slip: a) No smoothing; b) Light smoothing; c) Chosen smoothing; d) Over smoothed; e) Boundary condition at model bottom; f) Trade-off curves (negative y-axis) for the fit to the seismograms and the fit to the surface slip obtained with the boundary condition at the fault bottom (arrow marks the model roughness obtained with the chosen smoothing).

The solutions in Figure 3.9a-d have considerable slip at all depths. Each model has large displacements deep on the Homestead Valley (middle) fault segment. There were few aftershocks at depths greater than 15 km [*Hauksson et al.*, 1993], and because of decreasing strength and increasing plasticity [*Scholz*, 1990], we do not anticipate much high-frequency displacement at these depths. The solutions with the homogeneous boundary condition on the deepest fault elements enforce this assumption. The result with $\gamma = \varepsilon_0/2$, which adds the boundary condition at the bottom of the model, is shown in Figure 3.9e.

Results using the different smoothing weights are summarized in the two trade-off curves plotted in Figure 3.9f. This plot shows both the fit to the seismograms and the fit to the mapped surface offset for different smoothing weights and including the boundary condition at the fault bottom. As expected, the smoothing parameter controls the simple trade-off between model roughness, $\|\mathbf{Dm}\|^2$, and the fit to the seismograms. In contrast, the fit to the surface slip for different smoothing strengths has a well-defined minimum. We choose the smoothing value used in Figure 3.9c (indicated in Figure 3.9f with an arrow), which represents a compromise between the fit to the seismograms and the fit to the surface offset.

For this assumed value of smoothing, we perform the inversion for fault slip using a range of average rupture velocities, v_r, and evaluate each solution by its fit to the seismic data and the offset mapped by *Ponti* [1992]. Figure 3.10a shows that the location of the high-slip regions is strongly dependent on the rupture velocity so that the surface offset provides an important constraint on the true v_r. In this figure, the slip is summed for the two overlapping regions of the three fault segments. Although there are near-surface effects that can cause surface measurements to differ from the average slip in the adjacent 3x3 km^2 section of the fault, the most representative v_r is expected to be that which has the highest correlation with the mapped surface offset.

We find v_r = 2.5 km/s gives the best fit to the seismograms and a good fit to the surface displacement. In this comparison, the surface slip is not explicitly used in the inverse problem, but it provides a useful independent check on the solution. The variance reduction for both the seismograms and the surface slip is shown for the tested range of v_r in Figure 3.10b. The maximum in the fit to the seismograms is broadly peaked, with the range from 2.4 to 2.7 km/s producing the best results. A 2.5 km/s rupture velocity shows good agreement with the mapped surface displacement, albeit a slightly higher value (2.6

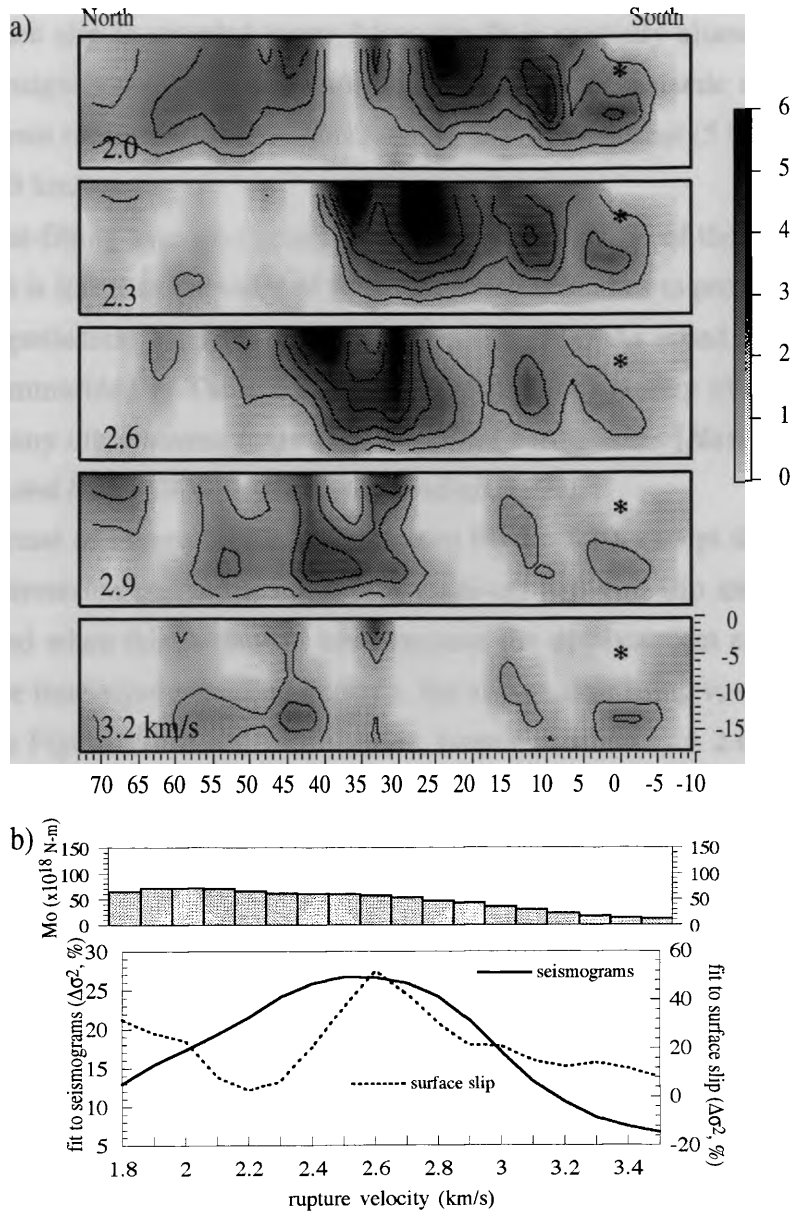

Figure 3.10. Comparison of fault slip solutions for the 1992 Landers earthquake using the single-window method and different average rupture velocities, and the corresponding agreement with the mapped surface slip. A rupture velocity of 2.5 km/s gives the best fit to the seismograms and an acceptable fit to the surface slip. a) Right-lateral slip amplitude solutions obtained for rupture velocities of 2.0, 2.3, 2.6, 2.9, and 3.2 km/s. The grayscale bar to the right and the 1 m contours indicate right-lateral displacement on the fault surface. Slip is summed for the overlapping portions of the fault. The hypocenter defines the horizontal origin and is indicated by a symbol at 4.5 km depth. b) Variance reduction ($\Delta\sigma^2$) as a function of rupture velocity for both the fit to seismograms and the fit to surface slip. The seismic moment obtained for each rupture velocity is shown in the bar chart with units of 10^{18} N-m.

km/s) attains the best correlation. Since the quantitative comparison of predicted to observed surface slip is sampled every 3 km, the fit is spatially aliased and this small difference is insignificant. Also shown in Figure 3.10b is the seismic moment obtained using the different rupture velocities. The moment is fairly constant (5 to 7×10^{19} N-m) for v_r less than 2.9 km/s.

The best-fitting average rupture velocity is roughly 70% of the local shear wave velocity, which is less than the value of 80% often used in studies to predict strong ground motion for hypothetical earthquakes [*Cohee et al.*, 1991]. As noted by *Hartzell et al.* [1991] and summarized in Table 1.1, an average rupture velocity of near 2.5 km/s is preferred in many other source inversions of crustal earthquakes [*Hartzell and Heaton*, 1983; *Hartzell and Iida*, 1990; *Hartzell and Mendoza*, 1991].

The format of Figure 3.11 is analogous to Figure 3.10, except that here the three time-window inversion method is used. The trade-off between slip amplitude and v_r is less pronounced when this method is used because the displacement can be distributed across the three time-windows. For example, the slip models using $v_r = 2.6$ and $v_r = 2.9$ km/s shown in Figure 3.11a are very similar; however, when $v_r = 2.6$ km/s, most slip occurs in the first window, and when $v_r = 2.9$ km/s, slip occurs equally in the first two windows. This is shown in Figure 3.11b, where the moment in each window is plotted for each rupture velocity. As seen in the tests using synthetic data, the greater flexibility of the multi-window method is evident in the relative uniformity of the variance reduction for a wide range of rupture velocity. This is in contrast to Figure 3.10b, where there is a well-defined maximum in the seismogram variance reduction at 2.5 km/s. The fit to the surface offset using the three time-window method does not help constrain the rupture velocity because for all values of v_r the predicted offset is larger than the observed, so the largest surface slip variance reduction occurs when the moment is smallest (at $v_r = 3.5$ km/s).

A comparison of Figures 3.10 and 3.11 also reveals two other familiar characteristics of the slip distribution and seismogram variance reduction seen in the solutions using synthetic data. The total seismic moment is larger but the seismogram fit is only slightly improved using three time-windows. Recall that in the sensitivity test the moment obtained using one time-window was 20% larger than the true moment, while the three time-window model overestimated the input moment by 40 to 60%.

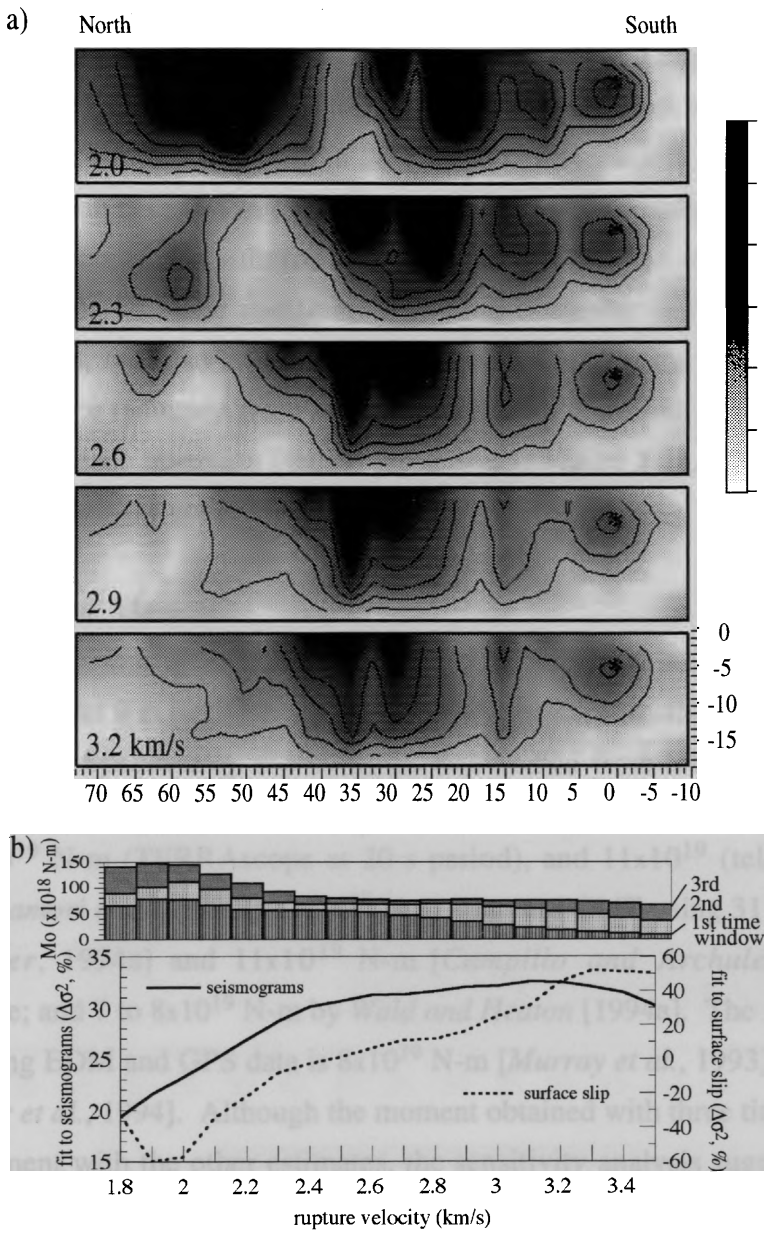

Figure 3.11. Comparison of fault slip solutions for the 1992 Landers earthquake using the three-window inversion method. a) Slip amplitude solutions obtained for average rupture velocities of 2.0, 2.3, 2.6, 2.9, and 3.2 km/s (in this case, the rupture velocity is determined by the time of the first time-window, not the centroid). The grayscale bar to the right and the 1 m contours indicate right-lateral displacement on the fault surface. b) Variance reduction ($\Delta\sigma^2$) as a function of rupture velocity for both the fit to seismograms and the fit to surface slip. The seismic moment obtained in each of the three time-windows is shown in the bar chart. The moment is nearly constant (7 to 8x10^{19} N-m) for rupture velocities greater than 2.3 km/s.

The best-fitting, single time-window solution is shown in Figure 3.12a. The largest displacement is 38 km north of the hypocenter and begins approximately 16 s after the initiation of rupture. There is good correlation with the surface slip over the entire fault length. The peak slip in the model at 28 km is not observed in the surface offset. If $\tau >> 0$, the solution is forced to match the observed displacements at the ground surface within some tolerance; this solution and the corresponding fit to the surface offset is shown in Figure 3.12b. The constrained solution is similar to Figure 3.12a at depths greater than 3 km, but also conforms to the mapped slip at the ground surface. The decrease in variance reduction from adding this constraint is small (1.2%). The preferred slip models using each inversion method are shown in Figure 3.13. These results include the surface slip boundary condition.

3.5.1.1 Seismic Moment

The total seismic moment for the single-window model is 6×10^{19} N-m and for the three-window model it is 8×10^{19} N-m. Moments determined in other studies range from 7 to 11×10^{19} N-m. Specifically, the moments determined from teleseismic and regional waveforms are: 7×10^{19} N-m (USGS CMT using 22 stations); 8×10^{19} N-m (teleseismic P and S), 8×10^{19} N-m (TERRAscope at 20 s period), and 11×10^{19} (teleseismic surface waves) [*Kanamori et al.*, 1992]; 11×10^{19} N-m (Harvard CMT using 31 stations); 8×10^{19} N-m [*Dreger*, 1994a] and 11×10^{19} N-m [*Campillo and Archuleta*, 1993] using TERRAscope; and 7 to 8×10^{19} N-m by *Wald and Heaton* [1994a]. The moment obtained from modeling EDM and GPS data is 8×10^{19} N-m [*Murray et al.*, 1993] and 9×10^{19} N-m [*Freymueller et al.*, 1994]. Although the moment obtained with three time-windows is in better agreement with the other estimates, the sensitivity analysis suggests this method tends to overestimate the moment required by the data and strongly depends on the specific choice of regularization. It is important to recognize that even though the multi-window model has a considerably larger moment than the single-window model, the fit to the seismograms is very similar.

The variability of seismic moment with data type is sometimes attributed to the variable bandwidth of the data. According to this interpretation, the smaller moment of the single time-window solution results from the limited long-period response of the strong-motion data. It is clear that the strong-motion data is sampling a limited portion of the radiated energy bandwidth. To explore this hypothesis we used only TERRAscope data

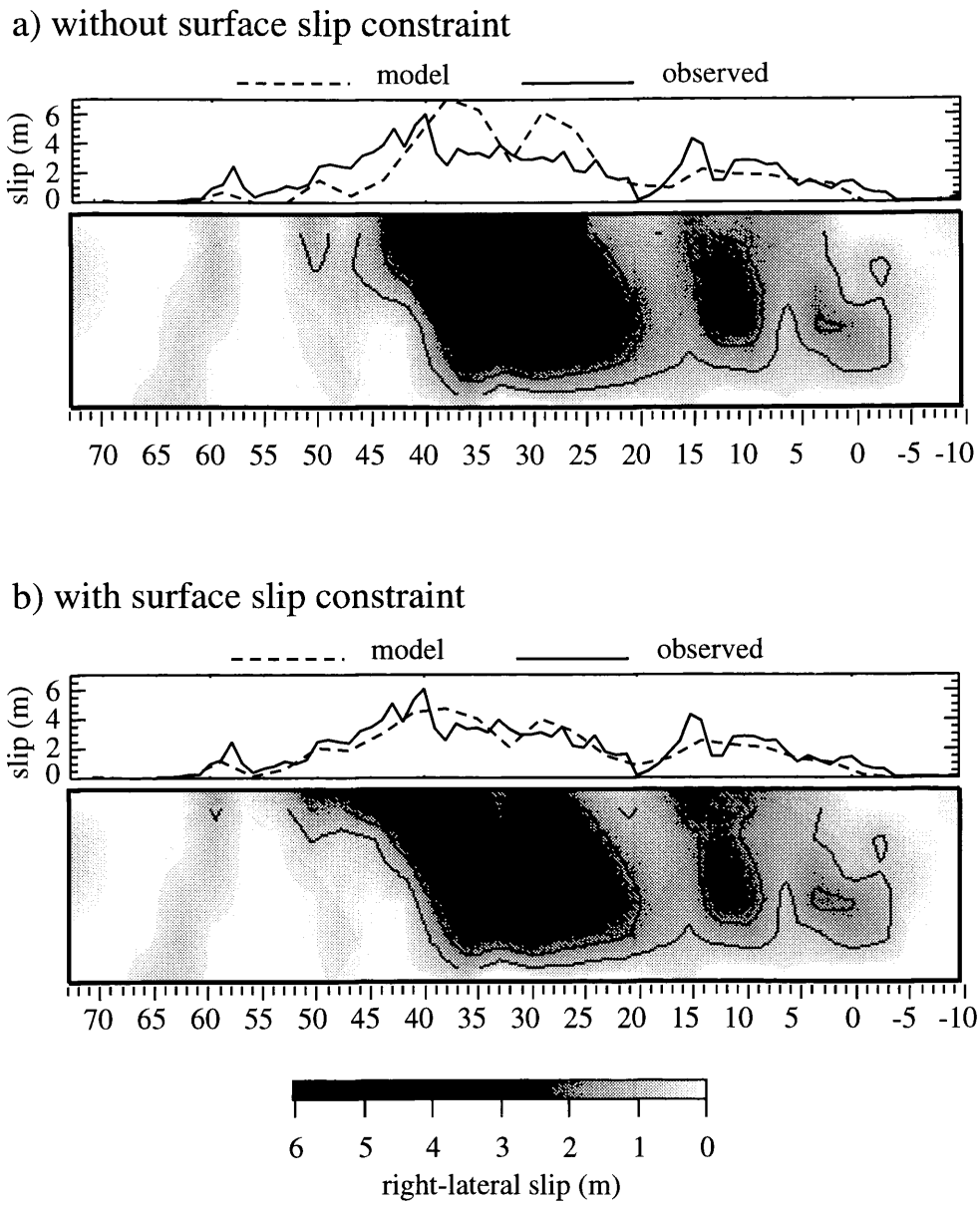

Figure 3.12. Preferred slip models using a 2.5 km/s constant rupture velocity with and without the surface slip boundary condition applied. Above each slip model is the comparison between the prediction (model) and the mapped slip. Note that the overall amplitude of the predicted slip is in good agreement with the observed surface slip. The grayscale bar and the 1 m contours indicate displacement on the fault surface. a) Slip model without surface slip constraint. Seismogram variance reduction is 26.7%. b) Slip model with surface slip constraint. Seismogram variance reduction is 25.5%.

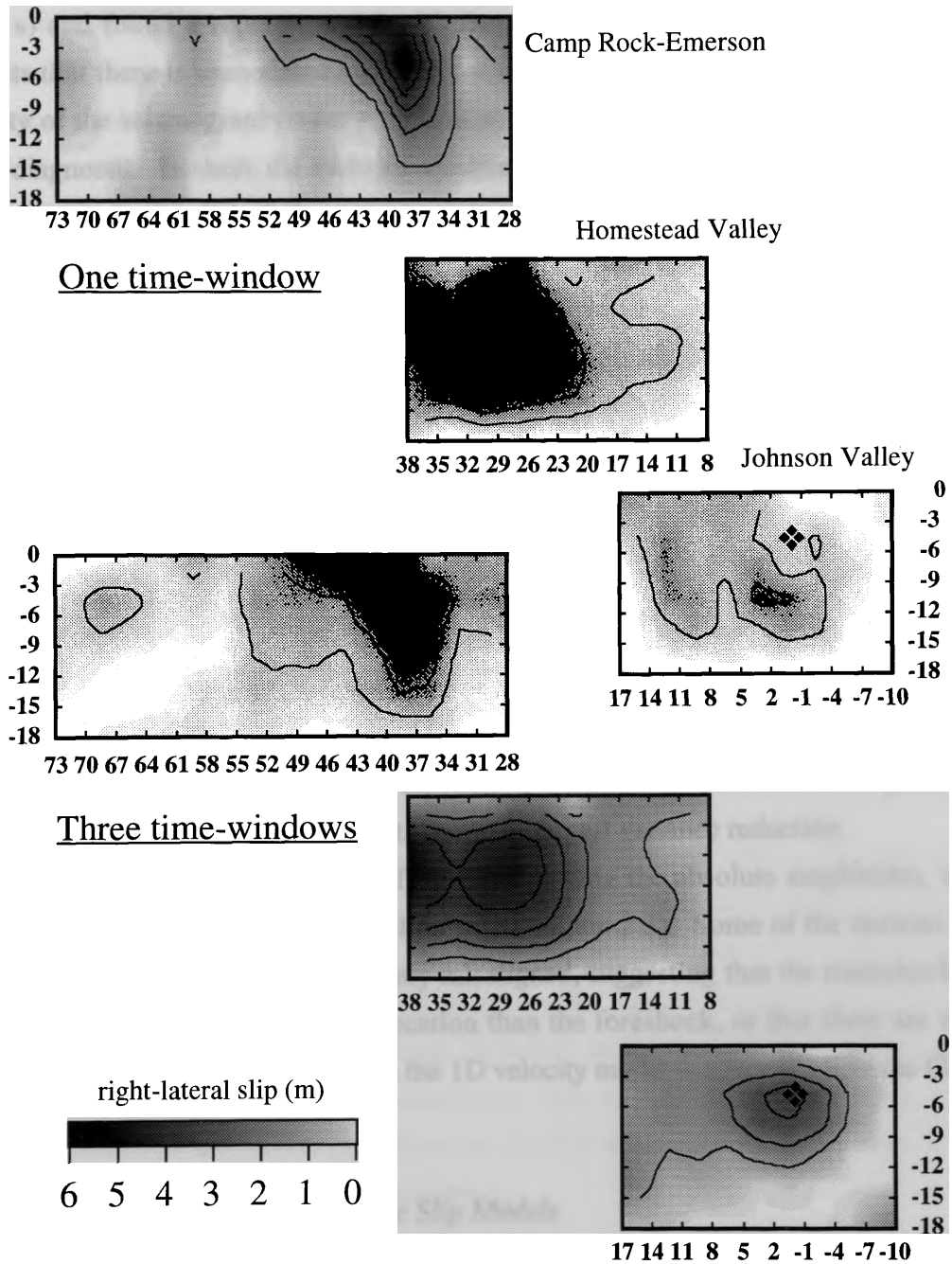

Figure 3.13. Best-fitting slip amplitude models for the Landers earthquake. The three fault segments from north to south are representative of the Camp Rock-Emerson (CRE), the Homestead Valley (HV), and the Johnson Valley (JV) faults. a) Three fault segment cross section of right-lateral slip amplitude obtained with the one time-window method and a rupture velocity of 2.5 km/s. The grayscale bar and the 1 m slip contours show displacement on the fault surface. The seismic moment is 6×10^{19} N-m. b) Cross section of best-fitting slip model obtained using the three time-window method and a first-window rupture velocity of 2.8 km/s. The moment of this model is 8×10^{19} N-m.

(to 50 s) and found a rupture model with the same approximate moment. This result suggests that there is unmodeled signal in the strong-motion data; however, because the majority of the seismogram power remained at periods between 5 and 15 s, this test may not be diagnostic. In short, the multiple window method fits more of the seismogram, but it is not clear whether it is fitting signal or noise or if a more accurate rupture model was obtained. Destructive interference in the Green's function summation is a likely explanation for the larger seismic moment in the multi-window result.

3.5.1.2 Model Fit of Data Seismograms

The fit to the three components of motion at each station is shown in Figure 3.14 for the single time-window and the three time-window models. The data are black solid lines and the model seismograms are plotted as dashed (single window) and gray (three windows) lines. The multiple window method fits the data slightly better than the single window method (31.0 vs. 25.5%). Both data and model seismograms are plotted at the same scale and the amplitude is normalized to the largest seismogram peak. The variance reduction is listed at the right of each seismogram for the single window result. Since each station holds equal weight and each component is weighted proportional to its power, the largest amplitude horizontal components show the largest variance reduction.

Most of the seismograms are fit well, including the absolute amplitudes, which vary from 0.7 to 28.1 cm in peak amplitude (see Figure 2.3). Some of the stations close to the epicenter (FHS, MVH) are slightly misaligned, suggesting that the mainshock may have initiated in a slightly different location than the foreshock, or that there are strong velocity variations not accounted for in the 1D velocity model used to calculate the Green's functions.

3.5.1.3 Comparison with Geodetic Slip Models

Geodetic coverage for the Landers earthquake allows independent estimation of the slip distribution using measurements of the horizontal displacement field [*Freymueller et al.*, 1994]. Because of the redundancy of the measurements, the associated error is well determined, allowing use of the appropriate covariance weighting when inverting for the slip distribution. The slip distribution estimated from geodetic data (see Chapter 4) is most similar to the model shown in Figure 3.13a, in particular on the Johnson Valley segment, but has higher slip amplitudes (the moment is 9×10^{19} N-m). As described in the next

chapter, we have assumed a slip model derived from geodetic observations in a linearized inversion for rupture history using seismograms as data. When the geodetic slip model is assumed, a fault model is obtained that matches the geodetic data, has larger moment, and fits the seismograms with modest perturbations to a constant-velocity rupture model. Recall that the tests suggest that if the slip distribution can be correctly determined, high-resolution features of propagation can be inferred from the seismograms.

The static displacements measured by various geodetic methods provide an independent check of the slip model. We use the single-window model shown in Figure 3.13a to compute predicted horizontal displacements at sites where co-seismic displacement is determined using GPS and EDM [*Freymueller et al.*, 1994], and synthetic aperture radar interferometry [*Massonnet et al.*, 1993]. The comparison of observed and predicted horizontal displacement shows good agreement in the direction, but a tendency to underestimate the observed amplitudes. Thus, although the seismic models have smaller total moment than the geodetic models, the slip distribution looks similar.

3.5.2 *Rupture Front Propagation*

3.5.2.1 *Linearized Inversion for Rupture Propagation*

We use the linear, one time-window solution obtained with a constant rupture velocity of 2.5 km/s (Figure 3.13a) as the initial model in a linearized inversion to optimize the rupture time of each fault element. As shown earlier in Figure 3.10, when a different rupture velocity is used, a different slip model results, demonstrating a strong trade-off between slip amplitude and rupture time [*Spudich and Frazer*, 1984]. Simultaneous estimation of rupture time and slip amplitude with sufficient data should be able to overcome this trade-off; however, without an *a priori* model covariance matrix, it is not clear how to weight the two types of unknowns.

Previous investigators have invoked a weighting that results in perturbations to these parameters that are deemed reasonable [e.g., *Beroza and Spudich*, 1988]. An alternative method is to allow the rupture time to vary by letting each fault element slip several times in adjacent time-windows [*Olson and Apsel*, 1982]. As discussed earlier, this approach suffers the disadvantage of requiring a large increase in the model dimension. Regardless of the approach used, recovering the time-dependent behavior of the rupture is difficult for the Landers earthquake because the large source-receiver

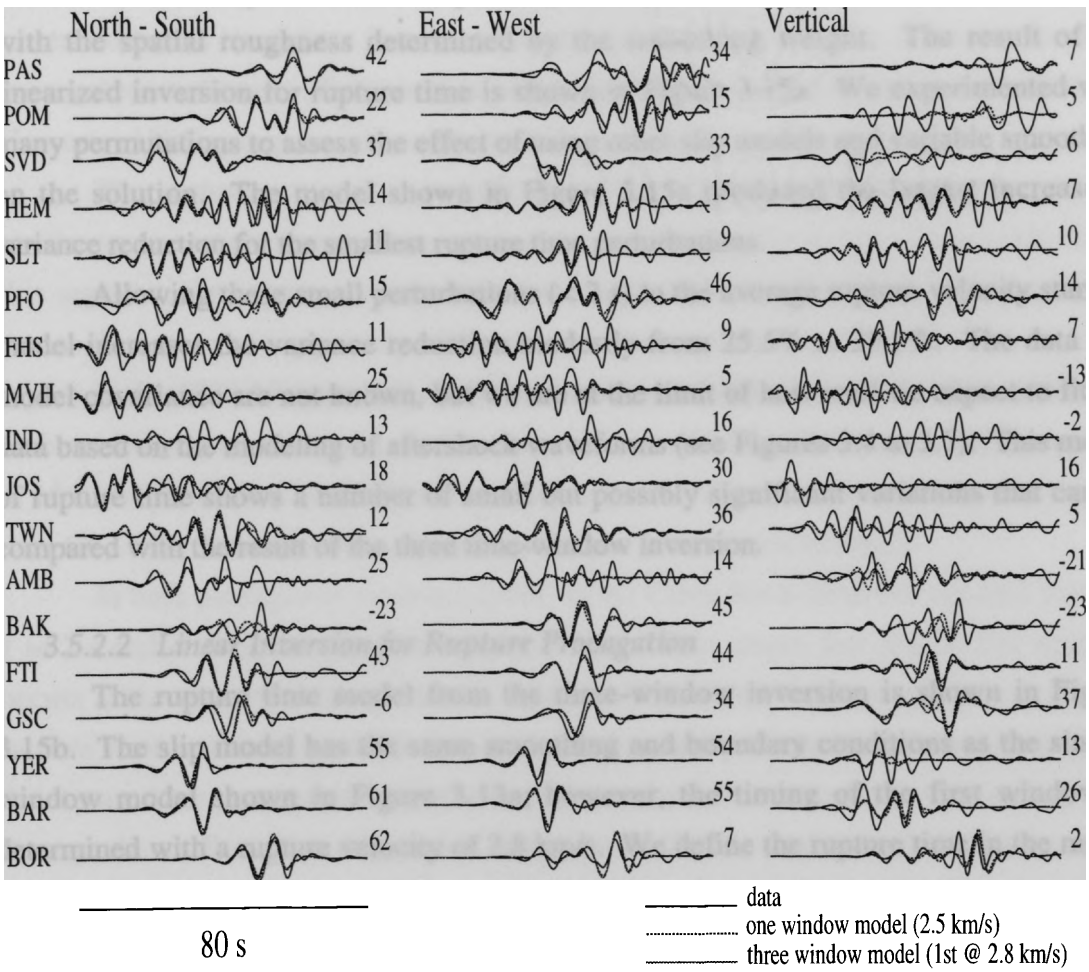

Figure 3.14. Fit to the recorded displacement seismograms using the linear solutions shown in Figure 13. The data seismograms (*solid*) and model seismograms (one window-*dashed*, three windows-*gray*) are plotted at the same amplitude scale. The variance reduction ($\Delta\sigma^2$) for each station component is listed to the right of the corresponding seismograms for the one-window solution. The average weighted variance reduction is 25.5% using one window and 31.0% using three windows.

distances necessitate using longer-period waveforms dominated by regional surface waves rather then body waves.

Recall that with the single-window approach, we separate the inversion for slip amplitude and rupture time to avoid the problem of relative weighting. However, because we first solve for slip and then for rupture time, the procedure favors a variable slip model, with the spatial roughness determined by the smoothing weight. The result of the linearized inversion for rupture time is shown in Figure 3.15a. We experimented with many permutations to assess the effect of using other slip models and variable smoothing on the solution. The model shown in Figure 3.15a produced the largest increase in variance reduction for the smallest rupture time perturbations.

Allowing these small perturbations (< 2 s) to the average rupture velocity starting model increases the variance reduction modestly from 25.5% to 29.1%. The data and model covariance are not known, but we are at the limit of how well we expect to fit the data based on the modeling of aftershock waveforms (see Figures 3.4 to 3.7). This model of rupture time shows a number of small but possibly significant variations that can be compared with the result of the three time-window inversion.

3.5.2.2 Linear Inversion for Rupture Propagation

The rupture time model from the three-window inversion is shown in Figure 3.15b. The slip model has the same smoothing and boundary conditions as the single-window model shown in Figure 3.13a; however, the timing of the first window is determined with a rupture velocity of 2.8 km/s. We define the rupture time in the multi-window model to be the slip-weighted temporal centroid for elements with slip greater than 1.5 m. In Figure 3.15b this centroid is contoured for comparison with Figure 3.15a.

Based on the sensitivity tests it is difficult to give strong preference to either rupture time model. It is likely that the single-window method recovers a reliable average rupture velocity of 2.5 km/s. The results with synthetic data suggest that details of these rupture propagation images are not particularly reliable due to the strong trade-off between slip amplitude and rupture time. Recovering the time-dependent behavior of the rupture is difficult for the Landers earthquake because the large source-receiver distances require using long-period (≥ 4 s) waveforms dominated by regional surface waves rather then body waves. One other lesson from the tests with synthetic data is that the rupture time details can be recovered if the slip distribution is obtained from independent data.

3.5.2.3 Features Common to Both Rupture Propagation Models

There are some general features common to both rupture models in Figure 3.15. Rupture velocity over the Johnson Valley segment in the hypocentral region appears relatively fast – fast rupture of this segment could have been facilitated by dynamic stress generated by the immediate foreshock that brought the fault closer to failure as the stress propagated northward. The transition of rupture from the Johnson Valley segment to the Homestead Valley segment is essentially the same as in a constant rupture velocity model.

The rupture across the southern part of the Homestead Valley segment is also similar to a constant rupture velocity model. At the high-slip region on the north end of this segment, the rupture velocity decreases somewhat, then increases as it propagates across the region of highest slip. This is somewhat reminiscent of rupture of a high slip region in the 1984 Morgan Hill, California earthquake [*Beroza and Spudich*, 1988]. In both models, the rupture front reaches the northern end of the Homestead Valley segment at 14 s (the same time as a 2.5 km/s average rupture velocity). The transition of rupture onto the Camp Rock-Emerson segment, however, is somewhat different.

In both propagation models, rupture on the Camp Rock-Emerson segment initiates 1 to 2 s earlier than the constant velocity model. This means that slip on this segment occurs at the same time as slip on the adjacent Homestead Valley segment – as though rupture were occurring on a through-going fault. On the Camp Rock-Emerson segment the rupture front propagates at a higher velocity at depth than near the surface and ruptures through the shallow high-slip region from below. This is similar to the behavior of the rupture front across the high-slip region on the Homestead Valley segment. The observation that the rupture front slows down as it encounters high-slip regions suggests that they were relatively further from failure before the mainshock either due to lower pre-stress, higher strength, or both [*Beroza and Spudich*, 1988]. Overall, rupture on this segment is faster in the three-window model (Figure 3.15b), which partially explains the broader area of large slip amplitude in Figure 3.13b.

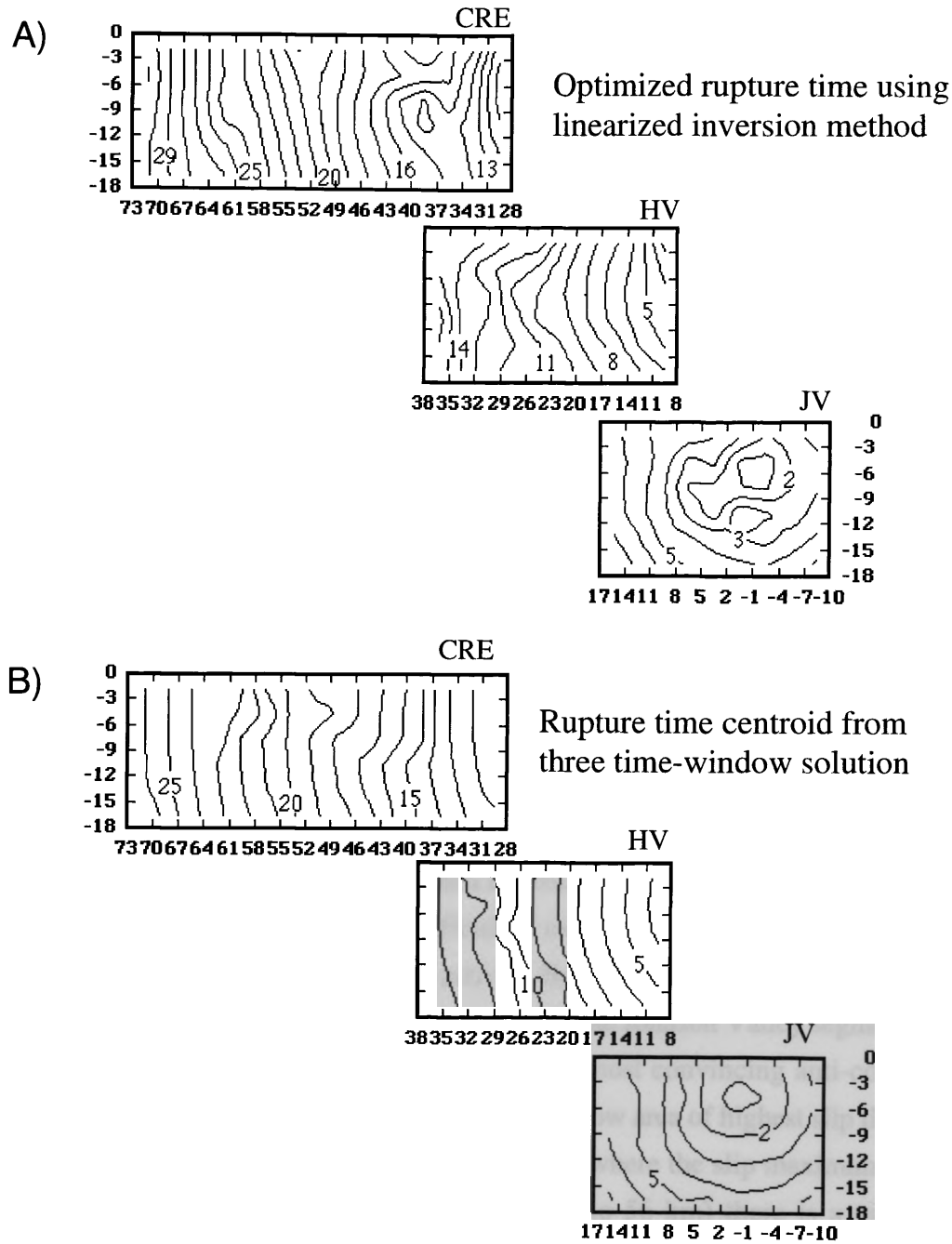

Figure 3.15. Best-fitting rupture propagation models for Landers mainshock. a) Contours of rupture time obtained using the linearized inversion and the slip model in Figure 3.13a. Contour interval is 1 s. b) Contours of the rupture time centroid from the three time-window solution in Figure 3.13b (for elements with slip greater than 1.5 m).

3.5.3 Spatial correlation with aftershocks

In this section, the slip distribution is compared with the distribution of aftershocks occurring on or near the mainshock fault plane. Figure 3.16 shows aftershocks from *Hauksson et al.* [1993] located within 2 km (±) of the fault together with the single time-window slip model.

The Johnson Valley segment has the least slip in the rupture model. The shallow hypocentral region does not have much in the way of either slip or aftershock activity. It may be that slip in the immediate foreshock relieved most of the stress in this area. The Johnson Valley segment is noteworthy in that it has an abundance of larger aftershocks relative to the other two segments. The correlation between regions of high slip with low aftershock activity and regions of low slip or of high slip gradients with abundant aftershock activity, which is seen for many earthquakes [*Mendoza and Hartzell*, 1988], is not readily apparent for this fault segment.

The aftershock distribution on the Homestead Valley segment is more diffuse. The southern Homestead Valley segment shows few aftershocks, no slip in our solutions, and is the site of the slip gap mapped at the surface. All of these observations suggest that there was little slip on this part of the fault. North of this, there is an area of concentrated aftershock activity (17 to 20 km) that is at the southern edge of the high-slip region. Farther north there is large slip at depth and a diffuse pattern of hypocenters. Because of uncertainty in aftershock depths it is difficult to evaluate how well the large slip region correlates with regions of low aftershock activity, but this segment appears to behave more like other mainshock-aftershock sequences than does the Johnson Valley segment.

The Camp Rock-Emerson fault displays the most convincing anti-correlation of slip amplitude and aftershock distribution. In the shallow area of highest slip there are few aftershocks shallower than 6 km over a broad region where the slip maximum is located. At the northern end of the mainshock rupture (47 to 56 km) there is a great deal of aftershock activity, consistent with the idea that the stress change induced by the mainshock is responsible for this activity.

The notion that aftershocks are caused by the mainshock stress change is qualitatively consistent with the observation that aftershocks occur in regions of low slip and not in areas of high slip. However, recent observations of the Loma Prieta mainshock-aftershock sequence [*Beroza and Zoback*, 1993], which take into account the sense of slip in the aftershocks, indicate that this hypothesis does not explain many of

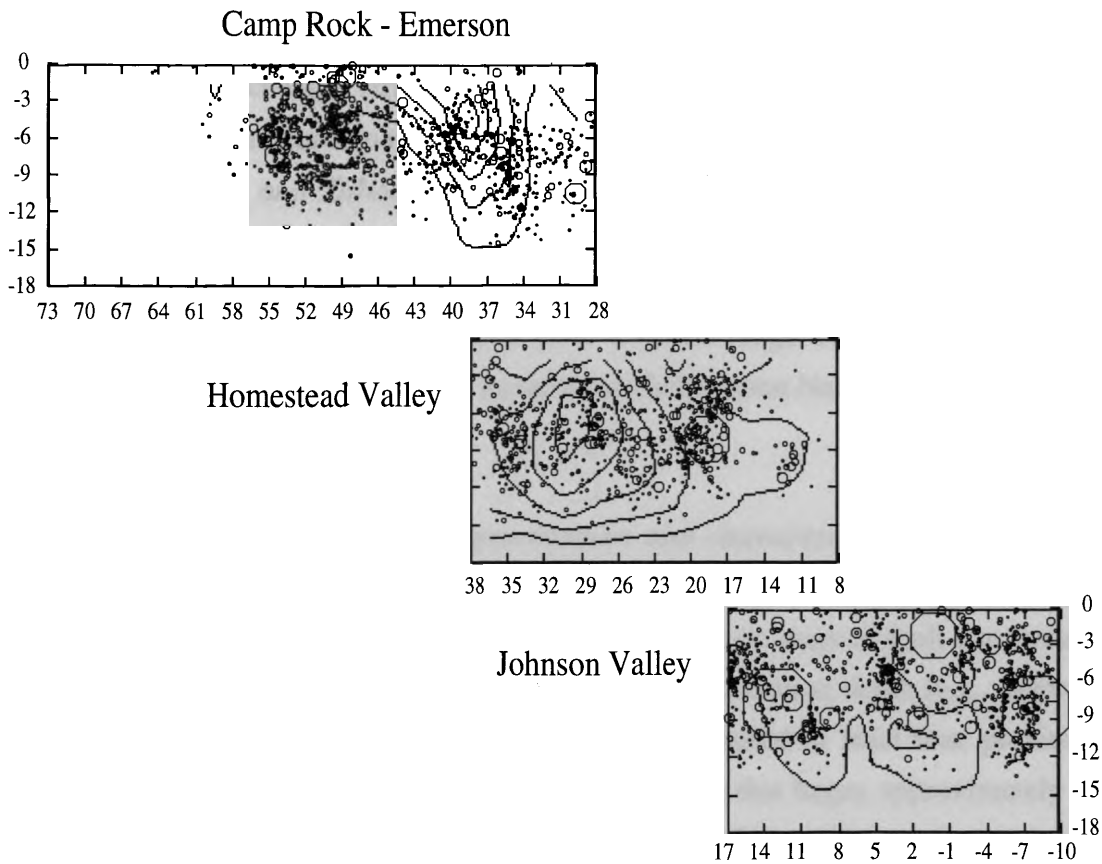

Figure 3.16. Cross section of the single time-window slip distribution (same as Figure 3.13a) compared with aftershock hypocenters within 2 km of the assumed mainshock fault plane. The size of the aftershock symbol is scaled to represent the source size assuming a constant stress drop of 3 MPa.

them. In addition, the seismicity triggered at great distances following the Landers earthquake, for which the static stress change was far smaller than the tidal stresses, provides further evidence for another mechanism of earthquake interaction [*Hill et al.*, 1993].

A plausible explanation for both of these observations is that the large transient stress changes in the dynamic field somehow weaken faults as they propagate through them. If such stress changes (fractions of a MPa) can trigger seismicity at great distance following the Landers earthquake, it is reasonable to assume that they can also trigger aftershocks [*Beroza and Zoback*, 1993] because the stresses experienced in the near-source region where aftershocks occur are on the order of the stress drop (i.e., at least several MPa). The Landers earthquake has given us a unique opportunity to study this problem because it triggered seismicity over a broad range of distances, from the mainshock fault plane itself to areas as far away as Yellowstone National Park [*Hill et al.*, 1993].

3.5.4 Implications for fault segmentation and characteristic earthquakes

The segmentation of faults is an important component of any attempt to anticipate the size of future earthquakes. Researchers have used geologic maps of fault segmentation at the Earth's surface to infer that there is similar segmentation at depth [e.g., *Schwartz and Coppersmith*, 1984]. The Landers mainshock ruptured at least four previously identified faults and was a continuation of seismic activity that began approximately two months earlier with the M_W 6.1 Joshua Tree earthquake. The northward progression of fracture in these earthquakes ruptured faults at the surface that had been thought to be independent.

In our model of the Landers earthquake, the rupture front propagates through the intersections of these fault segments with little effect on either the slip amplitude or rupture velocity. That the Landers earthquake ruptured across several fault segments without stopping suggests that fault segmentation, at least in its geologic expression at the Earth's surface, may not be a reliable indicator of the characteristic size of future earthquakes. Moreover, slip on the Camp Rock-Emerson segment died out in the middle of a straight segment of the fault, indicating that something other than segmentation was responsible for terminating the rupture. The Landers earthquake makes evident the inadequacy of relying

on geologically-mapped fault segmentation alone to anticipate the size of future earthquakes.

Conclusions

Aftershocks recorded at the TERRAscope stations are used to identify the passband over which a 1D velocity structure produces accurate Green's functions. Recordings of the mainshock in this frequency band are used to estimate slip amplitude and rupture time for the Landers earthquake. The preferred models with an average rupture velocity of 2.5 km/s are most consistent with near-source seismograms recorded in absolute time and slip amplitudes mapped at the surface.

The Landers earthquake started slowly with a foreshock approximately 3 s before the beginning of large-scale failure and grew steadily for over 16 s; the total rupture duration with the delayed origin time is 22 s, and the total seismic moment is at least 6×10^{19} N-m. The first 6 s ruptured the Johnson Valley segment with slip above 2 m and 20% of the seismic moment. The Homestead Valley segment ruptured from 5 to 14 s, producing 50% of the moment and displacements reaching 6 m in a large region that extends from the surface to the model bottom at 18 km depth. The Camp Rock-Emerson segment began to rupture at 13 s and contributed the remaining 30% of the total moment with displacements greater then 6 m in a shallow region that extends from the surface to 9 km depth.

There is evidence for a decrease in rupture velocity as the rupture front encounters several high-slip regions. As these regions fail, the rupture velocity increases. This behavior is similar to that observed for the Morgan Hill earthquake and suggests that heterogeneous pre-stress or strength, or both, are important in controlling rupture.

Chapter 4 — Partitioned Inversion for Earthquake Rupture Using Near-Source Seismic and Geodetic Observations

Abstract

In an earthquake, static deformation of the ground surface is a linear function of the slip amplitude at each point on the fault, while the near-source seismic wavefield is linearly related to the slip but nonlinearly related to the rupture propagation and sliding duration. Because a fundamental trade-off exists between slip amplitude and rupture time in the seismic wavefield, source models derived from seismograms cannot separate completely features attributable to each property, which degrades the model stability. And whereas models derived from geodetic data can image the final slip amplitude, they cannot resolve temporal properties of faulting. In this chapter I present a partitioned inversion scheme that takes advantage of the complementary strengths of each data type: the slip on the fault is determined from geodetic data and the rupture propagation and slip time-function are determined from seismic data. Sensitivity tests indicate that propagation models obtained in this manner are more reliable than those derived from seismic data alone. In sampling heterogeneous data sets such as this, it is desirable to know the full covariance and weight the data properly; however, the theory covariance – the most relevant with seismograms – is difficult to establish.

4.1 Introduction

Spudich and Frazer [1984] demonstrated that two very different rupture models, one with variable slip velocity and the other with variable rupture velocity, can produce an identical seismogram at a single observation point. One consequence of this trade-off is that features in a seismogram caused by rupture time variation can potentially be mapped

into incorrect slip variations, and vice versa. With a single seismogram it is impossible to separate these two effects; however, using multiple seismograms, this trade-off can be greatly reduced. In practice, since portions of the model often exhibit strong dependence on only the nearest observations, it is difficult to eliminate this trade-off entirely, which is then manifested as a decrease in the solution's uniqueness.

Stated more formally, the P-wave ground velocity $\dot{\boldsymbol{u}}$ in the $\hat{a}$ direction at observation point $\boldsymbol{x}$ from a dislocation at $\boldsymbol{y}$ with a $\dot{f}_r$ slip-velocity time function can be written as a line integral over the contours of equal arrival time $y(t,\boldsymbol{x})$:

$$\hat{a}\cdot\dot{\boldsymbol{u}}(\boldsymbol{x},t)=\ddot{f}_r(t)*\int_{y(t,\boldsymbol{x})} c(\boldsymbol{y},\boldsymbol{x})\,\left(\boldsymbol{s}_r\cdot\mathbf{G}_a\right)dl \tag{4.1}$$

where $\boldsymbol{s}_r$ is the slip velocity (which is approximately proportional to stress drop), and $\mathbf{G}_a$ is the Green's function amplitude. The isochron velocity is

$$c(\boldsymbol{y},\boldsymbol{x})=\left|\nabla_s t_a^p(\boldsymbol{y},\boldsymbol{x})\right|^{-1}, \tag{4.2}$$

and $t_a^p(\boldsymbol{y},\boldsymbol{x})$ is the arrival time at $\boldsymbol{x}$ of the P wave from the dislocation at $\boldsymbol{y}$. The surface gradient operator is given by

$$\nabla_s=\left(\mathbf{I}-\hat{\boldsymbol{n}}\hat{\boldsymbol{n}}\right)\cdot\nabla, \tag{4.3}$$

where $\hat{\boldsymbol{n}}$ is the normal to the fault surface and $\mathbf{I}$ is the identity matrix [*Spudich and Frazer*, 1984]. Equation 4.1 illustrates the fundamental trade-off between slip amplitude and rupture time in the recorded wavefield: observed ground velocity is a linear function of the slip amplitude (the integral of $\boldsymbol{s}_r$) and a nonlinear function of the rupture time. In other words, variations in ground velocity can be caused equivalently by spatial variations in $\boldsymbol{s}_r$, or by temporal variations in $c(\boldsymbol{y},\boldsymbol{x})$. In the context of inverting for kinematic models of faulting, equation 4.1 reveals that features of the slip model may be inappropriately mapped into rupture time variations, and vice versa, undermining the accuracy of each. Independent constraints on either part of the fault model will reduce this trade-off and lead to better solutions.

Inverse problems using seismograms as data are usually mixed-determined; that is, some portions of the model are effectively overdetermined and some are effectively underdetermined. At first glance, this is curious, because there are usually many more data points than model parameters, so the solution appears overdetermined. The difficulty arises from the fact that Green's functions from adjacent fault elements can be nearly identical and almost linearly dependent, and because large parts of the kernel matrix are sparse.

Because the near-source wavefield is a function of slip amplitude and the slip history and rupture time of each point on the fault surface, source models derived from seismic data are only possible if assumptions are made to constrain the trade-off between the different parameters. The vulnerability of this approach is that the resulting models unavoidably display prescribed characteristics.

In contrast, the static displacement field (the difference between position measurements made before and after the earthquake) depends only on the final slip offset and is not sensitive to the detailed rupture history. Earthquake models derived from geodetic data are simpler, comprised of fault area and displacement only, and arguably more stable [*Matthews and Segall*, 1993; *Segall and Du*, 1993; *Freymueller et al.*, 1994]; however, by itself this data reveals nothing about temporal aspects of the rupture. Both spatial and temporal properties of rupture are required for future progress in understanding earthquake source physics and strong ground motion.

This chapter presents an approach that utilizes seismic and geodetic data in a manner that takes advantage of their complementary attributes. The inverse problem is partitioned so that the slip amplitude distribution is estimated from geodetic measurements and the propagation model is derived from near-source seismograms. The method is applied to the M_W 7.3 Landers earthquake. As in the previous two chapters, the fault surface is represented by many small elements and a system of linear equations relating fault slip to surface displacement is solved with a non-negative least squares algorithm. The optimum smoothing weight is estimated by minimizing the cross-validated sum-of-squares, and the fault offset at the Earth's surface is incorporated as prior information [*Freymueller et al.*, 1994]. The resulting slip model is then held fixed in a linearized inversion for the rupture time (Section 2.3).

Because of the strong trade-off between changes in rupture time and changes in slip amplitude, it is improbable that temporal details of propagation can be recovered from

seismic data alone. If the slip amplitude can be determined accurately from independent information, then the propagation details can be imaged with much greater accuracy from the seismograms. This conclusion is demonstrated in Section 2.5.3, where a linearized inversion method is used to recover rupture time for different assumed slip models. The key result of this test is that if the correct slip distribution is used, the rupture time model can be recovered with impressive accuracy. The bottom of Figure 2.9 illustrates this result. It is not surprising that sensitivity tests confirm that the partitioned inversion yields more accurate rupture models than one based only on seismic data. What is more important, and less obvious, is that rupture propagation models derived from seismic data can be extremely unreliable.

In the linearized inversion, the rise time (duration of the triangular displacement source function) is assumed to be shorter than the shortest periods contained in the seismograms (in the present case, 4 s). The greatest source of error in the linearized inversion likely arises from errors in the theoretical Green's functions (the forward problem). The associated covariance is unknown and impossible to derive analytically, but the Green's function uncertainty can be estimated by how well aftershock waveforms can be fit with point-source dislocation models (Section 3.3). Using this approach, we can obtain some idea of the degree to which mainshock seismograms should be fit over a specific passband; this tolerance is the convergence criterion applied in the linearized inversion. A more complete discussion of how covariance can be incorporated is set forth in Section 4.4.

Most features of the geodetic slip model show good agreement with models derived from seismic data alone – although the slip at depth is smoother and the moment is uniformly larger (Section 3.5.1). The linearized inversion is used to find the best-fitting (in a least-squares sense) propagation model. The preferred model shows a decrease in propagation velocity as the rupture front encounters high-slip regions which suggests that pre-existing variations in stress or strength on the fault, or both, are important in controlling rupture dynamics [*Boatwright and Cocco*, 1995].

4.2 Seismic and Geodetic Observations

All known earthquakes with significant near-source seismic and geodetic observations are listed in Table 1.1. The Landers earthquake is the largest for which there are both numerous strong-motion seismograms and geodetic measurements. It is no

surprise that all events in Table 1.1 occurred during the last three decades. This period saw the development of the Global Positioning System (GPS) and improvements in the precision of distance ranging instruments allowing relative displacements to be measured with sub-centimeter and sub-millimeter accuracy, respectively. Concomitant with these technical developments has been an increased surveying effort [e.g., *Freymueller et al.*, 1994]. Seismic data sets are also improving because of technical developments (e.g., digital accelerometers) and the continuing deployment of modern instruments. Most well-recorded earthquakes have occurred in California (Table 1.1), where much of the seismic and geodetic field effort is focused.

The quantity of near-source seismic and geodetic observations for an earthquake of the size and duration of Landers is unprecedented; a few other earthquakes are similarly well-recorded (e.g., Loma Prieta, Northridge, Kobe), but none have comparable area and rupture duration. The quantity of data and the size of the earthquake provide a new opportunity to exploit each data type in a manner that takes better advantage of their particular strengths and provides an opportunity to obtain a higher-resolution image of an earthquake.

For example, consider the M_W 6.7 Northridge earthquake, which occurred in urban Los Angeles county in 1994. Ground motions from this event were measured by many seismic and geodetic instruments (Table 1.1). The area of the fault plane was approximately 140 km^2 and the rupture duration was roughly 7 s [*Wald and Heaton*, 1994b]. In comparison, the Landers earthquake had dimensions of ~1000 km^2 and a rupture duration of 24 s [*Cohee and Beroza*, 1994a]. During this 24 s period the dislocation propagated across a series of right-stepping fault segments over a distance of 70 km, in total spanning four previously identified faults. Perhaps most importantly, the fault plane broke the ground surface over its entire length, providing an important additional constraint on models of the earthquake.

Time-varying ground motion was recorded in the near-source region by eighteen seismometers shown in Figure 2.3 and listed in Table 3.1. The acceleration and velocity seismograms were integrated to displacement and are shown in Figure 3.3. These recordings comprise the seismic data used in this chapter and are described in Section 3.2.2. With these seismograms, we can image slip on the fault if we make assumptions about the direction of slip, velocity structure, rise time, and rupture propagation (Chapter 3).

The co-seismic displacement field at the Earth's surface is found by differencing pre- and post-earthquake measurements. Ideally the pre-earthquake measurements are made immediately before the event, but inevitably there is some time interval before the event occurs and it is necessary to correct the measurements to remove interseismic deformation. In the region surrounding the Landers fault, several different groups had surveyed various portions of the area using electronic distance meter (EDM) and GPS equipment in the few years preceding the mainshock. The differenced GPS measurements provide co-seismic displacement vectors and the EDM measurements allow line-length changes to be resolved. Because of the redundancy of the measurements, the associated errors can be determined, which, in turn, provides an estimate of the data covariance. A comprehensive discussion of this data is presented in *Freymueller et al.* [1994] and *Hudnut et al.* [1994].

4.2.1 Seismic Inversions

Two models of the Landers slip distribution obtained from seismic data are shown in Figure 3.13, and the corresponding fits to data are shown in Figure 3.14. The first model assumes a constant 2-s rise time everywhere on the fault; with this assumption we find a best-fitting constant rupture-velocity model (Figure 3.15a). The second approach permits variable rupture velocity by allowing slip to occur in three time-windows; the time-centroid for each element of the fault is contoured in Figure 3.15b.

The two solutions have important differences (Section 3.5.2) and each method has strengths and weaknesses (Section 2.5.3). Most importantly, the constant rupture velocity model cannot recover rupture velocity variations but is very stable; the three-window model contains velocity variations but is much less reliable.

The stability of each method is best illustrated by tests using synthetic data (Section 2.5.3) – the ability to recover an input slip and rupture time model is indicative of the resolution expected with real data, and artifacts found may also occur with recorded seismograms. The constant rupture velocity found with the one-window inversion is the correct average of the input model, but temporal details are not recovered. The three-window inversion returns a variable rupture velocity model, which appears more realistic; however, errors are introduced to compensate for the mislocated slip.

4.2.2 Geodetic Inversions

Co-seismic measurements of the horizontal displacement field allow independent estimation of the Landers slip distribution [*Freymueller et al.*, 1994]. Slip is constrained to be right-lateral and the fault offset at the surface is used as prior information. The best-fitting slip model for the same fault geometry as that used in the previous chapters (described in Section 3.2.1) is shown in Figure 4.1, and is very similar to the model presented in *Freymueller et al.* [1994]. The geodetic slip model in Figure 4.1 is also similar to the seismic models shown in Figure 3.13, but has uniformly larger amplitudes (the geodetic moment is 9.8×10^{19} N-m). The corresponding fit to 38 GPS displacement vectors and 58 line-length changes is shown in Figure 4.2 (only the data closest to the fault is shown). For display purposes, the line-length changes are used to determine displacement vectors in the GPS coordinate system [*Segall and Matthews*, 1988]. When modeling the geodetic data, we must recognize that the measurement error is very heterogeneous.

Ninety-five percent confidence ellipses are shown for each datum in Figure 4.2. The error at sites for which there was only single-frequency GPS measurements prior to the earthquake (open circles) are much greater than those with dual-frequency measurements (filled circles); line-length changes measured with EDM (triangles) have the smallest measurement error. The geodetic data covariance can be estimated from the errors, which allows the data to be weighted properly in the inversion. At each site, the model fits the observation to within the resolved tolerance.

4.3 Partitioned Inversion

In the partitioned inversion, the geodetic slip model (Figure 4.1) is assumed and the seismograms comprise the data in a linearized inversion to image details of the rupture propagation. Measurement error in seismic data is believed to be much smaller than error in the theory introduced by inaccurate Green's functions, but neither source of error is easy to measure. The degree to which mainshock seismograms should be matched is approximated by measuring the misfit of aftershock seismograms modeled with the same theoretical Green's functions (Section 3.3). Unfortunately, aftershock recordings are only available at four sites; however, they span the azimuthal range of the entire data set and are representative of the propagation paths for all stations.

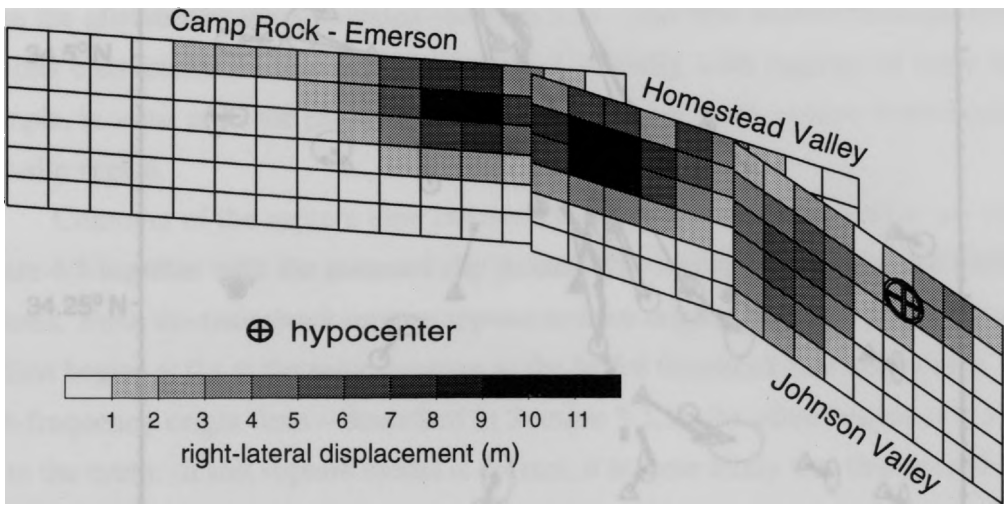

Figure 4.1. Slip amplitude distribution derived from geodetic measurements for the fault geometry described in Section 3.2.1. The cross section extends vertically from the surface to a depth of 18 km and the view perspective is looking east. The three segments represent the Camp Rock-Emerson, Homestead Valley, and Johnson Valley faults. Each segment is comprised of 3x3 km^2 fault elements. Displacement is constrained to be right-lateral and the surface offset is assumed as prior information. The peak amplitude is 11 m and the total moment is 9.8×10^{19} N-m.

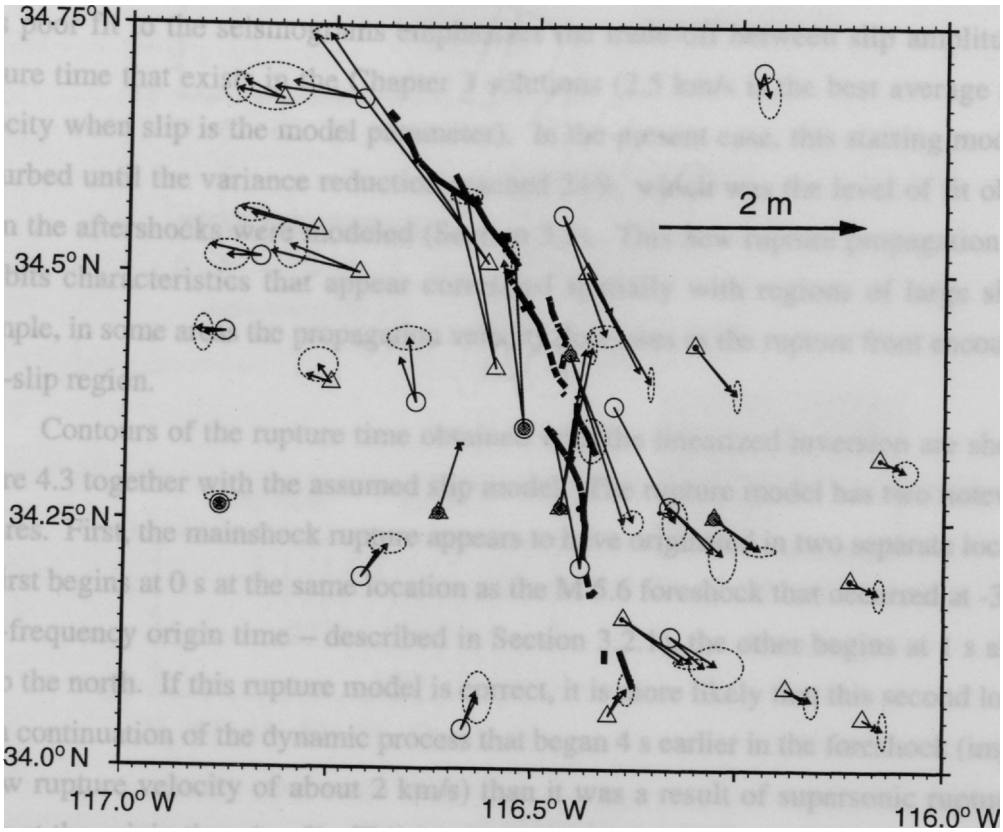

Figure 4.2. Fit to the observed horizontal displacements using the slip model from Figure 4.1. The 95% confidence ellipses are shown (dotted) for each datum and the corresponding model predictions are the vectors without an error ellipse. A 2 m displacement vector is plotted for scale. Dual-frequency GPS measurements are shown by filled-circles, single-frequency measurements are shown by open circles, and line-length changes are shown by triangles (for display purposes, the line-length changes are used to determine displacement vectors in the GPS coordinate system). Measurement errors associated with single-frequency receivers are greater than those with dual-frequency receivers; line-length changes have the smallest error.

The inversion procedure for determining the rupture propagation assuming a slip distribution is described in Section 2.3. In the present example, the starting rupture model has a constant velocity of 2.5 km/s and produces a negative variance reduction (-15%). This poor fit to the seismograms emphasizes the trade-off between slip amplitude and rupture time that exists in the Chapter 3 solutions (2.5 km/s is the best average rupture velocity when slip is the model parameter). In the present case, this starting model was perturbed until the variance reduction reached 24%, which was the level of fit obtained when the aftershocks were modeled (Section 3.3). This new rupture propagation model exhibits characteristics that appear correlated spatially with regions of large slip; for example, in some areas the propagation velocity decreases as the rupture front encounters a high-slip region.

Contours of the rupture time obtained with the linearized inversion are shown in Figure 4.3 together with the assumed slip model. The rupture model has two noteworthy features. First, the mainshock rupture appears to have originated in two separate locations: the first begins at 0 s at the same location as the M 5.6 foreshock that occurred at -3 s (the high-frequency origin time – described in Section 3.2.1), the other begins at 1 s about 7 km to the north. If this rupture model is correct, it is more likely that this second location was a continuation of the dynamic process that began 4 s earlier in the foreshock (implying a slow rupture velocity of about 2 km/s) than it was a result of supersonic rupture that began at the origin time (t = 0). This interpretation is consistent with recent evidence that earthquakes begin slowly, which is characterized by low rupture velocity, low stress drop, or both (Chapter 6).

The second interesting feature is a deceleration of the rupture as it meets with the shallow high-slip region on the Camp Rock-Emerson segment. This observation is consistent with the idea that regions of high-amplitude slip during faulting have greater strength excess prior to the earthquake [*Quin*, 1990; *Mikumo*, 1992].

Both propagation features are required by the seismic data when the geodetic slip model is assumed. This is shown in Figure 4.4, where the mainshock seismograms are plotted with the model predictions for both the starting model and the final rupture model.

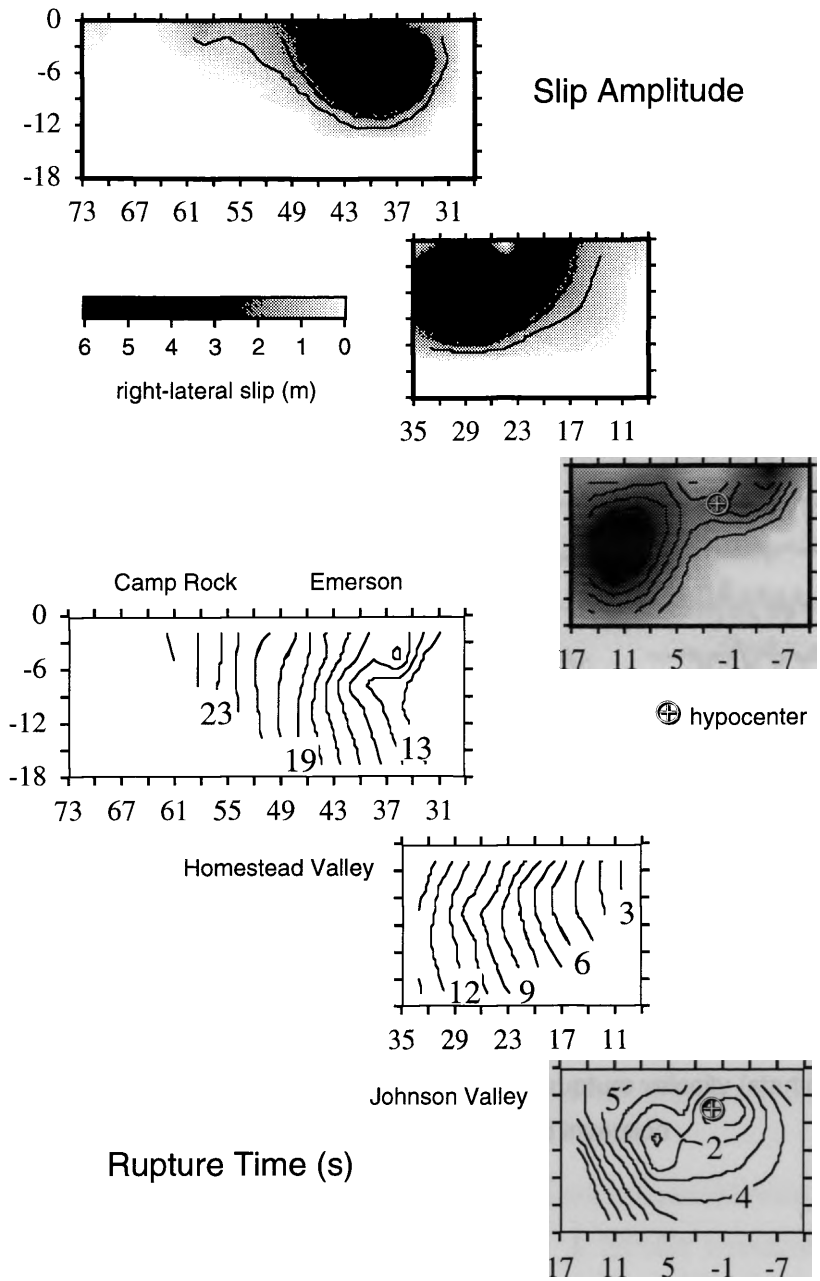

Figure 4.3. Rupture propagation model obtained from the near-source strong-motion seismograms (*bottom*) assuming the slip model (*top*) obtained from linear inversion of the geodetic observations. This slip model is the same as that shown in Figure 4.1 and is plotted here for comparison with the propagation model. The contours of slip show right-lateral displacement in m (meters) and the rupture time contour interval is 1 s.

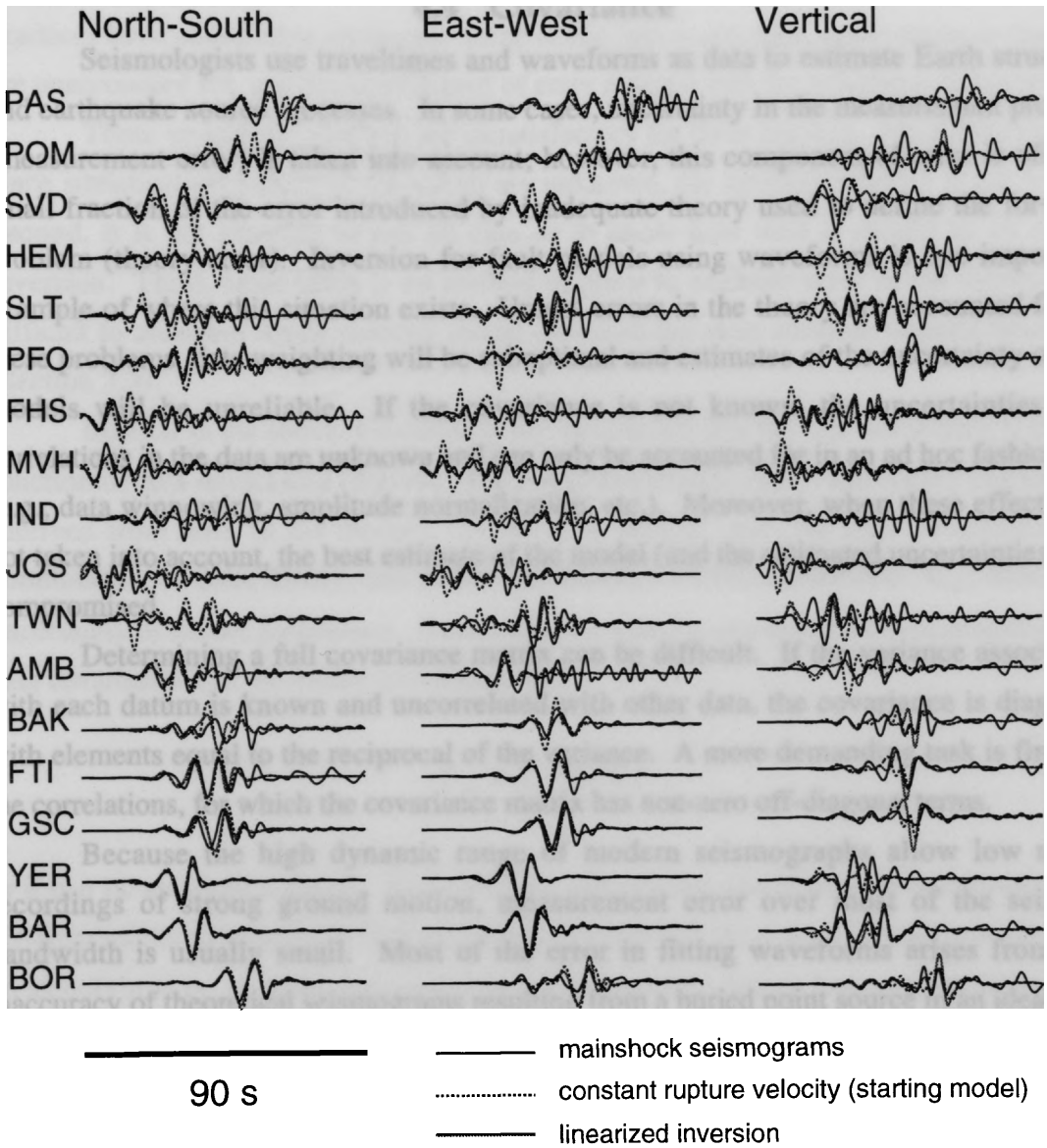

Figure 4.4. The fit to mainshock displacement seismograms (*black*) using two different models of rupture propagation: the starting model (constant rupture velocity – *dashed*) and the model from inversion (*gray*) that is shown in Figure 4.3. Mainshock seismograms are plotted for three components of motion at the eighteen stations shown in Figure 2.3 and listed in Table 3.1.

4.4 Covariance

Seismologists use traveltimes and waveforms as data to estimate Earth structure and earthquake source processes. In some cases, uncertainty in the measurement process (measurement error) is taken into account; however, this component of error is often a small fraction of the error introduced by inadequate theory used to define the forward problem (theory error). Inversion for fault models using waveforms is one important example of where this situation exists. Unless errors in the theory are accounted for in these problems, data weighting will be suboptimal and estimates of the uncertainty of the models will be unreliable. If the covariance is not known, the uncertainties and correlations in the data are unknown and can only be accounted for in an ad hoc fashion (e.g., data winnowing, amplitude normalization, etc.). Moreover, when these effects are not taken into account, the best estimate of the model (and the estimated uncertainties) are compromised.

Determining a full covariance matrix can be difficult. If the variance associated with each datum is known and uncorrelated with other data, the covariance is diagonal with elements equal to the reciprocal of the variance. A more demanding task is finding the correlations, for which the covariance matrix has non-zero off-diagonal terms.

Because the high dynamic range of modern seismographs allow low noise recordings of strong ground motion, measurement error over most of the seismic bandwidth is usually small. Most of the error in fitting waveforms arises from the inaccuracy of theoretical seismograms resulting from a buried point source in an idealized Earth model; this is an inevitable consequence of our incomplete knowledge of Earth structure. Additional error in the theory is introduced by the idealized fault geometry and its discrete representation.

In earthquake source inversions, error in the theory is most relevant and at least an order of magnitude larger than measurement error. A similar situation exists in the earthquake location inverse problem: error in the theory used to solve the forward traveltime problem is much larger than measurement error associated with picking an arrival time [*Tarantola and Valette*, 1982].

In the absence of the true covariance, we must make assumptions to weight the data. For instance, when certain regions at the surface have greater station density than others, seismograms are removed to avoid biasing the solution with an overabundance of data that may contain correlated errors. In some extreme cases, seismograms are given

greater weight if they are modeled successfully in preliminary analysis. These common practices have undesirable attributes: some of the data is not used, correlations in the data are unaccounted for, and the significance of error mapped into the solution is unknown.

These weighting practices are unsatisfactory for three reasons. Most importantly, since statistical properties of the errors are unknown, the optimal solution is not found. Second, it is not possible to use all data or to know how well it should be fit in the inversion. Third, since there is no method in place to evaluate error in the theory, it is difficult to ascertain which velocity model produces the most accurate Green's functions (Section 3.3).

Implicit in the above discussion is the assumption that the true covariance is only a function of data covariance (derived from the measurement error) and theory covariance (derived from error in the theory). In the most general case, the total covariance is a combination of data, theory, and model covariance. Model covariance, $\mathbf{C}_{\mathrm{m}}$, describes uncertainty of model parameters. It can either be found *a posteriori* from propagating the data covariance into the model covariance, i.e.,

$$\mathbf{C}_{\mathrm{m}} = \left(\mathbf{G}^{\mathrm{T}}\mathbf{C}_{\mathrm{d}}^{-1}\mathbf{G}\right)^{-1}, \tag{4.4}$$

or it can be assumed *a priori*. Since we lack information about relative uncertainties of different model parameters, it is reasonable to assume that the *a priori* model covariance is an identity matrix. A better approach is to use the geodetic data to find a slip model and its associated *a posteriori* model covariance, which could then be used in the inversion of seismic data.

To clarify the role of covariance weighting, we might consider the case of the general linear inverse problem. For the linear theory $\mathbf{Gm} = \mathbf{d}$, *Tarantola and Vallette* [1982] used a statistical approach to express the contribution of different errors on the total covariance. The probability distributions for the three sources of error are assumed to be Gaussian, so in each case the mean and associated covariance describe the probability:

$$P_{\mathrm{A}}(\mathbf{m}) \propto \exp\left[-\frac{1}{2}\left(\mathbf{m}-\langle\mathbf{m}\rangle\right)^{\mathrm{T}}\mathbf{C}_{\mathrm{m}}^{-1}\left(\mathbf{m}-\langle\mathbf{m}\rangle\right)\right] \tag{4.5}$$

$$P_{\mathrm{A}}(\mathbf{d}) \propto \exp\left[-\frac{1}{2}\left(\mathbf{d}-\mathbf{d}^{\mathrm{obs}}\right)^{\mathrm{T}}\mathbf{C}_{\mathrm{d}}^{-1}\left(\mathbf{d}-\mathbf{d}^{\mathrm{obs}}\right)\right] \tag{4.6}$$

$$P_{\mathrm{T}}(\mathbf{m}|\mathbf{d}) \propto \exp\left[-\frac{1}{2}(\mathbf{d}-\mathbf{Gm})^{\mathrm{T}}\mathbf{C}_{\mathrm{T}}^{-1}(\mathbf{d}-\mathbf{Gm})\right] \tag{4.7}$$

where $\mathbf{m}$ is the estimated model, $\langle\mathbf{m}\rangle$ is an *a priori* model, and $\mathbf{C}_{\mathrm{m}}$ is the model covariance. Similarly, $\mathbf{d}^{\mathrm{obs}}$ is the measured data, $\mathbf{d}$ is the true data, and $\mathbf{C}_{\mathrm{d}}$ is the data covariance; $\mathbf{G}$ is the kernel matrix that contains the forward theory, and $\mathbf{C}_{\mathrm{T}}$ is the theory covariance [*Menke*, 1984]. The subscript A means *a priori*. The total probability is the product of these three distributions, which is also Gaussian distributed [*Tarantola and Vallette*, 1982]. Using a maximum likelihood approach, we can express the model estimate as

$$\hat{\mathbf{m}} = \langle\mathbf{m}\rangle + \mathbf{G}^{-g}\left[\mathbf{d}^{\mathrm{obs}} - \mathbf{G}\langle\mathbf{m}\rangle\right] = \mathbf{G}^{-g}\mathbf{d}^{\mathrm{obs}} + [\mathbf{I}-\mathbf{R}]\langle\mathbf{m}\rangle \tag{4.8}$$

where,

$$\mathbf{G}^{-g} = \mathbf{C}_{\mathrm{m}}\mathbf{G}^{\mathrm{T}}\left[\mathbf{C}_{\mathrm{d}} + \mathbf{C}_{\mathrm{T}} + \mathbf{G}\mathbf{C}_{\mathrm{m}}\mathbf{G}^{\mathrm{T}}\right]^{-1} \tag{4.9}$$

and $\mathbf{R}$ is the resolution matrix [*Menke*, 1984]. If we do not have an *a priori* estimate of the model parameters and model covariance, we assume that $\mathbf{C}_{\mathrm{m}} = \alpha^2\mathbf{I}$, where $\alpha^2 = \infty$ (that is, the prior model has zero weight in the estimate). Likewise, if we do not know the data covariance, then $\mathbf{C}_{\mathrm{d}} = 0$ (the data contains no error). If, however, geodetic data is available, the geodetic model and associated *a posteriori* model covariance (equation 4.4) can be used as the *a priori* model estimate and model covariance in a seismogram inversion.

The theory covariance, $\mathbf{C}_{\mathrm{T}}$, describes the magnitude of error in the seismic theory and their correlations. It should be possible to estimate this covariance if there are recordings of aftershocks from all areas of the fault at each of the seismometer sites. To derive $\mathbf{C}_{\mathrm{T}}$ it is necessary to (1) estimate the theory error for each seismogram, (2) the correlation between the different seismograms, and (3) the correlation between points within each seismogram. The covariance can be written as $\mathbf{C}_{\mathrm{T}} = \sigma_i\sigma_j\mathbf{C}$, where $\mathbf{C}$ is a symmetric correlation matrix with unity on the diagonal, off-diagonal elements between 1 (perfect correlation) and -1 (perfect anti-correlation), and $\sigma_i\sigma_j$ are the standard deviations

of the ith and jth points in the seismogram (where i and j are the row and column indices of $\mathbf{C}$, respectively). The correlation matrix describes how errors are correlated within a seismogram, between different components, and between different stations.

The seismic wavefield in the near-source region is a mixture of direct P and S waves, surface waves, layer reverberations, scattering directly beneath the recording site, and energy scattered from velocity heterogeneities along the source-receiver propagation path. The significance of these different contributions, and the corresponding accuracy contained in synthetic seismograms, is a function of both frequency and time. The variances can be estimated by measuring the misfit between earthquakes of known mechanism and location and theoretical point-source seismograms. If recordings existed for every element of the discretized fault plane, it would be possible to compare the spectrum of the recordings with synthetic seismograms which would provide a measure of the frequency dependence of the error. If the event was recorded on all three components of motion, the correlated errors could be estimated. Similarly, if the event was recorded by multiple seismometers, correlations between components at different stations could be found. Since the error would exhibit strong frequency dependence (Figure 3.5), the misfit measurement and following covariance would naturally be represented in the frequency domain. To be used in the inverse problem, the data and theoretical seismograms would also be expressed in the spectral domain [*Mendez et al.*, 1990; *Cotton and Campillo*, 1995].

This approach has not yet been fully implemented in the analysis of an earthquake because the data (co-located earthquake seismograms) do not exist in sufficient quantity. There is, however, a growing awareness of the importance of co-siting instruments in aftershock deployments and in the use of higher dynamic range recording systems. Thus it is likely that in the future we will be able to determine theory covariance from microearthquake recordings.

Conclusions

The seismic wavefield is sensitive to both slip distribution and rupture propagation, whereas the static displacement field is only sensitive to the slip distribution. A partitioned inversion scheme is presented that takes advantage of the complementary nature of the two data types – the geodetic data is used to determine slip on the fault and the seismic data is used to image the propagation and slip history. Sensitivity analysis suggests that rupture propagation models obtained in this way are more reliable than those obtained using seismic data alone. A rupture model with a constant 2-s rise time and relatively simple rupture propagation fits both the seismic and geodetic data to within their estimated tolerances. In sampling heterogeneous data sets such as this, it is desirable to use the covariance to weight the data properly. Using the seismograms, we find that the theory covariance is most relevant, but difficult to establish.

Chapter 5 — Interpolating Empirical Green's Functions from Aftershock Seismograms

Abstract

Characteristics of high-frequency wave propagation through the Earth are contained in recorded seismograms. In contrast, theoretical seismograms calculated for idealized Earth models are approximations with errors that increase with frequency. In practice, recorded seismograms are problematic as Green's functions because in addition to wave propagation, they also include effects due to source location, mechanism, and size, as well as the instrument response. In this chapter, an inversion method that overcomes these difficulties is tested using aftershocks of the 1989 Loma Prieta, California, earthquake. The solutions fit the data reasonably well but are unable to predict missing seismograms as measured by cross-validation statistics. Two possible explanations for this result are (1) that the quantity of data is insufficient to describe the model (a site transfer-function) adequately, or (2) that errors in the source parameters (used to correct the seismograms) are too large to allow accurate solutions. Removing insignificant eigenvalues from the data emphasizes the site response and suppresses the source and path effects, thereby improving the cross-validation result; however, this filter also removes the highest frequency energy, which undermines the model's usefulness. In summary, cross-validation is an excellent method for evaluating model stability in complex inverse problems where data and model covariance are not known beforehand; the tested characterization of the site response is inadequate for Green's function interpolation using these data; and eigenvalue filtering is an efficient method for enhancing wave propagation effects occurring near the site.

5.1 Introduction

A critical ingredient in any inverse problem is the accuracy of the physical theory, or forward problem, that relates the observations to the model. When the inversion seeks a faulting model using near-source seismograms as data, the forward problem is the summed response of numerous point-source dislocations on a planar fault observed at discrete locations (seismometer sites) on the Earth's surface. The Earth response to an impulsive point source is termed the Green's function. In principle, theoretical Green's functions can be computed using arbitrarily complex models of the Earth, but in practice the structure is rarely known with enough detail to produce accurate waveforms at shorter wavelengths. Moreover, computational requirements become increasingly formidable as wavelengths decrease in heterogeneous three-dimensional (3D) velocity models. In the words of *Spudich and Archuleta* [1987],

> For the modeling of observed earthquake seismograms, or for prediction of ground motions in a specific region, the first factor limiting the accuracy of any Green's function calculation is simple ignorance of the earth structure at the site. In order to calculate Green's functions accurately at 5 Hz for a particular region, it is necessary to know the 3D shear-velocity structure on a scale of a few hundred meters both horizontally and vertically. Since such detailed knowledge of the earth's velocity structure may not be available in the near future, calculations of ground motions for real world situations are predestined to have errors.

Because theoretical Green's functions contain appreciable error at high frequencies, accurate prediction of the ground motion from a point source is inevitably bandlimited (in the forward problem) and it is thus impossible to recover short-wavelength faulting properties (in the inverse problem).

An alternative approach recognizes that at each seismometer only a portion of the velocity structure affects the wavefield, so that knowledge of the complete 3D structure is unnecessary. For each source location, the Earth response is required only at specific stations; hence, recorded seismograms from small earthquakes (small enough to appear as a point source) can be treated as *empirical Green's functions* [*Hartzell*, 1978]. Because of their accuracy at short wavelengths, empirical Green's functions have the potential to resolve more detailed properties of the earthquake than are possible with theoretical Green's functions.

Seismograms of small earthquakes (usually aftershocks) include the complete high-frequency response of the Earth. Unfortunately, they also include the instrument response, effects due to variable source mechanism and size, and they unevenly sample the volume of interest – in fact, areas of a fault plane with the largest slip amplitudes are typically the areas with the fewest aftershocks [*Mendoza and Hartzell*, 1988]. At near-source distances, these various effects in the recorded seismogram must be removed before they can be employed as Green's functions; in practice, this is a difficult task. As a result, empirical Green's functions have mostly been used in simple ways [*Hartzell*, 1978; *Kanamori et al.*, 1992], and most successfully for long distances and low frequencies where corrections to the recordings need only be approximate [*Ammon et al.*, 1993; *Dreger*, 1994b].

One procedure for addressing these difficulties is an interpolation method that accounts for known variations in the location, mechanism, and magnitude of the small earthquake, and solves for a *site transfer-function* that is represented as a time-varying response with simple dependencies on azimuth and incidence angle [*Spudich and Miller*, 1990]. Small earthquakes are assumed to be point sources for frequencies below the corner frequency. If the model can predict missing data (the definitive test of any interpolator), then it can be used to calculate the response of dislocations with arbitrary mechanism for any location within the sampled volume (the variance can be derived from the misfit of the omitted seismograms). The interpolated seismograms can be used to analyze high-frequency ground motions from large earthquakes in the same volume, which has the potential to improve the accuracy and resolution of the faulting models greatly. Since the *Spudich and Miller* [1990] procedure is formulated as an underdetermined inverse problem, it is particularly important that the validity of each model is established prior to its use in calculating Green's functions for analysis of mainshock seismograms.

In this chapter, we use aftershocks of the M_W 6.9 1989 Loma Prieta earthquake to find a site transfer-function model for an incident *S* wave at five seismometer sites. A more accurate and reliable slip distribution and rupture time model of this earthquake is important for assessing the potential for future earthquakes, and anticipating the severity of strong ground motion in them. The validity of the result is measured by the model's ability to reproduce individual aftershock seismograms that are removed from the data set, one at a time – a robust model should not depend heavily on any one datum (seismogram).

A cross-validation approach is used to measure the model's ability to predict each deleted seismogram and the weighted residuals are summed.

For the five locations examined in this study, cross-validation shows that the solutions exhibit strong dependence on individual seismograms and should not be used to interpolate Green's functions. In an effort to improve the models, we gathered aftershock seismograms for each station in a matrix and decomposed them into eigenvalues and eigenvectors using a singular value decomposition (SVD), and then reconstructed them using only the most significant eigenvalues (determined with a F-test). This filtering procedure has several attributes, but, most importantly, it retains common features in the seismograms, which emphasizes the site-response, and suppresses uncommon effects that are mostly attributable to differences in the propagation path and source. The greatest shortcoming of the filter is that the reconstructed seismograms (and hence the site transfer-function model) contain less energy at high frequencies. The inversion results obtained with the reconstructed data yield smaller cross-validation residuals, but their usefulness for interpolating Green's functions is weakened by the loss of the high-frequency signal.

5.2 Loma Prieta Aftershock Seismograms

The Loma Prieta earthquake occurred in a region that was densely instrumented with strong-motion accelerographs operated by the U.S. Geological Survey, the California Division of Mines and Geology, and the University of California at Santa Cruz. After the earthquake, three-component seismometers were co-located at accelerograph sites that recorded the mainshock; this deployment provided the aftershock seismograms used in this study. In choosing specific sites for the deployment, the scientists had three stated criteria: first, to instrument areas that experienced damage in the mainshock; second, to co-locate instruments with strong-motion accelerographs that recorded the mainshock; and third, to obtain uniform spatial coverage [*Mueller and Glassmoyer*, 1990]. The purpose of co-locating recorders at strong motion sites was to obtain aftershock seismograms that could be used as empirical Green's functions to model the mainshock strong ground motions. At twenty-one locations seismometers were installed adjacent to the strong-motion accelerometer that recorded the mainshock. The typical instrument package consisted of a six-channel GEOS system recording three-components from a Mark Products L-22D 2-Hz velocity seismometer and three-components from a Kinemetrics FBA-13 accelerometer, both at 200 samples/s [*Mueller and Glassmoyer*, 1990]. Gains were adjusted to maximize

the range of ground amplitude recorded on-scale: the velocity instruments were set to record the smaller aftershocks and the accelerometers were set to record the larger aftershocks.

The *Spudich and Miller* [1990] interpolation method requires dense sampling of the aftershock volume. Unfortunately, many sites were occupied for less than a week and did not record a sufficient number of events. The seismometer should be close to the earthquake to minimize complex propagation effects due to refractions and *P* to *S* conversions. For a small earthquake to be treated as a point source, it must have a corner frequency above the highest frequency of interest; in the present study, that meant using aftershocks of magnitude less than 4 and frequencies less than 3 Hz. There were five seismometer locations with an adequate number of recordings. The locations of the stations and aftershocks, and a discrete representation of the Loma Prieta mainshock fault plane [*Beroza*, 1991] are shown in Figure 5.1. The station characteristics are listed in Table 5.1. Two different cross sections of the fault grid, aftershock locations, and the five stations are shown in Figure 5.2. Only the non-zero elements (1x1 km^2) of the *Beroza* [1991] fault model are displayed. Our ultimate goal is to derive interpolated Green's functions for every element at each seismometer. We only use aftershocks occurring very near the fault plane – unfortunately, there are large areas of the fault with no recorded aftershocks.

Table 5.1. Co-located Seismometer Stations

Code	Location	Latitude (°N)	Longitude (°W)	Events (#)
CAP	Capitola	36.9740	121.9522	24
DMD	Anderson Dam	37.1642	121.6314	35
GA2	Gavilan College	36.9731	121.5680	27
KOI	Corralitos	37.0462	121.8031	107
SAR	Saratoga	37.2553	122.0311	73

In summary, the number of aftershocks available at a particular station is limited by the deployment duration, the subset of aftershocks occurring on or directly adjacent to the mainshock fault plane, and the noise characteristics of each site (a high noise level can

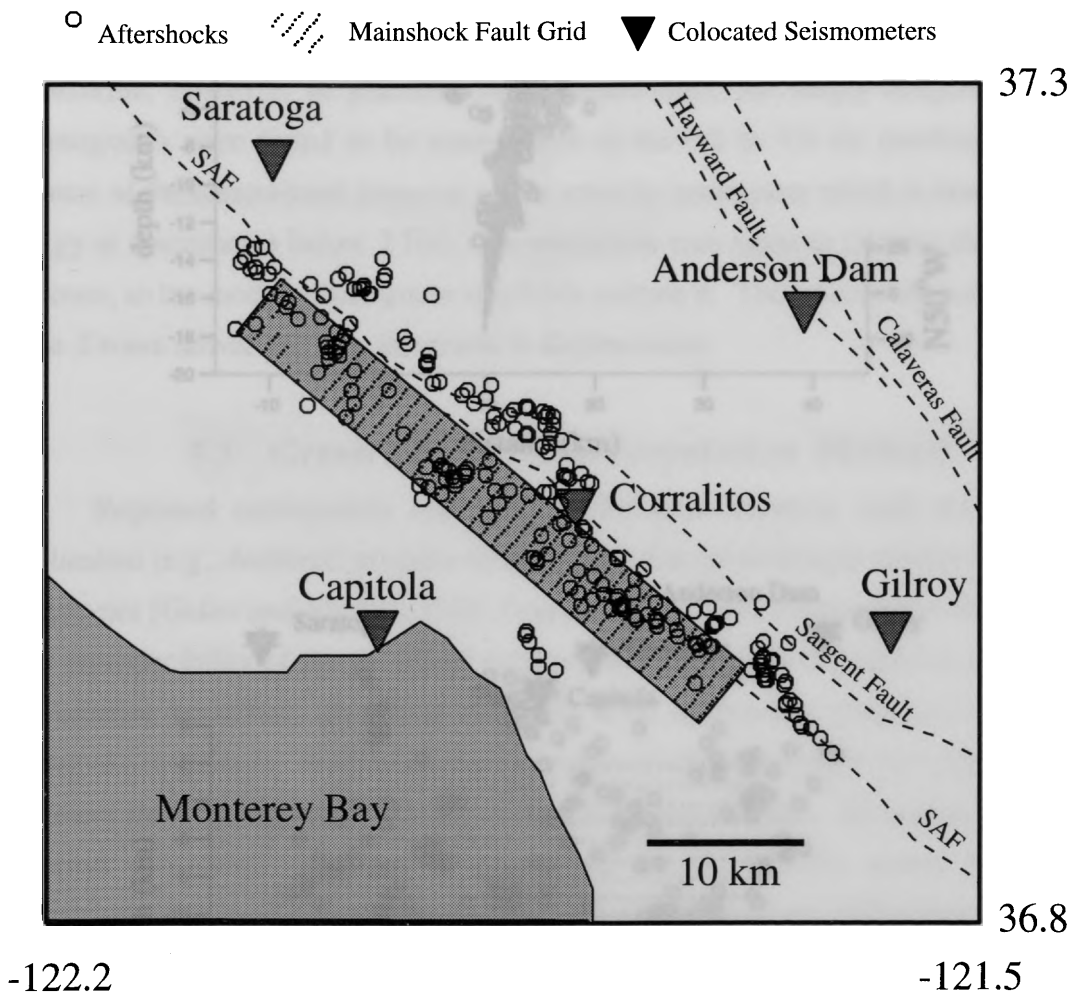

Figure 5.1. Map view of the Loma Prieta study area showing the mainshock fault plane [*Beroza*, 1991], the five co-located seismometers, and the aftershocks they recorded. The seismometers are shown by inverted triangles and the aftershocks by open circles. The fault plane strikes 130°, is 40 km long and 14 km wide (spanning 5 to 18 km depth), and dips 70° to the SW. Note that the stations have good azimuthal range and are within 25 km of the fault.

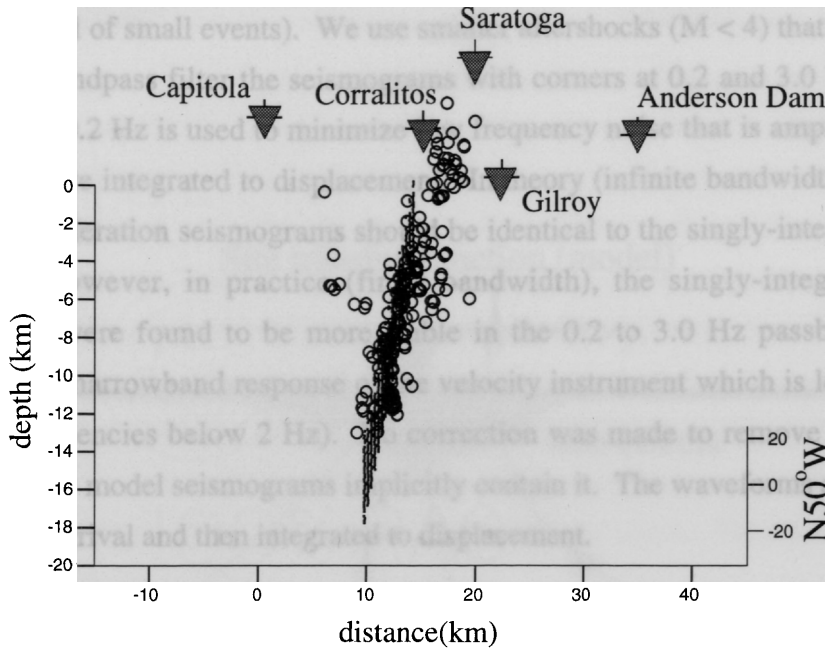

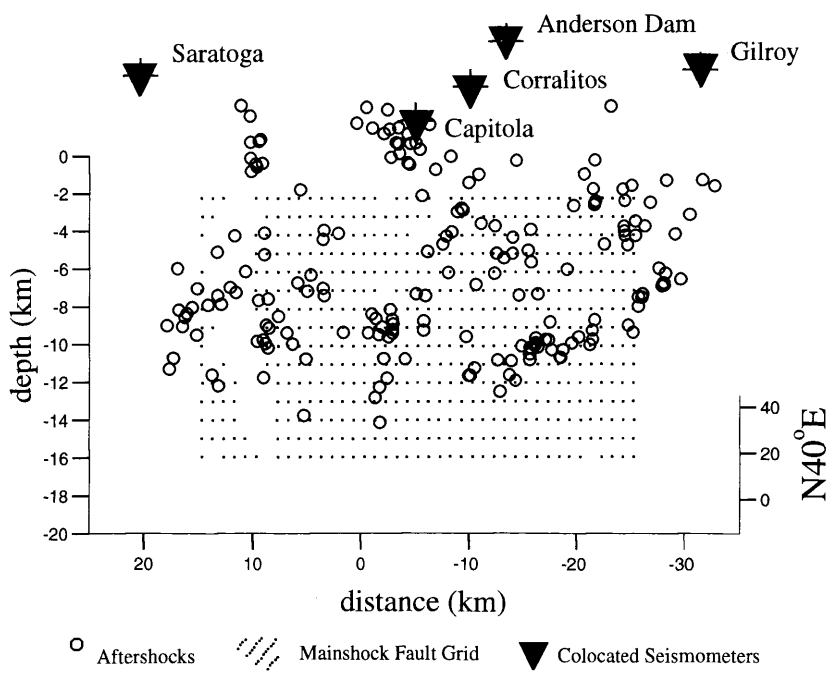

Figure 5.2. Two cross sections of the fault zone showing the aftershock locations and five stations used in the study. The first view (*top*) is looking N50°W (310°), along the strike of the fault. The second view (*bottom*) is looking N40°E (40°) perpendicular to the fault strike. Note that some areas of the fault have no aftershocks recorded by the five seismometers; it is in these areas where the interpolation method is most severely tested.

dwarf the signal of small events). We use smaller aftershocks (M < 4) that look like point sources and bandpass filter the seismograms with corners at 0.2 and 3.0 Hz. The high-pass corner at 0.2 Hz is used to minimize low frequency noise that is amplified when the seismograms are integrated to displacement. In theory (infinite bandwidth), the doubly-integrated acceleration seismograms should be identical to the singly-integrated velocity waveforms; however, in practice (finite bandwidth), the singly-integrated velocity seismograms were found to be more stable in the 0.2 to 3.0 Hz passband (probably because of the narrowband response of the velocity instrument which is less sensitive to energy at frequencies below 2 Hz). No correction was made to remove the instrument response, so the model seismograms implicitly contain it. The waveforms are first aligned at the *S*-wave arrival and then integrated to displacement.

5.3 Green's Function Interpolation Method

Repeated earthquakes occurring in the same location with the same focal mechanism (e.g., doublets) produce seismograms that are strikingly similar even at high-frequencies [*Geller and Mueller*, 1980; *Poupinet et al.*, 1984; *Frémont and Malone*, 1987]. This reproducibility of the wavefield demonstrates the ability of empirical recordings to characterize accurately the Earth response to an earthquake [*Hartzell*, 1978]. The earthquake magnitude (and fault area) need not be identical as long as the corner frequency is greater than the highest frequency energy in the seismogram. Of course, this Green's function characterization is only appropriate for the specific source location and seismometer site and the particular focal mechanism; this is where difficulties arise.

First, there are not recordings of sources for all desired locations. Second, it is difficult to remove completely the effect of the radiation pattern: all focal mechanism estimates contain errors, and even when they are very small, the amplitude modulation predicted for a double-couple dislocation model breaks down at higher frequencies because of complex scattering and diffraction by small-scale heterogeneities, particularly those in the near-surface geology [*Liu and Helmberger*, 1985; *Vidale*, 1989; *Bonamassa et al.*, 1991].

Given the aftershock and station coordinates, the mechanism and magnitude, and a layered velocity model, it is theoretically possible to correct the recorded seismogram and remove these effects. After these corrections are made, all that remains are effects due to

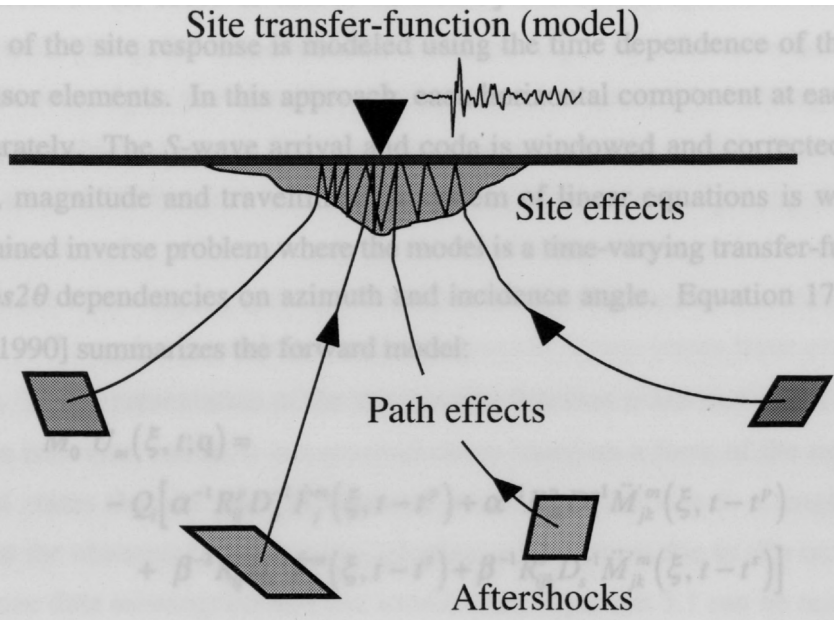

Figure 5.3. Schematic illustration of the forward model showing cross section of the Earth with four aftershocks and one seismometer located on a shallow low-velocity basin. The *Spudich and Miller* [1990] algorithm, as applied in this study, corrects the seismograms for the aftershock location, magnitude, and mechanism, and ignores path effects due to wave propagation away from the site. The model maps differences in the corrected seismograms into a site transfer-function that represents common scattering and propagation effects caused by small-scale velocity heterogeneity at the site (adapted from *Spudich and Miller* [1990]).

the propagation path, in particular those at the site where the velocity heterogeneity is greatest. This approach is schematically illustrated in Figure 5.3.

Spudich and Miller [1990] solved for a site response that is a function of azimuth and time. To model the angular dependence of the site, they set up an equivalent force and moment system at the receiver that is excited by incident P and S waves – the time dependence of the site response is modeled using the time dependence of the force and moment-tensor elements. In this approach, each horizontal component at each station is treated separately. The S-wave arrival and coda is windowed and corrected for source mechanism, magnitude and traveltime. A system of linear equations is written as an underdetermined inverse problem where the model is a time-varying transfer-function with $cos\theta$ and $cos2\theta$ dependencies on azimuth and incidence angle. Equation 17 of *Spudich and Miller* [1990] summarizes the forward model:

$$\begin{aligned} M_0^{-1}\dot{U}_m(\xi, t;\mathbf{q}) = \\ -Q_i\Big[\alpha^{-1}R_{ij}^p D_p^{-1}\dot{F}_j^m(\xi, t-t^p) + \alpha^{-1}R_{ijk}^p D_p^{-1}\ddot{M}_{jk}^{'m}(\xi, t-t^p) \\ + \beta^{-1}R_{ij}^s D_s^{-1}\dot{F}_j^m(\xi, t-t^s) + \beta^{-1}R_{ijk}^s D_s^{-1}\ddot{M}_{jk}^{'m}(\xi, t-t^s)\Big] \end{aligned} \tag{5.1}$$

where M_0 is the seismic moment, $\dot{U}_m(\xi, t;\mathbf{q})$ is the m component of velocity observed at ξ from a traction $\mathbf{q}$ at time t. Q_i is a term that accounts for the geometry of the dislocation, the fault orientation, and the azimuth and take-off angle to the receiver defined as

$$Q_i = n_i(\hat{\mathbf{d}}\cdot\hat{\mathbf{r}}) + d_i(\hat{\mathbf{n}}\cdot\hat{\mathbf{r}}) \tag{5.2}$$

where $\hat{\mathbf{d}}$ is the dislocation direction, $\hat{\mathbf{r}}$ is the tangent to the ray path, and $\hat{\mathbf{n}}$ is normal to the fault surface. The scalar variables α and β are the P- and S-wave velocities. The R terms describe the P- and S-wave radiation pattern of the aftershock, and are defined by equations 10 through 13 in *Spudich and Miller* [1990]. D_p and D_s are P- and S-wave amplitude terms that describe the amplitude decay as a function of the source and receiver velocity and density, and the source-receiver distance.

Equation 5.1 follows from the underlying premise of *Spudich and Miller* [1990], which can be written

$$U_i = F_j * G_{ij} + M_{jk} * G_{ij,k}. \tag{5.3}$$

This equation states that the observed displacement U is the sum of a three-component body force vector **F**(t) and a moment tensor **M**(t) with six independent elements, each convolved with the point-force Green's function G_{ij}. In other words, the method assumes that away from the site, the velocity model is smoothly varying and may be described by ray theory Green's functions in a layered velocity model. Near the surface, the Earth is assumed to be more heterogeneous, producing complex propagation effects at the site. These complex effects are represented by the three force and six moment tensor terms, which are time-varying and together represent the site transfer-function. The force terms have $cos\theta$ angular dependence, and the moment tensor terms have $cos2\theta$ angular dependence. This representation of the site transfer-function is not motivated by observed site response behavior; rather, it is a generalization based on a form of the representation theorem that states that the traction response across the fault due to a single impulsive point-force at the observer can be used to calculate seismograms due to slip on the fault.

For one data seismogram and one source term, Equation 5.1 can be rearranged into the form:

$$\begin{bmatrix} \dot{U}(\xi, \tau_1;\mathbf{q}) \\ \dot{U}(\xi, \tau_2;\mathbf{q}) \\ \dot{U}(\xi, \tau_3;\mathbf{q}) \\ \vdots \\ \dot{U}(\xi, \tau_L;\mathbf{q}) \end{bmatrix} = \begin{bmatrix} a_1 & 0 & 0 & 0 & \cdots & 0 \\ 0 & a_1 & 0 & 0 & \cdots & 0 \\ b_1 & 0 & a_1 & 0 & \cdots & 0 \\ 0 & b_1 & 0 & \ddots & \cdots & 0 \\ 0 & 0 & \ddots & & & \\ \vdots & & & & \ddots & 0 \\ \vdots & & & & & a_1 \\ \vdots & & & & \ddots & 0 \\ 0 & & & & & b_1 \end{bmatrix} \begin{bmatrix} \dot{F}_1(\xi, t_1) \\ \dot{F}_1(\xi, t_2) \\ \dot{F}_1(\xi, t_3) \\ \vdots \\ \dot{F}_1(\xi, t_N) \end{bmatrix} \tag{5.4}$$

where $a_j = -Q_i \alpha^{-1} R_{ij}^p D_p^{-1}$ and $b_j = -Q_i \beta^{-1} R_{ij}^s D_s^{-1}$ [*Spudich and Miller*, 1990]. If equation 5.4 is written as $\mathbf{U}_1 = \mathbf{A}_{11}\mathbf{W}_1$, then an equation with multiple data seismograms and source terms is

$$\begin{bmatrix} \mathbf{U}_1 \\ \mathbf{U}_2 \\ \vdots \\ \mathbf{U}_N \end{bmatrix} = \begin{bmatrix} \mathbf{A}_{11} & \mathbf{A}_{12} & \cdots & \mathbf{A}_{19} \\ \mathbf{A}_{21} & \mathbf{A}_{22} & \cdots & \mathbf{A}_{29} \\ \vdots & & & \vdots \\ \mathbf{A}_{N1} & \mathbf{A}_{N2} & \cdots & \mathbf{A}_{N9} \end{bmatrix} \begin{bmatrix} \mathbf{W}_1 \\ \mathbf{W}_2 \\ \vdots \\ \mathbf{W}_9 \end{bmatrix}, \tag{5.5}$$

or, more simply, $\mathbf{U} = \mathbf{AW}$. Since each of the nine source terms $\mathbf{W}$ are time varying, the total number of unknowns is $9M$, where M is the number of samples in the seismograms. The total length of the data vector $\mathbf{U}$ is NM, where N is the number of seismograms.

Equation 5.5 is written for a single scatterer, but it is straightforward to extend the system to include multiple scatters [*Spudich and Iida*, 1993]. The multi-scatterer inversion has more severe problems with underdeterminacy – the model has enough freedom to match each seismogram almost exactly, but the model variance is large.

To minimize the resolution-variance trade-off, we use only one scatterer located at the seismometer. The stability of the model is evaluated by measuring cross-validation residuals: removing one seismogram at a time, solving for a model using the remaining data, computing the model prediction for the omitted seismogram, and measuring the misfit.

5.4 Evaluating Models Using Cross-Validation

All inversion methods involve minimizing the misfit between observations and the synthetic data predicted by a model. The data variance is a measure of how well the measurements are fit and the model variance is a measure of the model's stability. Increased model variance implies increased model uncertainty; large changes in the model have small effect on the data misfit. In some cases, when the model is a linear function of the data, it is possible to express the model variance in terms of the data variance [*Menke*, 1984]. When the model and data are nonlinearly related, it is difficult to establish a direct relationship between the model and data variance. Fortunately, it is always possible to use a resampling approach to estimate model variance for nonlinear inverse problems. Resampling methods substitute raw computing power for theoretical analysis and can be routinely applied to arbitrarily complex nonlinear problems. The procedure is based on the idea that the given data set can be resampled multiple times forming multiple independent data sets. For each sample, a new model is found and the model variance is derived from

the ensemble of new models. The underlying philosophy in this approach is that statistics of errors in the data can be represented by variations in the data themselves.

Cross-validation is one widely-used resampling method [*Wahba*, 1990]. With this method each datum is removed from the set of n samples, the system is solved using the remaining n-1 samples, and a prediction is made from the model for the removed datum. *Efron and Gong* [1983] summarized cross-validation as

> (a) deleting the points x_i from the data set one at a time; (b) recalculating the prediction rule on the basis of the remaining n-1 points; (c) seeing how well the recalculated rule predicts the deleted point; and (d) averaging these predictions over all n deletions of an x_i

If the case of a n length vector of equally weighted data, the cross-validated estimate of the prediction error is the sum of the squared cross-validation residuals:

$$\frac{1}{n}\sum_{i=1}^{n}\left[x_i - \bar{x}_{(i)}\right]^2, \tag{5.6}$$

where $\bar{x}_{(i)}$ is the model prediction of x_i (with x_i removed from the data set). This cross-validation sum of squares (CVSS) has been used to optimize inversion parameters, such as the smoothing weight [*Matthews and Segall*, 1993; *Segall and Du*, 1993; *Freymueller et al.*, 1994].

In the present application, the CVSS is used to ascertain whether the force and moment terms are required by the data (no smoothing is required in our interpolation problem). In a broader sense, the cross-validation residual is a measure of how successful the interpolation model is in predicting missing seismograms. In this application, we delete one aftershock seismogram at a time from the data vector, perform the inversion, and measure the misfit between the model prediction and the omitted waveform. When comparing the two vectors (data $\boldsymbol{x}$ and model prediction $\bar{\boldsymbol{x}}$), we define the weighted cross-validation residual as

$$\left(\frac{\sum_{i=1}^{n}\left(x_i - \bar{x}_{(i)}\right)^2}{\sum_{i=1}^{n}x_i^2 + \sum_{i=1}^{n}\bar{x}_{(i)}^2}\right)^{1/2}, \tag{5.7}$$

which varies from $\sqrt{2}$ (perfectly anticorrelated), to 1.0 (uncorrelated), to 0 (perfect fit) [*Spudich and Miller*, 1990]. The cross-validated prediction error quantifies how well the model predicts the omitted data. Since the purpose of the model is to interpolate empirical Green's functions for locations where there are no aftershocks, cross-validation provides an appropriate measure of the model's utility.

Example data and model predicted seismograms for the five stations are shown in Figure 5.4. For each seismogram, the prediction is obtained from a model that was derived without using the corresponding seismogram in the data vector; hence, these are examples of the method in the interpolation mode. The character of the waveforms is generally similar for different earthquakes recorded at each station. For example, the seismograms at Gilroy have an impulsive *S*-wave arrival and relatively little coda, whereas the seismograms at Capitola are comparatively rich in high frequency energy and demonstrate more event-to-event variation. Since the inversion corrects the seismogram amplitude for the earthquake magnitude, small errors in the magnitude can cause large amplitude differences even when the waveform shape shows good agreement. This is most apparent in some of the examples recorded at Gilroy.

The cross-validation residuals are summarized in Figure 5.5 for the north-south component of motion (results for the east-west component are negligibly different). Most of the measurements fall between 0.8 and 1.0, indicating that the interpolated seismograms are not strongly correlated with their observed counterparts. In the trivial case where the predicted seismogram is a null vector, the residual value is 1.0, so it is clear that this site model should not be used to interpolate Green's functions for these stations.

The residuals were examined to determine why some seismograms are more predictable than others. An example of this analysis for the residuals at station Corralitos (north-south component) is shown in Figure 5.6. It is reasonable to expect a correlation between the magnitude of error in the source parameters and higher residuals – errors in the focal mechanism or the event location are examples of known errors that could lead to higher residuals. If such a correlation could be found, it could be used as a basis to weight the seismograms in the inversion. In Figure 5.6, the residuals are plotted against various aftershock parameters and the measures of their uncertainty. Unfortunately, we were unable to identify a trend for any parameter that explains the behavior of the residuals. We

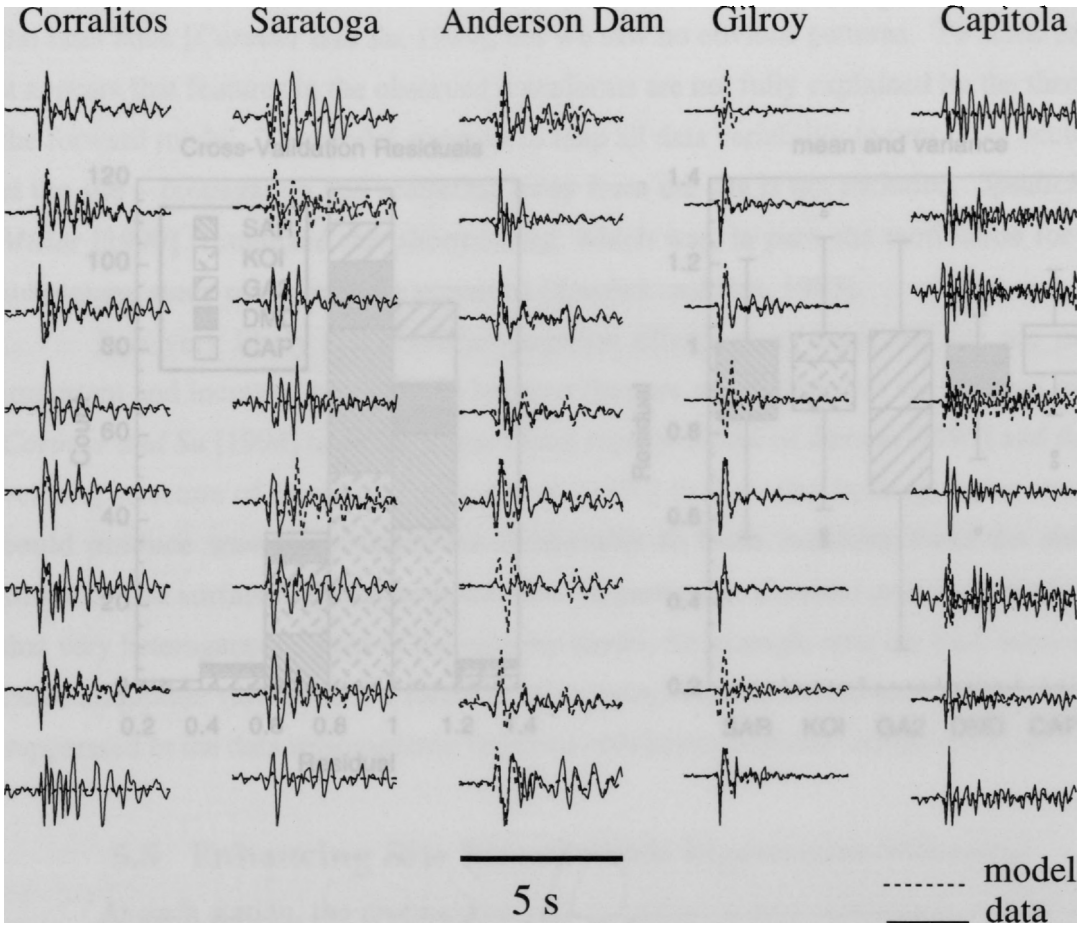

Figure 5.4. Example interpolation of seismograms. Select horizontal displacement seismograms are shown for each stations. In each case, the data seismogram is not used to obtain the model. The character of the waveforms is generally similar among different events at the same station. The seismograms are aligned 1 s before the *S*-wave arrival.

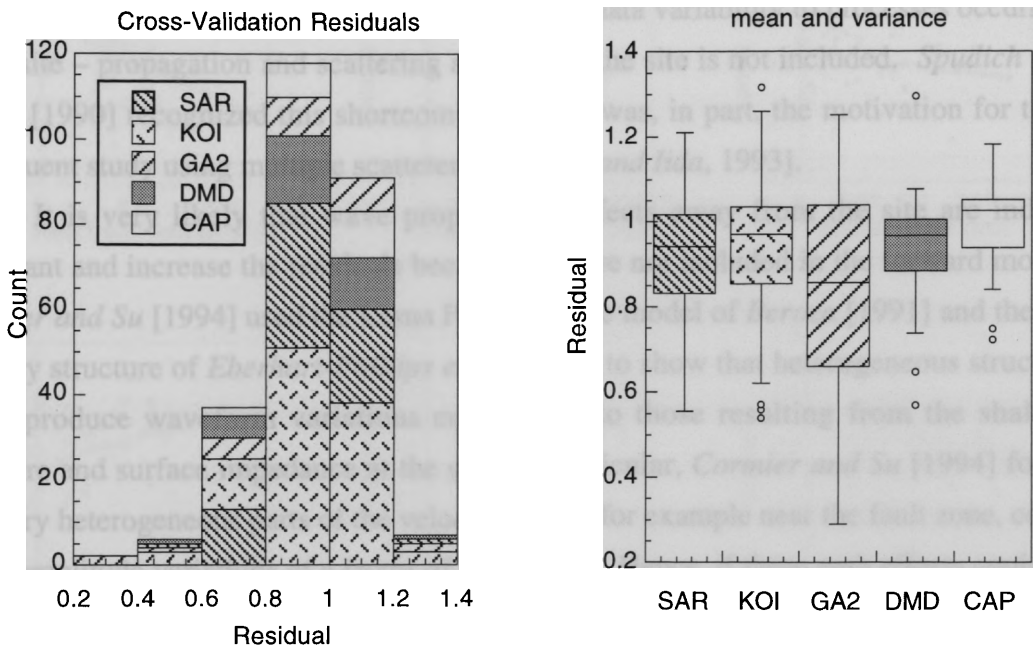

Figure 5.5. Cross-validation residuals for the five stations using the north-south component of motion. The histogram (*left*) and distribution (*right*) show that the interpolations are not strongly correlated with the data. Seismograms from station GA2 (Gilroy) have the least coda and produce the best interpolations; seismograms from station CAP (Capitola) show the least interevent commonalty and yield the poorest interpolations. The mean is shown by a horizontal line and 1 and 2 standard deviations of the mean are shown by error bars.

also examined whether aftershocks from some areas of the fault zone produced higher residuals than others, which might be caused by scattering or other propagation effects in the fault zone [*Cormier and Su*, 1994], but we saw no obvious patterns. To some extent, it appears that features in the observed waveforms are not fully explained by the theory in the forward model. The model attempts to map all data variability to processes occurring at the site – propagation and scattering away from the site is not included. *Spudich and Miller* [1990] recognized this shortcoming, which was, in part, the motivation for their subsequent study using multiple scatterers [*Spudich and Iida*, 1993].

It is very likely that wave propagation effects away from the site are indeed important and increase the residuals because they are not included in the forward model. *Cormier and Su* [1994] used the Loma Prieta rupture model of *Beroza* [1991] and the 3D velocity structure of *Eberhart-Phillips et al.* [1990] to show that heterogeneous structure could produce waveform variations comparable to those resulting from the shallow structure and surface impedance at the site. In particular, *Cormier and Su* [1994] found that very heterogeneous parts of the velocity model, for example near the fault zone, could cause amplitude variations of a factor of 10 or more. Hence, if these path effects could be suppressed in the data seismograms, the cross-validation residuals should decrease.

5.5 Enhancing Site Effects With Eigenvalue Filtering

At each station, the propagation path is unique to each aftershock, but the site is common. If correlated properties of the seismograms recorded at a particular site are enhanced, the result should be the suppression of uncorrelated path effects and random noise, and emphasis of the site response. For example, the local geology near the site could produce a characteristic eigenspectrum (e.g., resonance) with little or no dependence on azimuth or incidence angle [*Bard and Bouchon*, 1985]. Since the polarity of the *S* wave varies with the source mechanism, it is critical that a method for enhancing the site effect is able to accommodate sign changes. One method that satisfies these criteria uses a SVD to determine the eigenspectrum of all data recorded at a site, and then reconstructs the data using the largest eigenvalues. This technique was used by *Freire and Ulrych* [1988] to separate upgoing and downgoing wavefields in a vertical seismic profile.

All seismograms for one component at one station are gathered in a matrix. The row dimension is the number of points in the seismograms and the column dimension is the number of seismograms. Eigenvalues and eigenvectors are found with a SVD. The

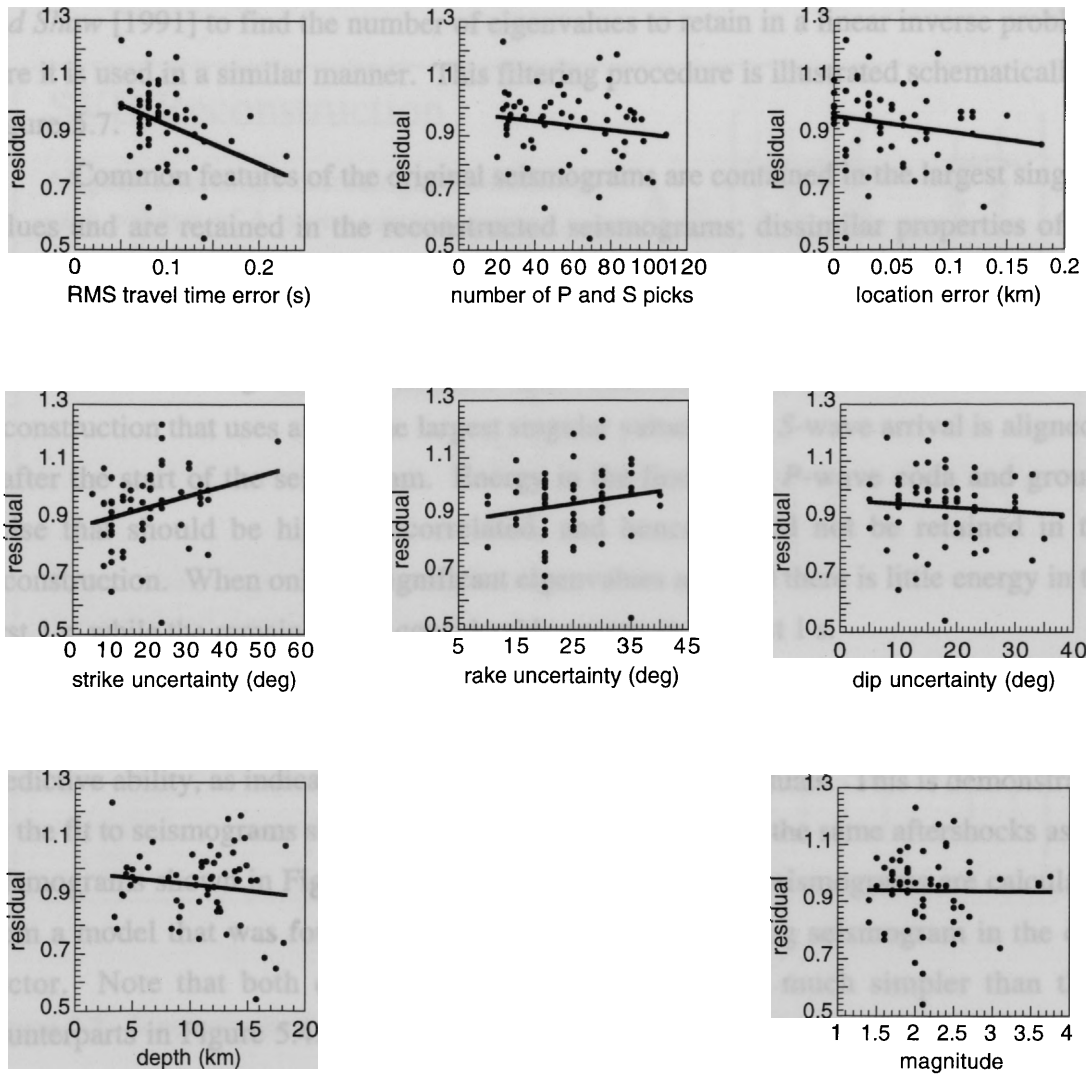

Figure 5.6. Comparison of cross-validation residuals with various source parameters for the north-south seismograms at station KOI (Corralitos). We were unable to identify a trend where higher residuals were correlated with increased error in the source parameter.

seismograms are then reconstructed using only the largest singular values. Eigenvalues are retained, starting with the largest, until further eigenvalues no longer add significantly to the prediction of the data as determined by an F-test. The F-test was used by *Jacobson and Shaw* [1991] to find the number of eigenvalues to retain in a linear inverse problem; here it is used in a similar manner. This filtering procedure is illustrated schematically in Figure 5.7.

Common features of the original seismograms are contained in the largest singular values and are retained in the reconstructed seismograms; dissimilar properties of the seismograms are removed. An example of a reconstruction is shown in Figure 5.8. The seismograms are reconstructed using only the first singular value, and the number that is determined to be significant with the F-test. Also shown is the remainder, that is, a reconstruction that uses all but the largest singular values. The *S*-wave arrival is aligned 1 s after the start of the seismogram. Energy in the first 1 s is *P*-wave coda and ground noise that should be highly uncorrelated, and hence should not be retained in the reconstruction. When only the significant eigenvalues are used there is little energy in the first 1 s, while the remainder has considerable energy in the first 1 s.

The reconstructed seismograms were used as the data and the inversion procedure (equation 5.1) was repeated. The resulting interpolation model demonstrates greater predictive ability, as indicated by smaller cross-validation residuals. This is demonstrated by the fit to seismograms shown in Figure 5.9, which are from the same aftershocks as the seismograms shown in Figure 5.4. As before, the predicted seismograms are calculated from a model that was found without using the corresponding seismogram in the data vector. Note that both data and model seismograms are much simpler than their counterparts in Figure 5.4. Specifically, there is less energy before the arrival of the *S*-wave, the amplitude of the coda is decreased, and the *S*-wave pulse is more coherent for different events at the same station. Overall, the seismograms exhibit greater interevent similarity at each station.

The cross-validation residuals are summarized in Figure 5.10. Using the filtered data, we reduce the residuals at some stations; however, because the site transfer-function contains less information at high frequencies, its usefulness for calculating empirical Green's functions (for modeling mainshock seismograms) is significantly reduced. The residuals show more variability among the five stations than observed in Figure 5.5. The stations KOI, DMD, and particularly GA2, all show marked improvement, while SAR and

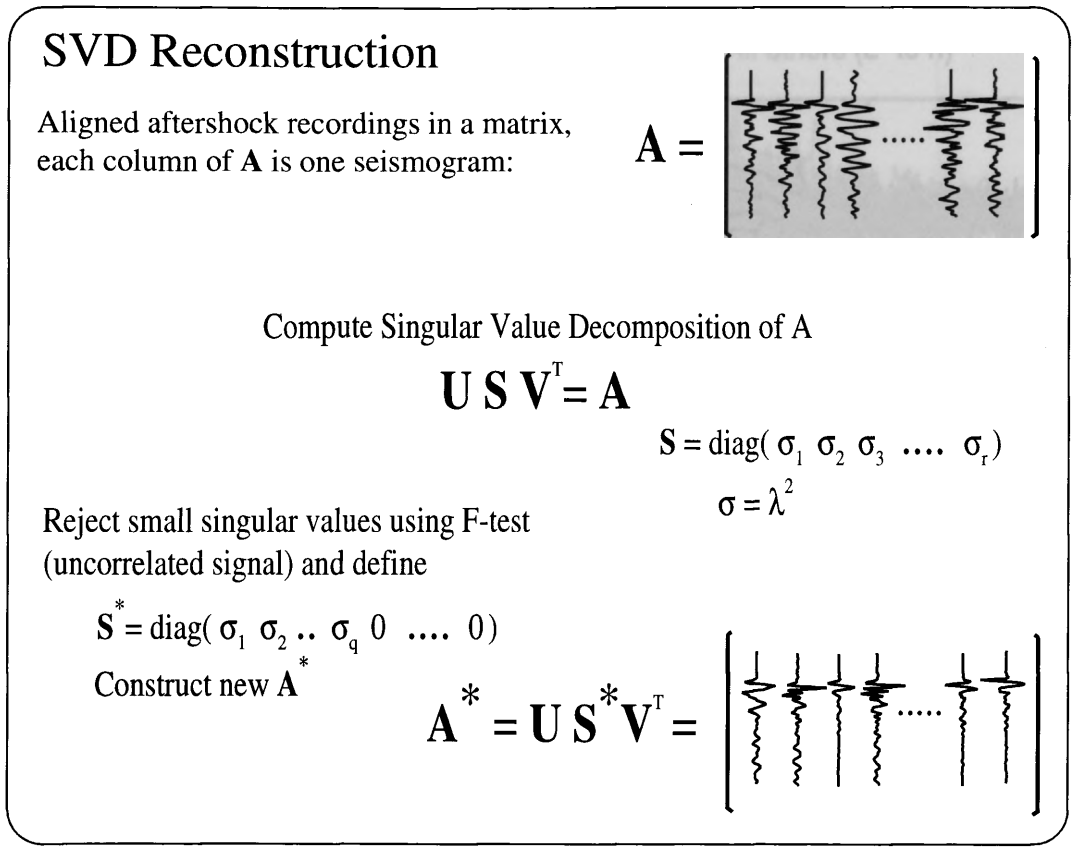

Figure 5.7. Schematic illustration of SVD reconstruction method. See text for description.

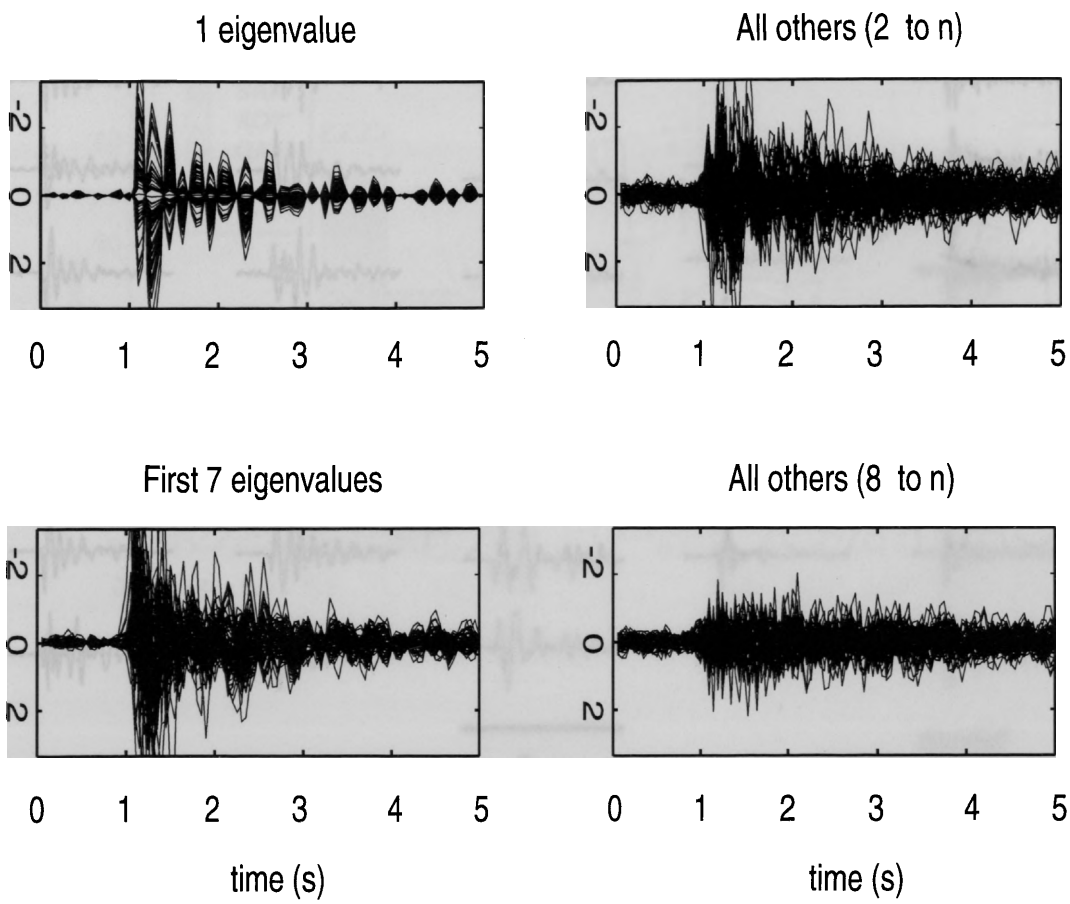

Figure 5.8. Example of eigenvalue filtering at station SAR. In each panel, the columns (seismograms) of the reconstructed matrix are superimposed. The top left panel is a reconstruction using just the largest eigenvalue, the top right is using all but the largest eigenvalues (2 to n). The bottom left reconstruction uses the first seven eigenvalues, and the bottom right uses all others (8 to n). The *S*-wave arrival is aligned 1 s after the start of the seismogram. Energy in the first 1 s is *P*-wave coda and ground noise that should be highly uncorrelated, and hence should not be retained in the reconstruction using the large eigenvalues.

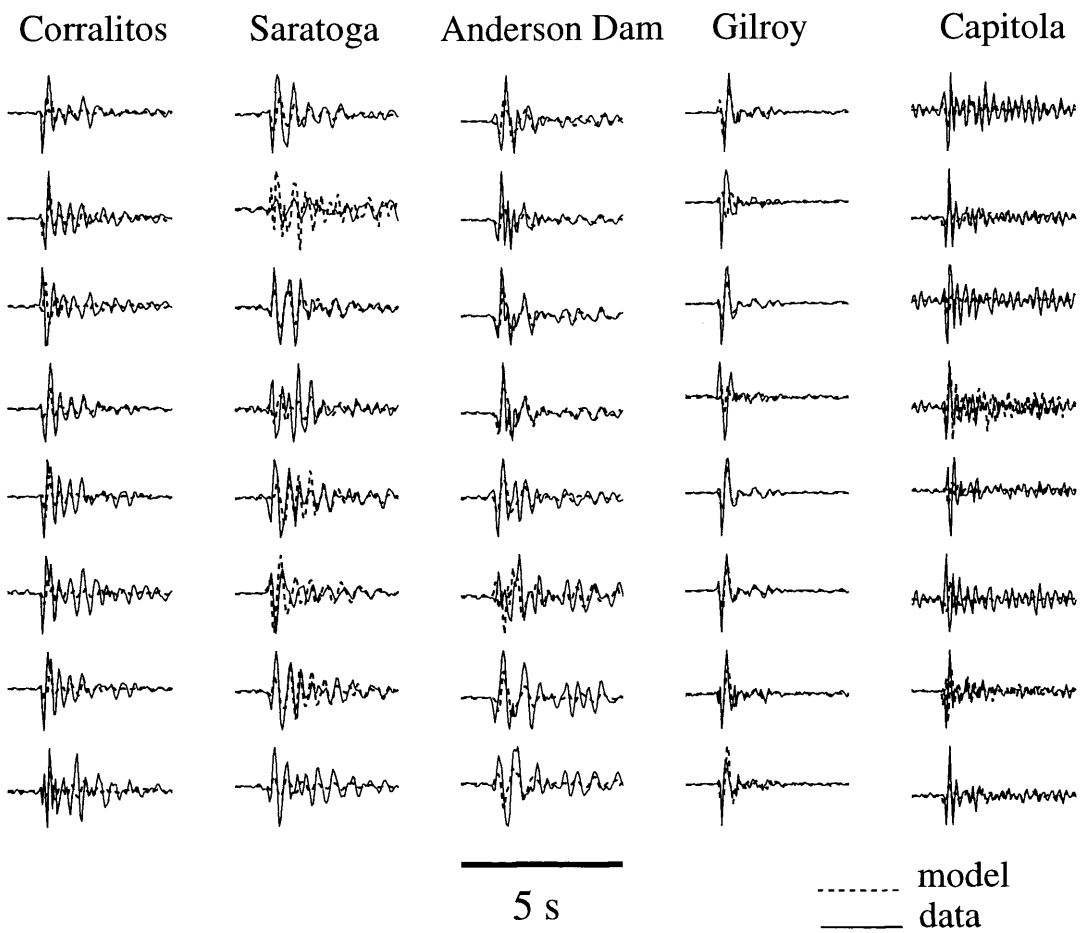

Figure 5.9. Fit to the data seismograms reconstructed using only the largest singular values. Select horizontal displacement seismograms are shown for each station. The event-station pairs are the same as those shown in Figure 5.4. Note the decrease in energy arriving during the first 1 s as compared to Figure 5.4.

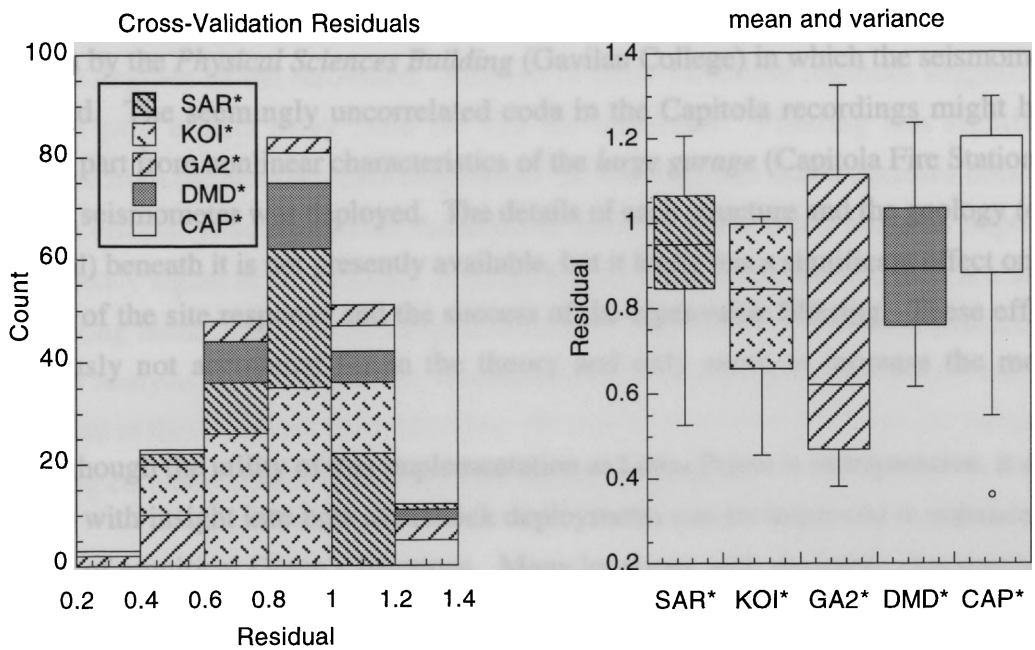

Figure 5.10. Cross-validation residuals for the five stations using reconstructed waveforms obtained by retaining the most significant singular values. The histogram (*left*) and distribution (*right*) show that the interpolated seismograms are better correlated with the data, compared to Figure 5.5, with greater variability between stations. The mean is shown by a horizontal line, and 1 and 2 standard deviations of the mean are shown by error bars.

CAP have nearly the same average residual. DMD is the only free-field site where the seismometer was buried in soil. At the four other sites the seismometers were deployed on the floor of small (1-story) structures. A structure can influence the recorded spectrum in unpredictable ways, decreasing the amplitude at some frequencies and increasing it at others. For instance, the simple pulse-like waveforms at Gilroy could be a result of attenuation by the *Physical Sciences Building* (Gavilan College) in which the seismometer was housed. The seemingly uncorrelated coda in the Capitola recordings might have resulted in part from nonlinear characteristics of the *large garage* (Capitola Fire Station) in which that seismometer was deployed. The details of each structure and the geology (e.g., fill material) beneath it is not presently available, but it likely has a significant effect on the coherency of the site response and the success of the eigenvalue filtering. These effects are obviously not accounted for in the theory and only serve to increase the model residuals.

Although the utility of this implementation at Loma Prieta is unimpressive, it does provide us with insight into how aftershock deployments can be improved to enhance the usefulness of empirical Green's functions. Many locations with desirable characteristics could have been used if more events had been recorded at them; in many cases, the deployment lasted only a short time, sometimes less than one week. Moreover, it is unfortunate that more seismometers were not deployed at free-field sites. There were many free-field strong motion instruments that had excellent mainshock records but were not co-located in the aftershock deployment. Finally, even if the site transfer-functions had been more successful at interpolating seismograms, the narrowband response of the recorded data would have limited their usefulness in modeling mainshock seismograms. Use of broadband seismometers is essential for the full exploitation of the potential of small earthquake seismograms. These factors face obvious economic and logistical obstacles, but they are necessary if we are to increase the use of recorded waveforms as empirical Green's functions.

Conclusions

The site transfer-function models fit the data reasonably well but do a poor job of interpolating missing seismograms. Two possible explanations for this are that the quantity of data is insufficient to characterize the site, or that uncertainties in the source parameters degrade model resolution. Analysis of cross-validation residuals suggests it is likely that path effects away from the site are important. Filtering less significant eigenvalues from the recorded data emphasizes the site-response and suppresses noise and some path effects, yielding smaller residuals at some stations, but it discards important high-frequency signal in the process. In summary, we find (1) cross-validation is a useful for estimating model variance in complex inversion procedures that are not amenable to theoretical analysis, (2) a simple site response model is inadequate for Green's function interpolation at these stations using this data, (3) eigenvalue filtering is a simple technique for isolating common effects associated with the site response.

Chapter 6 — Seismic Measurements of Earthquake Nucleation

Abstract

Near-source seismograms reveal that the first *P*-wave arrival from earthquakes is characteristically weak and erratic, and is followed subsequently by linear growth in ground velocity that can be modeled as a simple circular crack expanding at constant rupture velocity with uniform stress drop. The seismograms provide empirical evidence for a period of quasi-dynamic nucleation preceding dynamic earthquake rupture that is also predicted by theoretical models of fracture nucleation and growth and measured in laboratory experiments designed to simulate faulting. In this chapter, the duration of this seismic nucleation phase is measured objectively using the amplitude of the moment-jerk function, which is proportional to the product of dynamic stress drop and rupture velocity cubed for the circular crack model. New measurements are made for 24 earthquakes from three sources (the 1994 M_W 6.7 Northridge aftershock deployment, the Chiba accelerometer array near Tokyo, and the Global Seismic Network), and for 25 earthquakes examined previously by *Ellsworth and Beroza* [1995]. The seismograms are from stations located close to the earthquake (typically within one source-depth) and the wave propagation direction is close to vertical. Durations based on the moment-jerk amplitude confirm a scaling relationship identified by *Ellsworth and Beroza* [1995] for the same 25 earthquakes: the moment-jerk during initiation is smaller than the rest of the earthquake, and the duration of the seismic nucleation phase increases with the moment of the subsequent earthquake. In this study, the duration of the seismic nucleation scales with the seismic moment raised to the power 0.2.

6.1 Introduction

The best current models of earthquake rupture (based on fracture mechanics theory and laboratory experiments) suggest that a slow nucleation phase (low stress drop fracture occurring at velocities much lower than the elastic wave speed) should precede dynamic crack growth. If such a nucleation phase exists for earthquakes, it would be difficult to measure with a seismometer because its amplitude would be small and it might radiate no detectable high-frequency energy. Observation of this nucleation phase and the ability to explain it in terms of the timing and spatial association with the following earthquake could provide key evidence on the plausibility of short-term earthquake prediction.

There is recent seismic evidence from high-dynamic-range recording systems that many earthquakes do have an early seismic signature that is weak, which might represent an observable late stage of slow premonitory sliding in a nucleation zone that is otherwise aseismic [*Iio*, 1992, 1995; *Beroza and Ellsworth*, 1995; *Ellsworth and Beroza*, 1995 – hereafter referred to as *BE-EB*, 1995]. This observed weak beginning, termed the *seismic nucleation phase*, could be related to observations of fracture nucleation in controlled laboratory experiments [e.g., *Dieterich*, 1979; *Ohnaka et al.*, 1986; *Ohnaka and Kuwahara*, 1990; *Kilgore et al.*, 1993; *Blanpied et al.*, 1995], and properties of earthquake nucleation predicted by theoretical models [e.g., *Andrews*, 1976; *Rice*, 1980, 1992; *Das and Scholz*, 1981; *Dieterich*, 1986, 1992; *Rice and Gu*, 1983; *Ohnaka and Yamashita*, 1989; *Ohnaka*, 1993].

The model proposed by *Dieterich* [1986] suggests that slow, stable slip occurs until a critical crack radius, r_c, is exceeded. The critical radius is a function of the normal stress, loading conditions, and constitutive parameters that include the characteristic slip distance, D_c:

$$r_c = \frac{7\pi G D_c}{24\sigma\xi}, \tag{6.1}$$

where G is the shear modulus, σ is the normal stress, and ξ is a parameter that depends on specific constitutive parameters and experimental conditions. In a laboratory experiment designed to simulate strike-slip faulting, *Dieterich* [1986] measured an upper limit for D_c of 50 μm for a r_c that was estimated to be 5.3 m. Extrapolation of these measurements to the scale of large earthquakes suggests that D_c could reach 50 mm for r_c

= 5.3 km. In the experiment, slip that occurred in the final stages of the stable slip interval was roughly five times the amplitude of D_c; that is, for r_c = 5.3 km, the preslip could be as large as 25 cm [*Dieterich*, 1986], which might be detectable using near-source seismometers.

It is highly uncertain if extrapolation of the experimental results (to earthquake scale-lengths) is valid, or whether the laboratory conditions simulate all relevant earthquake physics (e.g., slip at high rupture velocity), nonetheless considerable effort has been focused on observing premonitory slip, in particular using borehole and long baseline strainmeters that detect slow, episodic deformation [*Agnew and Wyatt*, 1989; *Johnston et al.*, 1990]. Strainmeters are designed to measure long-period deformation, such as small amplitude displacement occurring hours or days before an earthquake. To date, no such premonitory deformation has been observed with these instruments [*Agnew and Wyatt*, 1989; *Johnston et al.*, 1990; *Wyatt et al.*, 1994].

At shorter time-scales (from seconds to hours), it is well-known that many large earthquakes are preceded by foreshocks. These observations have motivated many studies that examined the spatial and temporal relationships between foreshocks and mainshocks [e.g., *Das and Scholz*, 1981; *Jones*, 1984; *Ohnaka*, 1993; *Abercrombie et al.*, 1995; *Dodge et al.*, 1995]. The great 1960 M_W 9.5 Chilean earthquake is a striking example that included both traditional foreshocks (i.e., typical stress drops and rupture velocities) [*Cifuentes*, 1989], and slow deformation that radiated relatively low-frequency energy [*Kanamori and Cipar*, 1974; *Cifuentes and Silver*, 1989]. As discussed by *Dodge et al.* [1995], the term *foreshock* is not defined precisely in terms of its spatial and temporal association with the ensuing mainshock. They used *foreshocks in the strict sense* to denote events occurring a few hours or days prior to and within a few source dimensions of the mainshock. In the present study, the term foreshock implies a seismic event occurring in the few minutes before the mainshock in approximately the same location. Recent earthquakes in California with this type of immediate foreshock include 1989 M_W 6.9 Loma Prieta [*Wald et al.*, 1991], 1992 M_W 7.3 Landers [*Abercrombie and Mori*, 1994; *Dodge et al.*, 1995], and 1994 M_W 6.7 Northridge [*BE-EB*, 1995]. Other examples are documented in *BE-EB* [1995].

BE-EB [1995] suggested that these immediate foreshocks may represent a seismic nucleation phase; that is, the seismic signature of an intermediate stage following aseismic nucleation and preceding dynamic rupture – a period *Ohnaka* [1993] called quasi-dynamic

nucleation. They examined 30 earthquakes ranging in magnitude from 3 to 8 and detected a seismic nucleation phase for each. In some cases, the seismic nucleation phase began with a foreshock that was distinct in time from the mainshock (by seconds or fractions of a second), in others it was manifested as weak but continuous growth of the initial *P*-wave arrival. In all cases, the moment rate during this nucleation phase was observed to be lower than the moment rate at the beginning of the mainshock. In addition, they observed that the size and duration of the seismic nucleation phase increased with the size of the subsequent earthquake, suggesting that properties of the nucleation process may influence the ultimate earthquake; i.e., the longer the duration of the seismic nucleation phase, the larger the mainshock moment. They further argued that the size of the nucleation zone, and the displacement amplitude during nucleation, also increase with mainshock size.

A shortcoming of the approach used by *BE-EB* [1995] was that the measurement of the nucleation duration was determined subjectively; hence, the implied scaling relationships were uncertain. The error associated with identifying the first *P*-wave arrival (the beginning of the seismic nucleation phase) is usually negligible for seismograms recorded on broadband, high-dynamic-range systems – if the first arrival is distinct from the noise, it can be measured with a precision equal to the sampling interval. The more difficult procedure is defining the end of the nucleation phase and the beginning of normal dynamic rupture in the mainshock, which *BE-EB* [1995] termed the *breakaway* phase.

There are two ways to measure the breakaway time. The first seeks to identify an increase of moment acceleration that is large relative to the rest of the earthquake beginning; *BE-EB* [1995] picked the breakaway at the time when the seismic moment acceleration increased abruptly. The second approach seeks to identify an increase in moment acceleration that is large in an absolute sense. A potential problem with this second approach is that it treats all earthquakes similarly and does not account for known differences in source characteristics (e.g., stress drop, rupture velocity, displacement rise-time, etc.). Despite this potential difficulty, we find that an absolute level of moment acceleration results in a measurement of breakaway for the same earthquakes examined in *Ellsworth and Beroza* [1995] that are generally similar over all magnitudes. This suggests that the amplitude of moment acceleration is low, in an absolute sense, during the beginning of most earthquakes, and that the duration of this period is longer for larger earthquakes.

In addition to reexamining 25 of the 30 events presented in *Ellsworth and Beroza* [1995], we present new measurements of 24 earthquakes, some of which occur at greater depths (50 to 150 km) allowing possible dependencies attributable to source depth to be examined. For all earthquakes, we calculate the moment rate and moment jerk as a function of time, and define breakaway at the time when the moment jerk exceeds a prescribed level; this measurement defines the seismic nucleation phase in a purely objective manner.

Many studies have estimated the average stress drop of earthquakes [e.g., *Hanks and Wyss*, 1972; *Thatcher and Hanks*, 1973; *Kanamori and Anderson*, 1975; *Hanks and McGuire*, 1981; *Boatwright*, 1984; *Cocco and Rovelli*, 1989; *Mori and Frankel*, 1990; *Abercrombie and Leary*, 1993]. In these studies, either the static stress drop is calculated from the source dimension, or the dynamic stress drop is determined by measuring the initial slope of the velocity *P*-waveform or the root-mean-square (rms) acceleration of the *S* wave. In each case the stress drop determined is an average for the earthquake; temporal variations of stress release are not established.

In this paper we interpret the moment jerk in terms of the time-varying dynamic stress drop. Because this interpretation, which is predicated on an idealized circular crack model that grows at constant rupture velocity, breaks down at later times, this approach can only be appropriate for the initial *P* wave and the beginning of earthquake rupture. For the earthquakes examined, the median maximum stress drop is about 300 bars. The maximum stress drop does not depend on the earthquake magnitude and does not obviously depend on the earthquake depth. Using a stress drop of 50 bars (moment jerk of 1.4×10^{18} N-m/s^3) as the threshold yields measurements for the duration of the seismic nucleation phase that agree most closely with the picks made by *Ellsworth and Beroza* [1995] for the same earthquakes; however, the nucleation durations are shorter for the largest earthquakes. A 50 bar stress drop is a typical value for "average" earthquakes [*Kanamori and Anderson*, 1975; *Abercrombie and Leary*, 1993]. Using a higher stress drop (higher moment jerk) as the threshold yields measurements that agree better at large magnitudes, but there is less data because some events never reach the threshold and the nucleation phase is thus undefined. Calculation of the moment-jerk function requires a single seismogram; when multiple seismograms are available the measurement uncertainty can be assessed.

6.2 Examples of the Seismic Nucleation Phase

Historically, most near-source data have been recorded on analog seismographs with insufficient dynamic range and bandwidth to capture the initiation process. For most large earthquakes, the limited dynamic range of near-source high-gain seismographs is exceeded shortly after the *P*-wave arrival. Since the velocity structure beneath the site is rarely known in detail, it is difficult to relate the beginning of rupture measured on a high-gain instrument with seismograms from other locations. On the other hand, most low-gain instruments are triggered by the ground motion amplitude and can miss the first-arriving *P*-wave if its amplitude is small. Digital recording systems with high dynamic range (16-bit or better) allow measurement of the initial *P* wave and the subsequent mainshock pulse.

At teleseismic distances the seismic nucleation phase is too small to be observed for most earthquakes; at regional distances complex wave propagation effects (e.g., refractions) can distort the *P*-wave arrival. Observing an uncorrupted direct *P*-wave is most assured when the seismometer is within one source-depth of the epicenter where the wave propagation direction is close to vertical. In this geometry, propagation complexities are minimized and the theoretical Green's function used to derive the moment-rate function is accurate over a wide frequency range – from static displacement to the highest frequencies recorded. Because the nucleation phase is characteristically weak, clear detection requires a low-noise environment and a high-dynamic-range (i.e., 16-bit or better) recording system. In addition, seismometers with broadband response (i.e., 0.01 to 50 Hz) are required to obtain broadband moment-rate functions.

Three examples of the seismic nucleation phase measured within one source-depth are shown in Figure 6.1. In each example the seismogram is from a Northridge aftershock, measured with a STS-2 seismometer, and sampled at 200 sps by a 16-bit recording system. The pair of velocity seismograms are plotted at the same time scale but the magnification is different; the onset of the seismic nucleation phase is marked with an arrow. The first example in Figure 6.1 is a 12 km deep M 4.9 event recorded at an epicentral distance of 9 km. It has a weak beginning with a duration of approximately 0.2 s. The first half-second is enlarged showing that the *P*-wave arrival is weak initially and then grows linearly in time as predicted by a self-similar model of rupture at constant stress drop and rupture velocity.

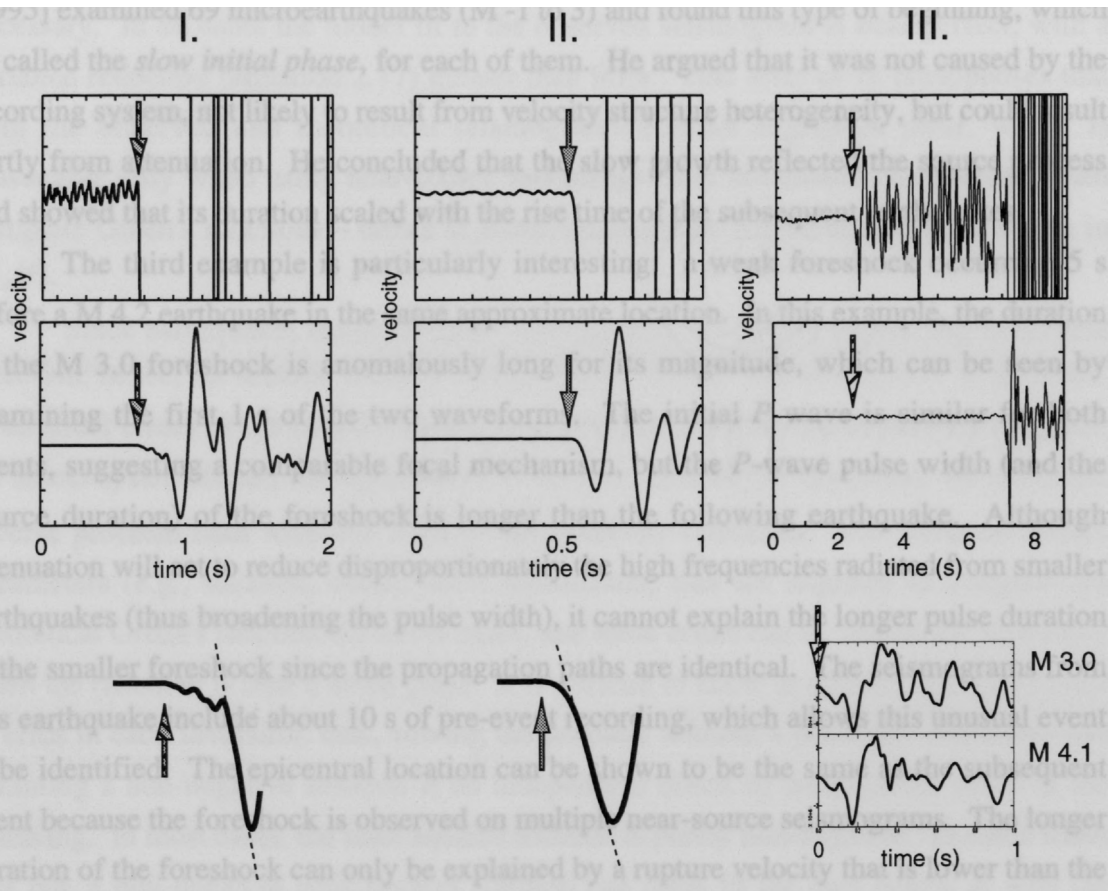

Figure 6.1. Three varieties of the seismic nucleation phase recorded on STS-2 seismometers with 16-bit dynamic range. In each example, two velocity seismograms are plotted at the same time scale but with different magnification. The top seismograms show the time of the first-arriving *P*-wave; the middle seismograms show that pick relative to the *P*-wave pulse; the bottom panel is yet an even larger enlargement of the *P*-wave arrival showing the eventual linear growth with time. In the third example, the bottom panel shows the *P* waveforms from the foreshock and the subsequent earthquake at the same time scale. Note the longer duration of the *P*-wave pulse for the M 3.0 foreshock compared to the M 4.2 event.

In the second example in Figure 6.1, the seismic nucleation phase is more subtle. In this recording the velocity grows continuously but approximately 0.05 s elapses before the growth is linear. It has been suggested that this emergent *P*-wave arrival could be caused by wave propagation effects (e.g., forward scattering), anelastic attenuation, or the response of the instrument, rather than reflect slow initial growth of the earthquake. *Iio* [1995] examined 69 microearthquakes (M -1 to 3) and found this type of beginning, which he called the *slow initial phase*, for each of them. He argued that it was not caused by the recording system, not likely to result from velocity structure heterogeneity, but could result partly from attenuation. He concluded that the slow growth reflected the source process and showed that its duration scaled with the rise time of the subsequent earthquakes.

The third example is particularly interesting: a weak foreshock occurring 5 s before a M 4.2 earthquake in the same approximate location. In this example, the duration of the M 3.0 foreshock is anomalously long for its magnitude, which can be seen by examining the first 1 s of the two waveforms. The initial *P* wave is similar for both events, suggesting a comparable focal mechanism, but the *P*-wave pulse width (and the source duration) of the foreshock is longer than the following earthquake. Although attenuation will act to reduce disproportionately the high frequencies radiated from smaller earthquakes (thus broadening the pulse width), it cannot explain the longer pulse duration of the smaller foreshock since the propagation paths are identical. The seismograms from this earthquake include about 10 s of pre-event recording, which allows this unusual event to be identified. The epicentral location can be shown to be the same as the subsequent event because the foreshock is observed on multiple near-source seismograms. The longer duration of the foreshock can only be explained by a rupture velocity that is lower than the following earthquake.

6.3 Moment Rate, Moment Jerk, and Stress Drop

The temporal growth of an earthquake can be described by the point-source moment-rate function, $\dot{M}_0(t)$. The moment-rate function is obtained by deconvolving a theoretical Green's function from an observed *P*-wave seismogram. We use half-space Green's functions that include the near-field contribution [*Johnson*, 1974], and fault plane solutions determined from first-motion data or teleseismic waveform inversions. Representing the structure as a half-space is an approximation but is reasonable given the simple propagation geometry. Green's functions calculated for layered velocity models

[*Saikia*, 1994] produce similar $\dot{M}_0(t)$. The deconvolution is solved in the time domain using both standard least-squares and non-negative least-squares. Rather than deconvolve the instrument response from the recorded seismograms, we convolve it with the Green's function because the result is more stable at high frequency. For some earthquakes a weak smoothing constraint is applied to stabilize the inversion, but for most no smoothing is necessary. In all cases the model fit to the observed seismogram is near-perfect, with a variance reduction (equation 2.17) greater than 90%. This level of fit presupposes that both the observed and theoretical seismograms contain negligible error, which is reasonable only when using near-source recordings from broadband seismometers and complete Green's functions – errors in either seismogram will be mapped into errors in $\dot{M}_0(t)$.

Since earthquakes occur on faults with friction, we do not expect slip to reverse direction; hence, the seismic moment and the $\dot{M}_0(t)$ should be non-negative at all times. Even small errors in the Green's function can result in a $\dot{M}_0(t)$ that is partially negative. To assess systematically the significance of error in each $\dot{M}_0(t)$ inversion, we solve the inverse problem both with and without the positivity constraint. For instance, source parameters (e.g., location, depth, focal mechanism) that are required to compute the theoretical Green's function are never exact, and these errors can be important, especially when the radiation is near a nodal plane. It is difficult to know in advance the importance of error in each inversion; thus, solving the problem without a positivity constraint and obtaining a non-negative solution is an independent check of assumptions made in the modeling. In most cases, the least-squares solution is purely non-negative. In cases when it is not, a non-negative least-squares solution can often fit the data nearly as well (as measured by the variance reduction). As a further check on the assumptions, the seismic moment obtained by integrating $\dot{M}_0(t)$ should agree closely with independent estimates.

In the dynamic solution for a circular dislocation expanding at constant rupture velocity with constant stress drop, the fault area grows as time squared and the seismic moment grows as time cubed. Since the far-field displacement is proportional to the moment rate, the far-field velocity seismogram will grow linearly with time until the rupture growth is inhibited by either strength heterogeneities or the finite size of the fault (i.e., the fault starts healing) [*Kostrov*, 1964; *Madariaga*, 1976]. This simple dislocation model is useful for interpreting seismograms and explaining them in terms of earthquake rupture dynamics. *BE-EB* [1995] used quadratic growth in $\dot{M}_0(t)$ to define the end of the

seismic nucleation phase (breakaway). They did this by identifying the first abrupt linear growth in the moment acceleration, $\ddot{\mathrm{M}}_0(t)$.

The static stress drop, $\Delta\sigma$, of a circular fault is

$$\Delta\sigma = \frac{7\pi}{16}\frac{\mu\bar{u}}{a}, \tag{6.2}$$

where μ is rigidity and a is the radius [*Eshelby*, 1957]. The seismic moment can then be written

$$\mathrm{M}_0 = \frac{16}{7}\Delta\sigma a^3 \tag{6.3}$$

(using the expression $\mathrm{M}_0 = \mu A\bar{u}$), where A is the fault area and $\bar{u}$ is the average displacement. *Boatwright* [1980] used equation 6.3 to express the moment in terms of the dynamic stress drop (or effective stress), τ_e,

$$\mathrm{M}_0 = \left(\frac{2\pi\tau_e a^3}{3}\right)\frac{C(v_r/\beta)}{v_r/\beta} \tag{6.4}$$

where v_r is the rupture velocity and β is the shear-wave speed [*Brune*, 1970]. $C(v_r/\beta)$ is called the Kostrov function [*Dahlen*, 1974] and is approximately equal to v_r/β for most earthquakes [*Boatwright*, 1980]. If we make this assumption, then the ratio of static stress drop to dynamic stress drop is

$$\frac{\Delta\sigma}{\tau_e} = \frac{7\pi}{24}. \tag{6.5}$$

and after substituting $v_r t$ for a, equation 6.4 becomes

$$\mathrm{M}_0(t) = \frac{2\pi}{3}\tau_e v_r^3 t^3. \tag{6.6}$$

Differentiating with respect to time yields an expression for the moment-rate

$$\dot{M}_0(t) = 2\pi\,\tau_e\,v_r^3\,t^2. \tag{6.7}$$

Two more time-derivatives yields the moment-jerk function, $\dddot{M}_0(t)$:

$$\dddot{M}_0(t) = 4\pi\,\tau_e\,v_r^3. \tag{6.8}$$

In words, for a radially expanding rupture observed in the perpendicular direction, the moment jerk is proportional to the product of the dynamic stress drop and the rupture velocity cubed. Using this expression, small $\dddot{M}_0(t)$ (e.g., the seismic nucleation phase) implies either low v_r, or low τ_e, or both, relative to the mainshock. At constant v_r, the dynamic stress drop is proportional to $\dddot{M}_0(t)$.

A fourth-order central difference formula with error proportional to h^4 is used to differentiate $\dot{M}_0$:

$$\dot{f}_j = \frac{f_{j-2} - 8f_{j-1} + 8f_{j+1} - f_{j+2}}{12h}, \tag{6.9}$$

where h is the sampling interval. Since $\dot{M}_0$ is differentiated twice, the result depends strongly on the accuracy of $\dot{M}_0$. A narrow triangular smoothing operator is applied before each derivative, which improves the stability of the result but also reduces temporal resolution (measuring the average stress drop for the entire earthquake is an extreme example of smoothing). Although the absolute stress drop estimates are dependent on the particular smoothing used, the relative amplitudes within $\dddot{M}_0$ are not. It is possible to get an idea of the variance of $\dddot{M}_0$ by making independent observations of the same earthquake using seismograms recorded at different locations.

If earthquake nucleation is indeed characterized by unusually low dynamic stress drop, it is sensible to define the end of nucleation at a time when $\dddot{M}_0(t)$ is no longer unusual. In this chapter we calculate $\dddot{M}_0(t)$ for each earthquake and interpret the results in terms of varying stress drop (by assuming that rupture velocity is constant). The assumption of constant rupture velocity is made for simplicity; the measured variations in $\dddot{M}_0(t)$ could represent variations in rupture velocity, stress drop, or both. In reality the rupture velocity is probably not constant [*Sato*, 1994]; however, it can be argued that it contributes less to variability in $\dddot{M}_0(t)$ than does variation in τ_e [*Quin*, 1990; *Mikumo and*

Miyatake, 1993, 1995]. Values of $\dddot{M}_0(t)$ are listed in Table 6.1 for representative combinations of τ_e and v_r; for these eight examples, $\dddot{M}_0$ spans more than an order of magnitude. With the present approach, it cannot be determined whether variations in $\dddot{M}_0(t)$ are attributable to rupture velocity or stress drop – in this study variations in $\dddot{M}_0(t)$ are interpreted as variations in stress drop, but this choice is arbitrary.

Table 6.1. Rupture Velocity and Stress Drop

Case	v_r (km/s)	τ_e (bars)	$\dddot{M}_0$ ($\times 10^{17}$ N-m/s^3)
1	2.8	6	2
2	2.8	10	3
3	2.8	30	8
4	2.8	60	16
5	2.8	100	28
6	2.2	20	3
7	2.8	20	6
8	3.2	20	8

In studies where direct measurement of v_r is possible, it is found that the rupture velocity is typically 70 to 80% of the shear wave velocity [*Geller*, 1976]; for crustal earthquakes the rupture velocity is usually near 2.8 km/s. There is great variability in estimates of static stress drop for earthquakes [*Hanks and Thatcher*, 1972; *Hanks and Wyss*, 1972; *Thatcher and Hanks*, 1973; *Kanamori and Anderson*, 1975; *Geller*, 1976; *Hanks and McGuire*, 1981; *Cocco and Rovelli*, 1989; *Mori and Frankel*, 1990; *Abercrombie and Leary*, 1993]. Typical values fall in the range from 1 to 100 bars (10 bars = 1 MPa), but estimates can range from less than 1 bar to over 1,000 bars. The rupture area of large earthquakes can be estimated using aftershocks but it is difficult to measure accurately the dimension of small earthquakes. Since estimates of static stress drop have a cube-root dependence on the source area, errors in the source dimension produce large errors in the corresponding estimates of static stress drop [*Boatwright*, 1984]. *Abercrombie and Leary* [1993] used borehole seismometers to demonstrate that near-surface attenuation can lower the corner frequency (used to infer source size) for seismograms recorded at the Earth's surface. Using borehole seismograms they detected source dimensions of less than 10 m and found static stress drops ranging from 1 to 1000

bars. They also found that the level of stress drop did not depend on earthquake size; earthquakes appeared self-similar over the range M -2 to 8.

Dynamic stress drop is an empirical measurement of the efficiency of energy radiation that does not depend on rupture area. *Boatwright* [1984] compared the static stress drop to the dynamic stress drop for eight aftershocks of the 1975 Oroville, California, earthquake recorded at multiple seismometers. By obtaining multiple estimates of each event, he was able to express the variance associated with each stress drop measurement. Overall, he found that the dynamic stress drop estimates were larger (~50%) and had smaller variance than the corresponding static estimates.

Since the *P*-wave displacement seismogram is proportional to the moment rate in the far-field [*Aki and Richards*, 1980], a *P*-wave velocity seismogram is proportional to the moment acceleration. When the Green's function is a simple impulse (in displacement), the dynamic stress drop can thus be estimated from the slope of the *P*-wave arrival on a velocity seismogram, or equivalently, by the rms acceleration. This approach yields the average dynamic stress drop and is only appropriate in the far-field. In this study, we use a time-varying characterization of dynamic stress drop and include near-field contributions (see Section 2.4).

We solve for the moment-rate function of 24 M 4 to 7 earthquakes (listed in Table 6.2) obtained from three sources: aftershocks of the 1994 Northridge earthquake; earthquakes recorded by the Chiba borehole array near Tokyo, Japan; and earthquakes that occurred adjacent to stations of the Global Seismic Network (GSN). In most cases the recording distance is less than one source-depth and the wave propagation is near-vertical. We use these moment-rate functions, together with 25 events from *Ellsworth and Beroza* [1995] (listed in Table 6.3), to estimate the time-varying dynamic stress drop for the beginning of 47 earthquakes (two events are included in both Tables 6.2 and 6.3).

6.4 Moment-Rate Functions

6.4.1 Northridge Aftershocks

Nine Northridge aftershocks (M 4.1 to 4.6) are examined in this study. They all occurred at depths less than 17 km – the locations, depths, magnitudes, and focal mechanisms are from *Hauksson et al.* [1995]. Figure 6.2 shows a map view of the aftershock locations and the close-in stations that recorded them. Ground motion was

Table 6.2. Earthquake Source Parameters

id	date	event	M	M_0 (N-m)	r_e (km)	z (km)	υ_{20} (s)	υ_{50} (s)	υ_{80} (s)	γ (s)	τ_{max}
1	21-Jan-1994	N1839 scfs	4.5	6.3e+15	11.1	10.6	0.17	0.18	0.20	0.33	160
2a	21-Jan-1994	N1842 scfs	3.2	7.1e+13	~10.0	~7.9				0.18	40
2b	21-Jan-1994	N1842 scfs	4.2	2.2e+15	10.0	7.9	5.03	5.03	5.03	0.18	1060
3	21-Jan-1994	N1852 nhfs	4.3	3.2e+15	12.5	8.9	0.02	0.02	0.02	0.21	1600
4	23-Jan-1994	N0855 scfs	4.1	1.6e+15	10.3	9.7	0.10	0.20	0.20	0.19	170
5	24-Jan-1994	N0415 pwgb	4.6	8.9e+15	14.0	8.9	0.05	0.06	0.06	0.29	490
6	24-Jan-1994	N0550 pwgb	4.3	3.2e+15	8.2	12.0	0.01	0.05	0.11	0.21	160
8	27-Jan-1994	N1719 nhfs	4.6	8.9e+15	17.7	16.3	0.04	0.04	0.04	0.30	550
9a	3-Feb-1994	N1623 pdam	2.4	3.8e+12	~5.4	~8.9				0.16	3
9b	3-Feb-1994	N1623 pdam	4.3	3.2e+15	5.4	8.9	3.51	3.51	3.51	0.16	470
10	6-Feb-1994	N1319 scfs	4.1	1.6e+15	12.8	11.9	0.02	0.05	0.07	0.22	90
11	27-Feb-1983	Chiba 8307	5.9	8.1e+17	35.2	72.	0.10	0.15	0.18	0.8	290
12	17-Dec-1984	Chiba 8420	5.0	3.5e+16	5.6	78.	0.01	0.01	0.01	0.23	420
13	8-Jun-1985	Chiba 8510	5.2	7.1e+16	15.1	64.	0.01	0.01	0.01	0.45	240
14	4-Oct-1985	Chiba 8519	6.0	8.8e+17	27.7	78.1	0.01	0.38	0.40	1.9	1240
15	17-Dec-1987	Chiba 8722	6.7	1.2e+19	44.7	58.	0.01	0.01	0.01	>3	1350
16	16-Jan-1988	Chiba 8806	5.0	3.5e+16	34.7	34.2	0.32	0.33	0.34	0.9	540
17	18-Mar-1988	Chiba 8816	5.6	3.1e+17	42.2	96.	0.01	0.01	0.01	1.7	240
18	19-Feb-1989	Chiba 8901	5.6	2.6e+17	47.7	55.	0.01	0.02	0.05	0.7	250
19	2-Jan-1990	Guam	5.8	5.8e+17	53.1	147.	0.58	0.62	0.66	1.9	350
20	12-Jun-1991	Erimo, Japan	5.8	5.2e+17	84.1	112.	0.64	0.78	0.88	2.2	110
21	27-May-1992	S. Karori, NZ	5.9	8.6e+17	95.5	85.	0.12	0.16	0.18	1.5	370
22	15-Jan-1993	Erimo, Japan	7.6	2.7e+20	154.	100.	1.46	1.52	1.88	1.5	260
23	25-Mar-1993	Erimo, Japan	6.0	1.1e+18	37.3	33.	0.04	0.10	1.50	3.4	160
24	11-Aug-1993	Guam	6.0	1.2e+18	96.0	56.	0.58	1.98	2.08	2.1	140
25	16-Aug-1993	Guam	6.0	9.7e+17	71.1	33.	0.08	0.12	0.16	2.1	200

r_e epicentral distance; z depth

υ_{50} duration of seismic nucleation phase determined with a 50 bar threshold

γ total earthquake duration minus υ_{50} (when defined)

τ_{max} maximum dynamic stress drop during earthquake beginning

recorded at 200 samples per second (sps) on 16-bit data loggers; the seismometer was either a STS-2 or a force balance accelerometer (FBA). Seismograms from the STS-2 instruments have superior broadband response and are used to obtain the $\dot{M}_0(t)$. Solving for $\dot{M}_0(t)$ at multiple stations allows the associated uncertainty to be estimated and reveals single-station bias that can result from rupture directivity.

Two example deconvolutions are shown in Figure 6.3: the initial *P*-wave arrival is unambiguous and equated with $t = 0$. In the least-square inversion, the data vector is the vertical component seismogram, the kernel matrix is comprised of a single Green's function seismogram shifted one time-sample in each subsequent column, and the model is $\dot{M}_0(t)$. The model and the fit-to-data are shown in Figure 6.3; the agreement is almost perfect. In the examples shown, the solutions obtained with least-squares and non-negative least-squares are essentially identical. In most cases, $\dot{M}_0(t)$ is a simple pulse that can be differentiated stably provided that $\dot{M}_0(t)$ is sampled finely. The moment acceleration is also shown in Figure 6.3; the slope is proportional to stress drop.

6.4.1.1 Low Stress Drop Foreshocks

Figure 6.4 shows seismograms and the corresponding $\dot{M}_0(t)$ for two pairs of events 2a & 2b, and 9a & 9b, the parameters of which are listed in Table 6.2. Event 2a is a M 3.0 foreshock that occurred 4.96 s before event 2b (M 4.2) in approximately the same epicentral location – the 4.96 s separation between the two *P*-wave arrivals is constant for the few stations at which it could be measured (seismograms from events 2a & 2b were used in Figure 6.1). Event 9a is a M 2.4 event that occurred 3.50 s before event 9b (M 4.3) in approximately the same epicentral location. A similar focal mechanism for events 2a & 2b is suggested by the similar waveform at station SCFS, but this is not the case for the pair 9a & 9b. Ground noise at station PDAM is relatively high and is of particular concern in the analysis of event 9a because of the weak signal strength. No source information exists for the two precursors (2a, 9a) and it was thus necessary to assume they had the same mechanism and depth as the following events, so their $\dot{M}_0(t)$ are less certain. Nonetheless, for each event pair the stress drop is much lower for the foreshocks.

This conclusion is evident in the raw *P*-wave pulse width for event 2 at station SCFS (discussed earlier in Section 6.2), and is confirmed by the maximum dynamic stress drop. The peak stress drop in events 2a and 9a are low compared to other earthquakes (Table 6.2), and are low compared to the subsequent earthquakes (events 2b and 9b). The

fact that each foreshock occurred in the same location a few seconds before the larger earthquake is consistent with the possibility that 2a and 9a represent the beginning of a quasi-dynamic instability (characterized by weak seismic radiation) that follows an aseismic nucleation phase. Of the nine Northridge aftershocks examined in this study, two exhibit these low-stress drop foreshocks. Detection of these weak foreshocks is only possible on the closest STS-2 recordings; at near-source FBA recordings (some within 10 km) the foreshock signal was not detectable above the noise.

6.4.1.2 Multiple Station Analysis

For each Northridge aftershock we determine $\dot{M}_0(t)$ using a minimum of two stations. In practice, seismograms recorded with the STS-2 seismometers produced better results than those recorded on FBAs, which could be attributable to lower noise characteristics of the site or the instrument. Because there are various sources of error that can degrade the accuracy of $\dot{M}_0(t)$, it is useful to examine the stability of the deconvolution. Variability in the total seismic moment among solutions from different stations results from inaccurate theoretical seismograms, which, in turn, is caused by focal mechanism errors, deviations from the idealized velocity model, and errors in the assumed instrument response. Examples of $\dot{M}_0(t)$ obtained from two different stations are shown in Figure 6.5 together with their corresponding derivatives, $\ddot{M}_0(t)$ and $\dddot{M}_0(t)$. These examples demonstrate that even when $\dot{M}_0(t)$ exhibit differences (e.g., the total seismic moment), the amplitude of $\dddot{M}_0(t)$ can be stable. The stability is enhanced by the smoothing applied prior to each derivative, which is the same for each seismogram shown. Note that the shape of $\dddot{M}_0(t)$ is demonstrably variable. This variability is expected and results primarily from the rupture directivity, although errors in $\dot{M}_0(t)$ can also produce temporal variations in $\dddot{M}_0(t)$. The preferred $\dot{M}_0(t)$ used to calculate $\dddot{M}_0(t)$ for each event is that from the closest station with an impulsive *P*-wave whose total moment best agrees with independent estimates. The seismic moment is derived from the local magnitude [*Hauksson et al.*, 1995] using the relation

$$\log_{10} M_0 = 1.5M + 9.05. \tag{6.10}$$

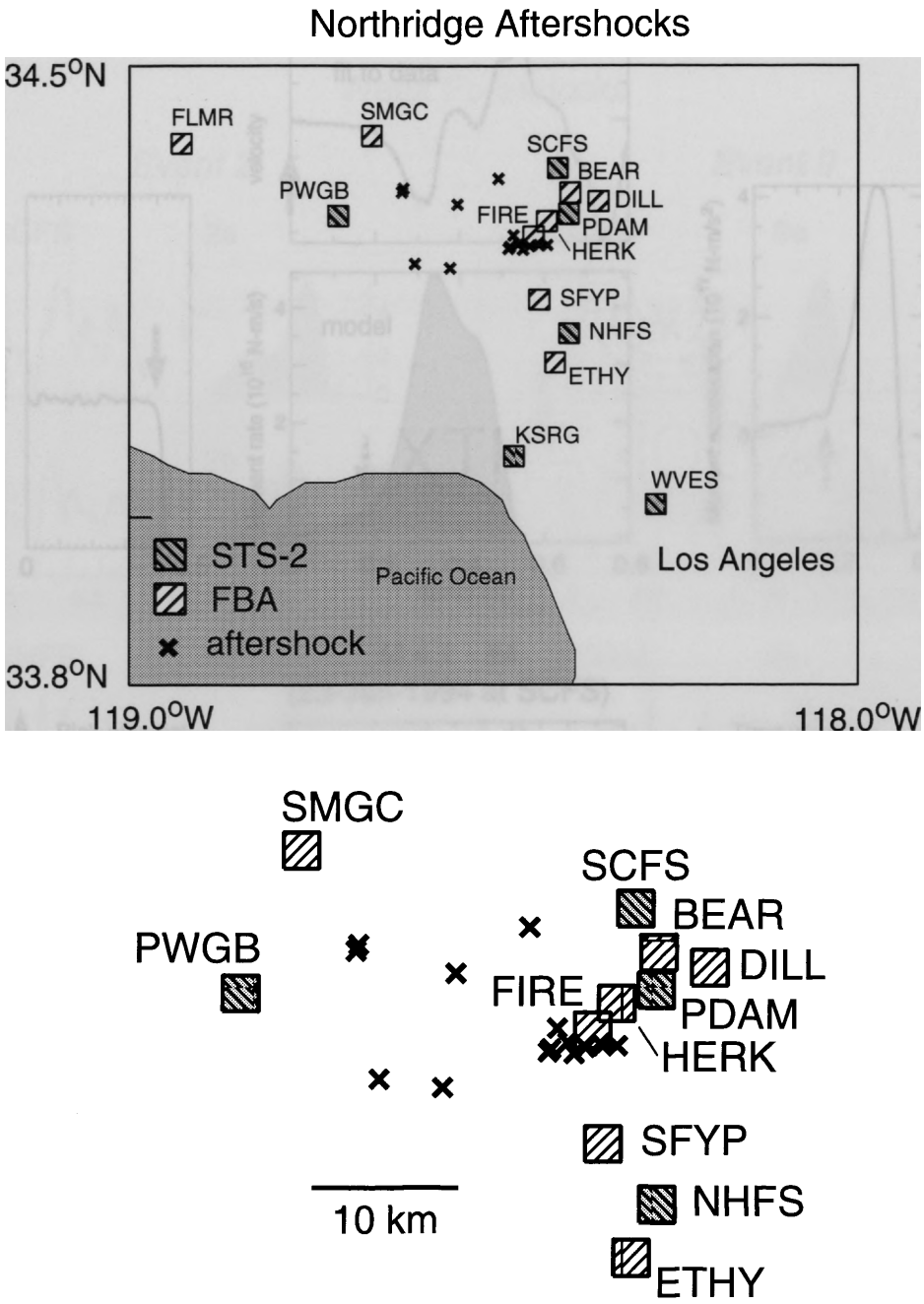

Figure 6.2. Map of the Northridge aftershocks and seismometer locations used in this study. The aftershocks are recorded by STS-2 and FBA seismometers on 16-bit systems. The STS-2 stations SCFS, PDAM, NHFS, and PWGB are used to derive the moment-rate functions.

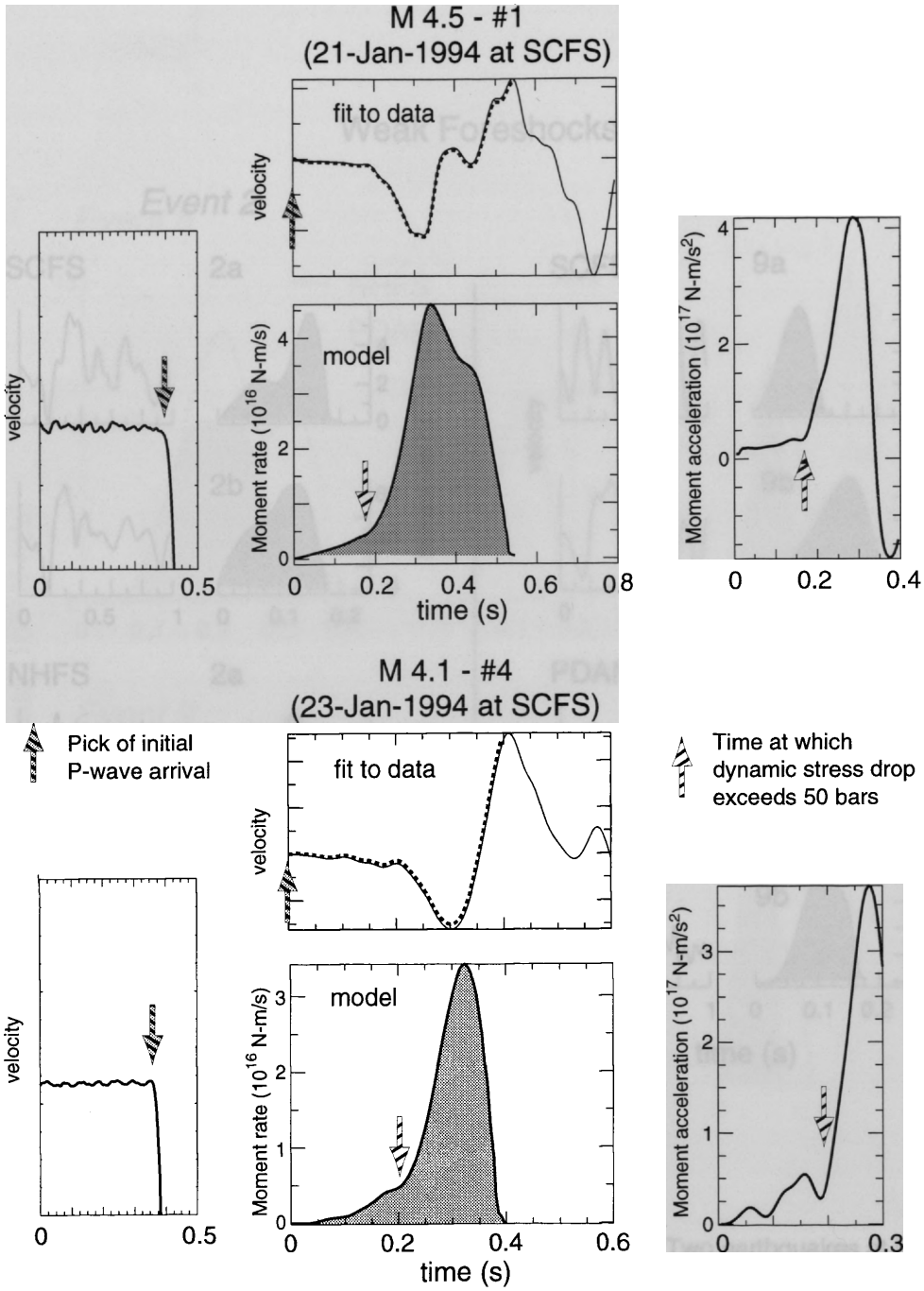

Figure 6.3. Example deconvolution for two Northridge aftershocks. The top and bottom examples have the same format: the pick of the first arriving *P*-wave is shown on the left; the data seismogram is top center and the model fit is shown by a dashed line; the bottom center is the moment-rate function which is the solution to the inverse problem. The moment-rate function is an approximate temporal description of energy release in the earthquake; however, it may be strongly affected by rupture directivity. The derivative of the moment-rate function is shown to the right. The slope of this function is proportional to stress drop (equation 6.8). The time at which the slope exceeds 50 bars is marked with an arrow.

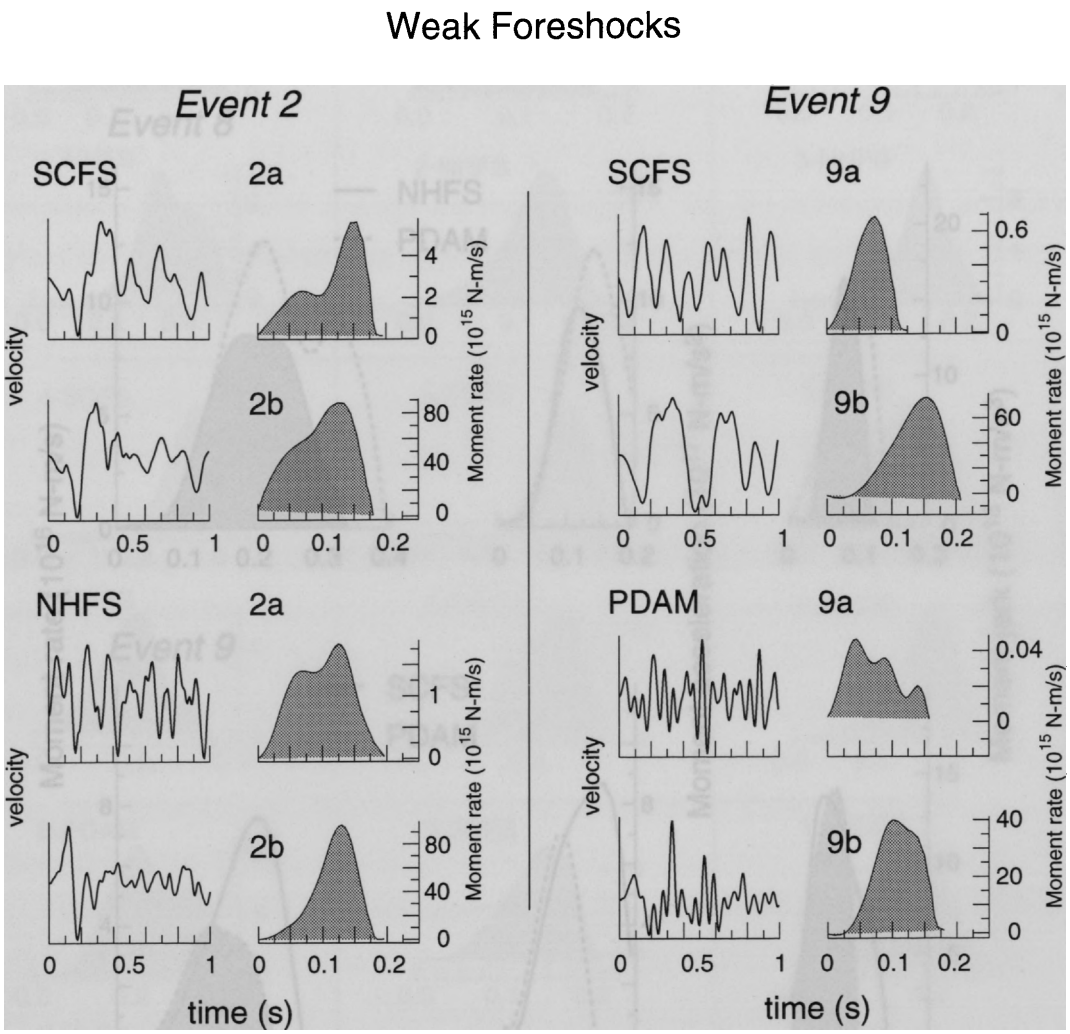

Figure 6.4. Two earthquakes at Northridge with weak foreshocks. Two earthquakes at Northridge were preceded by weak foreshocks (event 2a was 5 s before 2b, event 9a was 3.5 s before 9b). These foreshocks are only detectable on the closest STS-2 seismometers and have unusually long durations for their magnitudes suggesting low rupture velocity.

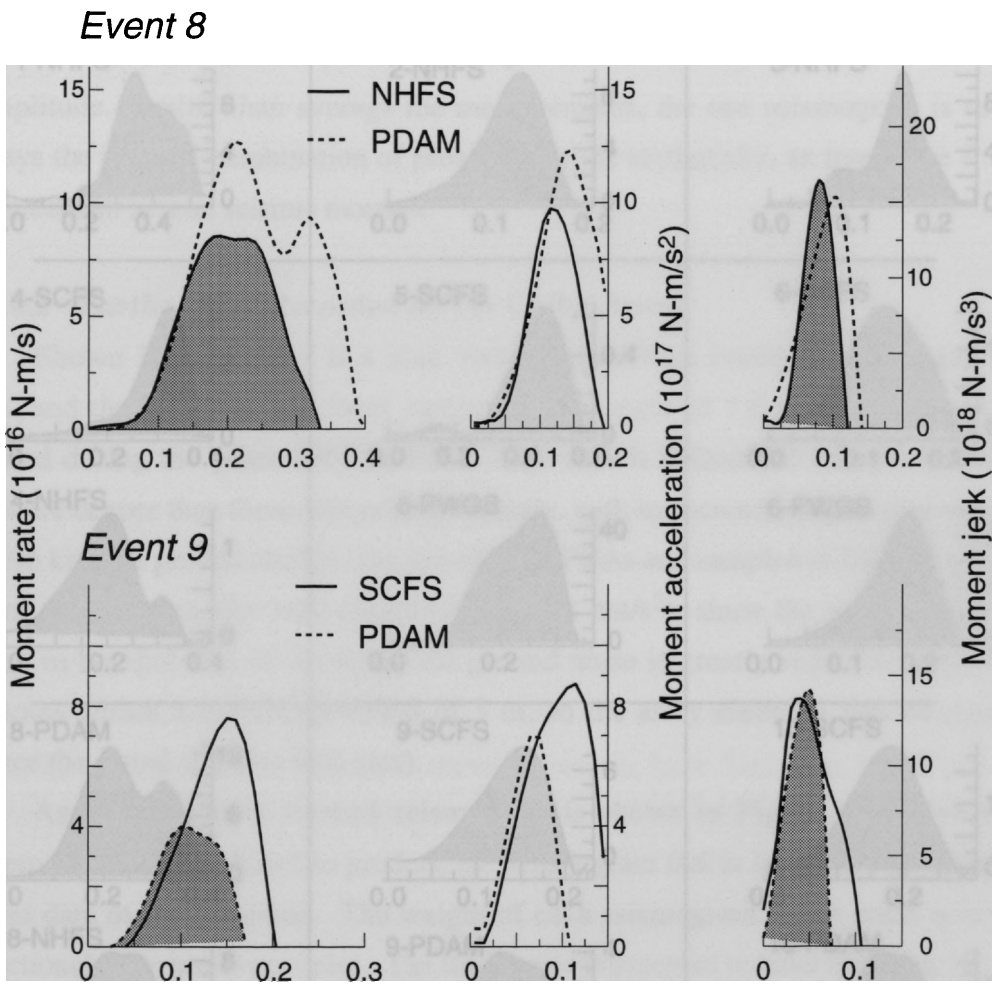

Figure 6.5. Example of moment-rate functions derived from different seismograms for the same earthquake. The moment-rate function is shown on the left, the moment acceleration is in the center, and the moment-jerk function is on the right. The moment jerk is proportional to stress drop at constant rupture velocity. For each earthquake, two solutions are obtained from different seismograms. Note that even when significant variability exists in the total seismic moment (integral of moment rate), the moment-jerk amplitude can be similar.

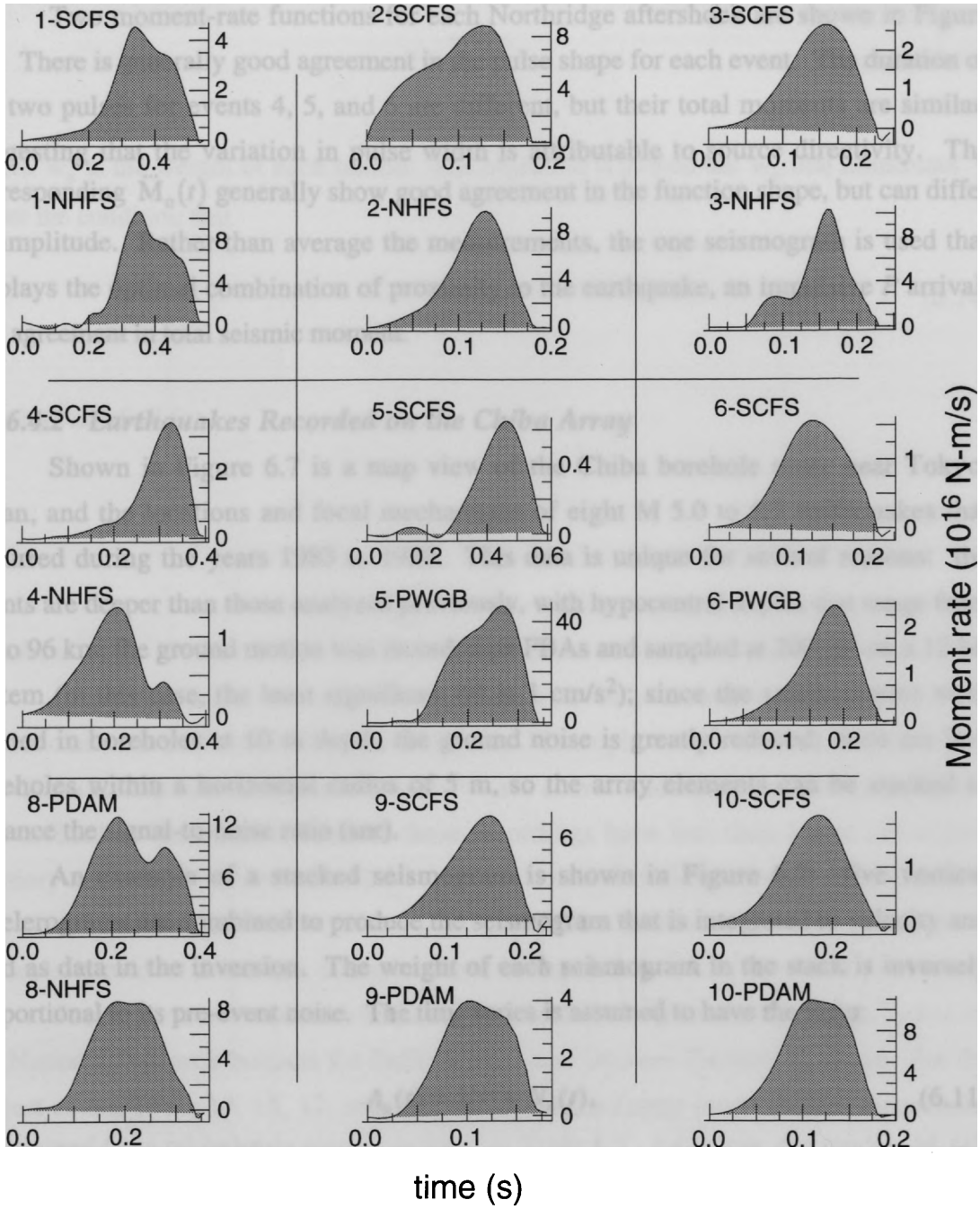

Figure 6.6. Moment-rate functions for all Northridge aftershocks (see Table 6.2). For each earthquake, the moment-rate function is derived at two stations. Pulse shape consistency implies a smaller rupture area or an observation angle perpendicular to the rupture plane; rupture directivity can cause the pulse duration to differ but the total seismic moment should be the same.

Two moment-rate functions for each Northridge aftershock are shown in Figure 6.6. There is generally good agreement in the pulse shape for each event. The duration of the two pulses for events 4, 5, and 6 are different, but their total moments are similar, suggesting that the variation in pulse width is attributable to source directivity. The corresponding $\dddot{M}_0(t)$ generally show good agreement in the function shape, but can differ in amplitude. Rather than average the measurements, the one seismogram is used that displays the optimal combination of proximity to the earthquake, an impulsive *P* arrival, and agreement in total seismic moment.

6.4.2 Earthquakes Recorded on the Chiba Array

Shown in Figure 6.7 is a map view of the Chiba borehole array near Tokyo, Japan, and the locations and focal mechanisms of eight M 5.0 to 6.7 earthquakes that occurred during the years 1983 to 1989. This data is unique for several reasons: the events are deeper than those analyzed previously, with hypocentral depths that range from 34 to 96 km; the ground motion was recorded on FBAs and sampled at 200 sps on a 12-bit system (in this case, the least significant bit is 1 cm/s^2); since the seismometers were located in boreholes at 10 m depth, the ground noise is greatly reduced; there are five boreholes within a horizontal radius of 5 m, so the array elements can be stacked to enhance the signal-to-noise ratio (snr).

An example of a stacked seismogram is shown in Figure 6.7: five vertical accelerograms are combined to produce the seismogram that is integrated to velocity and used as data in the inversion. The weight of each seismogram in the stack is inversely proportional to its pre-event noise. The time series is assumed to have the form:

$$A_n(t) = S(t) + N_n(t), \tag{6.11}$$

where $A_n(t)$ is the record for the *n*th station, $S(t)$ is the signal (assumed to be the same at every station), and $N_n(t)$ is the noise at the *n*th station. The average power of the noise at the *n*th station is

$$v_n \equiv \left\langle N_n^2(t) \right\rangle, \tag{6.12}$$

where $\langle\ \rangle$ indicates the mean value. And the total noise in the stack is

$$v = \sum_n w_n^2 v_n, \tag{6.13}$$

where w_n is the weight of each station. The objective is to find the w_n that minimizes v under the condition that

$$\sum_n w_n = 1, \tag{6.14}$$

which is satisfied for

$$w_n = \frac{1}{v_n \sum_n v_n^{-1}} \tag{6.15}$$

[*Riedesel et al.*, 1980].

After the array components are stacked into a single seismogram, the deconvolution is performed for each earthquake. Example deconvolutions are shown for two Chiba earthquakes in Figure 6.8. The *P*-wave arrival is identified on the accelerogram and defined as the origin. Because these recordings have less than 1 s of pre-trigger memory and were recorded on a 12-bit system, detection of the earliest *P*-wave arrival is much less certain than with the other seismograms used in this study. This ambiguity is particularly evident in the first example shown in Figure 6.8.

Source parameters were determined from local and regional arrays and provided by the National Research Institute for Earth Science and Disaster Prevention, Japan. For the largest events (#11, 14, 15, 17, and 18), the seismic moment (and moment magnitude) determined from teleseismic records is listed in Table 6.2. As before, the model, $\dot{M}_0(t)$, the fit-to-data, and $\ddot{M}_0(t)$ are shown. No regularization was required in these inversions with Chiba seismograms. The first example in Figure 6.8 illustrates the importance of considering both least-squares solutions (with and without the positivity constraint); the event duration, the total seismic moment, and $\ddot{M}_0(t)$ are different with each inversion method. The least-squares solution produces a better fit to the data and is the preferred solution. Moment-rate functions for the eight Chiba events are shown in Figure 6.9. The

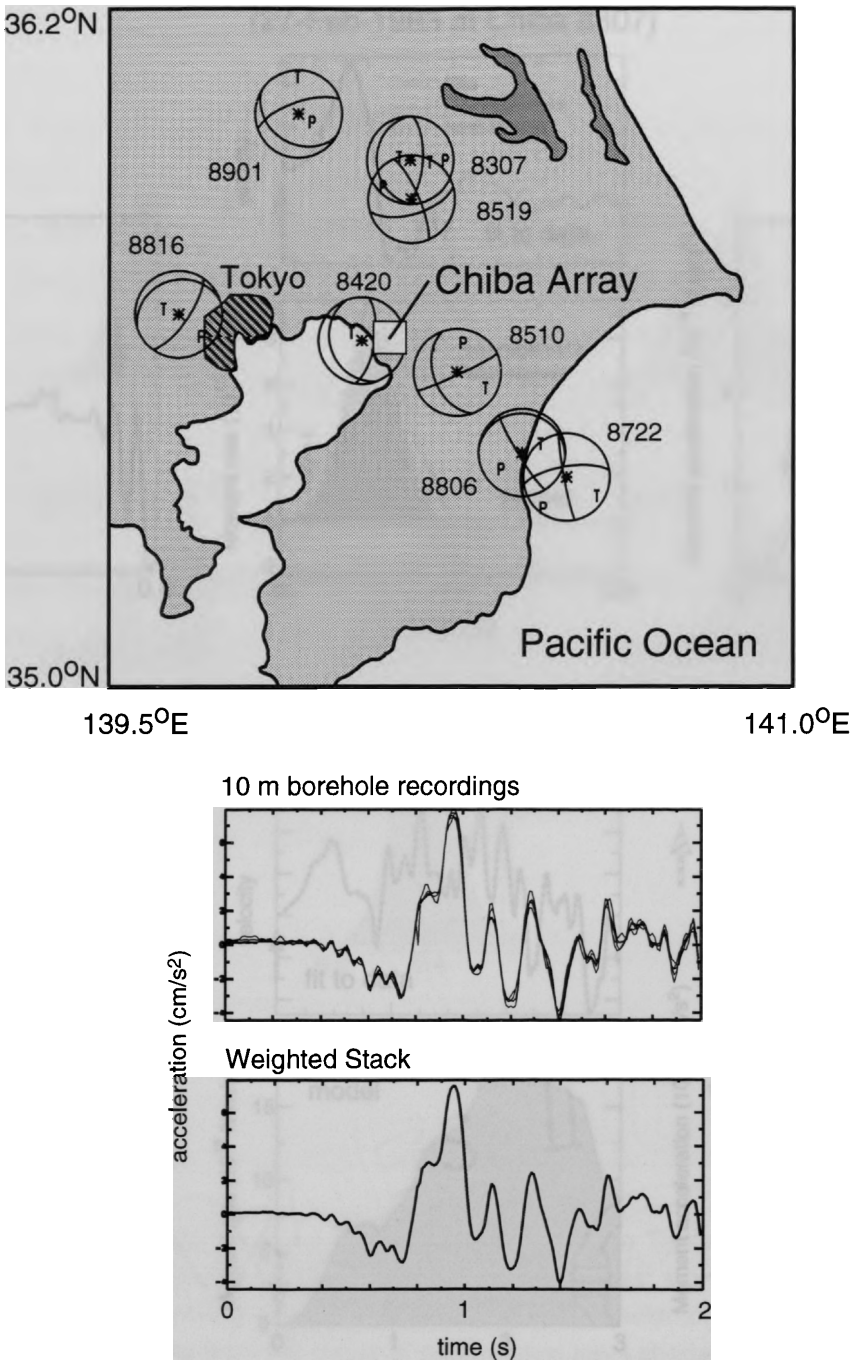

Figure 6.7. Map showing the Chiba borehole array and locations of earthquakes recorded by it. Accelerations were recorded on 12-bit data loggers (the least significant bit is 1 cm/s^2), which obscures detection of the first *P*-wave arrival; stacking five array elements (inset) increases the signal-to-noise ratio.

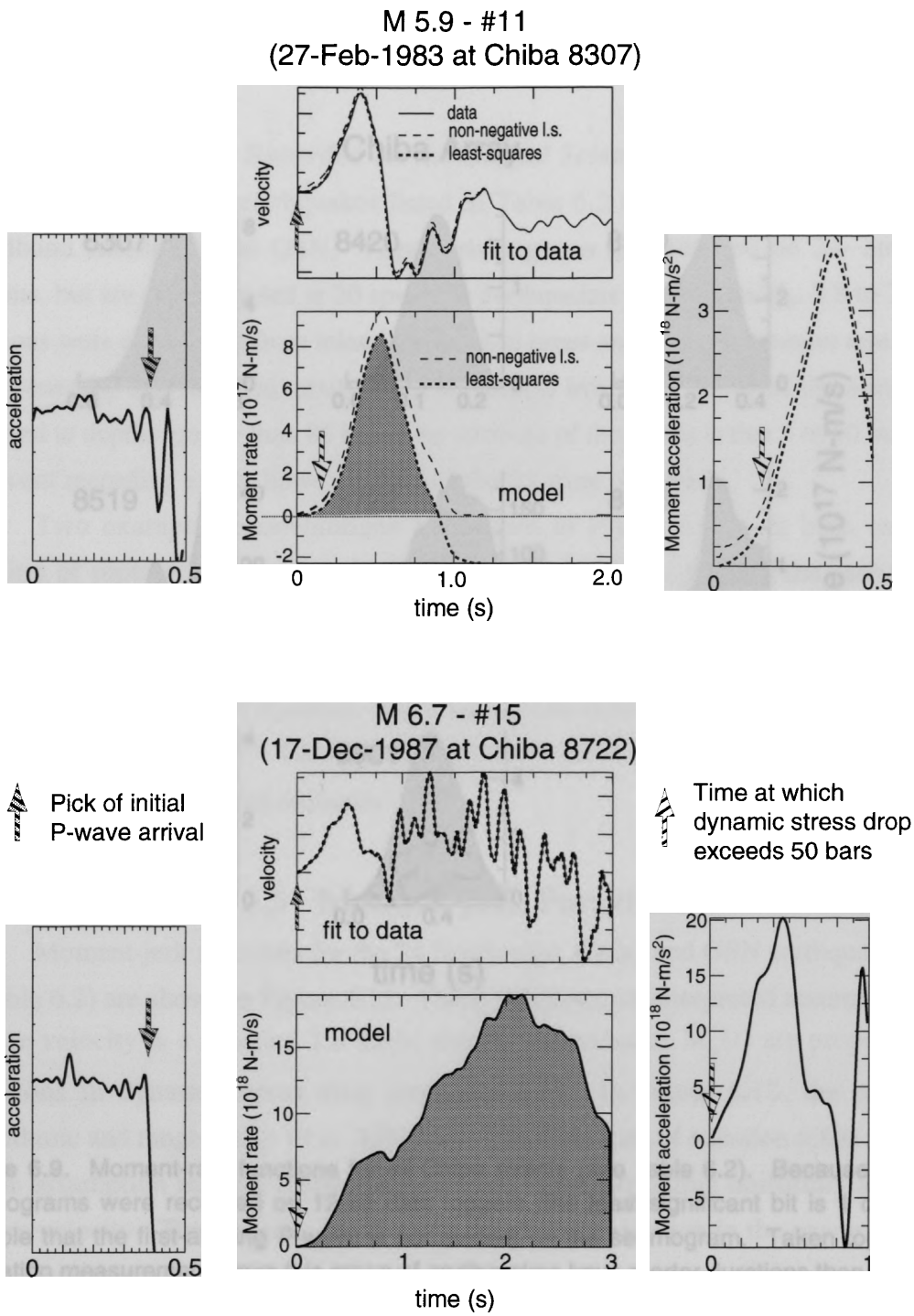

Figure 6.8. Example deconvolution of two earthquakes recorded by the Chiba array. Top and bottom earthquakes have the same format (see caption for Figure 6.3). In each case, the moment-rate function is shown at bottom center. The moment acceleration is shown on the right. The slope of this function is proportional to stress drop under certain assumptions (equation 6.8). The time at which the slope exceeds 50 bars is marked with an arrow.

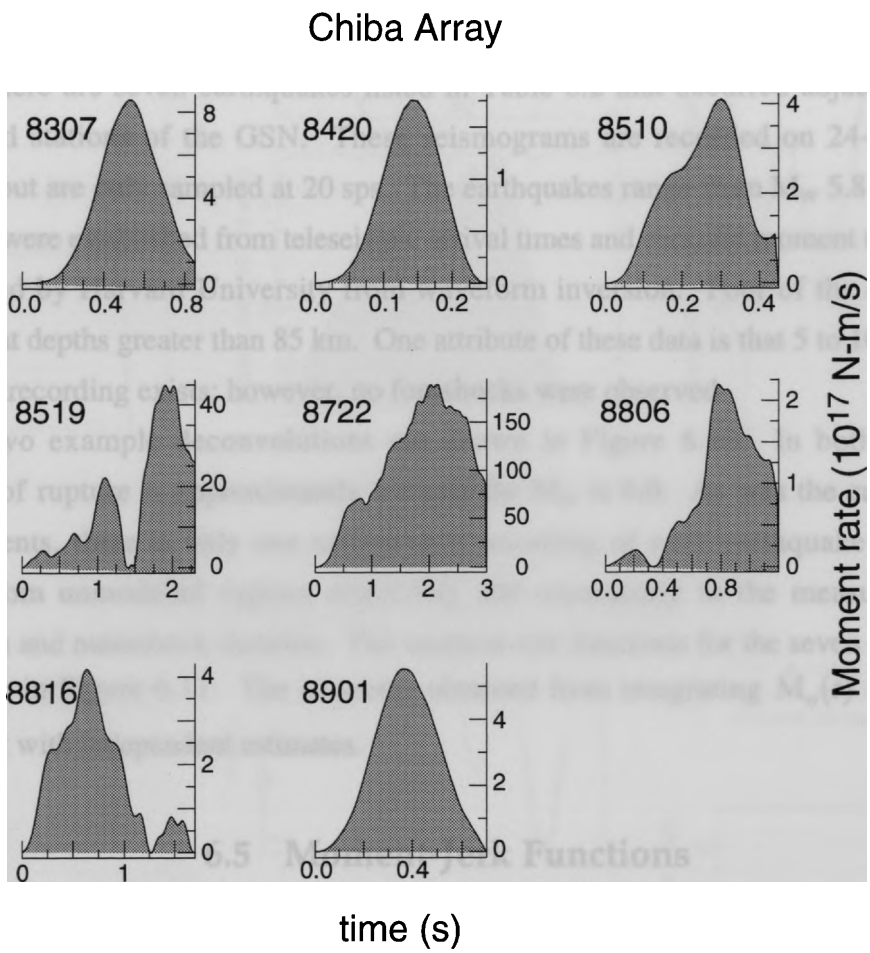

Figure 6.9. Moment-rate functions for all Chiba events (see Table 6.2). Because the Chiba seismograms were recorded on 12-bit data loggers (the least significant bit is 1 cm/s^2), it is possible that the first-arriving *P*-wave is not evident on the seismogram. Taken together, the nucleation measurements from this group of earthquakes have shorter durations than those from other events of comparable magnitude.

total seismic moments are in good agreement with independent estimates based on local magnitude and teleseismic waveforms.

6.4.3 Earthquakes Recorded on the Global Seismic Network

There are seven earthquakes listed in Table 6.2 that occurred adjacent to three broadband stations of the GSN. These seismograms are recorded on 24- and 32-bit systems, but are only sampled at 20 sps. The earthquakes range from M_W 5.8 to 7.6. The locations were established from teleseismic arrival times and centroid moment tensors were determined by Harvard University from waveform inversion. Four of the earthquakes occurred at depths greater than 85 km. One attribute of these data is that 5 to 10 minutes of pre-event recording exists; however, no foreshocks were observed.

Two example deconvolutions are shown in Figure 6.10. In both cases, the duration of rupture is approximately 4 s and the M_W is 6.0. As was the case with the Chiba events, there is only one near-source recording of each earthquake and hence, effects from unmodeled rupture directivity add uncertainty to the measurements of nucleation and mainshock duration. The moment-rate functions for the seven earthquakes are shown in Figure 6.11. The moments obtained from integrating $\dot{M}_0(t)$ are in good agreement with independent estimates.

6.5 Moment-Jerk Functions

Moment-jerk functions for the 24 Northridge, Chiba, and GSN earthquakes (listed in Table 6.2) are shown in Figure 6.12. These functions are interpreted assuming that the rupture velocity is a constant 2.8 km/s; that is, variations in $\dddot{M}_0(t)$ are proportional to variations in dynamic stress drop (equation 6.8). In Figure 6.12, the ordinate is logarithmic and ranges from 10 to 2000 bars. The derivation of equation 6.8 is predicated on the assumption that the rupture is a circular crack expanding uniformly at constant rupture velocity. The irregular behavior of moment acceleration in the examples shown earlier attests to the erratic nature of rupture growth during earthquakes. The slip distribution for large earthquakes (e.g., Landers) is known to be highly variable, with regions of large slip (asperities) separated by areas where the slip amplitude is much smaller (these asperities can often be correlated with peaks in the moment-rate function).

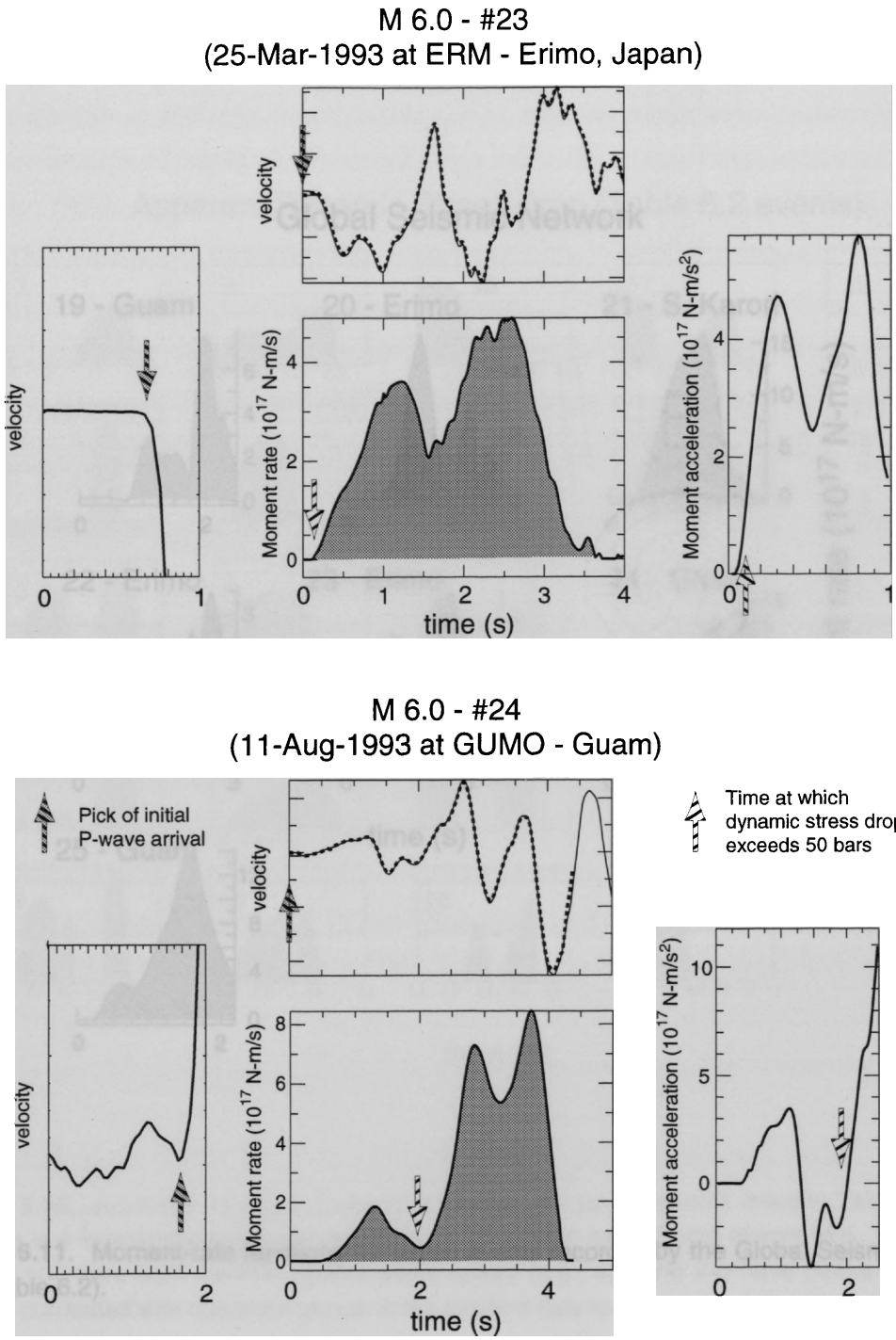

Figure 6.10. Example deconvolution for two events recorded by the Global Seismic Network. Top and bottom earthquakes have the same format (see caption for Figure 6.3). In each case, the bottom center is the moment-rate function and moment acceleration is shown on the right.

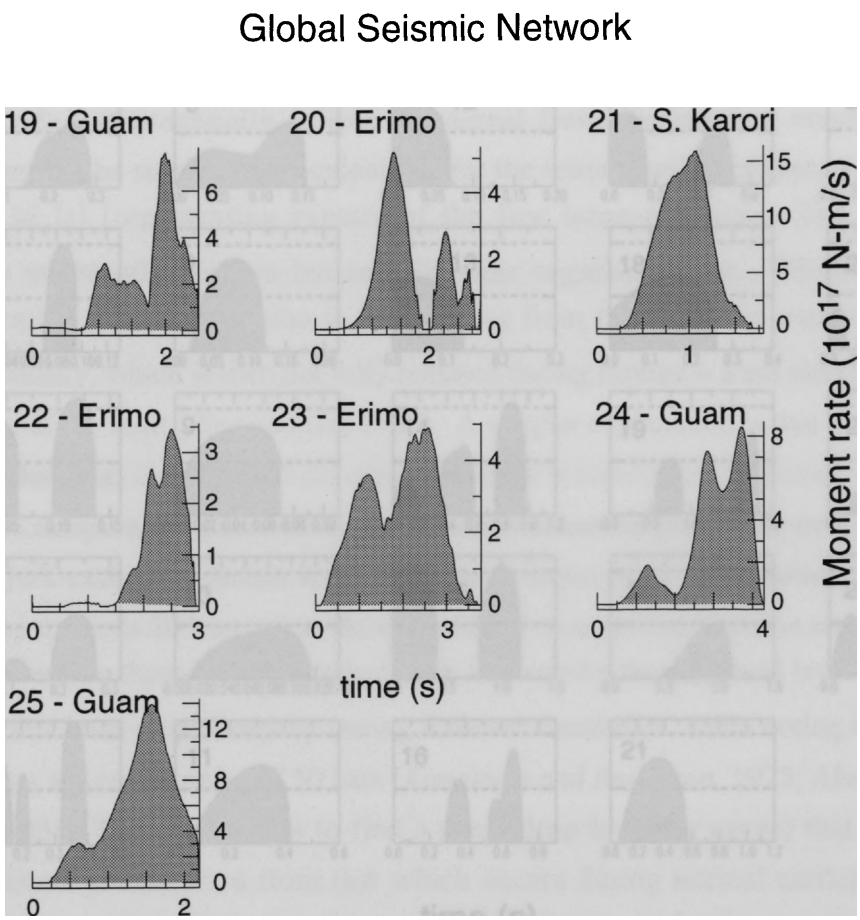

Figure 6.11. Moment-rate functions for seven events recorded by the Global Seismic Network (see Table 6.2).

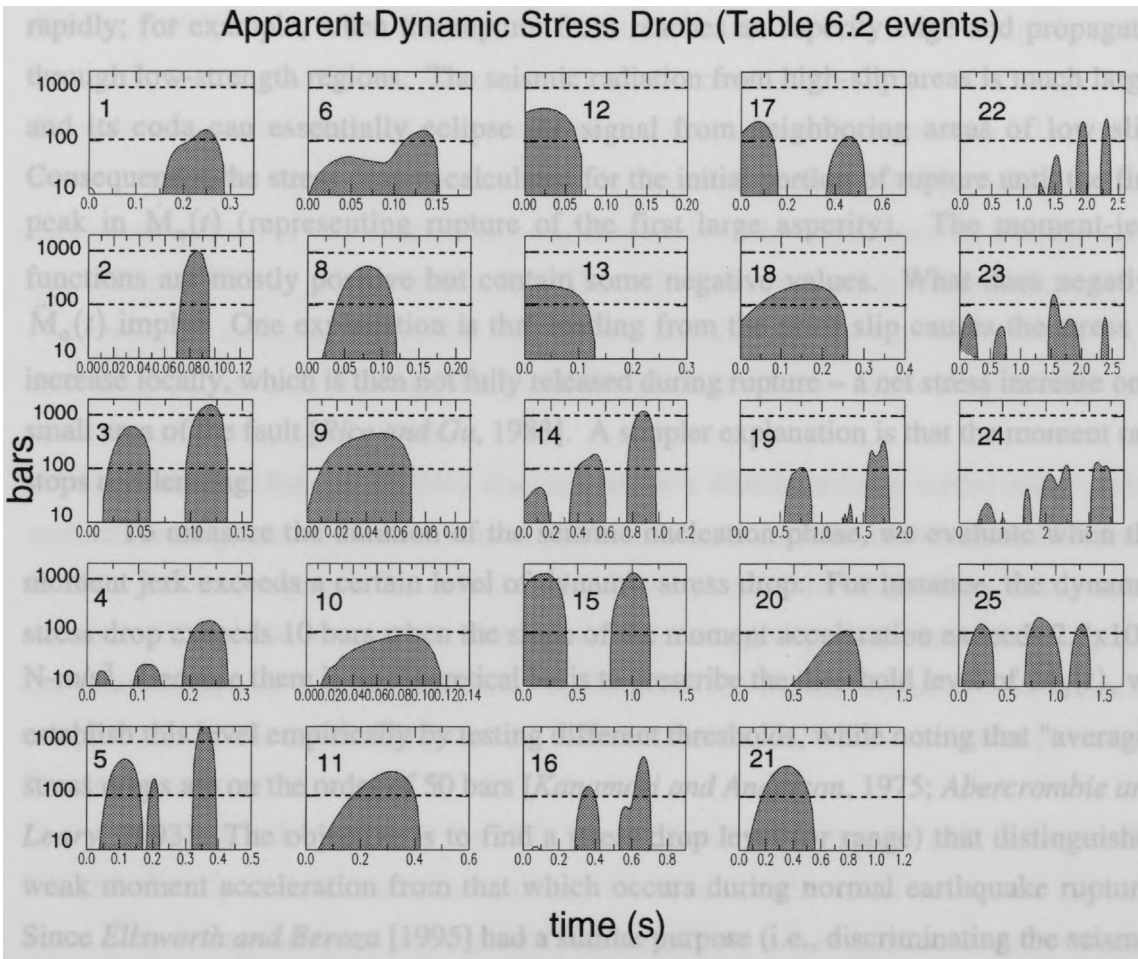

Figure 6.12. Apparent dynamic stress drop versus time for the events listed in Table 6.2. The ordinate is a logarithmic scale and ranges from 10 to 2000 bars. Some events (e.g., #12 and 13) exceed 100 bars from the first sample point; others (e.g., #23 and 24) have peaks that can be visually correlated with quadratic growth in the moment-rate function.

Equation 6.8 is most appropriate for the breakage of isolated asperities that exhibit linear growth in moment acceleration, rather than the entire earthquake rupture. The appropriateness of equation 6.8 breaks down when the rupture front acceleration changes rapidly; for example, when the rupture front reaches an asperity edge and propagates through low-strength regions. The seismic radiation from high-slip areas is much larger and its coda can essentially eclipse the signal from neighboring areas of low slip. Consequently, the stress drop is calculated for the initial portion of rupture until the first peak in $\dot{M}_0(t)$ (representing rupture of the first large asperity). The moment-jerk functions are mostly positive but contain some negative values. What does negative $\dddot{M}_0(t)$ imply? One explanation is that loading from the prior slip causes the stress to increase locally, which is then not fully released during rupture – a net stress increase on a small area of the fault [*Rice and Gu*, 1983]. A simpler explanation is that the moment rate stops accelerating.

To measure the duration of the seismic nucleation phase, we evaluate when the moment jerk exceeds a certain level of dynamic stress drop. For instance, the dynamic stress drop exceeds 10 bars when the slope of the moment acceleration exceeds 2.8×10^{17} N-m/s^3. Because there is no theoretical basis to prescribe the threshold level of $\dddot{M}_0(t)$, we establish this level empirically by testing different thresholds, while noting that "average" stress drops are on the order of 50 bars [*Kanamori and Anderson*, 1975; *Abercrombie and Leary*, 1993]. The objective is to find a stress drop level (or range) that distinguishes weak moment acceleration from that which occurs during normal earthquake rupture. Since *Ellsworth and Beroza* [1995] had a similar purpose (i.e., discriminating the seismic nucleation phase from the rest of the earthquake), it is natural that we compare our nucleation durations based on stress drop with their picks for the same events.

Moment-rate functions for the 25 largest earthquakes of *Ellsworth and Beroza* [1995] are shown in Figure 6.13. These events range in magnitude from 3.5 to 8.1 and include many well-studied earthquakes of the last two decades. For the largest events, only the first part of the $\dot{M}_0(t)$ was calculated; for smaller events, the $\dot{M}_0(t)$ was determined for the entire earthquake. The corresponding moment-jerk functions are shown in Figure 6.14. Although the maximum stress drop varies considerably among the events, in most cases the stress drop is low initially and grows during the beginning of rupture. The maximum stress drop does not vary systematically with earthquake magnitude, but larger earthquakes take longer to reach their maximum stress drop

(measured from the first-arriving seismic signal). More importantly, the time it takes earthquakes to reach the same level of apparent stress drop increases with earthquake size.

The maximum dynamic stress drop is listed in Table 6.3 for the *Ellsworth and Beroza* [1995] events. Because this list contains many well-studied earthquakes, it is interesting to compare the maximum stress drops obtained in this study with average stress drops determined by others. As expected, the maximum dynamic stress drop is larger than the average static stress drop; the most striking example is the 1994 M_W 6.7 Northridge mainshock (#5). For this event, *Wald and Heaton* [1994b] determined an average static stress drop of 70 bars using equation 6.2. This calculation was made for the entire rupture (7 s duration) assuming the radius was 8.7 km and the average slip was 121 cm. The moment-jerk function for the first 1 s indicates a maximum stress drop of 700 bars occurring at approximately 0.8 s.

Wald and Heaton [1994b] also solved for a distributed slip model using strong motion seismograms. The maximum displacement in their model is 350 cm and occurs in the first 1.5 s of rupture. To calculate the stress drop of this high-slip patch, we use equation 6.2 and assume a radius of 2 km with an average slip of 250 cm – for this patch, the static stress drop is about 600 bars. Neither the static nor the dynamic measurements are precise, but it is encouraging that the measurements are close for the initial part of the Northridge rupture.

A similar calculation for the 1992 M_W 7.2 Landers earthquake (#2) is less certain because the slip distribution is more poorly resolved; however, the maximum apparent stress drop during the first 4 s of rupture (300 bars, Table 6.3) is consistent with estimates of the static stress drop in the same period determined with the slip models presented in Chapter 3.

6.5.1 Comparison with Measurements of Ellsworth and Beroza [1995]

The nucleation duration is most similar to the results of *Ellsworth and Beroza* [1995] when the threshold value of $\dddot{M}_0(t)$ is set at 1.4×10^{18} N-m/s^3 – or a 50 bar stress drop at a rupture velocity of 2.8 km/s – this stress drop is a typical average value for crustal earthquakes [*Kanamori and Anderson*, 1975; *Abercrombie and Leary*, 1993]. This relationship is illustrated in Figure 6.15 where the durations obtained with 50 bars are compared to the *Ellsworth and Beroza* [1995] measurements. Also shown in Figure 6.15 is the range of the duration measurement obtained with stress drops between 20 and 80

Table 6.3. Parameters for Earthquakes in *Ellsworth and Beroza* [1995]

id	date	event	M_w	M_o (N-m)	r_h (km)	υ_{EB} (s)	υ_{20} (s)	υ_{50} (s)	υ_{80} (s)	γ_{EB} (s)	τ_{max}
1	19-Sep-1985	Michoacan	8.1	1.4e+21	25	5.0	0.40	1.15	3.05	50.0	580
2	28-Jun-1992	Landers	7.3	9.0e+19	21	3.0	0.50	1.75	3.05	20.0	280
3	25-Apr-1989	Mexico-viga	6.9	2.4e+19	27	0.53	0.50	1.25	2.05		230
4	18-Oct-1989	Loma Prieta	6.9	2.8e+19	25	1.6	0.35	0.65	0.70	9.00	350
5	17-Jan-1994	Northridge	6.7	1.0e+19	19	0.5	0.25	0.30	0.35	6.00	690
6	15-Oct-1979	Imperial Val	6.5	6.0e+18	19	0.59	0.12	0.47	0.48	15.0	400
7	9-Jun-1980	Victoria	6.4	4.8e+18	13	0.44	0.01	0.24	0.39		500
8	24-Oct-1993	Mexico-smr	6.4	5.8e+18	46	0.36	0.24	0.36	0.40		260
9	28-Jun-1992	Big Bear	6.2	2.0e+18	29	0.46	0.24	0.37	0.72		870
10	23-Apr-1992	Joshua Tree	6.1	1.4e+18	44	0.12	0.05	0.08	0.12	4.00	240
11	31-May-1990	Mexico-lla	5.9	7.5e+17	24	0.082	0.01	0.01	0.03	1.70	470
12	29-Jun-1992	Little Skull	5.8	4.8e+17	27	0.46	0.40	0.45	0.57	1.70	420
13	28-Jun-1991	S. Madre	5.5	2.8e+17	23	0.34	0.11	0.33	0.35	0.80	250
14	20-Mar-1994	North 10	5.3	8.9e+16	22	0.127	0.05	0.09	0.11	0.87	420
15	3-Dec-1988	Raymond	4.9	2.4e+16	16	0.11	0.01	0.11	0.12	0.80	370
16	16-Jan-1993	Gilroy	4.9	2.4e+16	29	0.21	0.16	0.21	0.24	0.80	130
17	14-Nov-1993	Parkfield	4.8	2.0e+16	15	0.20	0.17			0.30	40
18	11-Aug-1993	Halls Val.	4.7	1.3e+16	10	0.73	0.70	0.80		0.45	70
19	3-Feb-1994	North 03*	4.2	2.0e+15	26	0.047	0.03	0.04	0.05	0.26	660
20	6-Feb-1994	North 05*	4.1	1.4e+15	24	0.026	0.01	0.03	0.04	0.30	570
21	2-Feb-1994	North 02	3.8	5.0e+14	17	0.039	0.04	0.06	0.08	0.27	190
23	6-Feb-1994	North 06	3.7	3.5e+14	23	0.030	0.01	0.03	0.04	0.32	730
25	1-Feb-1994	North 01	3.6	2.5e+14	11	0.013	0.03	0.03	0.04	0.24	210
27	4-Feb-1994	North 04	3.5	1.8e+14	16	0.008	0.01	0.01	0.01	0.21	520
28	8-Mar-1994	North 09	3.4	1.3e+14	22	0.047	0.06	0.08	0.09	0.15	80

r_h hypocentral distance

υ_{EB} duration of seismic nucleation phase from *Ellsworth and Beroza* [1995]

υ_{50} duration of seismic nucleation phase determined with a 50 bar threshold

γ_{EB} total earthquake duration minus υ_{EB} from *Ellsworth and Beroza* [1995]

τ_{max} maximum dynamic stress drop during earthquake beginning

* events #19 and 20 are the same as events #9b and 10, respectively, in Table 6.2

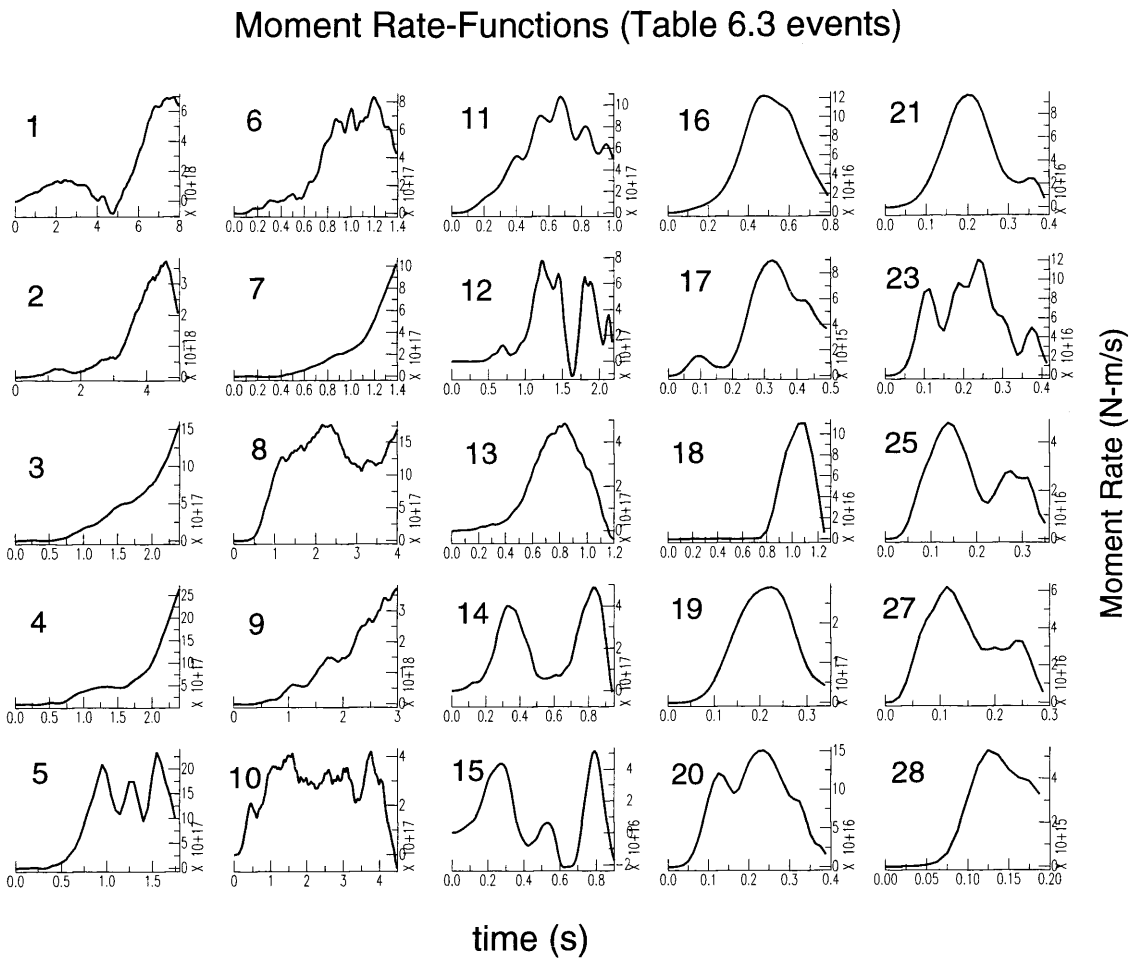

Figure 6.13. Moment-rate functions from *Ellsworth and Beroza* [1995] for events listed in Table 6.3. The events are plotted in order of decreasing magnitude from top to bottom, and left to right. The moment rate is determined only for the initial portion of the largest earthquakes. Note that the time scale varies by a factor of 20 from the largest to the smallest events.

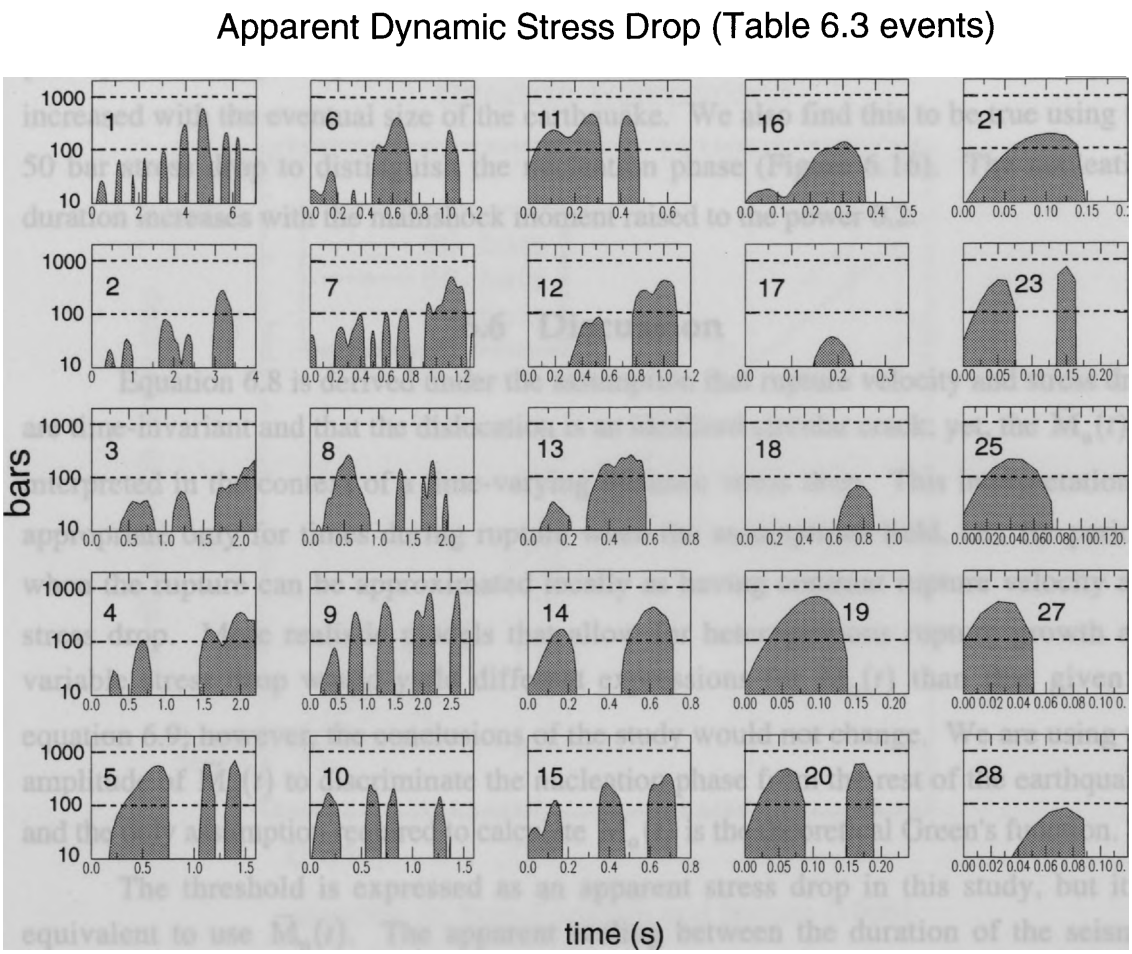

Figure 6.14. Apparent dynamic stress drop versus time for the earthquakes in Table 6.3. The ordinate is a logarithmic scale and ranges from 10 to 2000 bars for all events. Some events (e.g., #2 and 4) demonstrate weak beginnings the timing of which is corroborated by independent studies. Note that here the time scale varies by over 600 for the events shown.

bars. Two events (#16 and 17) never exceed 20 bars, indicating relatively low stress drop throughout the earthquake, and others (#1, 14, 27) exceed this level at the first sample point. The values of the nucleation duration determined with different thresholds are listed in Table 6.3 together with the nucleation duration measured by *Ellsworth and Beroza* [1995]. *BE-EB* [1995] observed that the duration of the seismic nucleation phase increased with the eventual size of the earthquake. We also find this to be true using the 50 bar stress drop to distinguish the nucleation phase (Figure 6.16). The nucleation duration increases with the mainshock moment raised to the power 0.2.

6.6 Discussion

Equation 6.8 is derived under the assumption that rupture velocity and stress drop are time-invariant and that the dislocation is an idealized circular crack; yet, the $\dddot{M}_0(t)$ is interpreted in the context of a time-varying dynamic stress drop. This interpretation is appropriate only for times during rupture when the assumptions hold, i.e., for periods when the rupture can be approximated locally as having constant rupture velocity and stress drop. More realistic models that allow for heterogeneous rupture growth and variable stress drop would yield different expressions for $\dddot{M}_0(t)$ than that given in equation 6.9; however, the conclusions of the study would not change. We are using the amplitude of $\dddot{M}_0(t)$ to discriminate the nucleation phase from the rest of the earthquake, and the only assumption required to calculate $\dddot{M}_0(t)$ is the theoretical Green's function.

The threshold is expressed as an apparent stress drop in this study, but it is equivalent to use $\dddot{M}_0(t)$. The apparent scaling between the duration of the seismic nucleation phase defined in this manner and the seismic moment is unambiguous; whether low $\dddot{M}_0(t)$ implies low stress drop, low rupture velocity, or rupture complexity that is not included in the model, remains an open question.

EB-BE [1995] proposed two contrasting models to explain the observed scaling between nucleation duration and mainshock size. The first interpretation, termed the cascade model, is that there is no difference between the beginning of large and small earthquakes. A large earthquake results when a small earthquake triggers a cascade of increasingly larger slip events. In this model, rupture continues to grow if it can cause successively larger fault elements to fail, and the size of the following mainshock is influenced by the dynamic properties of the last element that fails. In this interpretation, foreshocks occurring during the nucleation process represent the rupture of small,

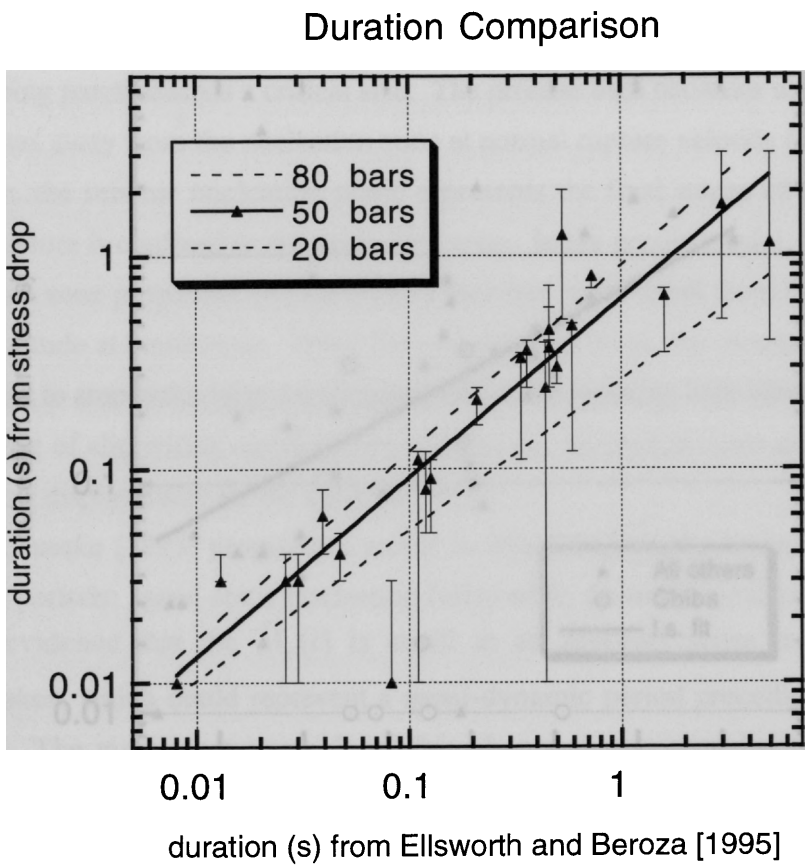

Figure 6.15. Comparison of nucleation duration measurements. The symbols show the duration of the seismic nucleation phase determined using a 50 bar threshold plotted against the durations measured by *Ellsworth and Beroza* [1995] for the same events; the range of each measurement is shown for 20 and 80 bar stress drop thresholds. Least-squares fits are shown by dashed and solid lines. The agreement is acceptable over a wide range of earthquake magnitude indicating that the time required to reach the threshold is longer for bigger earthquakes.

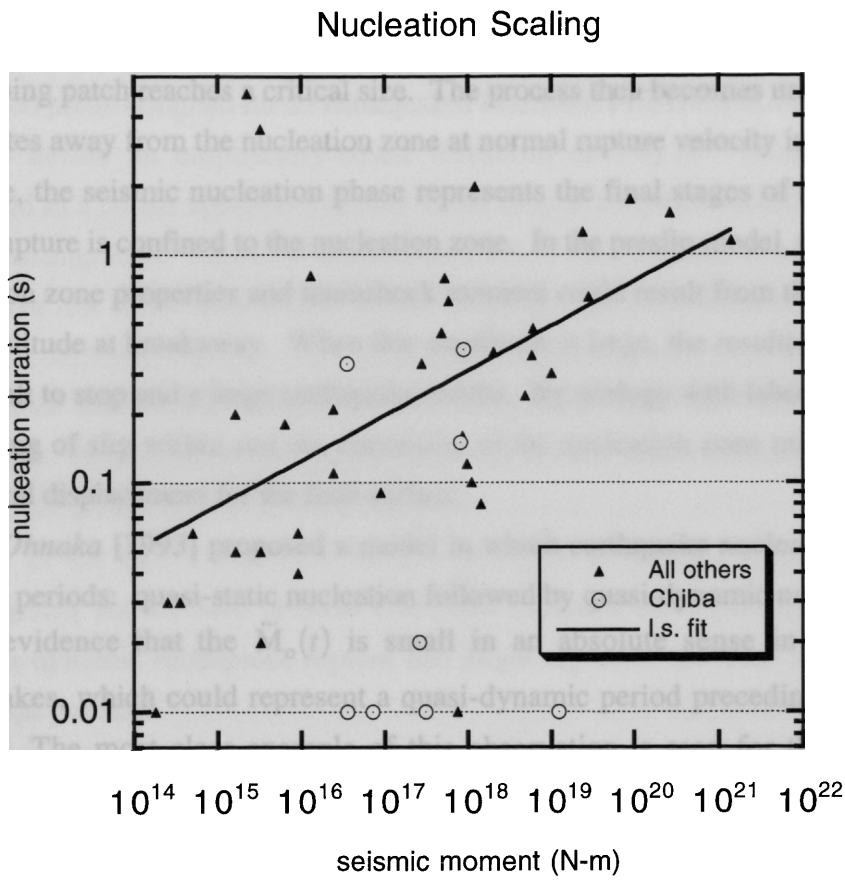

Figure 6.16. Nucleation duration versus seismic moment for 47 earthquakes examined in this study. Since the Chiba data is recorded on a 12-bit recording system, the pick of the initial *P*-wave is more uncertain than with the other seismograms. A least-squares fit to the measurements (excluding those from the Chiba seismograms) is shown by the solid line. A duration of 0.01 is the smallest measurement that can be obtained with this method and implies that no seismic nucleation phase is observed. The duration of the seismic nucleation phase scales with the seismic moment raised to the power 0.2,

relatively strong patches that break dynamically [*Das and Scholz*, 1981]. In this model, the stress drops of events in the cascade comprising the seismic nucleation phase should not be unusually low.

The second interpretation, termed the preslip model, is that the beginnings of small and large earthquakes are different. In the preslip model, failure initiates aseismically, with an episode of slow, stable sliding over a limited region that gradually accelerates until the slipping patch reaches a critical size. The process then becomes unstable, and fracture propagates away from the nucleation zone at normal rupture velocity in an earthquake. In this case, the seismic nucleation phase represents the final stages of this process during which rupture is confined to the nucleation zone. In the preslip model, the scaling between nucleation zone properties and mainshock moment could result from the magnitude of the slip amplitude at breakaway. When this amplitude is large, the resulting dynamic rupture is difficult to stop and a large earthquake results. By analogy with laboratory experiments, the scaling of slip within and the dimension of the nucleation zone may be controlled by the critical displacement for the fault surface.

Ohnaka [1993] proposed a model in which earthquake nucleation was separated into two periods: quasi-static nucleation followed by quasi-dynamic nucleation. We have shown evidence that the $\dddot{M}_0(t)$ is small in an absolute sense in the beginning of earthquakes, which could represent a quasi-dynamic period preceding normal dynamic rupture. The most clear example of this observation is seen for the two Northridge aftershocks shown in Figure 6.4. Both of these earthquakes were preceded by long duration events with low $\dddot{M}_0(t)$ that were only detectable with 16-bit recording systems located near the source. It is possible that many earthquakes have such premonitory slip that is not detected by current seismic instrumentation at greater distances. Our results identify a measurable difference in the $\dddot{M}_0(t)$ during nucleation compared to the mainshock, which is most consistent with the preslip model. Further, the duration of the weak initial phase increases with the size of the following earthquake. Near-source, high-dynamic-range (16-bit or better) recording systems with high sample rates (20 sps or better) are necessary to observe a weak seismic nucleation phase, and thus the number of events included in this study is small. The 47 events analyzed are not intended to represent all earthquake phenomena, they do, however, suggest that most earthquakes begin slowly and that the process responsible for this slow beginning exerts an influence on the eventual earthquake size.

Conclusions

Moment-rate and moment-jerk functions are presented for 47 earthquakes. It is observed that the moment jerk is small, in an absolute sense, during the beginning of earthquake rupture. The amplitude of the moment jerk is used to distinguish objectively the weak nucleation phase from the rest of the earthquake. Measurements of the seismic nucleation phase obtained for 25 earthquakes examined in *Ellsworth and Beroza* [1995] are used to define an empirically-based threshold of 1.4×10^{18} N-m/s^3, which can be expressed as a 50 bar apparent dynamic stress drop at a rupture velocity of 2.8 km/s under certain assumptions. Values of moment jerk below the threshold can be interpreted either in terms of low stress drop or low rupture velocity. The nucleation durations measured in this way confirm the scaling relationship described by *Ellsworth and Beroza* [1995]: the duration of the seismic nucleation phase increases with the subsequent mainshock magnitude. In this study, the nucleation duration increases with the mainshock moment raised to the power 0.2. This weak and erratic seismic phase reflects the first seismogenic features of the fault's transition from a locked to a dynamic state. The near-source seismograms shown here provide empirical evidence for a period of nucleation that precedes dynamic earthquake rupture and might represent the final stage of an aseismic nucleation process.

References

Abercrombie, R. and P. Leary [1993]. Source parameters of small earthquakes recorded at 2.5 km depth, Cajon Pass, Southern California: implications for earthquake scaling, *Geophys. Res. Lett.*, 20, 1511-1514.

Abercrombie, R. and J. Mori [1994]. Local observations of the onset of a large earthquake: 28 June 1992 Landers, California, *Bull. Seism. Soc. Am.*, 84, 725-734.

Abercrombie, R.E., I.G. Main, A. Douglas and P.W. Burton [1995]. The nucleation and rupture process of the 1981 Gulf of Corinth earthquakes from deconvolved broad-band data, *Geophys. J. Int.*, 120, 393-405.

Agnew, D.C. and F.K. Wyatt [1989]. The 1987 Superstition Hills earthquake sequence: strains and tilts at Pinon Flat Observatory, *Bull. Seism. Soc. Am.*, 79, 480-492.

Aki, K. and P.G. Richards [1980]. *Quantitative Seismology: Theory and Methods*, W.H. Freeman, New York.

Ammon, C.J. and G. Zandt [1993]. Receiver structure beneath the southern Mojave block, *Bull. Seism. Soc. Am.*, 83, 737-755.

Ammon, C.J., A.A. Velasco, and T. Lay [1993]. Rapid estimation of rupture directivity: application to the 1992 Landers (M_s = 7.4) and Cape Mendocino (M_s = 7.2) California earthquakes, *Geophys. Res. Lett.*, 20, 97-100.

Andrews, D.J. [1976]. Rupture velocity of plane strain shear cracks, *J. Geophys. Res.*, 81, 5679-5687.

Bard, P.Y. and M. Bouchon [1985]. The two-dimensional resonance of sediment-filled valleys, *Bull. Seism. Soc. Am.*, 75, 519-542.

Beroza, G.C. [1989]. Near-source imaging of seismic rupture, *Ph.D. Thesis*, 198 pp., Mass. Inst. of Tech., Cambridge, MA.

Beroza, G.C. [1991]. Near-source modeling of the Loma Prieta earthquake: evidence for heterogeneous slip and implications for earthquake hazard, *Bull. Seism. Soc. Am.*, 81, 1603-1621.

Beroza, G.C. and P. Spudich [1988]. Linearized inversion for fault rupture behavior: application to the 1984 Morgan Hill, California, earthquake, *J. Geophys. Res.*, 93, 6275-6296.

Beroza, G.C., and M.D. Zoback [1993]. Mechanism diversity of the Loma Prieta aftershocks and the mechanics of mainshock-aftershock interaction, *Science*, 259, 210-213.

Beroza, G.C. and W.L. Ellsworth [1995]. Properties of the seismic nucleation phase, *Tectonophysics*, (in press).

Blanpied, M.L., D.A. Lockner, and J.D. Byerlee [1995]. Frictional slip of granite at hydrothermal conditions, *J. Geophys. Res.*, 100, 13045-13064.

Boatwright, J. [1980]. A spectral theory for circular seismic sources; simple estimates of source dimension, dynamic stress drop, and radiated seismic energy, *Bull. Seism. Soc. Am.*, 70, 1-27.

Boatwright, J. [1984]. Seismic estimates of stress release, *J. Geophys. Res.*, 89, 6961-6968.

Boatwright, J., and M. Cocco [1995]. The effect of lateral variations of friction on crustal faulting, *J. Geophys. Res.*, (in press).

Bonamassa, O., J.E. Vidale, H. Houston, and S.Y. Schwartz [1991]. Directional site resonances and the influence of near-surface geology on ground motion, *Geophys. Res. Lett.*, 18, 901-904.

Bortugno, E.J. [1986]. Map showing recency of faulting, San Bernardino Quadrangle, California, 1:250,000, *Regional Geologic Map Series*, Dept. of Conservation, Sacramento, CA.

Brune, J. [1970]. Tectonic strain and the spectra of seismic shear waves from earthquakes, *J. Geophys. Res.*, 75, 4997-5009.

Campillo, M. and R.J. Archuleta [1993]. A rupture model for the 28 June 1992 Landers, California, earthquake, *Geophys. Res. Lett.*, 20, 647-650.

Cifuentes, I.L. [1989]. The 1960 Chilean earthquakes, *J. Geophys. Res.*, 94, 665-680.

Cifuentes, I.L. and P.G. Silver [1989]. Low-frequency source characteristics of the great 1960 Chilean earthquake, *J. Geophys. Res.*, 94, 643-663.

Cocco, M. and A. Rovelli [1989]. Evidence for the variation of stress drop between normal and thrust faulting earthquakes in Italy, *J. Geophys. Res.*, 94, 9399-9416.

Cocco, M. and F. Pacor [1993]. The rupture process of the 1980 Irpinia, Italy, earthquake from the inversion of strong motion waveforms, *Tectonophysics,* 218, 157-177.

Cohee, B.P., P.G. Somerville, and N.A. Abrahamson [1991]. Simulated ground motions for hypothesized $M_W = 8$ subduction earthquakes in Washington and Oregon, *Bull. Seism. Soc. Am.*, 81, 28-56.

Cohee, B.P. and G.C. Beroza [1994a]. Slip distribution of the 1992 Landers earthquake and its implications for earthquake source mechanics, *Bull. Seism. Soc. Am.*, 84, 692-712.

Cohee, B.P. and G.C. Beroza [1994b]. A comparison of two methods for earthquake source inversion using strong motion seismograms, in Earthquake Source Mechanics (eds. M Bonafede and M. Cocco), *Annali di Geofisica,* 37, 1515-1538.

Cormier, V.F. and W.-J. Su [1994]. Effects of three-dimensional crustal structure on the estimated slip history and ground motion of the Loma Prieta earthquake, *Bull. Seism. Soc. Am.*, 84, 284-294.

Cotton, F. and M. Campillo [1995]. Frequency domain inversion of strong motions: application to the 1992 Landers earthquake, *J. Geophys. Res.*, 100, 3961-3975.

CSMIP [1992]. Processed CSMIP strong-motion records from the Landers, California earthquake of June 28, 1992; OSMS 92-09, 92-11, 92-13, 93-01, *Calif. Dept. of Conserv. Reports*, Sacramento, CA.

Dahlen, F.A. [1974]. On the ratio of *P*-wave to *S*-wave corner frequencies for shallow earthquake sources, *Bull. Seism. Soc. Am.*, 64, 1159-1180.

Das, S. and C.H. Scholz [1981]. Theory of time-dependent rupture in the Earth, *J. Geophys. Res.*, 86, 6039-6051.

Das, S. and B.V. Kostrov [1990]. Inversion for seismic slip rate history and distribution with stabilizing constraints: application to the 1986 Andreanof Islands earthquake, *J. Geophys. Res.*, 95, 6899-6913.

Day, S.M. [1982]. Three-dimensional finite-difference simulation of fault dynamics: rectangular faults with fixed rupture velocity, *Bull. Seism. Soc. Am.*, 72, 705-727.

Dieterich, J.H. [1979]. Modeling of rock friction: 1. Experimental results and constituitive equations, *J. Geophys. Res.*, 84, 2161-2168.

Dieterich, J.H. [1986]. A model for the nucleation of earthquake slip, in Earthquake Source Mechanics (eds. S. Das, J. Boatwright, and C.H. Scholz). American Geophysical Union, M. Ewing v.6, Geophysical Monographs, 37, 37-47.

Dieterich, J.H. [1992]. Earthquake nucleation on faults with rate- and state-dependent strength, *Tectonophysics*, 211, 115-134.

Dodge, D.A., G.C. Beroza and W.L. Ellsworth [1995]. Foreshock sequence of the 1992 Landers, California, earthquake and its implications for earthquake nucleation, *J. Geophys. Res.*, 100, 9865-9880.

Dreger, D.S. [1994a]. Investigation of the rupture process of the 28 June 1992 Landers earthquake utilizing TERRAscope, *Bull. Seism. Soc. Am.*, 84, 713-724.

Dreger, D.S. [1994b]. Empirical Green's function study of the January 17, 1994 Northridge, California, earthquake, *Geophys. Res. Lett.*, 21, 2633-2636.

Du, Y., A. Aydin, and P. Segall [1992]. Comparison of various inversion techniques as applied to the determination of a geophysical deformation model for the 1993 Borah Peak earthquake, *Bull. Seism. Soc. Am.*, 82, 1840-1866.

Dziewonski, A.M., T.A. Chou, and J.H. Woodhouse [1981]. Determination of earthquake source parameters from waveform data for studies of global and regional seismicity, *J. Geophys. Res.*, 86, 2825-2852.

Eberhart-Phillips, D., V.F. Labson, W.D. Stanely, A.J. Michael, and B.D. Rodriguez [1990]. Preliminary velocity and resistivity models of the Loma Prieta earthquake region, *Geophys. Res. Lett.*, 17, 1235-1238.

Eberhart-Phillips, D., L. Hwang, and J. Mori [1992]. Preliminary results from the July 1992 seismic calibration experiment along the 1992 Landers rupture, *EOS Trans. Am. Geophys. Union*, 73, 382.

Efron, B. and G. Gong [1983]. A leisurely look at the bootstrap, the jackknife, and cross-validation, *The American Statistician*, 37, 36-48.

Ekstrom, G.A. [1987]. A broad band method of earthquake analysis, *Ph.D. thesis*, 226 pp., Harvard Univ., Cambridge, MA.

Ellsworth, W.L. and G.C. Beroza [1995]. Seismic evidence for an earthquake nucleation phase, *Science* , 268, 851-855.

Eshelby, J.D. [1957]. The determination of the elastic field of an ellipsoidal inclusion and related problems, *Proc. Trans. Roy. Soc. London, Series A*, 241, 376-396.

Frankel, A. [1992]. Comment on "Rupture process of the 1987 Superstition Hills earthquake from the inversion of strong-motion data" by D.J. Wald, D.V. Helmberger, and S.H. Hartzell, *Bull. Seism. Soc. Am.*, 82, 1511-1518.

Frankel, A. and L. Wennerberg [1989]. Rupture process of the M_S 6.6 Superstition Hills, California, earthquake determined from strong-motion recordings: application of tomographic source inversion, *Bull. Seism. Soc. Am.*, 79, 515-541.

Freire, S.L.M and T.J. Ulrych [1988]. Application of singular value decomposition to vertical seismic profiling, *Geophysics*, 53, 778-785.

Frémont, M.-J. and S.D. Malone [1987]. High precision relative locations of earthquakes at Mount St. Helens, Washington, *J. Geophys. Res.*, 92, 10223-10236.

Freymueller, J, N.E. King, and P. Segall [1994]. Coseismic slip distribution of the Landers earthquake, *Bull. Seism. Soc. Am.*, 84, 646-659.

Fukuyama, E. and K. Irikura [1986]. Rupture process of the 1983 Japan Sea (Akita-Oki) earthquake using a waveform inversion method, *Bull. Seism. Soc. Am.*, 76, 1623-1640.

Fukuyama, E. and T. Mikumo [1993]. Dynamic rupture analysis: inversion for the source process of the 1990 Izu-Oshima, Japan, earthquake (M=6.5), *J. Geophys. Res.*, 98, 6529-6542.

Geller, R.J. [1976]. Scaling relations for earthquake source parameters and magnitudes, *Bull. Seism. Soc. Am.*, 66, 1501-1523.

Geller, R.J. and C.S. Mueller [1980]. Four similar earthquakes in central California, *Geophys. Res. Lett.*, 7, 821-824.

Hanks, T.C. and M. Wyss [1972]. The use of body-wave spectra in the determination of seismic source parameters, *Bull. Seism. Soc. Am.*, 62, 561-589.

Hanks, T.C. and W. Thatcher [1972]. A graphical representation of seismic source parameters, *J. Geophys. Res.*, 77, 4393-4405.

Hanks, T.C. and R.K. McGuire [1981]. The character of high-frequency strong ground motion, *Bull. Seism. Soc. Am.*, 71, 1897-1919.

Hartzell, S.H. [1978]. Earthquake aftershocks as Green's functions, *Geophys. Res. Lett.*, 5, 1-4.

Hartzell, S. [1989]. Comparison of seismic waveform inversion results for the rupture history of a finite fault: application to the 1986 North Palm Springs, California, earthquake, *J. Geophys. Res.*, 94, 7515-7534.

Hartzell, S.H. and T.H. Heaton [1983]. Inversion of strong ground motion and teleseismic waveform data for the fault rupture history of the 1979 Imperial Valley, California, earthquake, *Bull. Seism. Soc. Am.*, 73, 1553-1583.

Hartzell, S. and T. Heaton [1986]. Rupture history of the 1984 Morgan Hill, California, earthquake from the inversion of strong motion records, *Bull. Seism. Soc. Am.*, 76, 649-674.

Hartzell, S. and M. Iida [1990]. Source complexity of the 1987 Whittier Narrows, California, earthquake from the inversion of strong motion records, *J. Geophys. Res.*, 95, 12475-12485.

Hartzell, S.H. and C. Mendoza [1991]. Application of an iterative least squares waveform inversion of strong motion and teleseismic records to the 1978 Tabas, Iran, earthquake, *Bull. Seism. Soc. Am.*, 81, 305-331.

Hartzell, S.H., G.S. Stewart, and C. Mendoza [1991]. Comparison of L_1 and L_2 norms in a teleseismic waveform inversion for the slip history of the Loma Prieta, California, earthquake, *Bull. Seism. Soc. Am.*, 81, 1518-1539.

Haskell, N.A [1964]. Radiation pattern of surface waves from point sources in a multi-layered medium, *Bull. Seism. Soc. Am.*, 54, 377-394.

Hauksson, E., L.M. Jones, K. Hutton, and D. Eberhart-Phillips [1993]. The 1992 Landers earthquake sequence: seismological observations, *J. Geophys. Res.*, 98, 19835-19858.

Hauksson, E., L.M. Jones, and K. Hutton [1995]. The 1994 Northridge earthquake sequence in California: seismological and tectonic aspects, *J. Geophys. Res.*, 100, 12335-12355.

Heaton, T.H. [1982]. The 1971 San Fernando earthquake; a double event?, *Bull. Seism. Soc. Am.*, 72, 2037-2062.

Heaton, T.H. [1990]. Evidence for and implications of self-healing slip pulses in earthquake rupture, *Phys. Earth and Planet. Int*, 64, 1-20.

Hill, D.P., P.A. Reasenberg, et al. [1993]. Seismicity in the western United States remotely triggered by the M 7.4 Landers, California, earthquake of June 28, 1992, *Science*, 260, 1617-1623.

Hough, S.E., J. Mori, E. Sembera, G. Glassmoyer, C. Mueller, and S. Lydeen [1993]. Southern surface rupture associated with the 1992 M7.4 Landers earthquake: did it all happen during the mainshock? *Geophys. Res. Lett.*, 20, 2615-2618.

Hudnut, K.W., Y. Bock, et al. [1994]. Co-seismic displacements of the 1992 Landers earthquake sequence, *Bull. Seism. Soc. Am.*, 84, 625-645.

Iio, Y. [1992]. Slow initial phase of the P-wave velocity pulse generated by microearthquakes, *Geophys. Res. Lett.*, 19, 477-480.

Iio, Y. [1995]. Observations of the slow initial phase generated by microearthquakes: implications for earthquake nucleation and propagation, *J. Geophys. Res.*, 100, 15333-15349.

Jacobson, R.S. and P.R. Shaw [1991]. Using the F-test for eigenvalue decomposition problems to find the statistically 'optimal' solution, *Geophys. Res. Lett.*, 18, 1075-1078.

Johnson, A.M., R.W. Fleming, and K.M. Cruikshank [1994]. Shear zones formed along long, straight traces of fault zones during the 28 June 1992 Landers, California, earthquake, *Bull. Seism. Soc. Am.*, 84, 499-510.

Johnson, L.R. [1974]. Green's functions for Lamb's problem, *Geophys. J. R. Astr. Soc.*, 37, 99-131.

Johnston, M.J.S., A.T. Linde, and M.T. Gladwin [1990]. Near-field high resolution strain measurements prior to the October 18, 1989, Loma Prieta M_s 7.1 earthquake, *Geophys. Res. Lett.*, 17, 1777-1780.

Jones, L.M. [1984]. Foreshocks (1966-1980) in the San Andreas system, California, *Bull. Seism. Soc. Am.*, 74, 1361-1380.

Kanamori, H. and J.J. Cipar [1974]. Focal process of the great Chilean earthquake May 22, 1960, *Phy. Earth Planet. Int.*, 9, 128-136.

Kanamori, H. and D.L. Anderson [1975]. Theoretical basis of some empirical relations in seismology, *Bull. Seism. Soc. Am.*, 65, 1073-1095.

Kanamori, H., H.-K. Thio, D. Dreger, E. Hauksson, and T. Heaton [1992]. Initial investigation of the Landers, California earthquake of 28 June 1992 using TERRAscope, *Geophys. Res. Lett.*, 19, 2267-2270.

Kilgore, B.D., M.L. Blanpied, and J.H. Dieterich [1993]. Velocity dependent friction of granite over a wide range of conditions, *Geophys. Res. Lett.*, 20, 903-906.

Kostrov, B.V. [1964]. Self-similar problems of propagation of shear cracks, *J. Appl. Math. Mech.*, 28, 1077-1087.

Lawson, C.L. and R.J. Hanson [1974]. *Solving Least Squares Problems*, Prentice-Hall, Englewood Cliffs, NJ.

Lees, J.M. and C. Nicholson [1993]. Three-dimensional tomography of the 1992 southern California earthquake sequence: constraints on dynamic earthquake rupture?, *Geology*, 21, 387-390.

Liu, H.-L. and D.V. Helmberger [1983]. The near-source ground motion of the 6 August 1979 Coyote Lake, California, earthquake, *Bull. Seism. Soc. Am.*, 73, 201-218.

Liu, H.-L. and D.V. Helmberger [1985]. The 23:19 aftershock of the 15 October 1979 Imperial Valley earthquake: more evidence for an asperity, *Bull. Seism. Soc. Am.*, 75, 689-708.

Madariaga, R [1976]. Dynamics of an expanding circular fault, *Bull. Seism. Soc. Am.*, 66, 639-666.

Matthews, M.V. and P. Segall [1993]. Estimation of depth-dependent fault slip from measured surface deformation with application to the 1906 San Francisco earthquake, *J. Geophys. Res.*, 98, 12153-12163.

Massonnet, D., M. Rossi, et al. [1993]. The displacement field of the Landers earthquake mapped by radar interferometry, *Nature*, 364, 138-142.

Mendez, A.J. and J.E. Luco [1990]. Steady state, near-source models of the Parkfield, Imperial Valley, and Mexicali Valley earthquakes, *J. Geophys. Res.*, 95, 327-340.

Mendez, A.J., A.H. Olson, and J.G. Anderson [1990]. A norm minimization criterion for the inversion of earthquake ground motion, *Geophys. J. Int.*, 102, 287-298.

Mendez, A.J. and J.G. Anderson [1991]. The temporal and spatial evolution of the 19 September 1985 Michoacán earthquake as inferred from near-source ground-motion records, *Bull. Seism. Soc. Am.*, 81, 844-861.

Mendoza, C. and S.H. Hartzell [1988]. Aftershock patterns and mainshock faulting, *Bull. Seism. Soc. Am.*, 78, 1438-1449.

Mendoza, C. and S.H. Hartzell [1989]. Slip distribution of the 19 September 1985 Michoacán, Mexico, earthquake: near-source and teleseismic constraints, *Bull. Seism. Soc. Am.*, 79, 655-669.

Menke, W. [1984]. *Geophysical Data Analysis: Discrete Inverse Theory*, Academic Press, Orlando, Florida.

Mikumo, T. [1992]. Dynamic fault rupture and stress recovery processes in continental crust under depth-dependent shear strength and frictional parameters, *Tectonophysics*, 211, 201-222.

Mikumo, T. and T. Miyatake [1993]. Dynamic rupture processes on a dipping fault, and estimates of stress drop and strength excess from the results of waveform inversion, *Geophys J. Int.*, 112, 481-496.

Mikumo, T. and T. Miyatake [1995]. Heterogeneous distribution of dynamic stress drop and relative fault strength recovered from the results of waveform inversion: the 1984 Morgan Hill, California, earthquake, *Bull. Seism. Soc. Am.*, 85, 178-193.

Mori, J. and A. Frankel [1990]. Source parameters for small events associated with the 1986 North Palm Springs, California, earthquake determined using empirical Green's functions, *Bull. Seism. Soc. Am.*, 80, 278-295.

Mueller, C. and G. Glassmoyer [1990]. Digital recordings of aftershocks of the 17 October 1989 Loma Prieta, California, Earthquake, *U.S. Geol. Surv. Open-File Rep. 90-503*, 147 pp.

Murray, M.H., J.C. Savage, M. Lisowski, and W.K. Gross [1993]. Coseismic displacements: 1992 Landers, California, earthquake, *Geophys. Res. Lett.*, 20, 623-626.

Nabelek, J.L. [1984]. Determination of earthquake source parameters from inversion of body waves, *Ph.D. thesis*, 346 pp., Mass. Inst. of Tech., Cambridge, MA.

Nur, A., H. Ron., and G.C. Beroza [1993]. The nature of the Landers-Mojave seismic line, *Science*, 261, 201-203.

Ohnaka, M. [1993]. Critical size of the nucleation zone of earthquake rupture inferred from immediate foreshock activity, *J. Phys. Earth*, 41, 45-56.

Ohnaka, M and T. Yamashita [1989]. A cohesive zone model for dynamic shear faulting based on experimentally inferred constitutive relation and strong motion source parameters, *J. Geophys. Res.*, 94, 4089-4104.

Ohnaka, M. and Y. Kuwahara [1990]. Characteristic features of local breakdown near a crack-tip in the transition zone from nucleation to unstable rupture during stick-slip shear failure, *Tectonophysics*, 175, 197-220.

Ohnaka, M., Y. Kuwahara, K. Yamamoto, and T. Hirasawa [1986]. Dynamic breakdown processes and the generating mechanism for high-frequency elastic radiation during stick-slip instabilities, in *Earthquake Source Mechanics* (eds. S. Das, J. Boatwright, and C.H. Scholz), M. Ewing v. 6, Geophysical Monographs, 37, 13-24, American Geophysical Union.

Olson, A.H. [1987]. A Chebyshev condition for accelerating convergence of iterative tomographic methods - solving large least squares problems, *Phys. Earth Planet. Inter.*, 47, 333-345.

Olson, A.H. and R.W. Apsel [1982]. Finite faults and inverse theory with applications to the 1979 Imperial Valley earthquake, *Bull. Seism. Soc. Am.*, 72, 1969-2001.

Ponti, D.J. [1992]. Quaternary chronostratigraphy and deformation history, Los Angeles basin, California: *NEHRP Sum. Tech. Rep.*, 24, 588-592.

Poupinet, G., W.L. Ellsworth, and J. Fréchet [1984]. Monitoring velocity variations in the crust using earthquake doublets: an application to the Calaveras fault, California, *J. Geophys. Res.*, 89, 5719-5731.

Press, W.H., B.P. Flannery, S.A. Teukolsky, and W.T. Vetterling [1989]. *Numerical Recipes*, Cambridge University Press, Cambridge.

Quin, H. [1990]. Dynamic stress drop and rupture dynamics of the October, 15, 1979 Imperial Valley, California, earthquake, *Tectonophysics*, 175, 93-117.

Rice, J.R. [1980]. The mechanics of earthquake rupture, in *Physics of the Earth's Interior* (eds. A.M. Dziewonski and E. Boschi), Italian Physical Society and North-Holland Pub. Co., 555-649.

Rice, J.R. [1992]. Fault stress states, pore pressure distributions, and the weakness of the San Andreas fault, in *Fault Mechanics and Transport Properties in Rocks* (eds. B. Evans and T.-F. Wong), Academic Press, 475-503.

Rice, J.R. and J.-C. Gu [1983]. Earthquake aftereffects and triggered seismic phenomena, *Pure and Appl. Geophys.*, 121, 187-219.

Riedesel, M.A., D. Agnew, J. Berger, and F. Gilbert [1980]. Stacking for the frequencies and Qs of ${}_0S_0$ and ${}_1S_0$, *Geophys. J. R. Astr. Soc.*, 62, 457-471.

Saikia, C.K. [1994]. Modified frequency-wavenumber algorithm for regional seismograms using Filon's quadrature - modeling of *Lg* waves in Eastern North America, *Geophys. J. Inter.*, 118, 142-158.

Sato, T. [1994]. Seismic radiation from circular cracks growing at variable rupture velocity, *Bull. Seism. Soc. Am.*, 84, 1199-1215.

Scholz, C. H., [1990]. *The Mechanics of Earthquake Rupture*, Cambridge University Press, Cambridge.

Schwartz, D.P., and K.J. Coppersmith [1984]. Fault behavior and characteristic earthquakes: examples from the Wasatch and San Andreas fault zones, *J. Geophys. Res.*, 89, 5681-5698.

Segall, P. and M.V. Matthews [1988]. Displacement calculations from geodetic data and the testing of geophysical deformation models, *J. Geophys. Res.*, 93, 14954-14966.

Segall, P. and Y. Du [1993]. How similar were the 1934 and 1966 Parkfield earthquakes?, *J. Geophys. Res.*, 98, 4527-4538.

Sieh, K., L. Jones, et al. [1993]. Near-field investigations of the Landers earthquake sequence, April to July 1992, *Science*, 260, 171-176.

Somerville, P., M. Sen, and B. Cohee [1991]. Simulation of strong ground motions recorded during the 1985 Michoacán, Mexico and Valparaíso, Chile Earthquakes, *Bull. Seism. Soc. Am.*, 81, 1-27.

Spakman, W. and G. Nolet [1988]. Imaging algorithms, accuracy, and resolution in delay time tomography, in *Mathematical Geophysics*, 155-188, D. Reidel, Dordrecht.

Spudich, P. and L.N. Frazer [1984]. Use of ray theory to calculate high-frequency radiation from earthquake sources having spatially variable rupture velocity and stress drop, *Bull. Seism. Soc. Am.*, 74, 2061-2082.

Spudich P. and R.J. Archuleta [1987]. Techniques for earthquake ground-motion calculation with applications to source parameterization of finite faults, in *Seismic Strong Motion Synthetics* (ed. B.A. Bolt), 205-265, Academic Press, London.

Spudich P. and D.P. Miller [1990]. Seismic site effects and the spatial interpolation of earthquake seismograms: results using aftershocks of the 1986 North Palm Springs, California, earthquake, *Bull. Seism. Soc. Am.,* 80, 1504-1532.

Spudich, P. and M. Iida [1993]. The seismic coda, site effects, and scattering in alluvial basins studied using aftershocks of the 1986 North Palm Springs, California, earthquake as source arrays, *Bull. Seism. Soc. Am.*, 83, 1721-1743.

Steidl, J.H., R.J. Archuleta, and S.H. Hartzell [1991]. Rupture history of the 1989 Loma Prieta, California earthquake, *Bull. Seism. Soc. Am.*, 81, 1573-1602.

Takeo, M. [1987]. An inversion method to analyze the rupture processes of earthquakes using near-field seismograms, *Bull. Seism. Soc. Am.*, 77, 490-513.

Tarantola, A. and B. Valette [1982]. Inverse problems=quest for information, *J. Geophys. Res.*, 50, 159-170.

Thatcher, W. and T.C. Hanks [1973]. Source parameters of southern California earthquakes, *J. Geophys. Res.*, 78, 8547-8576.

Thio, H.-K. and H. Kanamori [1995]. Moment-tensor inversions for local earthquakes using surface waves recorded at TERRAscope, *Bull. Seism. Soc. Am.*, 85, 1021-1038.

Vidale, J.E. [1989]. Influence of focal mechanism on peak accelerations of the Whittier Narrows, California, earthquake and its one aftershock, *J. Geophys. Res.*, 94, 9607-9613.

Wahba, G. [1990]. *Spline Models for Observational Data*, Society for Industrial and Applied Mathematics, Philadelphia, PA.

Wald, D.J. [1992]. Strong motion and broadband teleseismic analysis of the 1991 Sierra Madre, California, earthquake, *J. Geophys. Res.*, 97, 11033-11046.

Wald, D.J. [1995]. A preliminary dislocation model for the 1995 Kobe (Hyogo-ken Nanbu), Japan, earthquake determined from strong motion and teleseismic waveforms, *Seism. Res. Lett.*, v.66, no.4, 22-28.

Wald, D.J. and T.H. Heaton [1994a]. Spatial and temporal distribution of slip for the 1992 Landers, California earthquake, *Bull. Seism. Soc. Am.*, 84, 668-691.

Wald, D.J. and T.H. Heaton [1994b]. A dislocation model of the 1994 Northridge, California, earthquake determined from strong ground motions, *U.S. Geol. Surv. Open -File Rep. 24-278*, 55 pp.

Wald, D.J., D.V. Helmberger, and S.H. Hartzell [1990]. Rupture process of the 1987 Superstition Hills earthquake from the inversion of strong-motion data, *Bull. Seism. Soc. Am.*, 80, 1079-1098.

Wald, D.J., D.V. Helmberger, and T.H. Heaton [1991]. Rupture model of the 1989 Loma Prieta earthquake form the inversion of strong-motion and broadband teleseismic data, *Bull. Seism. Soc. Am.*, 81, 1540-1572.

Wang C.Y. and R. B. Herrmann [1980]. A numerical study of *P*-, *SV*-, and *SH*-wave generation in a plane layered medium, *Bull. Seism. Soc. Am.*, 70, 1015-1036

Wyatt, F.K., D.C. Agnew, and M.T. Gladwin [1994]. Continuous measurements of crustal deformation for the 1992 Landers earthquake sequence, *Bull. Seism. Soc. Am.*, 84, 768-779.